SETCOR
Conferences & Exhibitions

Nanotech Dubai 2015 International Conference Proceeding

http://www.setcor.org/conferences/Nanotech-Dubai-2015

Sonolytic Synthesis of Iron- and Alkaline Earth-Based Magnetic Nanomaterials : Single and Mixed Metal Nanostructured Materials

Gerard L. Moore[1], Dhananjay Kumar[2] and Kenneth L. Roberts[3,*]

[1] DuPont Chemical Company, DuPont Washington Works, 8480 DuPont Road, Washington, West Virginia, U.S.A.
[2] North Carolina A&T University, Department of Mechanical Engineering, Greensboro, NC, U.S.A.
[3] King Faisal University, College of Engineering, Department of Chemical Engineering, Al Hofuf, Al Ahsa, K.S.A.

Abstract: Fe_2O_3 and $CaCO_3$ nanomaterials are currently being investigated for nanotherapeutic applications such as medical bioimaging, drug delivery, gene therapy and targeted thermal cancer treatment. Sonolytic cavitation of metal-based parent materials has been demonstrated to be an effective synthesis route for the production of nanoparticles and other nanostructured materials. Fe-based and alkaline earth metal (Ca- and Mg-based) nanostructured materials were synthesized using ultrasonic irradiation. When specifically considering the application of bimetallic nanomaterials, additional design considerations included the control of relative metal compositions and requirements of production consistency regarding the layering of active metal on the surfaces of the nanomaterials.

Materials and Methods: $FeCl_2 \cdot 4H_2O$ (99+%, $CaCl_2 \cdot 2H_2O$ (99+% A.C.S reagent), $Mg(ClO_4)_2$ and NH_4OH (Certified ACS Plus) were used in this work without additional purification. Predetermined amounts of the single and binary metal chloride salt solutions were dispersed for 8 hours using an L&R Solid State/Ultrasonic T-28B bath with calculated amounts of ammonium hydroxide added to the metal chloride solutions both before and after sonication.

The precipitates were allowed to settle, separated via centrifugation and subsequently washed and dried using vacuum at 200 ^oC. X-ray diffraction (XRD) and Environmental Scanning Electron Microscopy (ESEM) were employed to investigate the nanocrystalline structure, elemental composition and surface morphology of the product materials. X-ray diffraction analyses were performed using a Bruker D8 ADVANCE Series-2 X-ray diffractometer (Bruker AXS) equipped with a CuKα radiation source (λ = 1.54 Å). The average crystallite sizes were estimated based on the peak-widths using the Scherrer equation. Environmental Scanning Electron Microscopy (ESEM) measurements were performed using an FEI Quanta 200 Field Emission Environmental Scanning Electron Microscope in high vacuum mode.

Results:

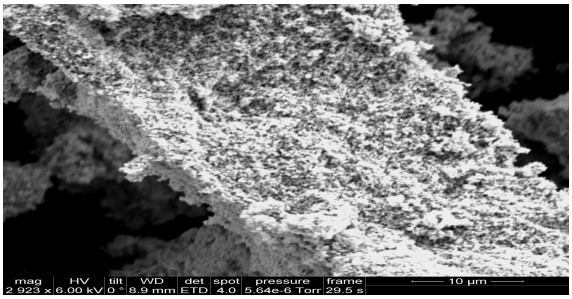

Figure 1: Ca-Fe Nanostructured Product.

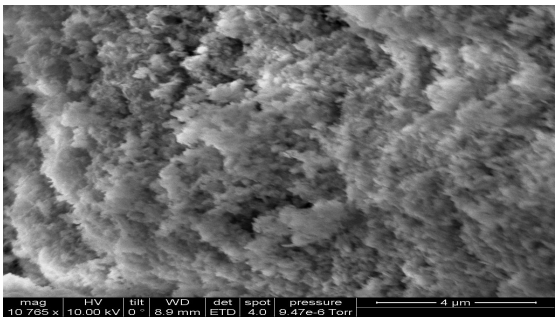

Figure 2: Mg-Fe Nanostructured Product.

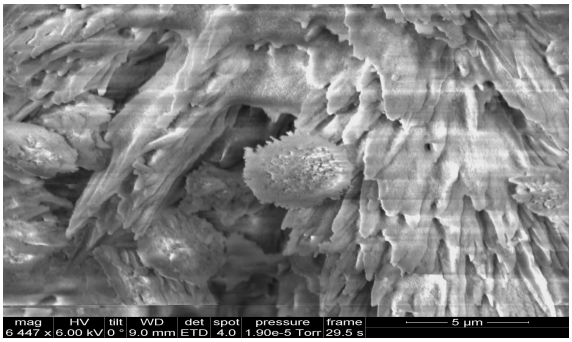

Figure 3: Ca-Mg Nanostructured Product.

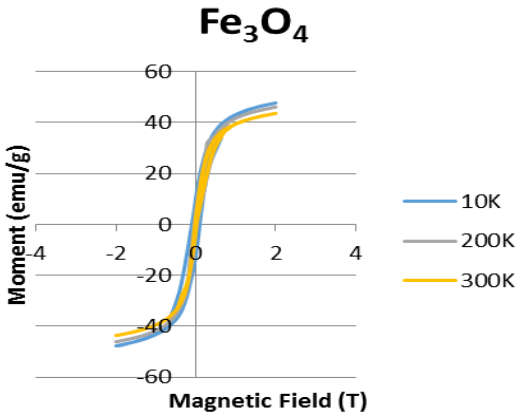

Figure 4: Magnetite SQUID Results.

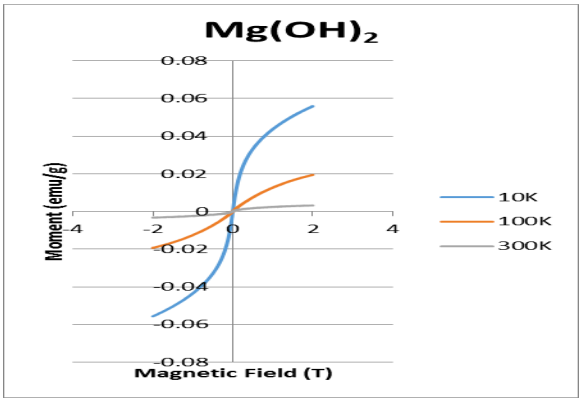

Figure 5: $Mg(OH)_2$ SQUID Results.

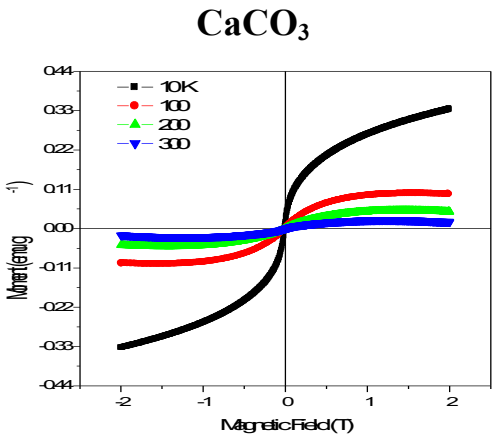

Figure 6: Calcite SQUID Results.

Conclusions: Fe, Ca and Mg-based chloride salts were reacted sonolitically with NaOH and the products characterized using XRD, elemental analysis, ESEM and SQUID measurements. Morphology and crystallite sizes were affected by the chemical composition of the synthesis mixture and upon the sequence of NH_3OH addition to the metal chloride solutions. Several interesting structural morphologies were produced in Mg/Ca, Mg/Fe, Mg/Ca mixtures and pure $CaCO_3$. Overall nanocrystallite sizes were estimated using Scherrer analysis to range from 5.92 to 72.13 nm.

Keywords Magnetite, Alkaline Earth Metals, Bimetallic, Nanostructured Materials, Sonolytic Synthesis, Ultrasonics, Magnetic Nanomaterials.

Acknowledgements The authors would like to thank the GEM Fellowship Program, the National Science Foundation Science and Technology Center for Environmentally Responsibly Solvents and Processes (CHE-9876674), Dr. Zhigang Xu (XRD analysis) with the National Science Foundation Science and Technology Center for Advanced Materials and Smart Structures, Dr. Wallace Ambrose and University of North Carolina CHANL, the Department of Chemical Engineering at North Carolina Agricultural and Technical State University, and the College of Engineering and Department of Chemical Engineering at King Faisal University for their support.

ONE-STEP SYNTHESIS OF GOLD NANOPARTICLES STABILIZED IN ACID-ACTIVATED MONTMORILLONITE FOR NITROPHENOL REDUCTION

F. Ammari*, S. Sakrane and M. Chenouf

LGPC, Department of chemical process engineering, Ferhat-Abbas Sétif-1 University
19000 Sétif, Algérie, phone : 213 36.92.51.33, fax : 213 36.92.51.33, e-mail: ammarifatima@yahoo.fr
* To whom correspondence should be addressed

ABSTRACT

Gold nanoparticles were prepared by one-step for the first time using chemical reduction from HAuCl4.3H2O gold precursor by sodium borohydride ($NaBH_4$) in presence of acid-activated montmorillonite us stabilizer. The obtained gold nanoparticles stabilized in montmorillonite were used as catalysts for reduction of 4-nitrophenol to aminophenol with sodium borohydride at room temperature. The UV-Vis results confirm directly the gold nanaoparticles formation. The XRD N_2 adsorption and MET results showed the formation of gold nanoparticles in the pores of montmorillonite with an average size of 5.7nm with uniform distribution. The reduction reaction of 4-nitrophenol into 4-aminophenol with $NaBH_4$ catalyzed by Au°-montmorillonite catalyst exhibits remarkably a high activity; the reaction was completed within 4.5min.
Keywords: gold; montmorillonite; 4-nitrophenol; nanoparticles; chemical reduction method.

1. INTRODUCTION

Synthesis of gold nanoparticles (AuNPs) has attracted much attention since the pioneering discovery of the high catalytic activity of supported gold nanoparticles in the reaction of CO oxidation at low temperature [1]. Reduction of 4-nitrophenol (4-NP) to 4-aminophenol (4-AP) is an important reaction in the preparation of analgesic and antipyretic agent such as paracetamol [2]. Apart from this; this reaction is mostly used us a reaction model for testing the gold nanoparticles reactivity [3]. Recently clay mineral have been attracted much attention because of their environmentally benign, cost and abundance. Deposition of highly dispersed small gold nanoparticles on the surfaces of montmorillonite and sepiolite was reported by Zhu et al. [4]. On the other hand, Letaief et al. [5] confirmed that AuNPs can be deposited on the external surface of sepiolite, moreover they found that the control of gold particle size can be achieved by controlling the acidic pre-treatment conditions of this clay mineral. In this research field, we used montmorillonite pre-acidified under gentle conditions for AuNPs stabilization; the AuNPs were obtained using chemical reduction method with some modification compared to reduction method reported in literature. In this study, the catalytic reduction of 4-nitrophenol by gold nanoparticles stabilized on montmorillonite using $NaBH_4$ as reductant agent was investigated. Moreover the resulting samples; montmorillonite and gold-montmorillonite were characterized by several methods, UV-Vis spectroscopy, X-ray Diffraction (XRD), transmission electron microscopy TEM and N_2 adsorption.

2. EXPERIMENTAL

The 2wt% Au stabilized in acid-activated montmorillonite (Amont) was prepared by one-step reducing 10ml of $HAuCl_4.3H_2O$ solution (0.05mmol Au) with 10ml of $NaBH_4$ aqueous solution (4mmol) in presence of 10ml of Amont suspension (0.5g). The $NaBH_4$ solution was added slowly and the mixture was kept under vigorous stirring for 1h at room temperature. After centrifugation and washing of three times with distilled water, the samples were dried overnight at 60°C and the collected samples were designed as Au-Amont. The preparations and storage were performed in the absence of light. The 4-nitrophenol reduction was carried out in liquid phase at room temperature. Typically, 10ml of $NaBH_4$ (10mmol) aqueous solution was added to 10mg of Au-Amont (0.2mg Au) previously dispersed in 10ml of distilled water, at this mixture 10ml of aqueous solution of 4-NP (0.1mmol) was added under vigorous stirring. The molar ratio of Au:4-NP:$NaBH_4$ used in this reaction was 1 :100 :10000. The reduction process was monitored by UV-Vis absorption spectrometry.

3. RESULTS

UV-Vis spectrometry results immediately confirmed the gold nanoparticles formation by analysis of suspension of gold-montmorillonite during preparation**.** A large band centred at 520nm corresponding to small gold particles was observed. BET results showed that, after acidification, the surface area of Na-mont increased, but significant decrease of surface area was observed for Au-Amont. The diameter pore value confirmed the presence of mesopores on Na-mont and A-mont samples. The decrease in surface area on Au-Amont can be attributed to nanoparticles gold stabilization within the mesopores of acidified montmorillonite. The insertion of gold nanoparticles into montmorillonite was also confirmed bby the XRD analysis. TEM images confirmed that the gold particles appeared as homogeneously dispersed on the A-mont stabilizer with observed average particle size of 5.7nm. In this study, gold nanoparticles AuNPs were successfully prepared in one-step by using a facile preparation method in presence of acid-activated montmorillonite as stabilizer agent. The catalytic activity of the synthesized Au-Amont was investigated for 4-nitrophenol with an excess amount of $NaBH_4$. A good linear correlation has been obtained and a calculated value of rate constant is about 1.79 10^{-2} s^{-1}, this result confirmed the high activity of Au-Amont in 4-NP reduction. This work represents the use of acid-activated montmorillonite for gold nanoparticles synthesis in one-step by a simple method; this facile preparation can be used for other metal nanoparticles preparation.

REFERENCES

1. Haruta, M.; Yamada, N.; Kobayashi, T.; Iijima, S. Journal of Catalysis. 115 (1989) 301.
2. Y. Niu, R M. Crooks Comptes Rendus Chimie 6, Issues 8–10 (2003) 1049.
3. K. Kuroda, T. Ishida, M. Haruta, Journal of Molecular Catalysis A: Chemical 298 (2009) 7.
4. L Zhu, S Letaif, Y Liu, F Gervais, C Detellier Applied Clay Science 43 (2009) 439.
5. S Letaif, Y Liu, S Grant, C Detellier Applied Clay Science 53 (2011) 236.
6. C. Lin, K. Tao, D. Hua, Z. Ma and S. Zhou Molecules ,18 ISSN 1420-3049 (2013) 12610.

Higher Order Modes Excitation of Micro Clamped-Clamped Beams

N. Jaber, A. Ramini, A. Carreno, M.I Younis
King Abdullah University of Science and Technology, Thuwal, KSA

ABSTRACT
In this study, we present experimental investigation of electrically actuated clamped-clamped microbeam resonators. The objective is to excite the higher order modes of the microbeams using partial electrodes with shapes that induce strong excitation of the mode of interest. The devices are fabricated using polyimide as a structural layer coated with Nickel from top and Chrome and Gold layers from bottom. Using a high frequency laser Doppler vibrometer, the first three resonance frequencies are revealed via white noise signals. Then, we studied the nonlinear dynamics of the microbeamsnear these resonance frequencies by applying forward and backward frequency sweeps with different electro dynamical loading conditions. The reported results prove the ability to excite higher order modes effectively using partial electrodes. Using a half electrode, the second mode is excited with high amplitude compared with almost zero response using the full electrode. Also, using the two-third electrode configuration increases the third mode resonance amplitude compared with the full electrode under the same electrical loading conditions. Such micro-resonator is shown to be promising in gas and mass detection applications.

Keywords
Resonator, electrostatic, higher order modes, partial electrode, microbeam.

1. INTRODUCTION
MEMS or Micro-electromechanical systems are devices and technologies that have been derived from the microelectronics industry. Researchers investigated ways to create Micro-electromechanical devices using microelectronic fabrication method. MEMS devices have salient features, such as the smaller sizes, the ability to work in harsh environments and power efficiency [1, 2].

In particular, MEMS resonators such as microplates and microbeams are the main building block of many MEMS sensors and actuators that are used in variety of applications, such as toxic gas sensors [3], mass and biological sensors [4,5], temperature sensors[6], force and acceleration sensors [7], and earthquake detectors [8]. The demand to develop sensors with high sensitivity and low power consumption is driving the development of micro-beam based resonators [3, 4]. MEMS resonators are excited using different types of forces, such as electromagnetic [9, 10], thermal [11], and electrostatic [8]. Electrostatic actuation is the most commonly used method because of its simplicity and availability [12]. An efficient approach to improve the oscillation of electrostatically actuated resonator is to use parametric excitation [13] and secondary resonance [14]. Moreover, Alsaleem *et al* [15] proved experimentally and analytically that MEMS resonator can be stabilized using a delayed feedback controller.

In this paper, we present experimental data of an electrically actuated micro clamped-clamped beams near their resonance frequencies.

2. BACKGROUND
MEMS resonators excited near their higher order modes have been proposed for mass and gas detection. Exciting the resonators near their higher order modes improve the sensitivity and the quality factor of the mass sensor. Jen *et al* [10] defined the sensitivity S_n and the quality factor Q_n of a resonant cantilever as

$$S_n = \frac{\omega'_n - \omega_n}{m} \approx \frac{-\omega_n}{2m_{eff}} \tag{2.1}$$

$$Q_n = 3\pi bh\omega_n (256\mu)^{-1} \tag{2.2}$$

where m is the cantilever mass, m_{eff} is the n^{th} mode effective mass of the cantilever, ω_n is the resonance frequency of the cantilever, ω'_n is the final resonance frequency after detecting a mass, b is the beam width, h is the thickness and μ is the air viscosity. As noticed from Eq. (1.1) and Eq. (1.2) the sensitivity and the quality factor are directly proportional to the excited mode number. High quality factor implies a sharper and stable resonance peak. This can be achieved through increasing ω_n and decreasing m_{eff} ; both are achieved through high-order mode excitations.

3. DESIGN
Our goal is to excite the higher modes by changing the lower electrode configuration such that it, to some extent, resembles the excited mode shape of the clamped-clamped micro-beam. As we can see in Fig. 1, we use full electrode to excite first mode, half electrode to excite the second mode, and two-third electrodes spaced out along the beam length to excite the third mode.

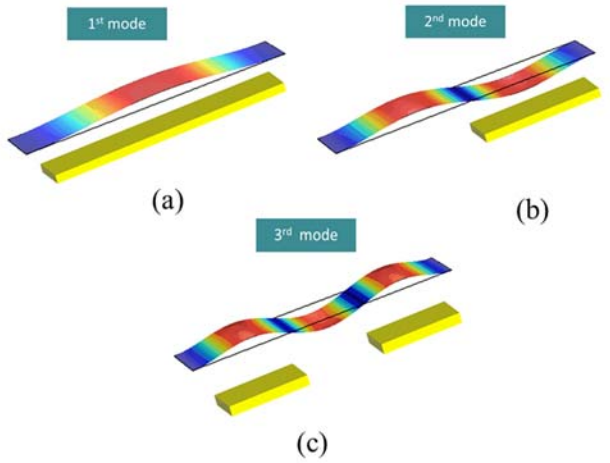

Figure 1: Clamped-clamped mode shapes with different lower electrode configuration. (a) Full electrode. (b) Half electrode. (c) Two-third electrode.

4. FABRICATION

The clamped-clamed microbeam resonators are fabricated using the in-house process developed in [16, 17], Fig. 2. The microbeam consists of a 6 µm Polyimide structural layer coated with 500 nm Nickel layer from top and 50nm Chrome, 250 nm Gold and 50 nm Chrome from bottom which form the upper electrode. The lower electrode is placed directly underneath the microstructure and composed of gold and chrome layers. The lower electrode length and position matches the excited mode of vibration shape and provides the actuation force to the resonator. The two electrodes are separated with a 2 µm air gap. When the two electrodes connected to an external excitation force the resonator vibrates in the out-of-plane direction. Fig. 2 shows a schematic illustrating the various layers of the fabricated resonator.

Color	Material	Thickness	Length	Width	Modulus of Elasticity	Density
	Silicon Wafer	5 mm				
	SiO_2	500 μm				
	Cr	50 nm	400 μm	40 μm	279 GPa	7190 Kg/m^3
	Au	500 nm			79 GPa	19300 Kg/m^3
	Au	250 nm	400 μm	40 μm	79 GPa	19300 Kg/m^3
	Pi	6 μm	400 μm	50 μm	8.5 GPa	1400 Kg/m^3
	Ni	500 nm	400 μm	50 μm	70 GPa	8908 Kg/m^3

Figure 2: Cross sectional view of the fabricated microbeam.

5. CHARCTRIZATION

In this section we describe the experimental set up used for testing the devices and measuring the initial profile, gap thickness and the out-of-plane vibration. The characterization is conducted on three microbeams that have different lower electrode configuration: full electrode, half electrode and two-third electrode.

The experimental setup consists of a micro system analyzer (MSA), which is a high-frequency laser Doppler vibrometer, under which the microstructure is placed to measure its vibration, data acquisition cards and amplifier to provide actuation signals of wide range of frequencies and amplitudes, and a vacuum chamber equipped with ports to pass the actuation signal and measure the pressure. Also, it is hooked up to a vacuum pump that reduces the pressure up to 20 mPa . The setup is shown in Fig.3.

5.1 Topography characterization

The initial profile of the micro-beams is revealed using an optical profilometer, which generates a 3-D map of the microstructure as seen from top for the half electrode micro-beam, Fig. 4. The combined thickness of the micro-beam and air gap is around 9 µm, which is slightly smaller from the design nominal value of 9.35 µm. Also, the micro structure profile is fully straight without any curvature or curling.

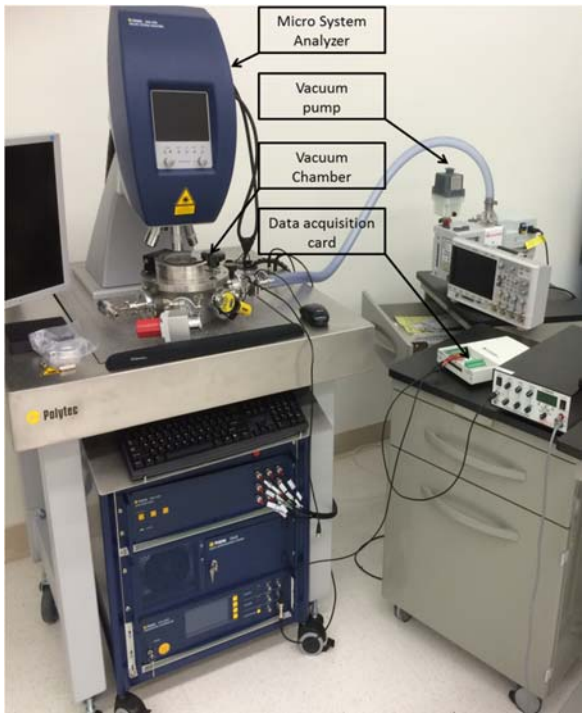

Figure 3: Experimental setup used for testing the MEMS devices.

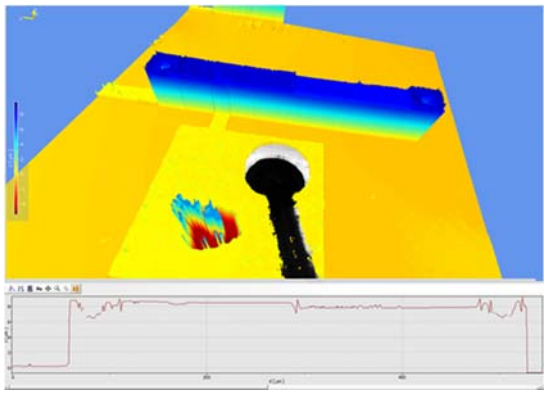

Figure 4: A 3D map of the microbeam as seen from top.

5.2 Natural frequencies

We experimentally measured the first three natural frequencies by connecting the wire bonded chip to the MSA function generator and applying a white noise signal. The MSA measures the microstructure vibration at the laser point position. Also, it has the capability to reveals the mode shape of the vibration.

5.2.1 Full electrode

The microstructure is excited with a white noise of V_{DC} = 10 V and V_{AC} = 8.5 V. We also scan the vibration at different points along the beam length to reveal the modeshapes. First, the test is performed for the case of a full electrode. The acquired frequency response curve is shown in Fig. 5, which reveals the values of the first and third mode natural frequencies ω_1 = 158 kHz, and ω_3 = 729 kHz. The RMS value of the scanned mode shape is reported in Fig.6.

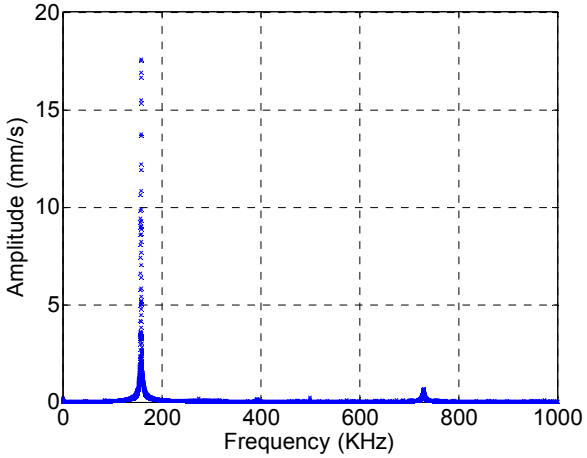

Figure 5: Frequency response curve of a full electrode microbeam to white noise actuation signal. V_{DC} = 10 V and V_{AC} = 8.5 V. at 20 *mPa* chamber pressure.

We notice at ω_1 in Fig. 6(a) that all the points are vibrating whereas at ω_3 Fig. 6(b) there are two nodal points. This result matches the clamped-clamped structure first and third vibration mode shape.

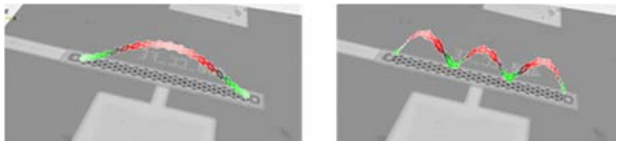

(a) (b)

Figure 6: RMS values of the vibrational mode shapes of full electrode microbeam at (a) ω_1 = 158.2 kHz, (b) ω_3 = 729 kHz.

5.2.2 Half electrode

The microstructure is next excited with a white noise of V_{DC} = 30 V and V_{AC} = 24.5 V. Also here we scan the vibration at different points along the beam length. The acquired frequency response curve is shown in Fig. 7 revealing the values of the first, second, and third mode natural frequencies ω_1 = 161 kHz, ω_2 = 398 kHz and ω_3 = 731 kHz, respectively. The RMS values of the scanned mode shapes are reported in Fig.8. This result illustrates the ability to excite the second mode using half electrode configuration.

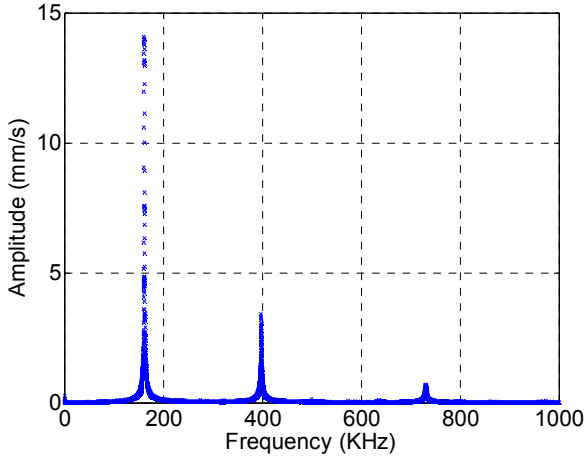

Figure 7: Frequency response curve of a half electrode microbeam to white noise actuation signal. V_{DC} = 30 V and V_{AC} = 24.5 V. at 20 *mPa* chamber pressure.

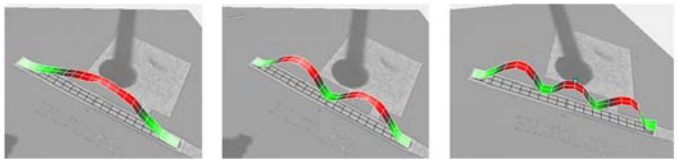

(a) (b) (c)

Figure 8: RMS values of the vibrational mode shapes of a half electrode microbeam at (a), ω_1 =161 kHz, (b) ω_2 = 398 kHz and ω_3 = 738 kHz.

5.2.3 Two-third electrode

Next, the microstructure is excited with a white noise at V_{DC} = 30 V and V_{AC} =16 V. The acquired frequency response curve is shown in Fig. 9 and it reveals the values of the first and third mode natural frequencies ω_1 = 157.9 kHz and ω_3 = 721 kHz, respectively. The RMS value of the scanned mode shape is reported in Fig.10. As shown; the amplitude of the third mode is higher compared with the full and half electrode configuration.

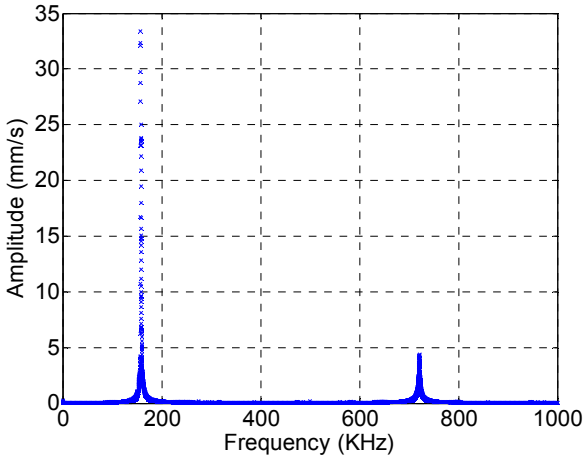

Figure 9: Frequency response curve of a two-third micro-beam to white noise actuation signal. V_{DC} = 30 V and V_{AC} = 16 V. at 20 *mPa* chamber pressure.

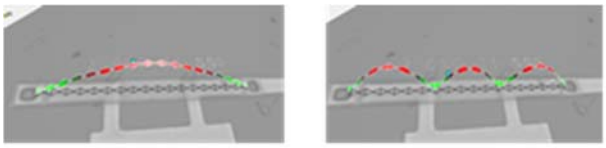

(a) (b)

Figure 10: RMS values of the vibrational mode shapes of full electrode micro-beam at (a) ω_1 = 157.9 kHz, (b) ω_3 = 721 kHz.

5.3 Frequency sweep

We experimentally investigate the nonlinear response of the microbeams near the first three resonance frequencies via frequncy sweep tests. The micro-beams are excited using the data acquisition card and the vibration is detected using the MSA. The excitation signal is composed of an AC signal V_{AC} superimposed to a DC signal V_{DC}.

The AC signal frequency is swept around the resonance frequency of interest. The frequency response curve is generated by taking the steady state amplitude of the motion and focusing the laser at the mid-point of the microbeam for the first and third mode measurement and at quarter of the beam length for the second mode measurement. In the following subsection the frequency response curves are reported for the different microbeams at different electrodynamical loadings and at 20 *mPa* chamber pressure.

5.3.1 First mode

Figure 11 shows the variation of the frequency response curve as the AC voltage is increased for different lower electrode configuration near the first resonance. As expected, using the full electrode configuration we achieved higher amplitude near the first mode compared with the other two configurations under the same conditions of electro dynamical loading and vacuum chamber pressure. Also, a hardening effect is reported due to the cubic nonlinearities from mid-plane stretching.

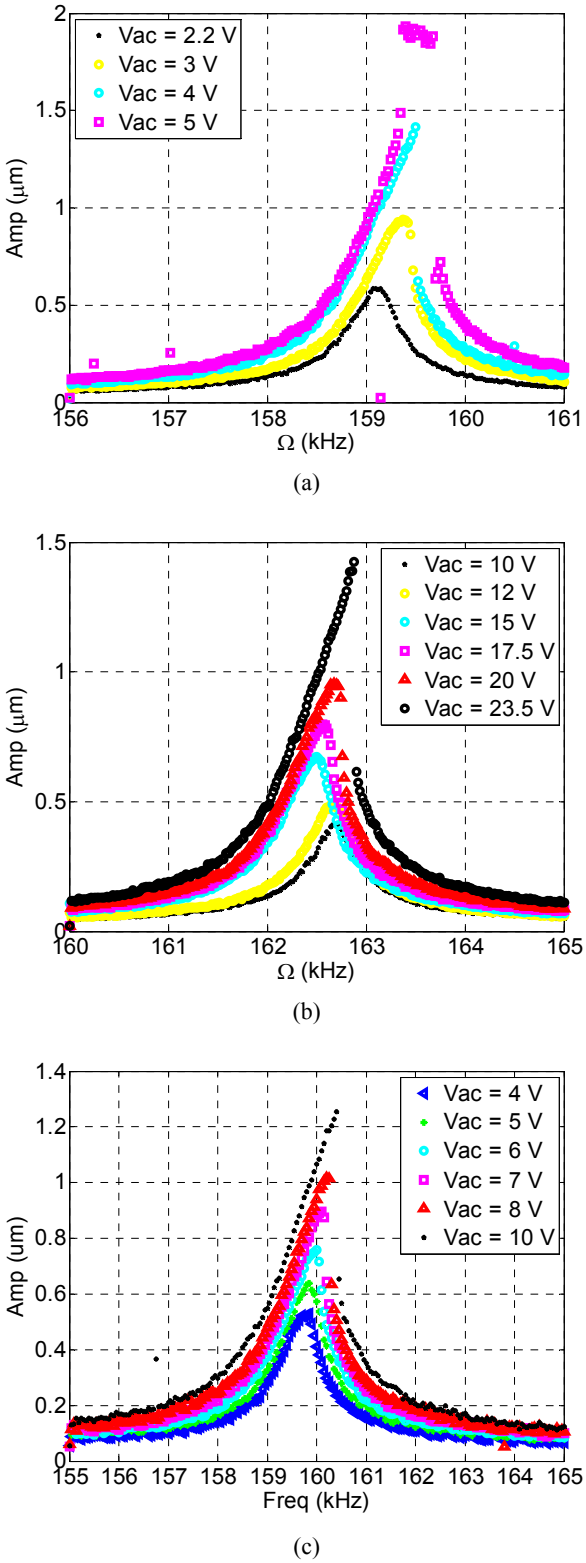

Figure 11: Frequency response curve for the microbeam near the first resonance with different lower electrode configuration. Vdc = 5 V. (a) Full electrode configuration, (b) half electrode configuration, (c) two-third electrode configuration.

5.3.2 *Second mode*

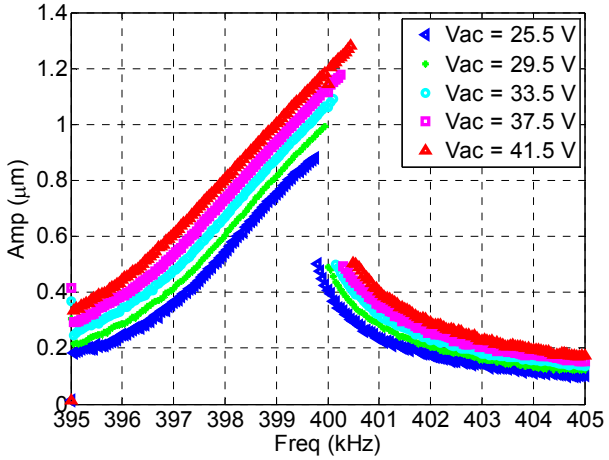

Figure 12: Frequency response curve for micro-beam near the second resonance with half electrode actuation. Vdc = 30 V.

Figure 12 shows the variation of the frequency response curve as the AC voltage is increased near the second mode resonance for the half electrode configuration. Using a half electrode, the second mode is excited with high amplitude compared with no response using the full and two-third configuration. In addition, a hardening effect is reported due to the cubic nonlinearities.

5.3.3 *Third mode*

Figure 13 shows the variation of the frequency response curve as we increase the AC voltage for the full and two-third electrode configuration near the third resonance. Using the two-third electrode configuration enhanced the excitation of the third mode where only one-third of the AC voltage is required to achieve the same vibration amplitude using the full electrode configuration. In Figure 14, a high vibration amplitude showing hardening nonlinearities is reported for different AC loadings.

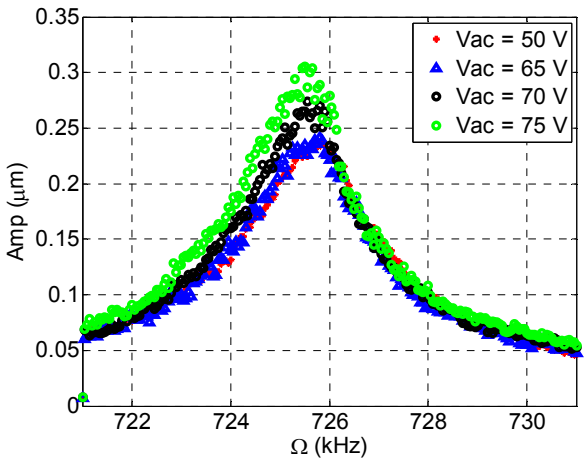

(a)

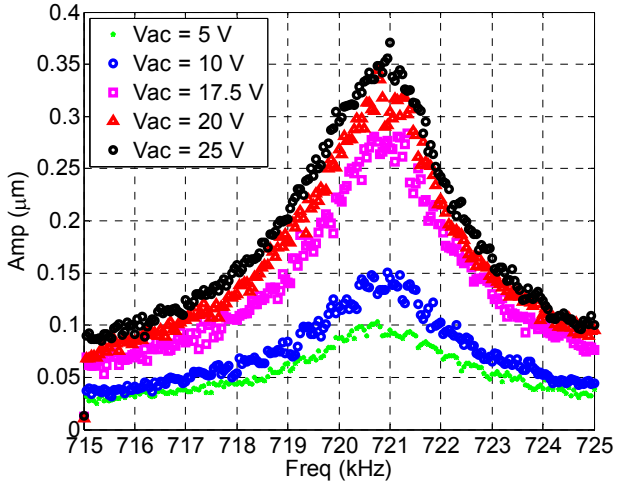

(b)

Figure 13: Frequency response curve for micro-beam near the third natural frequency with two-third lower electrode configuration. Vdc = 20 V. (a) Full electrode configuration. (b) two-third electrode configuration.

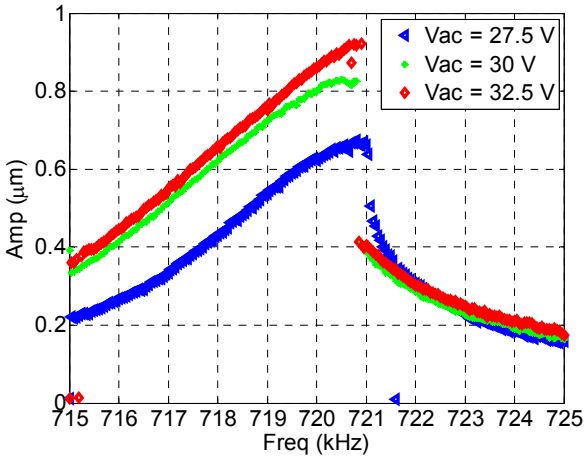

Figure 14: Frequency response curve for the microbeam near the third natural frequency with two-third lower electrode configuration. Vdc = 20 V

6. CONCLUSION

In this paper, we investigated the dynamics of clamped-clamped microbeam electrically actuated by an AC source with variable frequency superimposed to a DC voltage. The initial beam profile and dimensions are identified by using the optical profilometer. We proved the ability to excite the second mode resonance by using a half electrode configuration. In addition, the third resonance amplitude is amplified significantly by using the two-third lower electrode configuration. Also, a hardening behavior is reported due to the cubic nonlinearities among all the modes due to the dominating effect of mid-plane stretching. This capability of exciting the higher order modes can have a promising application in MEMS based mass, gas and humidity sensors.

7. REFERENCES

[1] Kim, B., et al. "Using MEMS to build the device and the package." Solid-State Sensors, Actuators and Microsystems Conference, 2007. TRANSDUCERS 2007. International. IEEE, 2007.

[2] Kim, Bongsang, et al. "CMOS Compatible Wafer-Scale Encapsulation MEMS Resonators." ASME 2007 InterPACK Conference collocated with the ASME/JSME 2007 Thermal Engineering Heat Transfer Summer Conference. American Society of Mechanical Engineers, 2007.

[3] Subhashini, S., and A. Vimala Juliet. "Toxic gas sensor using resonant frequency variation in micro-cantilever." Sustainable Utilization and Development in Engineering and Technology (STUDENT), 2012 IEEE Conference on. IEEE, 2012.

[4] Dohn, Søren, et al. "Enhanced functionality of cantilever based mass sensors using higher modes and functionalized particles." Solid-State Sensors, Actuators and Microsystems, 2005. Digest of Technical Papers. TRANSDUCERS'05. The 13th International Conference on. Vol. 1. IEEE, 2005.

[5] Burg, Thomas P., et al. "Vacuum-packaged suspended microchannel resonant mass sensor for biomolecular detection." Microelectromechanical Systems, Journal of 15.6 (2006): 1466-1476.

[6] Hsu, Wan-Thai, John R. Clark, and Clark T-C. Nguyen. "A resonant temperature sensor based on electrical spring softening." Tech. Dig., 11th Int. Conf. on Solid-State Sensors Actuators (Transducers' 01), Munich, Germany. 2001.

[7] Kim, Hyeon Cheol, et al. "Inertial-grade out-of-plane and in-plane differential resonant silicon accelerometers (DRXLs)." Solid-State Sensors, Actuators and Microsystems, 2005. Digest of Technical Papers. TRANSDUCERS'05. The 13th International Conference on. Vol. 1. IEEE, 2005.

[8] Ramini, Abdallah, Karim Masri, and Mohammad I. Younis. "Electrostatically actuated resonant switches for earthquake detection." Mechatronics and its Applications (ISMA), 2013 9th International Symposium on. IEEE, 2013.

[9] Piekarski, B., et al. "Fabrication of suspended piezoelectric microresonators."Integrated Ferroelectrics 24.1-4 (1999): 147-154.

[10] Jin, Dazhong, et al. "High-mode resonant piezoresistive cantilever sensors for tens-femtogram resoluble mass sensing in air." Journal of Micromechanics and Microengineering 16.5 (2006): 1017.

[11] Rinaldi, Gino, Muthukumaran Packirisamy, and Ion Stiharu. "Quantitative boundary support characterization for cantilever MEMS." Sensors 7.10 (2007): 2062-2079., 40(6), 563-574.

[12] Younis, Mohammad I. MEMS Linear and Nonlinear Statics and Dynamics: Mems Linear and Nonlinear Statics and Dynamics. Vol. 20. Springer, 2011.

[13] Kalyanaraman, Rakesh, et al. "Equivalent area nonlinear static and dynamic analysis of electrostatically actuated microstructures." Microsystem technologies 19.1 (2013): 61-70.

[14] Rhoads, Jeffrey F., et al. "The non-linear dynamics of electromagnetically actuated microbeam resonators with purely parametric excitations."International Journal of Non-Linear Mechanics 55 (2013): 79-89.

[15] Nayfeh, Ali H., and Mohammad I. Younis. "Dynamics of MEMS resonators under superharmonic and subharmonic excitations." Journal of Micromechanics and Microengineering 15.10 (2005): 1840.

[16] Marnat, Loïc, et al. "New movable plate for efficient millimeter wave vertical on-chip antenna." IEEE Transactions on Antennas & Propagation (2013).

[17] Alfadhel, Ahmed, et al. "Three-Axis Magnetic Field Induction Sensor Realized on Buckled Cantilever Plate." Magnetics, IEEE Transactions on 49.7 (2013): 4144-4147.

The Design and Investigation of a Novel Nano Dye Sensitized Solar Cell (DSSC) with Utilizing Coating Paints on Porous Surface to Promote Energy Efficiency

M. Khodayai Mafi [a], B. Hormozi [a*], H. Shafie [a], H. Fathinejad Jirandehi [b]

[a] Chemistry Department, Faculty of Science, Islamic Azad University, Arak Branch, Arak, Iran

[b] Chemistry Department, Faculty of Science, Islamic Azad University, Farahan Branch, Farahan, Iran

(Corresponding author. Email: behnoudhormozi.chem@Gmail.com)

Abstract:

Manufacturing of Dye-sensitized solar cells (DSSC) compounds among the other solar cells is simple and because of its low-cost production, they are offering devices for the large-scale and inexpensive conversion of the solar energy. However, the conversion efficiency relatively low and needs an intensive research work to improve it. The upside of this sort of cells is that different materials can be utilized for sensitive parts of the device. The purpose of this research is evaluation component of the energy efficiency of light-sensitized solar cells based on porous silica. Unique properties of porous silica substrate, such as high surface area, mechanical and thermal stability, volume and diameter of the high risk makes to the solar colours (Dye Solar) Cells of this type of structure used effectively in the context of crystalline silica dispersed porous and due to this type of bed volume with a specific morphology, which would increase the efficiency. The solar colours (Dye solar) based on a porous substrate are observed and detected by XRD and XRF techniques and also the tin oxide coating on a porous silica substrate has been studied by techniques of SEM. On the other side, the efficiency of solar energy components factors such as type, colour and, temperature, surface area, the coating were examined and appropriate amounts in each case was optimized. In this investigation, nano blocking layer of Titanium dioxide and Tin dioxide with applying spray pyrolysis deposition in (SPD) was coated on this dye sensitized solar cell.

Keywords: Dye solar, Photo voltaic cells, Nano layer, Spray pyrolysis deposition (SPD), Paint, porous substrates, Colour conversion coating, DSSC.

1. Introduction:

Dye sensitized solar cells (DSSCs) are devices for the conversion of visible light into electricity based on sensitization of wide band-gap semiconductors [1]. Commonly, the photoanode is prepared by adsorbing a dye into a porous TiO_2 layer. By this approach, the dye enables the generation of electricity with visible light, extending the performance of semiconductor to collect photons at lower energy [1, 2]. In the late 1960s, dye-sensitized solar cell was discovered that illuminated organic dyes can generate electricity at oxide electrodes in electrochemical cells [3]. In an effort to understand and simulate the primary processes in photosynthesis the phenomenon was studied at the University of Berkeley with chlorophyll extracted from spinach (bio-mimetic or bionic approach) [4]. On the basis of such experiments electric power generation via the dye sensitization solar cell (DSSC) principle was demonstrated and discussed in 1972 [5]. The instability of the dye solar cell was identified as a main challenge. Its efficiency could, during the following two decades, be improved by optimizing the porosity of the electrode prepared from fine oxide powder, but the instability remained a problem [6]. A modern DSSC, the Graetzel cell, is composed of a porous layer of titanium dioxide nanoparticles, covered with a molecular dye that absorbs sunlight, like the chlorophyll in green leaves. The titanium dioxide is immersed under an electrolyte solution, above which is a platinum-based catalyst. As in a conventional alkaline battery, an anode (the titanium dioxide) and a cathode (the platinum) are placed on either side of a liquid conductor (the electrolyte) [7].
A group of researchers at the Swiss Federal Institute of Technology has reportedly increased the thermo stability of DSC by using amphiphilic ruthenium sensitizer in conjunction with quasi-solid-state gel electrolyte. The stability of the device matches that of a conventional inorganic silicon based solar cell. The cell sustained heating for 1,000 h at 80 °C. The group has previously prepared a ruthenium amphiphilic dye Z-907 (cis-Ru(H2dcbpy)(dnbpy)(NCS)2,where the ligand H2dcbpy is 4,4′-dicarboxylic acid-2,2′-bipyridine and dnbpy is 4,4′-dinonyl-2,2′-bipyridine) to increase dye tolerance to water in the electrolytes. In addition, the group also prepared a quasi-solid-state gel electrolyte with a 3-methoxypropionitrile (MPN)-based liquid electrolyte that was solidified by a photo chemically stable fluorine polymer, poly (vinylidenefluoride-co-hexafluoropropylene (PVDF-HFP) [7].
The enhanced performance may arise from a decrease in solvent permeation across the sealant due to the application of the polymer gel electrolyte. The polymer gel electrolyte is quasi-solid at room temperature, and becomes a viscous liquid (viscosity: 4.34 mPa·s) at 80 °C compared with the traditional liquid electrolyte (viscosity: 0.91 mPa·s). The much improved stabilities of the device under both thermal stress and soaking with light has never before been seen in DSCs, and they match the durability criteria applied to solar cells for outdoor use, which makes these devices viable for practical application [8,9].
The first successful solid-hybrid dye-sensitized solar cells were reported [10]. To improve electron transport in these solar cells, while maintaining the high surface area needed for dye adsorption, two researchers have designed alternate semiconductor morphologies, such as arrays of nanowires and a combination of nanowires and nanoparticles, to provide a direct path to the electrode via the semiconductor conduction band. Such structures may provide a means to improve the quantum efficiency of DSSCs in the red region of the spectrum, where their performance is currently limited [7]. On August 2006, to prove the chemical and thermal robustness of the 1-ethyl-3 methylimidazolium tetracyanoborate solar cell, the researchers subjected the devices to heating at 80 °C in the dark for 1000 hours, followed by light soaking at 60 °C for 1000 hours. After dark heating and light soaking, 90% of the initial photovoltaic efficiency was maintained, the first time such excellent thermal stability has been observed for a liquid electrolyte that exhibits such a high conversion efficiency. Contrary to silicon solar cells, whose performance declines with increasing temperature, the dye-sensitized solar-cell

devices were only negligibly influenced when increasing the operating temperature from ambient to 60 °C [7].
Wayne Campbell at Massey University, New Zealand, has experimented with a wide variety of organic dyes based on porphyrin [7-10]. In nature, porphyrin is the basic building block of the hemoproteins, which include chlorophyll in plants and hemoglobin in animals. He reports efficiency on the order of 5.6% using these low-cost dyes.[11].
An article published in Nature Materials demonstrated cell efficiencies of 8.2% using a new solvent-free liquid redox electrolyte consisting of a melt of three salts, as an alternative to using organic solvents as an electrolyte solution. Although the efficiency with this electrolyte is less than the 11% being delivered using the existing iodine-based solutions, the team is confident the efficiency can be improved [12].
A group of researchers at Georgia Tech made dye-sensitized solar cells with a higher effective surface area by wrapping the cells around a quartz optical fiber.[13][14] The researchers removed the cladding from optical fibers, grew zinc oxide nanowires along the surface, treated them with dye molecules, surrounded the fibers by an electrolyte and a metal film that carries electrons off the fiber. The cells are six times more efficient than a zinc oxide cell with the same surface area.[13] Photons bounce inside the fiber as they travel, so there are more chances to interact with the solar cell and produce more current. These devices only collect light at the tips, but future fiber cells could be made to absorb light along the entire length of the fiber, which would require a coating that is conductive as well as transparent.[13] According the researches of the University of Michigan said a sun-tracking system would not be necessary for such cells, and would work on cloudy days when light is diffuse [13].
Researchers at the École Polytechnique Fédérale de Lausanne and at the Université du Québec à Montréal claim to have overcome two of the DSC's major issues [7]. Dyesol and CSIRO announced in October a Successful Completion of Second Milestone in Joint Dyesol / CSIRO Project. Dyesol Director Gordon Thompson said, "The materials developed during this joint collaboration have the potential to significantly advance the commercialisation of DSC in a range of applications where performance and stability are essential requirements. Dyesol is extremely encouraged by the breakthroughs in the chemistry allowing the production of the target molecules. This creates a path to the immediate commercial utilisation of these new materials [15].

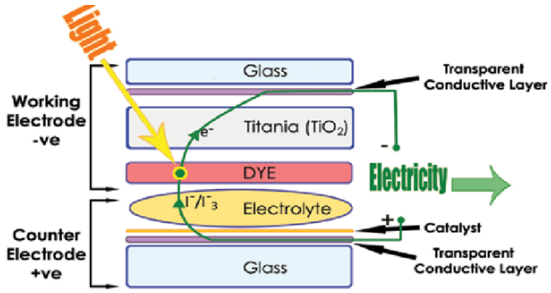

Figure.1. Scheme of dye sensitized solar cell (Reference: [19])
Dyesol and Tata Steel Europe announced in November the targeted development of Grid Parity Competitive BIPV solar steel that does not require government subsidised feed in tariffs. TATA-Dyesol "Solar Steel" Roofing is currently being installed on the Sustainable Building Envelope Centre (SBEC) in Shotton, Wales [7].

2. Materials and Methods:

In this study, to create a novel high performance of dye-sensitized solar cells some materials including titanium dioxide, tin dioxide, Tin (IV) chloride pentahydrate, triton X-100 surfactant, ammonium fluoride, ethanol, methylthioninium chloride, ethylene glycol, deionized water,

zeolite, potassium iodate and etc. were utilized. On the other side, to investigate the electrical, physicochemical and other parameters of the formation process, the instruments of centrifuge (Alc4232SiGma), UV/Vis spectrophotometer (perkin elmer lambda 35), XRD (Simens, D-500), XRF, SEM (JEOL JSM-5800), Muffle furnace, oven (OF-02G), Digital Multimeter (Snowa-2831) and digital balance (Sartorius-2810) were applied.
Between many thin film processing techniques, the technique of spray pyrolysis deposition (SPD) is one of the most efficient ones. Fabrication of this dye-sensitized solar cell (DSSC) is happened by depositing TiO_2 layer on SnO_2:F transparent conducting layer, both of which are prepared by SPD method.

3. Discussion and Conclusion:

Generally, dye-sensitized solar cells have been formed from three main parts. The first above part is a transparent anode made of fluoride-doped tin dioxide (SnO2:F) deposited on the back of a (typically glass) plate. On the back of this conductive plate is a thin layer of titanium dioxide (TiO2), which forms into a highly porous structure with an extremely high surface area. TiO2 only absorbs a small fraction of the solar photons. The plate is then immersed in a mixture of a photosensitive and a solvent. After soaking the film in the dye solution, a thin layer of the dye is left covalently bonded to the surface of the TiO_2 [7]. The main mechanism of DSSCs is including absorption of incident photon by complex photosensitizers on the TiO_2 surface and then the photosensitizers are excited from the ground state (S) to the excited state (S^*). The excited electrons are injected into the conduction band of the TiO_2 electrode. This results in the oxidation of the photosensitizer (S^+). At the next step, the injected electrons in the conduction band of TiO_2 are transported between TiO_2 nanoparticles with diffusion toward the back contact (TCO) and the electrons finally reach the counter electrode through the circuit. Subsequently, the oxidized photosensitizer (S^+) accepts electrons from the I^- ion redox mediator leading to regeneration of the ground state (S), and the I^- is oxidized to the oxidized state, I_3^-. Finally, the oxidized redox mediator, I_3^-, diffuses toward the counter electrode and then it is reduced to I^- ions. The efficiency of a DSSC depends on four energy levels of the component including the excited state (approximately LUMO) and the ground state (HOMO) of the photosensitizer, the Fermi level of the TiO_2 electrode and the redox potential of the mediator (I^-/I^{3-}) in the electrolyte [7].
In this investigation, a novel DSSC is invented by using a special porous bed contained zeolite structure and also methylthioninium chloride as dye. After preparing zeolite bed in a thermal program with maximum temperature point 760 ^{0}C, tin dioxide (SnO2) into lattice network of porous bed was deposited, as well with the least amount of electrical resistivity.

Figure.2. curing process of porous bed of DSSC.

The results show a considerable electrical efficiency of this dye sensitized solar cell by comparison with other ones. According the data values of table.1 the DSSC, in which porous

bed has been applied, has better efficiency (0.14) by comparison the other designed one without porous bed (0.11).

Table.1. the data values of efficiency and FF of the dye sensitive solar cells without porous surface and with porous bed in radiant power 7.3 mW/cm^2.

(%) η	ff	I_{SC} (μA)	V_{oc} (mV)	Porosity	Type of Bed
0.11	0.29	56	210	+	SnO_2:F
0.14	0.37	70	279	-	SnO_2:F:Zeolite

To calculate the energy transformation efficiency equation.1 was used. Pm, Isc and Voc were defined as radiant power, current intensity of electrical circuit and electrical potential differences, recpectively.

$$\eta = \frac{\text{outputpower}}{\text{inputpower}} \times 100$$

$$= \frac{P_m\,(\text{mW/cm}^2)}{\text{Light intensity}\,(\text{mW/cm}^2)} \times 100$$

$$= \frac{I_{sc}\,(\text{mA/cm}^2) \times V_{oc}\,(\text{V}) \times \text{FF}}{\text{Light intensity}\,(\text{mW/cm}^2)} \times 100$$

(Equation.1)

In conclusion, this dye sensitive solar cell has some considerable characteristics and upsides such as, high electrical efficiency, increase in production of voltage, decrease in consumption of deposited materials because of improvement the active surface of the DSSC bed. The results showed that the designed DSSC with a porous bed could be more efficient by comparison the other one without a porous zeolite bed.

References

[1]. B. O'Rregan, M. Gratzel, A low-cost, high-efficiency solar cell based on dye-sensitized colloidal TiO_2 films, Nature 353 (1991) 737.

[2]. G. Calogero, G. D. Marco; "Red Sicilian orange and purple eggplant fruits as natural sensitizers for dye-sensitized solar cells"; solar Energy Materials & solar cells; 92 (2008) 1341-1346.

[3]. Gerischer,H.; Michel-Beyerle,M.; Rebentrost, E.; Tributsch, H. (1968). "Sensitization of Charge-Injection into Semiconductors with Large Band Gap". Electrochimica Acta 13 (13): 1509–1515.

[4]. Tributsch, H.; Calvin, M. (1971). "Electrochemistry of Excited Molecules: Photoelectrochemical Reactions of Chlorophylls". Photochem. Photobiol. 14 (14): 95–112.

[5]. Tributsch, H. (1972). "Reaction of Excited Chorophyll Molecules at Electrodes and in Photosynthesis". Photochem.Photobiol. 16 (16): 261–269.

[6]. Matsumura, M.; Matsudaira, S.; Tsubomura, H.; Takata, M.; Yanagida, H. (1980). "Dye Sensitization and Surface Structures of Semiconductor Electrodes". Ind. Eng. Chem. Prod. Res. Dev. 19 (3): 415–421.

[7]. www.wikipedia.com.

[8]. Wang, Peng; Zakeeruddin, Shaik M.; Moser, Jacques E.; Nazeeruddin, Mohammad K.; Sekiguchi, Takashi; Grätzel, Michael (2003). "A stable quasi-solid-state dye-sensitized solar cell with an amphiphilic ruthenium sensitizer and polymer gel electrolyte". Nature Materials 2 (6): 402–7.

[9]. Gratzel, M (2003). "Dye-sensitized solar cells". Journal of Photochemistry and Photobiology C: Photochemistry Reviews 4 (2): 145.

[10]. Nathalie Rossier-Iten, "Solid hybrid dye-sensitized solar cells: new organic materials, charge recombination and stability", École Polytechnique Fédérale de Lausanne, 2006.
[11]. Wang, Q; Campbell, Wm; Bonfantani, Ee; Jolley, Kw; Officer, Dl; Walsh, Pj; Gordon, K; Humphry-Baker, R; Nazeeruddin, Mk; Grätzel, M (2005). "Efficient light harvesting by using green Zn-porphyrin-sensitized nanocrystalline TiO2 films". The journal of physical chemistry. B 109 (32): 15397–409.
[12]. Bai, Yu; Cao, Yiming; Zhang, Jing; Wang, Mingkui; Li, Renzhi; Wang, Peng; Zakeeruddin, Shaik M.; Grätzel, Michael (2008). "High-performance dye-sensitized solar cells based on solvent-free electrolytes produced from eutectic melts". Nature Materials 7 (8): 626–30.
[13]. Bourzac, Katherine (2009-10-30). "Wrapping Solar Cells around an Optical Fiber". Technology Review. Retrieved 2009-10-31.
[14]. Benjamin Weintraub, Yaguang Wei, Zhong Lin Wang (2009-10-22). "Optical Fiber/Nanowire Hybrid Structures for Efficient Three-Dimensional Dye-Sensitized Solar Cells". Angewandte Chemie International Edition 48 (47): 8981–5.
[15]. Dye-sensitized solar cell. Dyesol (2011-10-21). Retrieved on 2012-01-06.
[16] K. Murakami, I. Yagi and S. Kaneko, J. Am. Ceram. Soc., 79 (1996) 2557.
[17] M. Okuya, S. Kaneko, K. Hiroshima, I. Yagi and K. Murakami, J. Euro. Ceram. Soc., 21 (2001) 2099.
[18] M. Okuya, K. Nakade and S. Kaneko, Sol. Ener. Mater. Sol. Cells, 70 (2002) 425.
[19] www.dyesol.com.

Effect of Polysacccharide Chemistry on the Solution Concentration of Nanoparticle Polysaccharides-Drug Complexes

Sonal Mazumder[a]

[a]Department of Chemical Engineering

Birla Institute of Science and Technology, Pilani, Rajasthan - 333031, India

*Corresponding author:

Sonal Mazumder
Department of Chemical Engineering, BITS Pilani, Rajasthan - 333031
Tel: +91 1596515725, Fax: +91 1596 244183
E-mail address: sonal.mazumder@pilani.bits-pilani.ac.in

ABSTRACT

Nanoparticles of antiviral drugs, ritonavir (RTV) and efavirenz (EFV) with several novel polysaccharides were produced by a rapid precipitation process. Particles were purified by dialysis and dried powders were recovered after freeze drying. Particle diameters as measured by dynamic light scattering were in the range 100-200 nm. The target drug loading in the particles was 25 wt % and the drug loading efficiencies ranged from 62-96%. All the nanoparticles afforded increased solution concentration and faster release compared to the pure drugs.

Keywords: Ritonavir, Efavirenz, polymers, nanoparticles, multi-inlet vortex mixer, drug release

1. INTRODUCTION

Oral administration of therapeutic agents is the easiest and frequently preferable mode of drug delivery, as there is no requirement for hospitalization which requires medical infrastructure, a critical issue in underdeveloped countries. In addition, patient compliance in taking oral medications is greater than with injected formulations [1]. However, it is important

and challenging to attain the desired pharmacokinetic profile for a given drug, especially one with poor aqueous solubility [2]. There are several factors in the GI tract which can limit the bioavailability of drugs in the intestine such as tissue barriers (mucosa, microvilli) and physiological factors (varying pH, enzymes, transporter mechanisms). Dissolution is quite often the rate-limiting step, which ultimately controls drug bioavailability [3].

A challenge in designing nanocarrier drug delivery systems is finding the optimized particle size that will result in desired release characteristics. The control of drug release kinetics from the nanocarrier can become difficult. Drug diffuses out of smaller nanocarriers faster, resulting in burst effects instead of sustained or controlled drug delivery over prolonged periods of time [4]. The drug release kinetics can be improved by increasing the size of the nanocarriers, which results in lower drug loss and prolonged drug release with a lower burst effect [5]. Increasing the polymer-drug particle size may however hinder their transport across membranes.

Thus this work focuses on establishing a methodology for preparing well-defined drug-polymer complexes relatively rapidly and in a manner that can produce particles with high drug loadings. The particle sizes and drug loading is studied thoroughly to test control and reproducibility of the particle formation process. The suppression of drug crystallinity and miscibility with polymers is to determine the ability of polymers to stabilize against crystallization in nanoparticles. Drug release and solution concentration are studied to determine impact of polymer structure and particle size on these key parameters and to test the main hypothesis.

2. MATERIALS AND METHODS

2.1 Materials

Tetrahydrofuran (anhydrous, ACS reagent, ≥99.0% inhibitor free) was used as received. Acetonitrile (HPLC grade, >95 %) was used for HPLC analysis without further purification. RTV and EFV (Sigma Aldrich, India) were used without further purification (Figure 1a and Figure 1b). The polysaccharides were samples from Eastman Chemical Company. Reverse osmosis (RO) water was used for DLS measurements and in the formation of polymer/drug nanoparticles.

Carboxymethyl cellulose acetate butyrate (CMCAB), cellulose adipate and other ω-carboxyalkanoate (e.g., suberate and sebacate) esters of the renewable natural polysaccharide cellulose have shown potential for forming complexes with hydrophobic drugs [25].

Table 1. Abbreviation and properties of cellulose derivatives

Polymer	Polymer Abbreviation	DS (CO_2H)	DS (Other)	DS (Total)	Solubility Parameter ($MPa^{1/2}$)	Molecular weight ($x10^3$)	T_g (°C)
Carboxy methyl cellulose acetate butyrate	CMCAB	0.33	Ac 0.44, Bu 1.64	2.41	19	22.0	137
Cellulose Acetate Propionate 504-0.2 Adipate 0.33	CAP Adp 0.33	0.33	Ac 0.04; Pr 2.09	2.46	20.56	12.0	125
Cellulose Acetate Propionate Adipate 0.85	CAP Adp 0.85	0.85	Ac 0.04; Pr 2.09	2.98	21.27	9.7	110
Cellulose Acetate 320S sebacate	CA 320S Seb	0.57	Ac 1.82	2.39	22.36	25	117

2.2 Nanoparticle preparation by rapid precipitation in the Multi Inlet Vortex Mixer

Flash nanoprecipitation of polymer-drug complexes was carried out in a four-jet Multi-Inlet Vortex Mixer that accommodates four streams.[23,26]. Polymer and drug (RTV/EFV) were dissolved in THF (organic stream) which was injected into the mixer with three other water streams. The four inlet streams are tangential to the mixing chamber and the exit stream comes from the center of the chamber. The nanoparticles were formed at a nominal Reynolds number of 5,000. The injected volume ratio of THF to Millipore water was 1:10 v/v. Polymer concentration in THF was 10 mg/mL. The effect of the loading of the RTV and EFV was investigated over the target loading of 25 wt% of the total solids on a dry basis. Also the effect of drug loading on release of drug from the different polymer nanoparticles was explored.

2.3 Nanoparticles recovery, solvent removal and drying

Since the particles exit from the MIVM in a mixed organic-water phase, it was necessary to remove the solvent and any unincorporated drug from the particles. Thus, particles were processed by dialysis followed by freeze drying. The dialyzed particles were dried in a LABCONCO freeze dryer at 0.018 mbar for 2 days.

2.4 Characterization

Drug loading and drug release were measured using an Agilent 1200 Series HPLC system which consisted of a quaternary pump, online degasser, manual injector with a 20-μL sample loop and Agilent chemstation LC 3D software. Chromatography was conducted in reverse mode using acetonitrile and phosphate buffer (0.05M, pH 5.65). Dynamic light scattering (DLS) measurements of the nanoparticle sizes were performed before and after dialysis using a Malvern Zetasizer Nano-ZS (Malvern Instruments Ltd, Malvern, UK) at a wavelength of 633 nm and with a scattering angle of 173˚ at 25 ± 0.1 ºC. Crystallinity of

nanoparticles was evaluated by powder X-ray diffraction (PXRD) and differential scanning calorimeter (DSC).

In order to study dissolution of the nanoparticles, typically, equivalent amount of RTV/EFV or nanoparticles was dispersed in potassium phosphate buffer (80 mL, pH 6.8) at 37°C for 5 h. The apparatus used in the release experiments consisted of 250-mL jacketed flasks with circulating ethylene glycol/water (1:1) to control the temperature. The mixture was constantly stirred at 200 rpm with a magnetic stir bar. Aliquots (0.8 mL) were withdrawn from the suspensions every 0.5 hour (during the first 2 hours), then every hour for 5 h. Phosphate buffer (pH 6.8, 0.8 mL) was added to maintain constant volume after each aliquot was withdrawn. Samples were ultracentrifuged at 13,000 rpm (equivalent of 16060 g's) in an accuSpin Micro (Fisher Scientific) for 10 minutes. The supernatant was recovered, and the solution concentration was determined by HPLC.

3. RESULTS AND DISCUSSION

The drug composition, size, crystallinity and solubility of the nanoparticles were investigated. The role of polymers in enhancing solubility and inhibiting drug crystallinity in the particles is also discussed.

3.1 Drug incorporation in particles

All samples showed good batch-to-batch reproducibility. There was some loss of free drug during the processing steps like dialysis. Nanoparticle drug loading efficiency was comparable (88-96 %) for all cellulosic polymers. The cellulose derivatives are hydrophobic in nature and therefore able to retain more hydrophobic drug after processing. There were not any significant differences between the trends of RTV and EFV loading in the particles.

3.2 Particle size analysis

Particle size analysis of nanoparticles by dynamic light scattering

The particle sizes from all three processing steps for all the drug compositions were found to be between 100-200 nm with a polydispersity index approximately 0.2. The particle sizes were comparable after mixing and dialysis with a standard deviation of approximately ±30 nm. However, significant aggregation was observed after freeze drying. The addition of trehalose before freezing at a weight ratio trehalose:nanoparticles of 1:10 resulted in a significant reduction in particle size and polydispersity index

3.3 Crystallinity of nanoparticles

The influence of novel polysaccharides upon possible phase transformation in polymer-RTV and polymer-EFV nanoparticles was investigated through X-ray diffraction. The PXRD pattern of the drugs as-received had distinctive peaks. Finally, the PXRD of solid dispersions of the nanoparticles showed no diffraction peaks, indicating that they contained amorphous drug. Adp 0.85-EFV, CA 320S Seb-EFV, CMCAB-EFV showed no diffraction peaks implying the drugs were mostly amorphous. RTV has a sharp melting peak at 126° C when measured in DSC. During the scanning of RTV-containing nanoparticles, no endotherm was observed around the melting point of ritonavir indicating that ritonavir was present in its amorphous state.

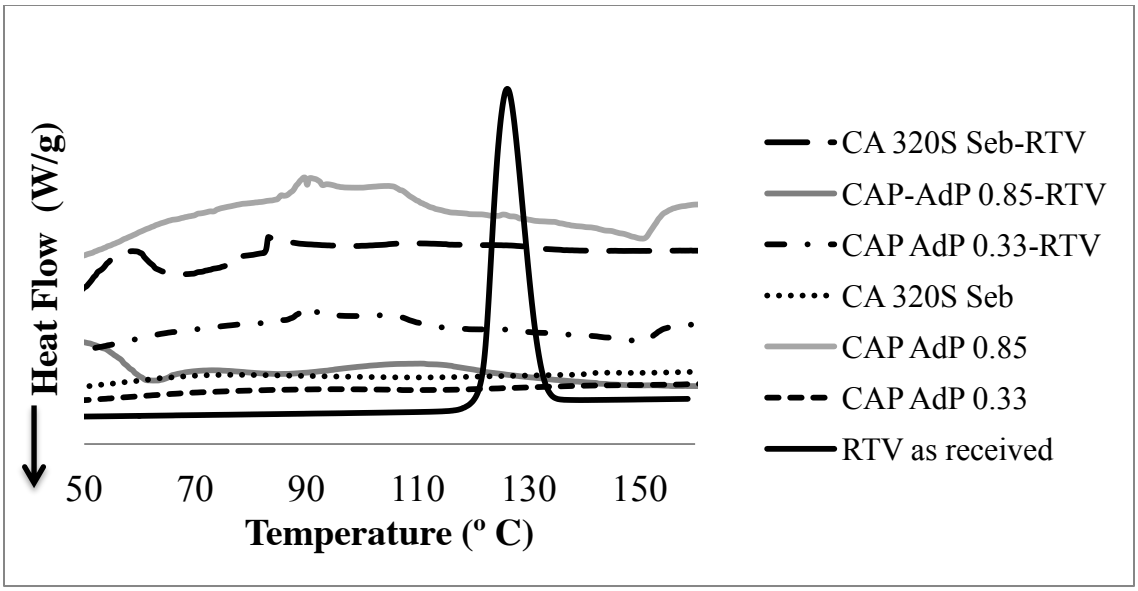

Figure 3. First DSC scan showing melting peak of RTV at 126° C. No such peak is observed in any of the polymer-drug nanoparticles.

3.5. Dissolution studies

There was almost 10- 20 fold increase in solubility of RTV from cellulose derivatives compared to the crystalline drug as-received. Among the cellulose derivatives, the CAP Adp 0.33 showed lesser increase in solubility compared to the others with respect to the free drug. However, there was not much difference in the solubility concentration among the cellulose derivatives. CMCAB showed the best results among all the polymers.

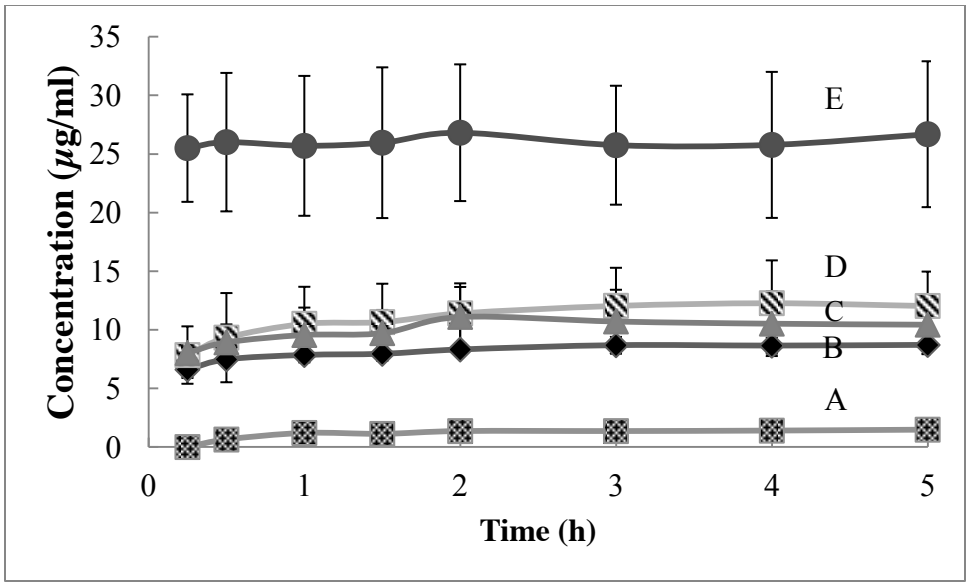

Figure 4a. Concentration profile of RTV (A) as received, (B) from CAP Adp 0.33, (C) from CA 320S Seb, (D) from CAP Adp 0.85, (E) from CMCAB. The error bars represents standard deviation of results from 3 batches.

The amorphous blends with cellulose derivatives significantly increased the solubility of both RTV and EFV, and the supersaturated solutions remained stable with respect to drug re-precipitation over the course of the experiment. This suggests that the polymers not only stabilized the amorphous drugs in the solid state, but also helped stabilize the dissolved drugs in solution.

4. CONCLUSIONS

This study demonstrates a method for producing cellulose derivative nanoparticles containing RTV and EFV, with well-defined sizes (100 nm – 200 nm). The multi-inlet vortex mixer was used to control particle size and nucleation rate, and flash nanoprecipitation was shown to be an effective method for making these nanoparticles. The particles were processed by dialysis followed by freeze drying; a suitable cryoprotectant trehalose was used for inhibiting particle aggregation during freeze drying. The drug loading efficiency in the final particles was

88-96 %. The polymers were effective in entrapping the drug in its amorphous state in the particle. This increased the solubility of the drugs in buffer solution. There was an increase in percentage drug release from the nanoparticles compared to pure crystalline drug. Therefore, nanoparticles of polysaccharides-drug complexes showed potential for enhancing the solubility and sustained release of poorly soluble drugs (RTV and EFV).

ACKNOWLEDGEMENT

The author gratefully acknowledge funding and support from the Macromolecules and Interface Institute and the National Science Foundation, (under Contract # DMR 0909065). The authors also thank Rick Caudill, Research Specialist, Department of Sustainable Biomaterials, VirginiaTech for his assistance with the PXRD. The author also acknowledge Haoyu Liu, Junia Pereira, Kevin Edgar and Richey Davis of Macromoleculer Interface Institute, VirginiaTech for their inputs and help with analysis.

5. REFERENCES

1. Lavelle, E. C.; Sharif, S.; Thomas, N. W.; Holland, J.; Davis, S. S., The importance of gastrointestinal uptake of particles in the design of oral delivery systems. *Advanced Drug Delivery Reviews* **1995,** *18* (1), 5-22.
2. Daugherty, A. L.; Mrsny, R. J., Regulation of the intestinal epithelial paracellular barrier. *Pharmaceutical Science & Technology Today* **1999,** *2* (7), 281-287.
3. Gaucher, G.; Satturwar, P.; Jones, M.-C.; Furtos, A.; Leroux, J.-C., Polymeric micelles for oral drug delivery. *European Journal of Pharmaceutics and Biopharmaceutics* **2010,** *76* (2), 147-158.
4. (a) Gref, R.; Minamitake, Y.; Peracchia, M.; Trubetskoy, V.; Torchilin, V.; Langer, R., Biodegradable long-circulating polymeric nanospheres. *Science* **1994,** *263* (5153), 1600-1603; (b) Fu, K.; Harrell, R.; Zinski, K.; Um, C.; Jaklenec, A.; Frazier, J.; Lotan, N.; Burke, P.; Klibanov, A. M.; Langer, R., A potential approach for decreasing the burst effect of protein from PLGA microspheres. *Journal of Pharmaceutical Sciences* **2003,** *92* (8), 1582-1591.
5. Ilevbare, G. A.; Liu, H.; Edgar, K. J.; Taylor, L. S., Understanding Polymer Properties Important for Crystal Growth Inhibition—Impact of Chemically Diverse Polymers on Solution Crystal Growth of Ritonavir. *Crystal Growth & Design* **2012,** *12* (6), 3133-3143.

6. (a) Liu, Y.; Cheng, C.; Prud'homme, R. K.; Fox, R. O., Mixing in a multi-inlet vortex mixer (MIVM) for flash nano-precipitation. *Chemical Engineering Science* **2008,** *63* (11), 2829-2842; (b) http://www.sigmaaldrich.com/catalog/product/sigma/sml0536?lang=en&region=US.
7. Ariza, R. M. Design, Synthesis, and Characterization of Magnetite Clusters using a Multi Inlet Vortex Mixer. Virginia Polytechnic Institute and State University, Blacksburg, Virginia, 2010.

Synthesis and Characterization of $Ce_{.80}Gd_{0.20}O_{1.90}$ (GDC) Nanowires for LT-SOFCs

Khagesh Kumar Tanwar[1], V Divya Bhargavi[1], Nandini Jaiswal[1], Devendra Kumar[1], Om Parkash[1*]
[1]Department of Ceramic Engineering, Indian Institute of Technology,
Banaras Hindu University, Varanasi-221005

ABSTRACT

Nanowires of $Ce_{.80}Gd_{0.20}O_{1.90}$ (GDC) have been prepared using wet chemical precipitation synthesis route. Nanocomposite of these nanowires has been prepared to stabilize it at higher temperature for application in low temperature solid oxide fuel cells. Single phase formation has been confirmed by X-ray diffraction. GDC nanowires have been mixed with eutectic binary mixture of lithium and sodium carbonates in wt. ratio of 4:1. Carbonates act as grain growth inhibitor and increase the stability of nanowires due to low sintering temperature of 700 °C. Single phase formation has been found in the composite i.e. carbonates are present as an amorphous phase. Microstructure shows that GDC nanowires in the matrix are present with high aspect ratio.

Keywords: GDC; Nanowires; Wet chemical precipitation; XRD; SEM.

1. INTRODUCTION

Solid oxide fuel cells (SOFCs) are highly efficient electrochemical devices which convert chemical energy into electrical energy without involving the combustion step. SOFCs have three components in which a dense solid electrolyte is sandwiched between to porous electrodes, an anode and a cathode. As the heart of SOFCs, electrolytes play an essential role as concerns the overall cell performance. In the past decades, the development of advanced electrolyte materials has been an active research topic. SOFCs using conventional solid electrolyte, yttria stabilized zirconia (YSZ), works at high temperature, 800-1000 °C [1]. This high working temperature has been a great challenge for the engineering of the materials for various components of SOFCs. Doped ceria, especially gadolinia and samaria-doped ceria (GDC and SDC), possess an ionic conductivity of 10^{-2} Scm^{-1} at 600 °C [2]. Doped ceria, however, exhibit some electronic conductivity and deleterious lattice expansion due to conversion of Ce^{+4} to Ce^{+3} in reducing atmospheres [3]. This reduces the efficiency and cell performance [3]. Efforts have been made to explore solid electrolytes working in the low temperature range 300-600 °C by the introduction of liquid phase in the grain boundaries/interfaces forming the composite electrolyte [4]. The composite electrolyte generally contains two phases. One is the doped ceria solid solution. The other is the salt usually an amorphous phase. It displays either a molten status such as the mixture of Li_2CO_3 and Na_2CO_3 at its melting point [4]. It has been demonstrated that the interface provides a highway channel for ionic transport leading to an enhanced ionic conductivity. Interface density and the contact area between the two phases are the parameters that should be considered. Larger the interface, higher will be the ionic conductivity. Therefore, reducing the particle size of both the phases will contribute to a higher ionic conductivity. The effective conductivity may reduce with increase of second phase if the interaction between two phases is less.

More importantly, in nanostructured system, the larger area of interface and grain boundaries will produce a high-density of mobile defects in the space-charge region [5].

Nanostructured materials have attracted growing interest for use in many applications because many of their properties are enhanced as compared to those of bulk materials [6, 7]. Recently, 1D nanomaterials, i.e., nanowires, nanotubes, nanorods, nanobelts, have become the focus of intensive research due to their unique and unusual properties such as dimensional confinement and anisotropy [8, 9]. Due to extremely low yield of existing approaches such as hard or soft template-based [10] Mamoun Muhammed and co-workers have found a chemical route for the synthesis of samarium doped ceria (SDC) nanowires by homogeneous precipitation of lanthanide citrate complex in aqueous solutions as precursor followed by calcination [11].

In the present study, $Ce_{.80}Gd_{0.20}O_{1.90}$ (GDC) nanowires have been synthesized by homogeneous precipitation of lanthanide citrate complex. GDC nanowires were mixed with eutectic mixture of Li_2CO_3 and Na_2CO_3 $(Li_{0.52}\ Na_{0.48})_2\ CO_3$ (LNCO) to stabilize them at high working temperature, 700 °C. Prepared nanocomposite was characterized using DTA/TGA, XRD and SEM.

2. EXPERIMENTAL

2.1 Synthesis

$Ce_{.80}Gd_{0.20}O_{1.90}$ (GDC) nanowires were prepared by wet chemical precipitation route. Stoichiometric amount of ceric ammonium nitrate $(NH_4)_2$ Ce $(NO_3)_6$ (99.9 % purity, Loba Chemie) and Gd_2O_3 (99.9 % purity, Sigma Aldrich) and citric acid (99.5 % purity, Loba Chemie) were taken as the starting materials. Gd_2O_3 was heated at 800 °C for 1 h to remove the absorbed moisture and then cooled in the furnace to 500 °C. After that the sample was stored in a vacuum desiccator to cool to room temperature. Then weighed amount of Gd_2O_3 was dissolved in dilute nitric acid and heated at 100 °C till dryness to obtain $Gd(NO_3)_3$. Then $Gd(NO_3)_3$ was dissolved in double distilled water to obtain a transparent solution. Stoichiometric amount of nitrate solutions were mixed to obtain 0.2 M solution (total mole of cations per liter of solution). Similarly citric acid was dissolved in double distilled water to prepare 0.6 M solution. In this process citric acid (H_3Cit) is an important reagent in this synthetic route of GDC nanowires. It is a polyprotic acid, which can take various deprotonated ionic forms (H_2Cit^-, $HCit^{2-}$ and Cit^{3-}) in aqueous solutions depending

1*Corresponding Author: Tel:+91-542-6701791; Fax:+91-542-2368428
Email address: oprakash.cer@itbhu.ac.in

upon pH [11]. Due to chelate formation, the carboxylates can form stable coordination complexes with various metal ions [12]. This synthesis procedure is started with one-phase solution containing the lanthanide ions (Ln^{3+}) and H_3Cit.

Equal volume of metal ions and citric acid solutions were mixed in a beaker adjusting the optimized pH to 2.0 by the addition of 6 M NaOH solution with constant stirring [12]. The beaker was sealed and then kept in an oven at 110 °C for 24 hrs. A white precipitates was collected by centrifugation at 1100 rpm for 15 min. Then it was washed several times using distilled water and ethanol followed by drying at 120 °C overnight. Then precursor was calcined at 400 °C for 2 hrs [11]. The calcination reaction is given below:

$$Ce_{0.80}Gd_{0.20}(C_6H_5O_7) + 4.7O_2 \rightarrow Ce_{0.80}Gd_{0.20}O_{1.90} + 6CO_2 + 2.5H_2O \quad (1)$$

Then the powder was mixed with 20 wt. % $(Li_{0.52}Na_{0.48})_2CO_3$ (LNCO) for the formation of nanocomposite. The nanocomposite was heated at 650 °C and quenched for formation of amorphous phase of carbonate in nanocomposite. Powder XRD of the nanocomposite was done for the confirmation of amorphous nature of carbonate. The DTA/TGA was performed for the confirmation of decrease in melting temperature of carbonates compared to its pure state in with presence of GDC nanowire.

2.2 Characterization

2.2.1Differential thermal analysis/ Thermogravimetric analysis (DTA/TGA)

DTA/TGA of as prepared precursor was done using SETARAM DTA/TGA in the temperature range ambient to 750 °C in N_2 atmosphere at the heating rate of 10 °C/min.

2.2.2 Powder X-Ray Diffraction

Powder X-ray diffraction of the calcined and sintered powders was recorded using a Rigaku high resolution powder X-Ray diffractometer employing Cu $K_{\alpha 1}$ radiation and Ni-filter at room temperature. Data were collected in the bragg angle of $20° \leq 2\theta \leq 80°$.Diffraction pattern were indexed using X'pert high score standard software. The average crystalline size, D was determined using Scherrer's formula.

$$D = \frac{0.9\lambda}{\beta cos\theta}$$

Where β is the full width at half maxima (FWHM) excluding instrument broadening, λ (1.54065 Å) is the wave length of X-rays and θ is Bragg angle. β is taken for the strongest Bragg's peak corresponding to (111) reflection.

2.2.3 Scanning electron microscope

Sintered pellets were polished using emery papers of grade 1/0, 2/0, 3/0, and 4/0 (Sia, Switzerland) followed by polishing on a velvet cloth using diamond paste of grade ¼-OS-475 (HIFIN). Then polished samples were chemically etched with HCL (66.67% concentration) for 20 sec followed by washing with double distilled water and drying at 100 °C. Micrographs were recorded using INSPECT 50 FEI scanning electron microscope.

3. RESULTS AND DISCUSSION

DTA/TGA curve of the nanowire composite is shown in Fig. 1. According to TGA curve around 3.5% weight loss observed till 120°C due to the removal of moisture. There is no weight loss observed in the temperature range 100 °C to 700 °C.

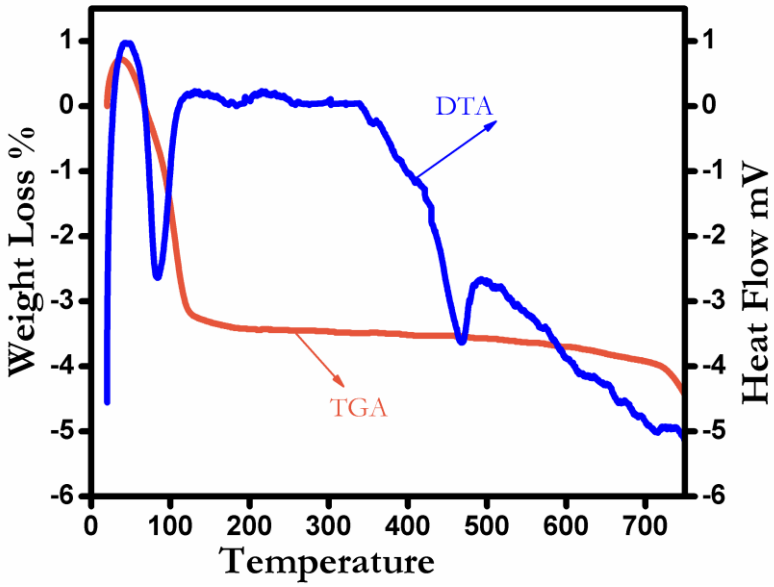

Figure 1 DTA/TGA curve of nanocomposite.

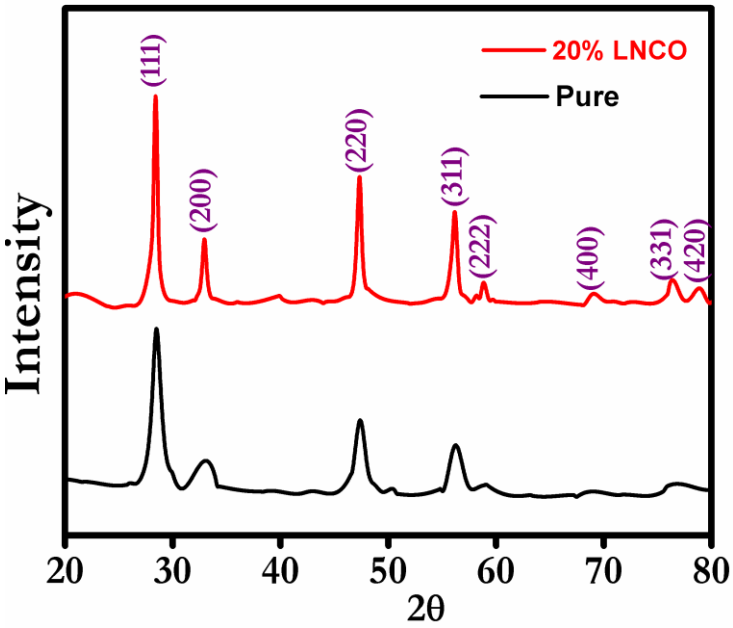

Figure 2 Powder X-Ray pattern of pure GDC and GDC/20 %($Li_{0.52}Na_{0.48})_2CO3$ (LNCO)

Two endothermic peaks have been observed in the DTA curve. One in the range 80-110 °C corresponds to evaporation of moisture adsorbed on the sample. Second peak is at 465 °C due to melting of carbonates. After that no peak was observed up to 750 °C. Powder X-ray diffraction (XRD) pattern of the calcined powder is presented in Fig. 2. All the observed peaks of resultant GDC nanowires are indexed to the cubic fluorite-type structure CeO_2 (JCPDS NO. 75-0162) with a lattice constant of 5.423 Å. The lattice constant is slightly larger than the lattice constant of

pure CeO_2 (5.411 Å), due to replacement of larger sized Gd^{3+} ion leading to lattice expansion of ceria which confirms that the Gd^{3+} ion have entered the crystal lattice of CeO_2. The average crystalline size of GDC nanowires calculated by Scherrer's equation is ~20.0 nm. Scanning electron microscope (SEM) image (Fig. 2) shows that the GDC nanowires have high aspect ratio, length more than 20 µm and diameter range 200nm to 900nm.

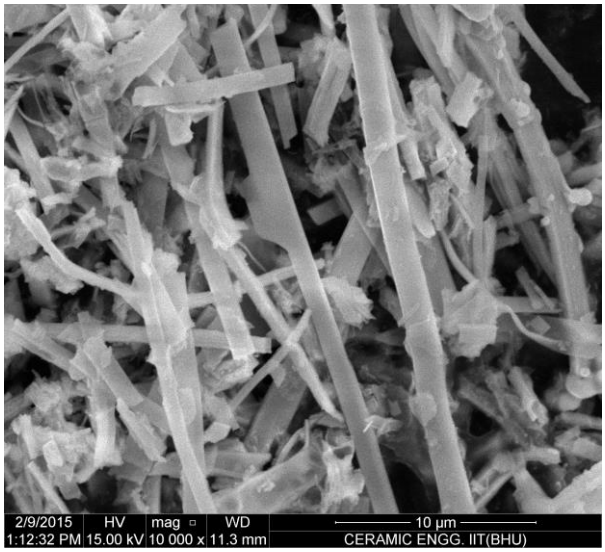

Figure 3 SEM image of GDC nanowires

4. CONCLUSIONS

Nanowires of $Ce_{.80}Gd_{0.20}O_{1.90}$ (GDC) have been synthesized by wet chemical route. Powder X-ray diffraction pattern shows that the observed peaks of resultant GDC nanowires can be indexed to the cubic fluorite-type structure CeO_2 this confirms the formation of single phase. Nanocomposite of GDC have been prepared by mixing of $Ce_{.80}Gd_{0.20}O_{1.90}$ (GDC) nanowires and $(Li_{0.52}\ Na_{0.48})_2\ CO_3$ (LNCO) in a weight proportion of 4:1 followed by calcination at 650 °C and quenching to ambient temperature to get amorphous phase of carbonates. Micrograph shows the formation of nanowires with high aspect ratio.

5. ACKNOWLEDGEMENT

Thanks to Department of Science and Technology, New Delhi for financial support.

6. REFERENCES

[1]. Yicheng, Z., Chun, X., Yujie, W., Zhuoran, X. and Yongdan, L. 2012. Quantifying multi-ionic conduction through doped ceria/carbonate composite electrolyte by a current-interruption technique and product analysis. *Int. J. of Hydrogen Energy*. 37, 13 (Mar. 2011), 8556-8561.

[2]. Brett, D.J.L., Atkinson, A., Brandon, N.P. and Skinner, S.J. 2008. Intermediate temperature solid oxide fuel cells. *Chem. Soc. Rev*. 37, (Aug, 2008), 1568–1578.

[3]. Steele, B.C.H and Heinzel A. 2001. Materials for fuel-cell technologies. *Nature*. 414, 15(Nov. 2001), 345–352.

[4]. Liangdong, F., Chengyang W., Mingming C. and Bin Z. 2013. Recent development of ceria-based (nano)composite materials for low temperature ceramic fuel cells and electrolyte-free fuel cells. *J. of Power Sources*. 234, 21 (Feb. 2013), 154-174.

[5]. Antonino, S. A., Peter, B., Bruno, S., Jean M.T. and Walter V. S. 2005. Nanostructured materials for advanced energy conversion and storage devices. *Nature Materials*. 4, 1 (May. 2005), 366-377.

[6]. Paul, A., Paul, F. B., Welford, A. C., Jack, C., David, A. D., Michael, L. K., George, L. M., Joel, S. M., Mark, A. R., Peter, J. R., Samuel I. S. and Mark E. Thompson. 1999. From Molecules to Materials: Current Trends and Future Directions. *Adv. Mater*. 10, 8 (Jan. 1999), 1297-1394.

[7]. Mamoun M., Thomas, T. 2003. Nanostructured Materials and Nanotechnology: Overview. *J. Korean Ceram. Soc*. 40, 19(Nov. 2003), 1027-1046.

[8]. Younan, X., Peidong, Y., Yugang, S., Yiying. W., Brian, M., Byron, G., Yadong,Y., Franklin, K. and Haoquan, Y. 2003. One-Dimensional Nanostructures: Synthesis, Characterization, and Applications. *Adv. Mater*. 15, (Marc. 2003), 353-389.

[9]. Sang-Min, L., S-Nam C. and Jinwoo, C. 2003. Anisotropic Shape Control of Colloidal Inorganic Nanocrystals. *Adv. Mater*. 15, 7 (Marc. 2003), 441-444.

[10]. Yujiang, S., Robert, M. G., Rachel, M. D., Haorong, W., Yan, Q., Eric, N. C., William, A. S., James, E. M. and John, A. S. 2007. Synthesis of Platinum Nanowire Networks Using a Soft Template. *Nano Lett*. 7, 14 (Nov. 2007), 3650-3655.

[11]. Ying, M., Xiaodi, W., Shanghua, L., Muhammet, S. T., Bin, Z., and Mamoun Muhammed. 2010. Samarium-Doped Ceria Nanowires: Novel Synthesis and Application in Low-Temperature Solid Oxide Fuel Cells. *Adv. Mat*. 22, 12 (April 2010), 1640-1644.

[12]. Vanhoyland, G., Pagnaer, J., D'Haen, J., Mullens, S., Mullens, J. and Mullens, J. 2005. Characterization and structural study of lanthanum citrate trihydrate $[La(C_6H_5O_7)(H_2O)_2]\cdot H_2O$. *Solid State Chem*. 178, (Jan. 2005), 166-171.

Cytotoxicity reduction as a main challenge on gold nanorods synthesis using seedless silver-assisted method

J Valkovičová[1, 2*], V Bernard[1], J Drbohlavová[2,3]

[1]Masaryk University, Faculty of Medicine, Department of Biophysics, Brno, Czech Republic

[2]Brno University of Technology, Faculty of Electrical Engineering and Communication, Department of Microelectronics, Brno, Czech Republic

[3] Brno University of Technology, Central European Institute of Technology, CEITEC, Brno, Czech Republic

E-mail: valkovicova.jirina@gmail.com

Abstract. Gold nanoparticles (AuNPs) are considered as one of the most promising agents for medicine due to their exceptional qualities. A big task is to prepare the biocompatible nanostructures which are all uniform and reproducible in a given size. Mainly the AuNPs toxicity complicates their medical *in vivo* applications. We have focused on the suitable techniques in protocol using seedless silver-assisted method and further surface modifications for the purpose of elimination the toxicity. The influence of three basic reagents concentrations, namely $HAuCl_4$ and $AgNO_3$ in growth solution and the added seed solution on the final product was investigated in the combination with different solvents. The NPs physical properties were evaluated and compared with commercial sample. The main interest was kept on cytotoxicity, which was evaluated on human ovarian carcinoma cells A2780 via MTT. A significant differences in cells viability caused by various parameters were observed.

1. Introduction

Cancer, tumors, and chemotherapy – the attention gained by these phenomena indicates how important and grave topic it is. That is the reason why this issue has got public, mainly scientists' interests all around the word. Nanoparticles (NPs) are considered as one of the most promising agents for cancer therapy. They are being investigated as drug carriers, photothermal agents, contrast agents and radiosensitisers [1-3].

The anisotropic (nonspherical) metal nanostructures like gold nanorods (AuNRs) are very appreciated for their shape-dependent optical properties. Due to the different absorption of visible light along length and width of NRs, multiple plasmon bands arise in the UV-Vis-NIR absorption spectrum of AuNRs solution [4]. The plasmon peak position varies with different aspect ratios (AR) and small changes in the AR of AuNRs cause dramatic changes in the transmitted colors [5]. A big advantage is AuNRs tunable size and shape, which can be made by small and easy changes in the synthetic protocols. These changes can make big differences in final properties [6]. Due to this fact, the AuNRs have an extensive spectrum of biomedical applications, from macromolecules separation or targeted drugs delivery to target cancer therapy [2]. NRs with low aspect ratio and with plasmon resonance in NIR are used not only as therapy agents, but also for imaging [7]. This discovery made from NPs used in photothermal therapy the theranostic anticancer agents (NPs that assist in both, the therapy and

diagnosis). It represents one of the best options of cancer treatment compared with the traditional chemotherapy [8,9]. There are several problems that are necessary to be solved in the preparation of AuNRs. A serious task is to prepare the biocompatible nanostructures which are monodispersed and reproducible in a given size. The frequent cellular toxicity complicates AuNRs use and negatively affects the application, mainly in medicine. The main reason of toxicity is caused by presence of cetyltrimethylammonium bromide (CTAB) which is used as the most common surfactant in the wet synthesis. AuNRs have been proved to display significant cytotoxicity to human cells because of the highly cytotoxic property of free CTAB [10]. The problem can be solved by convenient way of AuNRs preparation or by coating nanostructures with a substance compatible with the human body. But the AuNRs modification is very challenging mainly because of CTAB covering. If the CTAB structure around the rods is disturbed, complete or partial aggregation can happen easily during AuNRs functionalization. Consequently, it leads to lose of the unique AuNRs optical properties [11,12]. The AuNRs toxicity has become an issue getting to the forefront of scientists [13]. A number of *in vitro* studies on the AuNRs cytotoxicity have been performed, but with the contradictory results. to some reports, the AuNRs cytotoxicity decreases with the NPs size [14]. Other studies published that the toxicity related to the shape and that the anisotropic NPs have greater effect than spherical NPs of the same size have [15]. A few studies also reported that the reaction of AuNRs and cells is is influenced primarily on the cell type rather than on the NPs size and cellular uptake [16].
In the present work, we have focused on the suitable techniques in protocol using sedless silver-assisted method and further surface modifications for the purpose of alleviating the toxicity. The influence of three basic reagents concentrations, namely of the $HAuCl_4$ and $AgNO_3$ in growth solution and the added seed, on the final product was investigated in combination with different solvents. The physical NPs properties were evaluated and compared with commercial one. Human ovarian carcinoma cells A2780 were used to evaluate the cytotoxicity.

2. Materials and methods

2.1. Materials

Chloroauric acid ($HAuCl_4.3H_2O$), sodium borohydride ($NaBH_4$), silver nitrate ($AgNO_3$), L-Ascorbic acid ($C_6H_8O_6$), methylthiazoletetrazolium bromide (MTT) $C_{18}H_{16}BrN_5S$, sodium dodecyl sulfate (SDS) ($CH_3(CH_2)_{11}OSO_3Na$) were purchased from Sigma Aldrich, cetyltrimethylammonium bromide (CTAB) ($C_{19}H_{42}BrN$) from Fluka and polyethylenglycole (PEG) ($C_{2n+2}H_{4n+6}O_{n+2}$) from Aldrich. All chemicals have been used as purchased. Deionized water (Millipore, with Millipore Quantum EX Ultrapure Organex Filter Cartridge) or phosphate buffered saline (PBS) were used as solvents in the preparations. The human ovarian carcinoma cells A2780 cells were cultivated in RPMI-1640 medium with l-glutamine purchased from Bio Tech, Ltd., Prague, Czech Republic. Gold colloidal nanorods (10 nm) stock solution in PBS was gained by Sigma–Aldrich.

2.2. Gold nanorods synthesis

AuNRs were synthesized by using modified seeding method with CTAB as a surfactant [17,18]. The first step before each synthesis was to prepare CTAB in aqueous solution and heated it to at least 26 °C (Krafft point of CTAB) in warm water bath until the CTAB was well dissolved. Before each synthesis it was also necessary to make a fresh $NaBH_4$ solution and cool it to a temperature of 5 °C. These steps make the AuNRs preparation faster, more efficient and successful.

2.2.1. Preparation of gold seed solution

Seed solution contained 5.0 mL of 0.2 M CTAB aqueous solution mixed with 5.0 mL of 0.0005 M $HAuCl_4$. Then, 0.6 mL of freshly prepared ice-cold ($t \approx 5$ °C) 0.01 M $NaBH_4$ was added under vigorous stirring. The colour immediately changed to yellow-brown, which indicated the formation of small anisotropic AuNPs (≈ 1 nm). Afterwards, the solution was stirred for next 2 min and then gently

heated (to ≈ 30 °C) for at least 25 min in order to well decompose all $NaBH_4$. The seed solution was usually used immediately after its preparation, within 24 hours at the latest.

2.2.2. Preparation of growth solution

Growth solution was made by mixing of 5 mL of 0.2 M CTAB with 5 mL of 0.01–0.001 M $HAuCl_4$. The solution turns opalescent yellow. After gentle stirring, 0.5–2 mL of 0.08 M ascorbic acid was added and the solution was shaken. Ascorbic acid as a mild reducing agent changed the colour of growth solution from yellow to colorless indicating the reduction of gold (III) to gold (I). Finally, 0.15–0.45 mL of 0.004 M $AgNO_3$ at 25 °C was added.

The final AuNRs were formed by the addition of 50–160 μL of the seed solution to the growth solution at 27–30 °C. The color of the solution gradually changed to dark blue during 5 min. The AuNRs with the highest and smallest AR were chosen as representative samples. These products were supplemented by syntheses with different solvent (PBS).

2.3. PEG coating

The most toxic AuNRs were modified by thiol-terminated polyethylene glycol (PEG) to increase the biocompatibility. A final AuNRs solution was centrifuged at 14,000 rpm for 20 min, decanted, and resuspended in water to remove the excess of CTAB. PEG was added in the range of 2–3 mg to 10 mL of AuNRs solution. The mixture was stirred for 48 h at room temperature. After 48 h the solution was centrifuged at 14,000 rpm for 20 min, the supernatant was removed and the residue was redispersed in 10 mL of solvent and centrifuged again. This procedure was repeated for several times.

2.4. Equipment and characterization tools

The fundamental size and shape analysis was done with Scanning Electron Microscope (SEM) Tescan FE MIRA II LMU. The information about shape and size was obtained from analytical Transmission Electron Microscope Jeol, JEM 2100F, 200 kV, with Schottky autoemission cathode, from Institute of Physics of Materials at Academy of Sciences in Brno. The high-resolution images were evaluated by using software Gatan, Digital Micrograph. Before the SEM and TEM observation, 1 mL of each final solution was centrifuged for 30 min at a speed of 14.000 rpm to separate the NPs. The supernatant was removed after the centrifugation and the residue was redispersed in 1 mL of solvent and centrifuged again. After repeating the above procedures for several times, the final precipitate was redispersed in 1 mL of ultra-pure water or PBS. For SEM observation, 5 μL of the AuNRs were dropped on the silicon wafer (coated with Al, Ni or Ti thin layer) and dried in the air. To analyze the optical properties of AuNPs, UV-Vis absorbance spectra of samples were measured by using the Spectronic Helios Alfa spectrophotometer from Faculty of Chemistry, BUT. UV-Vis measurements were performed for wavelengths ranging from 300 nm up to 1100 nm using 4 mL of sample solution in a spectrophotometer cuvette (Sigma Aldrich). Infrared spectra were measured using FT-IR Spectrometr Thermo Scientific Nicolet iS10 at Faculty of Chemistry, BUT. All spectra were recorded at the resolution of 4 cm^{-1} over the wave number range of 400–4000 cm^{-1}.

2.5. Cell viability test

MTT assay was performed on human ovarian carcinoma cells A2780 cultivating in RPMI-1640 medium with l-glutamine in atmosphere of 95% air and 5% CO_2 at 37 °C. Cells were placed into 96-well plates at a density of $5 \cdot 10^4$ cells in 200 μL of culture medium Roswell Park Memorial Institute (RPMI) with AuNRs suspension of variable concentrations (1, 10, 20, 50 μL/200 μL) prepared in deionized water/medium/PBS. 12 replicate wells were employed for each tested AuNRs concentration. Negative controls were made by cells which were not exposed to AuNRs. 20 μL of solution containing 5 μg/1 mL of MTT dissolved in PBS was added to each well after 24/48 h of incubation.. Next, blue-purple colored formazan product was expected to be formed by MTT after 4 h of incubation at 37 °C. At this point, the medium was removed and the formazan was dissolved in 200 μL of 10% SDS. After

10 min, a resulting violet solution with absorbance at 570 nm was measured by EL800 microplate reader (Bio-Tek, USA) at Masaryk University.

3. Results and discussion

3.1. AuNRs syntheses

The effect of various reagents concentrations on the AuNRs formation and properties was investigated by the analysis of AR and absorption maximum of all samples. It was necessary to normalize the real values of reagent concentration as well as AR and absorption maximum of AuNRs to obtain adequate and comparable dependencies of concentration influence of single reagents (Table 1). The values were sorted from the minimum to the maximum and the numbers 1-4 were assigned to '1' meaning the minimum, and to '4' representing a maximum value.

Table 1. Conversion table of real concentration values on normalized values

	SEED					c [$HAuCl_4$]					c [$AgNO_3$]				
c NV	c RV/µL	AR RV	AR NV	λ RV/nm	λ NV	c_{rv} RV/M	AR RV	AR NV	λ RV/nm	λ NV	c RV/µL	AR RV	AR NV	λ RV/nm	λ NV
1	50	1.9	4	632	3	0.001	1.6	2	620	1	150	2.2	1	628	2
2	80	1.4	2	624	2	0.005	1.4	1	624	3	250	2.7	3	628	2
3	120	1.6	3	632	3	0.01	3.1	4	632	4	350	4.3	4	640	4
4	160	1.3	1	616	1						450	2.4	2	616	1

c – concentration, NV / normalized value, RV – real value, AR – aspect ratios

It has been established that the AuNRs with the highest AR were prepared with the lowest tested amount of added seed solution(50 µL), the lowest tested concentration of $HAuCl_4$ (0.001 M) and the second highest tested amount of $AgNO_3$ (350 µL). On contrary, the product with the smallest AR was gained by the highest tested amount of added seed solution (160 µL), the tested concentration of $HAuCl_4$ of 0.005 M and again by using of 350 µL $AgNO_3$ () (Figure 1). The LPSR is closely related to AuNRs size. We asssumed that the position of absorbance maximum increases with increasing AR. Based on the results, the expectation was confirmed and the influence of single reagent concentration was the same as in the previous case with AR (Figure 1).

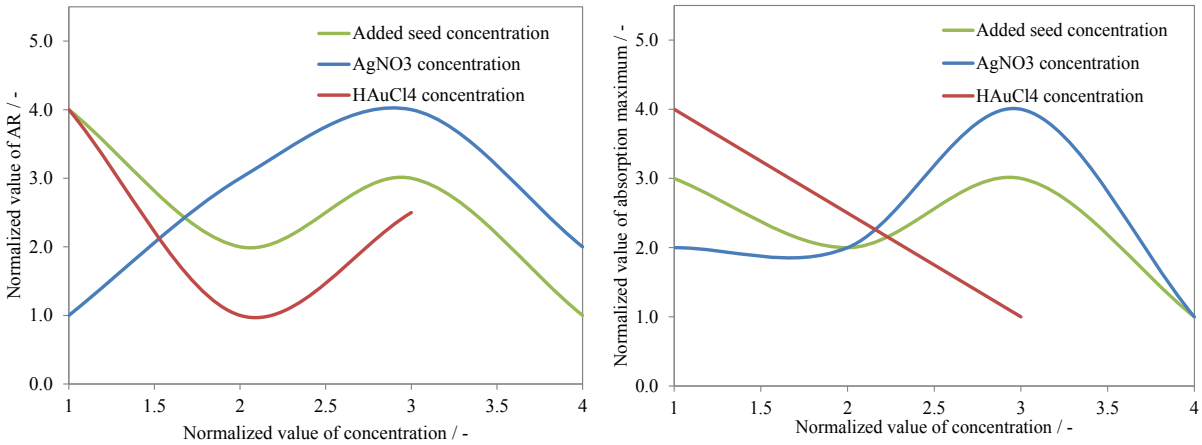

Figure 1. Normalized values dependence of AR (left) and absorption maximum (right) on the concentration change of various reagents

Based on the obtained results two samples have been chosen to cover as much as possible different parameters for evaluating the cytotoxicityvia size and AR. The first product was made by mixing of

0.01 M $HAuCl_4$, 120 mL of $AgNO_3$ and 150 µL of seed (Figure 2). According to SEM analysis, the biggest and the most robust AuNRs were prepared with the protocol. In this case, the highest NRs concentration was also obtained. The UV-VIS spectra of the sample showed the maximum absorption is at 620 nm. The smallest AuNRs with the highest AR were synthetized by mixing of 0.001 M $HAuCl_4$, 350 µL of $AgNO_3$ and 50 µL of seed solution (Figure 3). According to UV-Vis spectra, there is a red-shift of LPR maximum to 660 nm unlike in comparison to previous sample. Both spectra showed a significant response right at the beginning. It was probably caused by oversaturation of growth solution by ascorbic acid due to the lower pH (2.57).

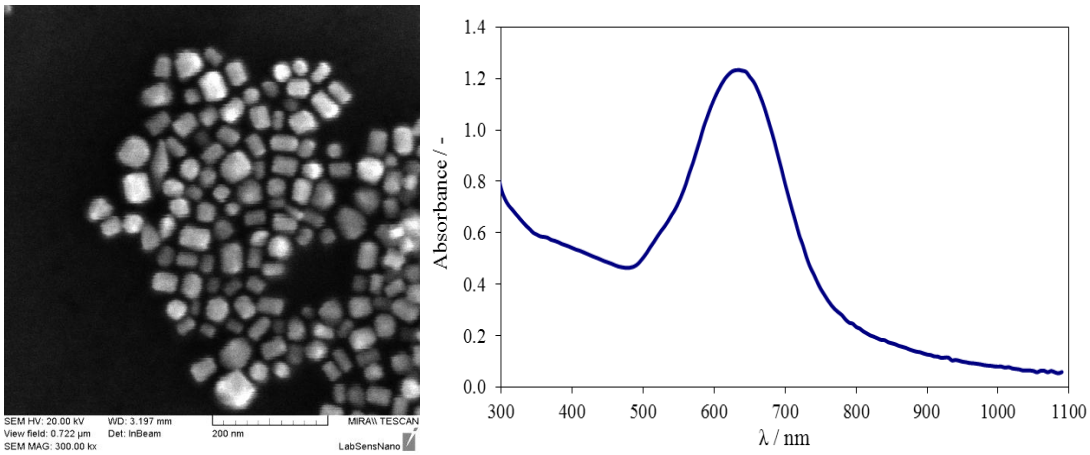

Figure 2. SEM image gold nanorods at magnification of 200 nm (left) and corresponding UV-VIis spectra (right)

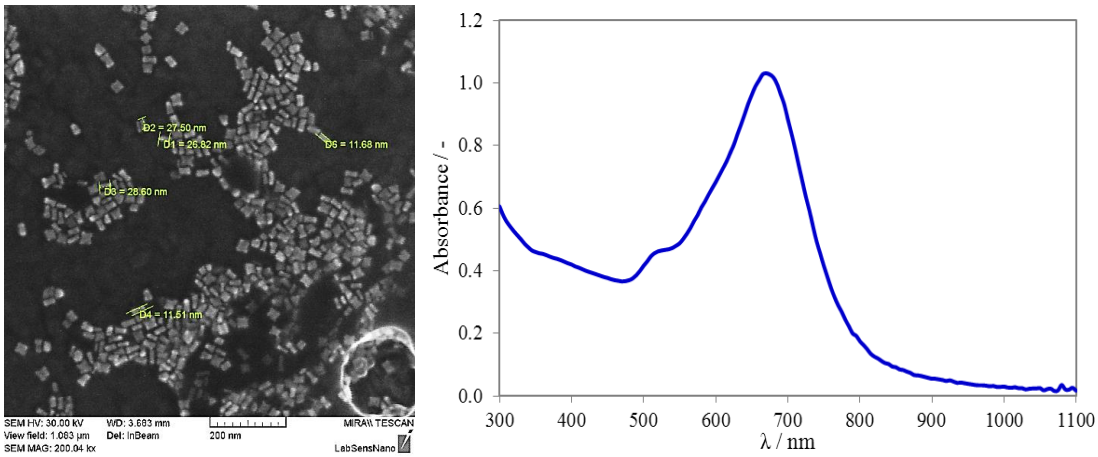

Figure 3. SEM image gold nanorods at magnification 200 nm (left) and corresponding UV-Vis spectra (right)

3.2. PEG modification

PEG was used to functionalize the AuNRs surface in order to improve the *in vivo* stability and decrease their cytotoxicity. Modifications of chosen AuNRs differing from each other in the amount of added PEG were tested (*Table 2*). UV-Vis spectra showed that the absorbance of AuNR significantly decreased after the modification with PEG (*Figure 4*). It could be caused by lower concentration of PEG-AuNRs due to multiple washing after modification. The successful modification was confirmed by comparing final FTIR spectrum of PEG modified AuNRs with reference PEG spectrum (Figure 4). The identical peaks were presenting in all cases. Mainly, the peak around 1110 cm^{-1} (C-O vibrations in ethers) is the most decisive indicator in the evaluations of PEG spectra. The presence of the peak is complied completely with PEG presence, because the other possible reagents, mainly CTAB, does not absorb in this region. TEM observation provided visible AuNRs core coated with PEG (*Figure 5*).

Table 2. Evaluation of AuNRs modification with different c[PEG]

	concentration/ mg/10 mL	λ_{max}/nm
PEG 1	2.1	616
PEG 2	3.0	616

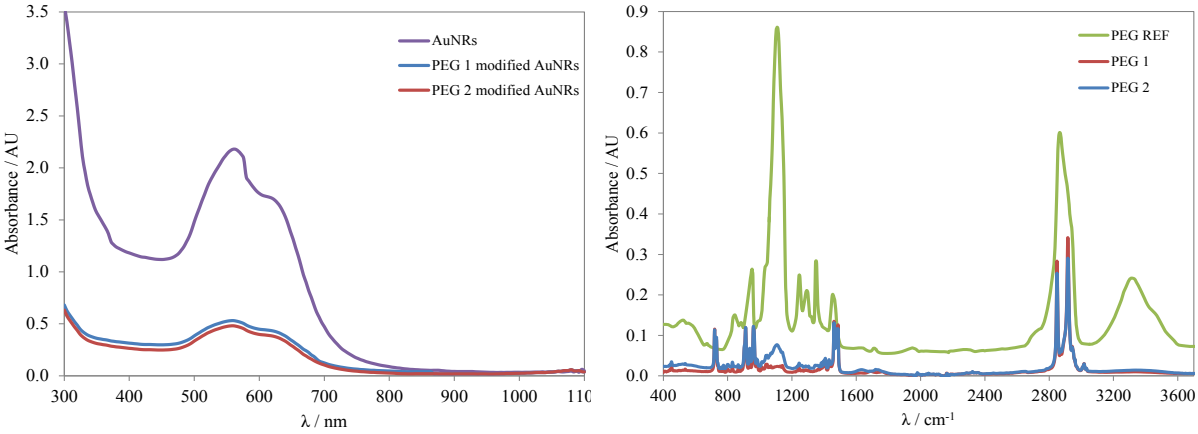

Figure 4. UV-VIS spectra of AuNRs and AuNRs with PEG cover(left) and FTIR spectra of PEG modified AuNRs compared with reference FTIR spectrum of PEG

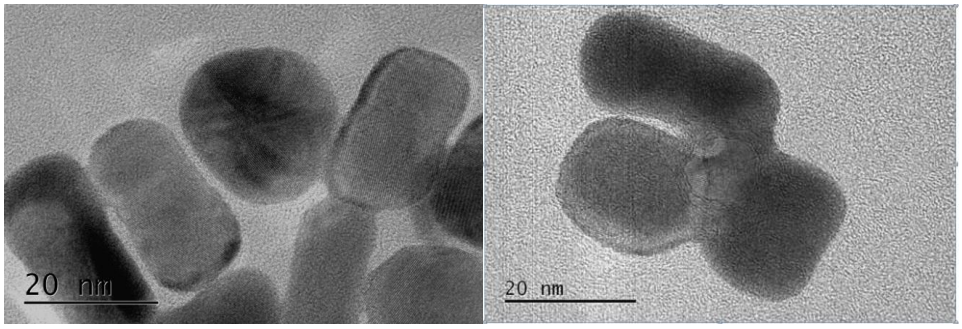

Figure 5. TEM images of gold nanorods before (left) and after (right) the modification with PEG

3.3. MTT

The MTT viability assay was performed to estimate the cytotoxicity of chosen AuNRs samples to human ovarian carcinoma cells A2780. The influence of PEG modification on cells viability improvement was also tested. The toxicity of representative samples was compared to commercial ones gained from Sigma Aldrich. Different AuNRs concentrations (1, 10, 20, and 50 µL in 200 µL) each having 12 replicates wells were investigated in the experiment. Viability was determined by absorption at 570 nm. Input logical assumption was that the lower used AuNRs concentration caused the lower toxicity. It follows that the highest cell viability should be at the lowest AuNRs concentrations. The expectation was confirmed by the MTT test. Based on the results, the highest cells viability was performed by the lowest tested concentration of each sample. It was also predicted that the higher concentration of PEG brought about the higher cells viability but both of samples showed the same toxicity. Pursuant to the results, the highest viability was performed by the PEG concentration, in contrast with the lowest viability caused by the nonmodified robust AuNRs. The toxicity level of substances under the experimental conditions at a given time and in a given cell type could be represented by the IC50 (half maximal inhibitor concentration). It is the concentration of noxae, which produces 50% of the maximum cell death. The lower toxicity is exhibited by the higher IC50. Consequently, all of samples at concentration higher than 20 µL/200 mL caused 50 % cell death

(Figure 6). At the end, the toxicity of representative samples was compared with toxicity of commercial 10 nm AuNRs which have much lower toxicity resulting much higher IC50.

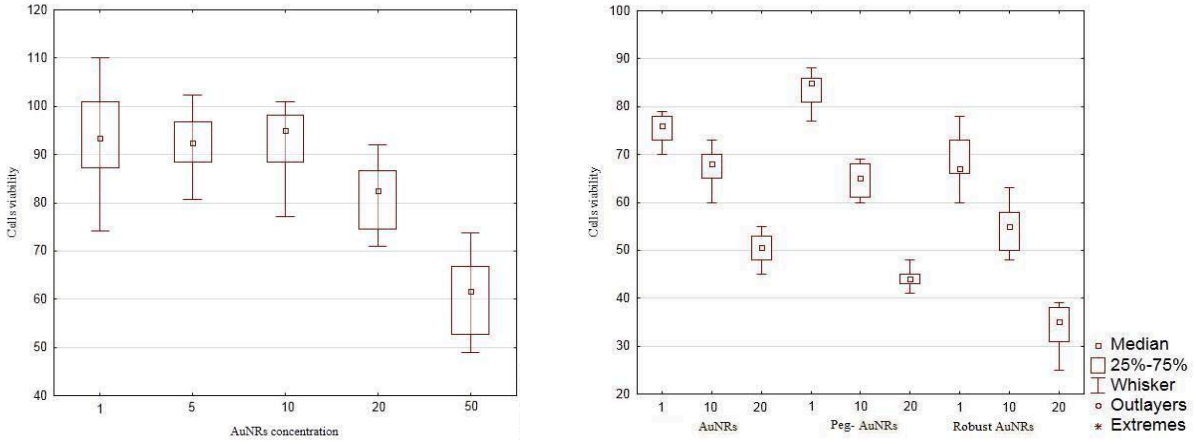

Figure 6. Cell viability A2780 after incubation time 24 h: commercial 10 nm AuNRs (left) and the representative samples (right)

4. Conclusions

In this work, the seedless growth method was used for the AuNRs preparation. The main aim was to create stable and monodispersed colloidal solution containing uniform and biocompatible AuNRs and investigate their cytotoxicity. Their final chemical and physical properties were examined with respect to possible further biomedical applications, mainly for ultrasound interactions with cells.

The AuNRs were prepared by addition of small spherical AuNPs representing seed solution to growth solutions. Growth solution usually contained gold salt, surfactant and reducing agent. AuNRs were synthesized by using CTAB as a surfactant. CTAB is very appreciated not only as an essential component in the anisotropic AuNRs growth but also for the subsequent AuNRs stability guaranteed by noncovalent coating. The problem is the toxicity of CTAB. Free CTAB is known to be highly cytotoxic for cells. In order to remain CTAB coated rods soluble, it is necessary to retain the concentration of free CTAB in solution above a certain value. This could be achieved by AuNRs centrifugation or modification with PEG. The final AuNRs were obtained by various processes. The influence of three basic reagents, namely the concentration of $HAuCl_4$ and $AgNO_3$ in growth solution and the amount of added seed on the final product was investigated in combination with different solvents . The synthesis conditions of AuNRs were modified in order to understand the influence of each reagent on the length, width, AR, and consequently the optical properties of prepared AuNRs. AR and absorption maximum of AuNRs played an important role of investigated endpoints. It was found out that the best results in the form of the highest NPs ARs and LPSR were obtained by the smallest seed addition together with the smallest concentration of $HAuCl_4$ and with $AgNO_3$ amount of 350 μL. It was also confirmed that the AR was very closely related to LPS and it exists almost linear dependece between them. The final product was modified with PEG mainly in order to improve its *in vivo* stability and decrease its cytotoxicity. PEG-modification was tested at two different condiditons varying from each other in the amount of added PEG. The presence of PEG was tested based on the knowledge about FTIR spectrum of PEG and TEM analyses. The possibility of biomedical applications was demonstrated by MTT test. Dramatic biocompatibility improvement was performed by PEG modified AuNRs. It could be caused by similar reduction of the toxic effect of presented CTAB The influence of different AuNRs solvent (PBS vs. water) was not significant. It was also find out that the toxicity is increasing with the AuNRs size.

In conclusion, the main outcome of this work is the synthesis of whole new spectrum of different sized gold nanorods, which were all almost uniform and monodisperse. Futhermore, the improvement of their biocompatibility for *in vivo* application was reached by PEG modification which was also confirmed by MTT test.

References

[1] HUANG, Y. et al. Biomedical nanomaterials for imaging-guided cancer therapy. *Nanoscale*, 2012, vol. 4, no. 20, pp. 6135-6149. ISSN 2040-3364.

[2] DRBOHLAVOVA, J. et al. Nanocarriers for anticancer drugs-new trends in nanomedicine. Current drug metabolism, 2013, vol. 14, no. 5, pp. 547-564. ISSN 1389-2002.

[3] YAO, S. et al. Fluorescent labeling of cellular targets and multicolor imaging with gold nanorods. Dyes *and Pigments*, 2014, vol. 101, no. 0, pp. 286-294. ISSN 0143-7208.

[4] LOHSE, S. E. a MURPHY, C. J. The Quest for Shape Control: A History of Gold Nanorod Synthesis. *Chemistry of Materials*, 2013, vol. 25, no. 8, pp. 1250-1261. ISSN 0897-4756.

[5] PÉREZ-JUSTE, J. et al. Gold nanorods: Synthesis, characterization and applications. *Coordination Chemistry Reviews*, 2005, vol. 249, no. 17–18, pp. 1870-1901. ISSN 0010-8545.

[6] MURPHY, C. J. et al. The Many Faces of Gold Nanorods. *The Journal of Physical Chemistry Letters*, 2010, vol. 1, no. 19, pp. 2867-2875. ISSN 1948-7185.

[7] NAGESHA, D. et al. In vitro imaging of embryonic stem cells using multiphoton luminescence of gold nanoparticles. *International Journal of Nanomedicine*, 2007, vol. 2, no. 4, pp. 813-819. ISSN 1176-9114.

[8] ALKILANY, A. M. et al. Gold nanorods: Their potential for photothermal therapeutics and drug delivery, tempered by the complexity of their biological interactions. *Advanced Drug Delivery Reviews*, 2012, vol. 64, no. 2, pp. 190-199. ISSN 0169-409X.

[9] CAI, W. et al. Applications of gold nanoparticles in cancer nanotechnology. *Nanotechnology, Science and Applications*, 2008, vol. 1, pp. 17-32.

[10] DYKMAN, L. a KHLEBTSOV, N. Gold nanoparticles in biomedical applications: recent advances and perspectives. *Chem Soc Rev*, 2012, vol. 41, pp. 2256 - 2282.

[11] VIGDERMAN, L. et al. Functional Gold Nanorods: Functional Gold Nanorods: Synthesis, Self-Assembly, and Sensing Applications (Adv. Mater. 36/2012). *Advanced Materials*, 2012, vol. 24, no. 36, pp. 5016-5016. ISSN 1521-4095.

[12] VIGDERMAN, L. et al. Quantitative Replacement of Cetyl Trimethylammonium Bromide by Cationic Thiol Ligands on the Surface of Gold Nanorods and Their Extremely Large Uptake by Cancer Cells. *Angewandte Chemie International Edition*, 2012, vol. 51, no. 3, pp. 636-641. ISSN 1521-3773.

[13] TANG, Y. et al. In vitro cytotoxicity of gold nanorods in A549 cells. *Environmental Toxicology and Pharmacology*, no. 0. ISSN 1382-6689.

[14] ALKILANY, A. M. a MURPHY, C. J. Toxicity and cellular uptake of gold nanoparticles: what we have learned so far? *Journal of Nanoparticle Research*, 2010, vol. 12, no. 7, pp. 2313-2333. ISSN 1388-07641572-896X.

[15] AGARWAL, R. et al. Mammalian cells preferentially internalize hydrogel nanodiscs over nanorods and use shape-specific uptake mechanisms. *Proceedings of the National Academy of Sciences*, 2013, vol. 110, no. 43, pp. 17247-17252.

[16] HAUCK, T. S. et al. Assessing the Effect of Surface Chemistry on Gold Nanorod Uptake, Toxicity, and Gene Expression in Mammalian Cells. *Small*, 2008, vol. 4, no. 1, pp. 153-159. ISSN 1613-6829.

[17] ALI, M. R. K. et al. Synthesis and Optical Properties of Small Au Nanorods Using a Seedless Growth Technique. *Langmuir*, 2012, vol. 28, no. 25, pp. 9807-9815. ISSN 0743-7463.

[18] JANA, N. R. et al. Seed-Mediated Growth Approach for Shape-Controlled Synthesis of Spheroidal and Rod-like Gold Nanoparticles Using a Surfactant Template. *Advanced Materials*, 2001, vol. 13, no. 18, pp. 1389-1393. ISSN 1521-4095.

Nanocomposite nanowebs with self-cleaning property

N. Kizildag, N. Ucar
Istanbul Technical University, Textile Engineering Department, Istanbul, Turkey

ABSTRACT
In this study, polyacrylonitrile (PAN) nanowebs containing TiO_2 nanoparticles were successfully prepared by electrospinning technique. TiO_2 content was varied as 1 wt% and 10 wt%. Morphology, mechanical properties and photodegradation ability of the nanowebs were investigated. Uniform nanofibers were obtained. While breaking stress increased with 1 wt% TiO_2 addition, decrease was observed at the TiO_2 content of 10 wt%. The results of photodegradation with methylene blue (MB) aqueous solution demonstrated excellent photocatalytic activity of TiO_2 incorporated PAN nanowebs. TiO_2 incorporated nanowebs with the self-cleaning property may find applications in medical textiles, filtration, etc.

Keywords
Electrospinning, functionalization, nanofiber, nanocomposite, self-cleaning, TiO_2.

1. INTRODUCTION
Electrospinning method enables the production of functionalized membranes with the incorporation of nanoparticles into a polymer matrix. Among different types of nanoparticles, TiO_2 nanoparticles are known for great availability, non-toxicity, stability, low cost and efficiency and have received remarkable attention for the self-cleaning applications since they effectively decompose organic contaminants under UV light (Daels et al. 2014). Im et al. (2007) prepared electrospun PAN-based nanofiber webs containing TiO_2 and reported that the TiO_2 containing nanowebs suspending on the dye solution had a dye removal efficiency of 60%. Jeun et al. (2011) reported the production of composite of PAN nanoweb containing sol-gel-derived TiO_2 of nanometer size and the effect of the e-beam irradiation on the photocatalytic ability of the nanowebs. While the nonirradiated PAN/TiO_2 nanofibers degraded methylene blue at the low rate of 58.6% for 3 h, e-beam irradiation resulted in a significant increase in the photodegradation ability (72.5%) of the nanowebs. Although there are some studies regarding the production of PAN/TiO_2 composite nanofibers, they are mainly focused on the morphological, structural properties and photodegradation ability of the nanowebs. In this study, polyacrylonitrile nanowebs containing TiO_2 nanoparticles were successfully prepared by electrospinning technique and morphological, mechanical properties and photodegradation ability of the nanowebs were investigated.

2. EXPERIMENTAL

2.1 Materials
Polyacrylonitrile (PAN) (Sigma Aldrich, 181315, average Mw:150.000g/mol), titanium dioxide (TiO_2) (Sigma Aldrich, 634662), dimethylformamide (DMF), methylene blue (Sigma Aldrich, 66720) were used as received.

2.2 Method
The required amount of TiO_2 were added to the required amount of DMF and homogenized with ultrasonic tip for 10 minutes and with ultrasonic bath for 45 min. Then PAN was added to this dispersion and dissolved by stirring with a magnetic stirrer at 40˚C, 300 rpm for 3 hours. The concentration of PAN was kept constant as 7 w%.
Horizontal electrospinning setup which contained a syringe pump, a high voltage power supply (0–50 kV), and a grounded rotating collector was used in the production of the nanofibers. Electrospinning solution was fed from the syringe of 10 ml. through a capillary tip with a diameter of 1.25 mm. using the syringe pump. The applied voltage was 15 kV, the distance between the tip and the collector was 10 cm and the flow rate of the spinning solution was 1 ml/h.
Scanning electron microscopy (SEM; EVO MA 10) was used to obtain SEM images of the nanowebs. From the diameters of at least 50 randomly selected nanofibers, average nanofiber diameters were calculated. Mechanical properties of the webs were measured using a tensile tester with a 100N load cell at a crosshead speed of 20 mm/min. Mitutoyo digital micrometer was used to measure the thicknesses of the specimens. The photocatalytic activities of the nanowebs were assessed by photodegradation of MB under UV irradiation from a distance of 40 cm. 300W Osram Ultra-Vitalux lamp was used for the UV-irradiation. Nanowebs of 0.06 g were immersed in 50 g MB aqueous solution (10 ppm). After exposure to UV-light for 2 h, the concentration of the MB was measured with PharmaSpec 1700 UV-Vis spectrophotometer in 250-1100 nm range. The photodegradation efficiency was calculated as $(A_0 - A_x)/A_0$ where A_0 is the absorbance value of MB solution at 663 nm. and A_x is the absorbance value of the solution at 663 nm after exposure to UV-light for 2 hours. Polyacrylonitrile nanowebs were considered as the reference.

3. RESULTS and DISCUSSIONS

3.1 Morphology
SEM images of pure and composite nanowebs are presented in Figure.1.

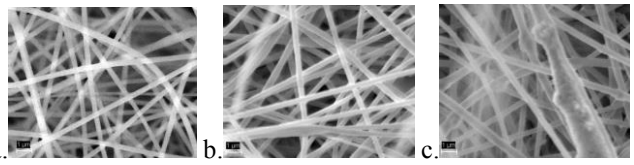

Figure.1 SEM images of a. 100%PAN, a. PAN-1% TiO_2; c.PAN-10%TiO_2 nanoweb.

While 100% PAN and PAN-1%TiO_2 nanofibers were uniform in structure and bead-free, many beads were observed on the nanofibers with 10% TiO_2 content.

The diameters of the nanofibers are presented in Table 1.

Samples	Diameter (nm)
PAN	312.67±11.34
PAN-1% TiO_2	389.62±14.72
PAN-10% TiO_2	493.31±23.97

Table.1 Diameters of the electrospun nanofibers

Addition of the nanoparticles to the polymer solutions generally increases the concentration of the electrospinning solution which result in an increase in nanofiber diameters. Besides affecting concentration, charge carriers such as conductive particles affect the conductivity of the solution; thus having an opposite effect on nanofiber diameter (Heikkilä et al. 2009; Kizildag et al. 2014). In our study, as a result of the TiO_2 addition, nanofiber diameter increased. Also higher variation in average nanofiber diameter was observed with higher TiO_2 content.

3.2 Mechanical Properties

Mechanical properties of the nanofibers are presented in Table.2.

Samples	Tensile Stress (MPa)	Elongation (%)	E-modulus (MPa)
PAN	1.56±14.48	17.24±13.97	12.64±13.98
PAN-1% TiO_2	2.11±15.62	9.00±23.22	12.32±28.38
PAN-10% TiO_2	1.45±17.36	13.81±11.86	9.59±16.28

Table.2 Mechanical properties of the electrospun nanofibers

Fillers are reported to improve the tensile breaking stress of the nanocomposites while they decrease the elongation values and increase the E-modulus values (Paul et al. 2008). In our study, TiO_2 addition resulted in an increase at 1% loading which is considered to be the result of the filler effect. But on further increase in TiO_2 content, the tensile stress of the nanocomposite nanowebs decreased. While 1% TiO_2 addition resulted in a decrease in elongation, increase in TiO_2 content resulted in increase in elongation. The decrease was due to the addition of a stiff material to the structure while the increase in elongation with the increase in TiO_2 content was thought to be the result of possible agglomeration and concomitant void formation around the agglomerates.

3.3 Photodegradation Ability

The absorbance values at 663 nm and the photodegradation efficiencies are presented in Table.3.

Samples	Absorbance at 663 nm.	Photodegradation efficiency (%)
PAN	0.84	40.43
PAN-1% TiO_2	0.26	81.56
PAN-10% TiO_2	0.13	90.78

Table.3 Photodegradation efficiency of the nanowebs.

The exposure of TiO_2 nanoparticles to UV light with an energy that matches or exceeds their band gap energy leads to the excitation of electrons from the valence band to the conduction band, leaving holes in the valence band. These electrons and holes lead to the formation of hydroxyl and oxygen radicals, which react with contaminants resulting in their decomposition (Daels et al. 2014; Bedford et al. 2010; Deveau et al. 2007). When a piece of PAN nanoweb was immersed into the MB solution and exposed to UV-light for 2 hours, the concentration of MB solution decreased 40% which was due to the adsorbance and absorbance of MB. Addition of TiO_2 to the nanoweb structure and increase in TiO_2 content resulted in further decrease in MB solution concentration which was due to the decomposing ability of the TiO_2 in the nanofiber structure.

4. CONCLUSIONS

Polyacrylonitrile nanowebs containing TiO_2 nanoparticles were successfully prepared by electrospinning technique. Uniform nanofibers with diameters between 312 and 493 nm. were obtained. While breaking stress increased with 1 wt% TiO_2 addition, decrease was observed at the TiO_2 content of 10 wt%. The results of photodegradation with methylene blue aqueous solution demonstrated excellent photocatalytic activity of TiO_2 incorporated PAN nanowebs. Under the studied conditions, the photodegradation efficiency of TiO_2 incorporated nanowebs reached up to 90% after 2 hour illumination with UV-light. TiO_2 incorporated nanowebs with the self-cleaning property may find applications in medical textiles, filtration, etc.

Acknowledgements

The support of ITU-BAP through Project 37676 is acknowledged.

References

Bedford, N.M., Steckl, A.J. (2010), Photocatalytic Self Cleaning Textile Fibers by Coaxial Electrospinning, *ACS Appl. Mater. Interfaces*, 2(8), 2448-2455.

Daels, N., Radoicic, M., Radetic, M., Van Hulle S.W.H., De Clerck, K. (2014), Functionalisation of electrospun polymer nanofibre membranes with TiO_2 nanoparticles in view of dissolved organic matter photodegradation, *Sep. Purif. Technol.*, 133, 282-290.

Deveau, P.A., Arsac, F., Thivel, P.X., Ferronato, C., Delpech F., Chovelon, J.M., Kaluzny, P., Monnet, C. (2007), Different methods in TiO_2 photodegradation mechanism studies: Gaseous and TiO_2-adsorbed phases, *J. Hazard. Mater.*, 144, 692-697.

Heikkilä P., Harlin A. (2009), Electrospinning of polyacrylonitrile (PAN) solution: Effect of conductive additive and filler on the process. *eXPRESS Polymer Letters*., 3(7), 437-445.

Im J.S., Kim, M.I., Lee, Y.S. (2008), Preparation of PAN-based electrospun nanofiber webs containing TiO_2 for photocatalytic degradation, Materials Letters 62, 3652-3655.

Jeun J.P., Park D.W., Seo, D.K., Kim, H.B., Nho, Y.C.,, Kang P.H. (2011), Enhancement of Photocatalytic Activity of PAN-Based Nanofibers Containing Sol-Gel-Derived TiO_2 Nanoparticles by E-Beam Irradiation, *Rev. Adv. Mater. Sci.* 28, 26-30.

Kizildag, N., Ucar, N., Karacan, I., Onen, A., Demirsoy, N. (2014), The effect of the dissolution process and the polyaniline content on the properties of polyacrylonitrile/polyaniline composite nanoweb, Journal of Industrial Textiles, published online, December 2014, DOI: 10.1177/1528083714564636.

Paul, D.R., Robeson L.M. (2008), Polymer nanotechnology: Nanocomposites, *Polymer*, 49, 3187-3204.

Synthesis and characterization of hydroxyapatite based nanocomposites for structural applications

M.Gond[b], A.Mishra[a] S.B.Kumar[a] D.Roy[a]

[a]Department of Materials and Metallurgical Engineering, NIFFT, Ranchi -834003, India
[b]Department of Manufacturing Engineering, NIFFT, Ranchi-834003, India

1.0 Abstract

Bone is a composite material consisting of hydroxyapatite $Ca_{10}(PO4)_6(OH)_2$ [HAp] crystals as a main phase embedded in biologically produced organic matrix. The immune system of the human body exclusively rejects any materials foreign to the body [1]. Synthetic biomaterials need HAp at least in the structure including it to avoid being rejected by living bone. Hydroxyapatite is chemically similar to the mineral component of bones and hard tissues in mammals. It is one of few materials that are classed as bioactive, meaning that it will support bone ingrowths and osteointegration when used in orthopedics, dental and maxillofacial applications. HAp ceramics are reported with osteoconductivity that is being capable of supporting bone apposition and forming a chemical bond with bone [2]. But HAp does not have the mechanical strength to enable it to succeed in long term load bearing applications.

Here in this paper we will discuss, how to increase its mechanical property by using nano Titania (TiO2) as reinforcing material in Hydroxyapatite (HAp) based composite. Hydroxyapatite (HAp) based nanocomposites were prepared by dispersion of Titania (TiO2) nanoparticles using low energy ball milling and were studied in comparison with coarse particle reinforced composites. The Titania (TiO2) nanoparticle powder was prepared by noval route of mechanical milling at different condition (Dry and Wet Milling) for different time. The Particle obtain and was characterized by using XRD. Particle size as small as 12 nm was obtain. The powders (HAp and TiO2) were consolidated using microwave sintering and then characterized using XRD, SEM, and TEM. It was found that Titania particles exist in the matrix of crystalline calcium phosphate (Ca2P2O7¬). TEM analysis showed the presence of nanoparticles in the composite powders. SEM showed lower porosities in the nanoparticles reinforced composite when compared with its coarse particle counterpart. Micro hardness analysis showed considerable improvement in hardness of HA when reinforced with nanoparticles of Titania.

2.0 Introduction

Polymer based nanomaterials have a wide range of applications but their commercial interest has caused a lot of research for structural applications. The areas of applications span wide from biological implants (bone and teeth) to aerospace, marine and military applications. The present

work is aimed at obtaining better structural properties by the development of nanocomposites using an inorganic polymer (Hydroxyapatite $Ca_{10}(PO_4)_6(OH)_2$) as the base material.

Hydroxyapatite has the ability to integrate in bone structures and support bone ingrowths, without breaking down or dissolving (i.e. it is bioactive).This property of HA enables it to be used in biological implants [3]. But HA does not have sufficient mechanical strength to enable itself to succeed in long term load bearing applications. This is why researchers all over the world have been developing methods for improving this property of HA and hence enabling its usage in structural applications but popularly has been used as bioceramic coatings and as bone filler materials.

Researchers have also been trying to improve the mechanical strength of HA in the form of nanocomposites by reinforcing the HA matrix with harder, better load bearing materials. Many researchers have been studying the use of metals as fillers [4], [5] and [6] for quite some time now. But this method has become less popular now because of its higher processing cost and complex fabrication methods. However extensive research is being done on the use of ceramic nanomaterials as fillers. There has also been lot of research being conducted for the use of Al_2O_3 and ZrO_2 as filler materials for HA based composites. But the concern in this field is the biocompatibility of these fillers. Kong et al [7] have done extensive work in improvement of biocompatibility of Al_2O_3/HA and ZrO_2 / HA composites and also have found optimal compositions for the above composites in load bearing applications.

So in order to find harder, better load bearing ceramic filler materials which is bio compatible and possess better anti-bacterial properties nano-TiO_2 is chosen. In almost all of these cases, the size of the titanium dioxide particles is an important factor affecting the final performance of the materials. It is not surprising therefore, that much research has been focused upon the reduction of particle size. Mechanical milling route has been considered as a good method to synthesize ultra-fine metallic oxide [8].Mechanical milling process is a high-energy ball milling operation that involves repetitive welding, fracturing, and re-welding of powder particles. Recently, the process has been regarded as an effective tool to synthesize metastable phases, e.g. supersaturated solid solution amorphous alloys and nano crystalline materials [9-11]. Generally, it is found that the different methods produce different results. Furthermore, the same method using different amount of the starting materials produce powder of different size [12]. Accordingly, it prompted us to investigate the factors in detail which may have important effect upon the particle size.

In this paper, titanium dioxide nano-powders were prepared by the Mechanical milling. X-ray diffraction (XRD) and Transmission electron microscopy (TEM), of milled powders was used to study the effect on the microstructures and grain size. In the later stage of this paper consolidation of composite powders has also been studied and SPS has been studied more popularly. The mechanical properties of spark plasma sintered nano composite powders have produced enhanced indentation and fracture toughness [13]. Thus, SPS compacts of nanoZrO2/ Al2O3-HA composite powders have been considered for load-bearing orthopedic implants because of its unique fracture toughness and strength. Porous HA ceramics have been sintered effectively and this process could get a sintered ceramic more rapidly at much shorter sintering time and lower sintering temperature than that of the conventionally heat sintering process. Furthermore, the microwave-sintered samples showed much smaller grain size and more uniform microstructure and resulted in bio-ceramic with a comparable compressive strength of that obtained in conventional method [14].

3.0 Experimental Work

3.1 Preparation of nano TiO_2 powder:

Commercially available micron sized powders of TiO_2 (99%Pure, LOBA Chemic Pvt Ltd, Mumbai) were used. The milling was performed in a planetary ball mill (FRITSCH, GERMANY). Initially the particle size of the TiO_2 were measured with the help of a Particle size analyzer (Particle Sizer Annlysett-22,FRITSCH) During milling the weight ratio of the ball to the powder was maintained at 10:1. The balls and vials are made of tungsten carbide.

3.2 Characterization:

The particle size of the TiO_2 before milling was measured with the help of a particle size analyzer (Particle Sizer Annlysett-22,FRITSCH). As receive and milled powders were characterized by X-ray diffraction (XRD) technique. X-ray diffraction analysis was carried out using CuKα radiation on a Philips PW1840 diffractometer using a step size of 0.05^0 (2θ). Prior to these analyses, XRD peaks were corrected for the effects of the Kα_2 radiation and instrumental broadening. The particle size of the ball milled TiO_2 powders (wet & dry) were computed by the XRD technique using single line profile analysis [15].
The microstructure, crystallite size were studied using the JEM 2100 HRTEM operated at an acceleration voltage of 200 kV in bright field modes. Selected area diffraction (SAD) patterns were obtained to identify the phases at specific locations using appropriate aperture and tilt.

3.3 Processing of composites:

HA powder of 99% purity with an average particle size ~20 μm (Loba Chemie Pvt Ltd, Mumbai) and 5% Coarser size, 5% nanosized TiO_2 powder were used for preparing (HA+ 5%TiO_2) green powder mix.
The synthesized composites were then consolidated using microwave sintering techniques at temperatures around 1400 ˚C. The composite powders were characterized using TEM. The sintered pellets were characterized using SEM and XRD analysis. Micro hardness measurements were taken and compared with pure HA.

4.0 Results and discussion

4.1 TiO_2 Nano Powder Preparation:

The particle size distribution of the TiO_2 powder prior to mechanical milling is shown in Figure 1. The size distribution profile of the powder clearly shows that the distribution is fairly wide ranging from 0.195μm to 23.08μm.

Figures 2 and 3 show the results of XRD analysis of the mechanically milled TiO_2 powders in dry and wet condition.

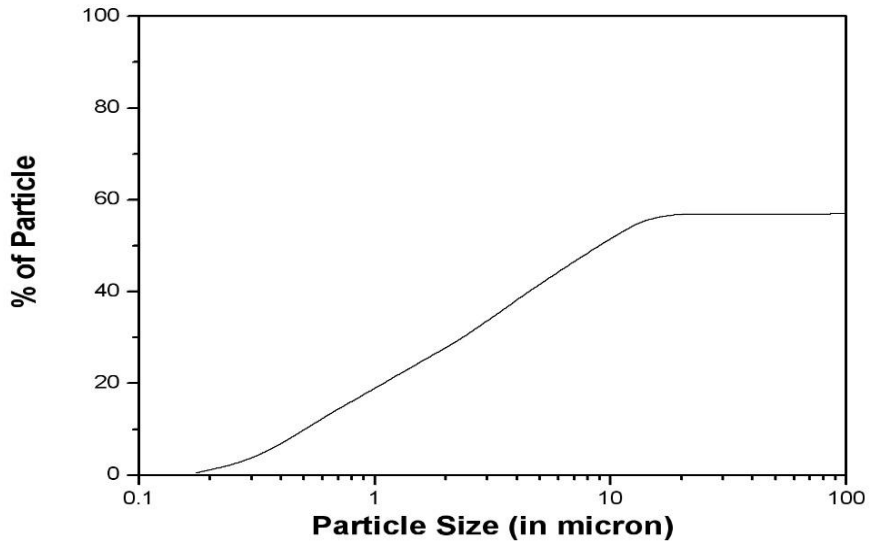

Figure 1 Particle size distribution of TiO_2 powder sample before ball milling.

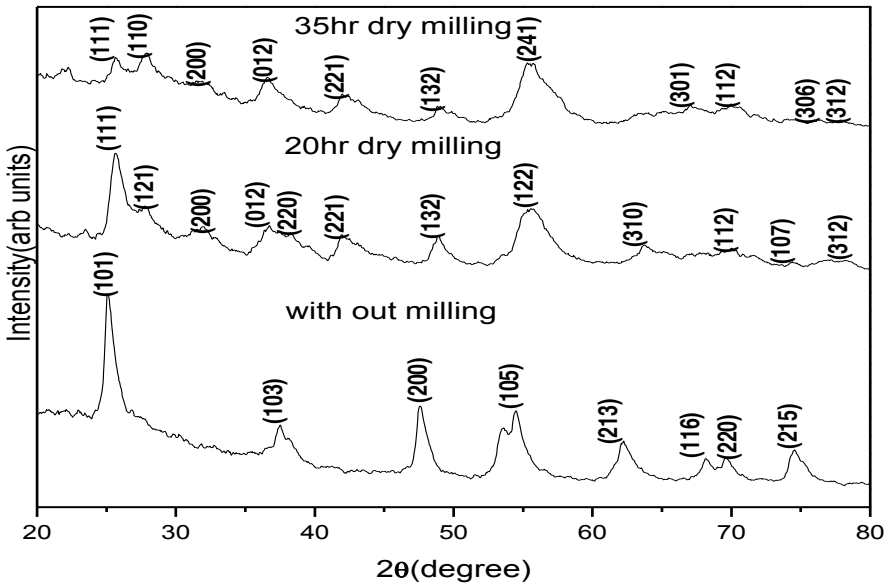

Figure 2 XRD spectra of TiO_2powder (a) After 20h dry milling (b) After 35h dry milling (c) without milling.

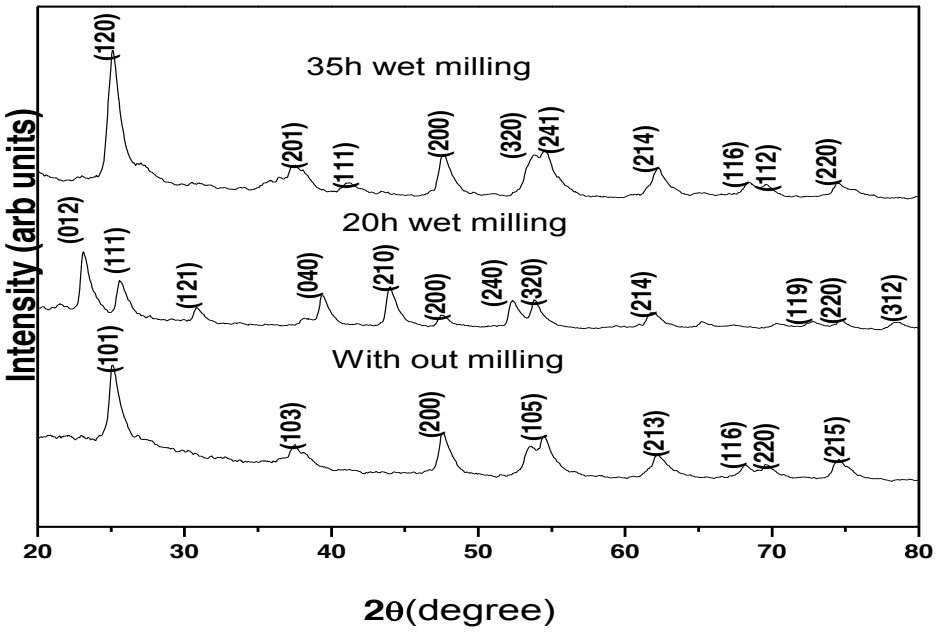

Figure 3 XRD spectra of TiO_2powder (a) After 20h wet milling (b) After 35h wet milling (c) without milling.

4.2 Processing of Composite:

The sintered samples were characterized using XRD technique. Fig 4 shows the XRD plots obtained for the samples. It can be seen from figure 4 (a) that the titania nanoparticles reinforced HA pellet shows all the characteristic peaks of crystalline TiO2 but rest of the peaks were identified to be a crystalline phase of calcium phosphate $Ca_2P_2O_7$. The formation of this phase can be attributed to the loss of water upon sintering. Fig 4(b) of coarse particle reinforced composite also indicates the formation of $Ca_2P_2O_7$ by the identification of all its characteristic peaks. However the titania phase in the coarse particle composite exists in Ti_3O_5 form thereby indicating the occurrence of a phase transformation during sintering. All the peaks were identified using JCPDS standards and it can be seen that there is a good match both in terms of intensity and position of the peaks.

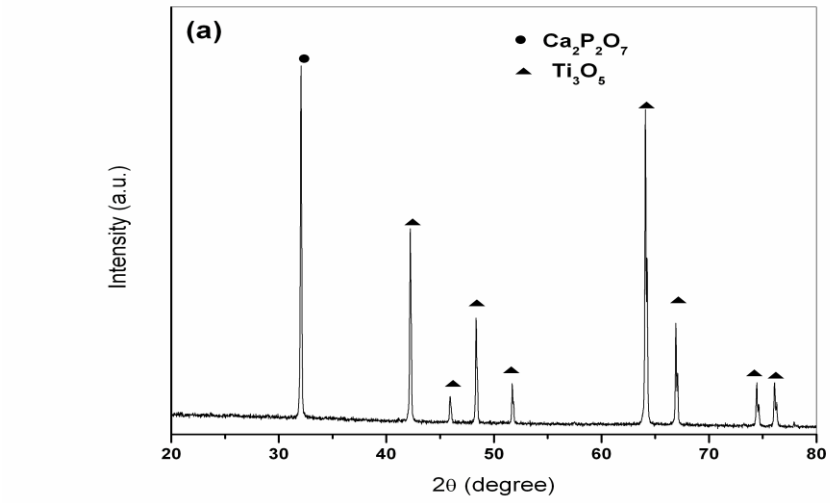

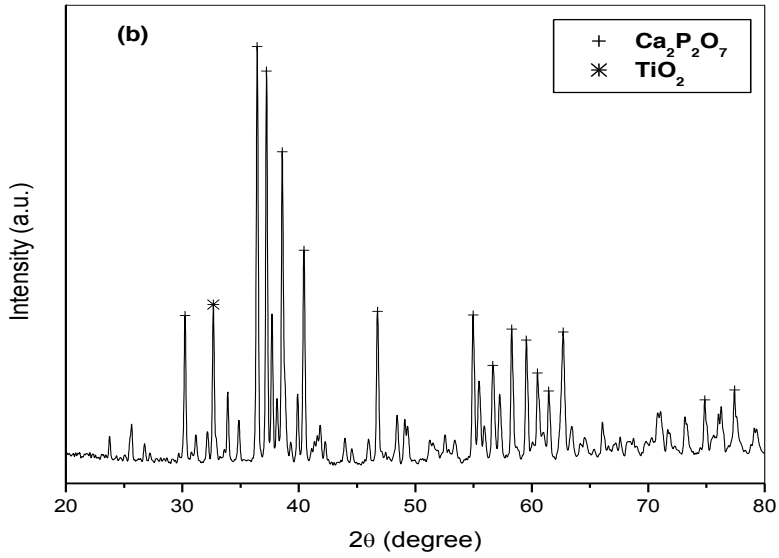

Figure 4, XRD plots of (a) coarse particle reinforced (b) nano particle reinforced TiO_2-HA composite.

Scanning electron microscopy of the sintered pellets was performed fig 5(a) shows the presence of low porosities in the nanoparticle reinforced TiO_2-HA composite indicating very good sintering. However the coarse particle reinforced composite does not show good sintering fig 5(b). It can be clearly seen that the samples had fairly high porosity with clearly visible isolated particles sticking to each other. This can be attributed to the fact that the nanoparticles, due to its high surface area to volume ratio and also higher diffusivity shows better sintering capability than that of its coarse counterparts. EDAX results confirm the presence of titania and crystalline calcium phosphate. The scanning electron micrographs were taken using JKOL JSM-5800 scanning electron microscope. The presence of titania and HA were confirmed using EDAX measurements.

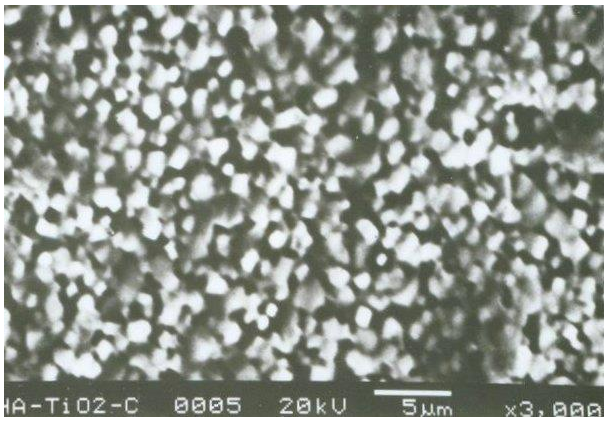

(a)

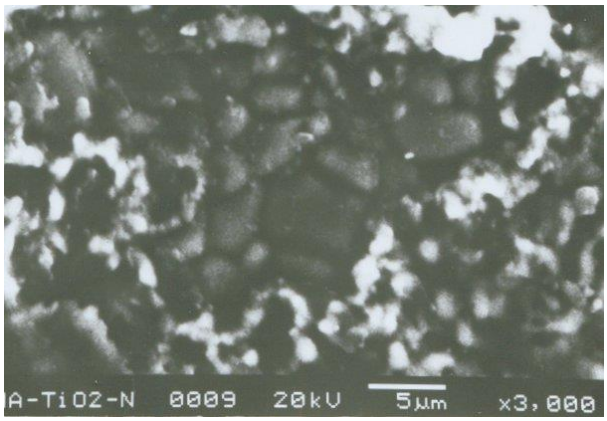

(b)

Figure 5, SEM micrographs of (a) coarse particle reinforced (b) nano particle reinforced TiO_2-HA composite.

Transmission electron microscopy was performed on the composite powders figure 6. The TEM images were taken using JEM 3000 transmission electron microscope.

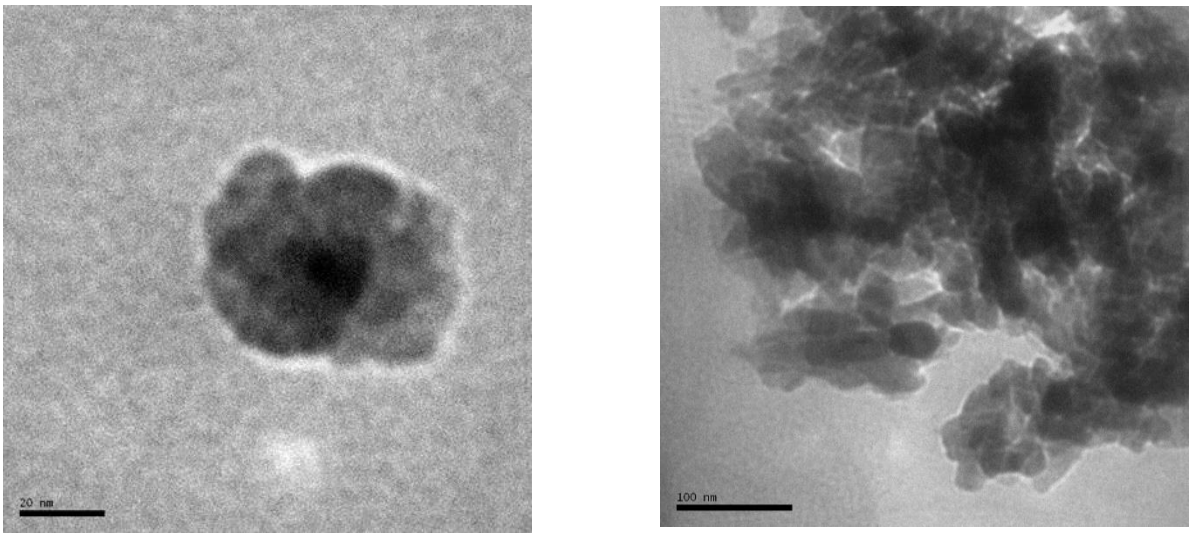

Figure 6, TEM images of nano particles reinforced in TiO_2-HA composite.

Microhardness testing was performed using Leica microhardness tester on the two samples viz. nanoparticle reinforced and coarse particle reinforced. The Vickers microhardness of the coarse particle composite sample was measured to be 466 HV and that of the nano particle composite was 631 HV. Both the composites show better hardness than the hardness of pure HA. As shown in Figure 7.

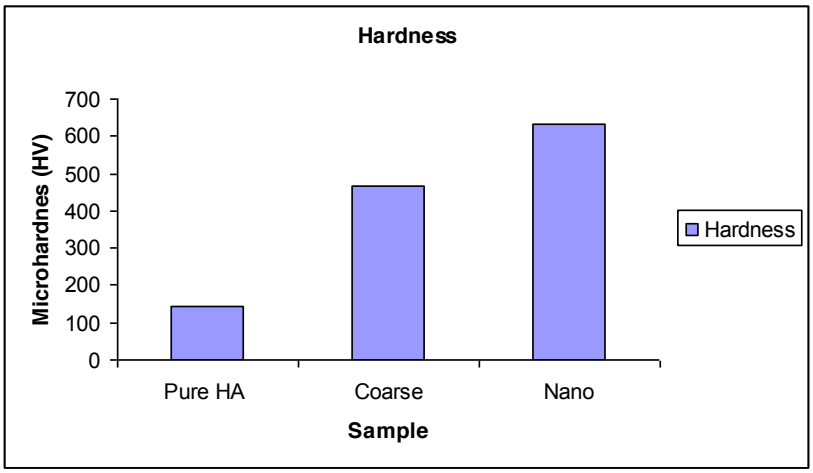

Figure 7:

5.0 Conclusion:

Nano-TiO_2 powders have been prepared by mechanical milling method successfully. By controlling the conditions properly, nano-TiO_2 powders with the grain size less than 12 nm could be obtained successfully by milling technique.

The ball milling method provides a novel way for the dispersion of Titania particles into an HA matrix. The high rate of heating provided by the usage of microwave sintering enables faster, more efficient and better sintering. The Titania nanoparticles reinforced composite showed much higher hardness) and both the composites were considerably harder than the pure HA hardness (obtained from literature).This fact can be attributed to the suppression of dislocation movement due to the reinforcements and also to the better sintering due to the enhanced diffusivity of nanoparticles.

References

[1] G Saraswathy et al, Bull. Mater. Sci., Vol. 24, No. 4, **2001**, pp. 415–420.

[2] DeGroot, K. (**1981**) Bioceramics consisting of calcium phosphate salts. *J. Biomaterials* 1, 47-50.

[3] C.Q. Ning, Y. Zhou. Biomaterials 23 (2002) 2909–2915

[4] S. Thian, N.H. Loh, K.A. Khor, S.B. Tor. Biomaterials 23 (**2002**) 2927–2938.

[5] Alessandro Sgambato et al. Materials Science and Engineering C23 (**2003**) 419–423.

[6] Ductile Particle Toughening Of Hydroxyapatite Ceramics Using Platinum R. E. Cleggand G.D.Paterson. SIF **2004** Structural Integrity and Fracture.

[7] Young-Min Kong, Chang-Jun Bae, Su-Hee Lee, Hae-Won Kim, Hyoun-Ee Kim. Biomaterials 26 (**2005**) 509–517.

[8] SakkaS. Am. Ceram. Soc. Bull.**64** (1985) 1463.

[9] OehringM., KlassenT., and BormannR., J. Mater. Res. 8, (1993)2819

[10] GuoW, IasonnaA., MaginiM., MartelliS,, and PadellaF., J, Mater Sci 29, (1994).2436

[11] KochC.C, CavinO.B, MckameyC.G. and ScarbraighJ.C., Appl. Phys, Lett, 43, (1983) 1017

[12] ZoulinC.U.IJ. Mater. Sci. Technol.**15** (1999) 71

[13] R. Kumar a, K.H. Prakash b, P. Cheang, K.A. Khor. Acta Materialia (**2005**).

[14] Xinlong Wang, Hongsong Fan, Yumei Xiao, Xing dong Zhang. Materials Letters 60 (**2006**) 455–458

[15] KlugH.P., AlexanderL. E., *X-ray Diffraction Procedures for Polycrystalline and Amorphous Materials*, 2nd ed. (John Wiley & Sons, New York), 1974, 643.

Effect of Solvents on the Dispersion of Graphene Nanoplatelets in Nanohydroxyapatite for Load Bearing Body Implants

MM. Feven,[1] M. Khalid,[1*] CT. Ratnam,[2] ME. Hoque,[3]

[1]Division of Manufacturing and Industrial Processes, Faculty of Engineering, University of Nottingham Malaysia Campus, Jalan Broga, 43500 Semenyih, Selangor, Malaysia

[2]Bioengineering Research Group, Faculty of Engineering, University of Nottingham Malaysia Campus, Jalan Broga, 43500 Semenyih, Selangor, Malaysia

[3]Radiation Processing Technology Division, Malaysian Nuclear Agency, Bangi, Selangor, Malaysia

*Corresponding author Tel: +6(03) 8924 8775; Fax: +6 (03) 8924 8017
Email: khalid.siddiqui@nottingham.edu.my

Abstract: Hydroxyapatite (HA) has been widely considered for medical applications due to its biocompatibility as well as chemical and biological affinity with the bone tissue. However, due to its weak mechanical properties, the application in load bearing body implants is limited. Therefore, in this research to overcome this limitation, 0.01g of 8nm graphene nanoplatelets (GNP) was added to the HA. Furthermore, different solvents such as water, ethanol and acetone were used to disperse the GNP. The synthesised HA/GNP blend was characterized using thermogravimetric analysis (TGA), x-ray diffraction (XRD), scanning electron microscopy (SEM), zeta-Sizer, Brunauer-Emmett-Teller (BET) and Fourier transform infrared spectroscopy (FTIR). The FESEM results show that GNP was homogeneously dispersed into the HA. Moreover, an increase in the thermal stability of the HA in the order of acetone > ethanol > water was depicted by the TGA results. The XRD, FTIR, BET and zeta-sizer results revealed the chemical compositions and particle size of the synthesised HA/GNP blend has the characteristics of HA with smallest nanoparticle obtained in order of acetone < ethanol < water.

Keywords: Load bearing body implants, nanohydroxapatite, graphene nanoplatelets, ultrasonication, dispersant

1. Introduction

Body implants are designed to mimic the properties of human bone and act as a support until the broken or damaged bone is healed (Liebschner et al., 2003). It is crucial that the body

implants mimic the natural extracellular matrix (ECM) structurally and functionally for a successful regeneration to take place (Tuzlakoglu et al., 2005). These properties are mainly affected by the material used to develop the body implant. As a result, we chose hydroxyapatite (HA). HA is the major component of the inorganic segment of our bone, which happens to be a biocompatible material with excellent osteoconductive properties. Furthermore, HA is bioceramic material which can easily be synthesised and be used for medical application. However, HA is brittle in nature, making it prone to failure due to fatigue, which limits its usage in load bearing body implants. In orde to improve the properties, metals and their alloys, carbon nanotubes as well as polymers have been used and shown positive enhancement (Fan et al., 2014). In addition, graphene a single-atom thick sheet of hexagonally arrayed carbon atom has attracted a tremendous attention due its high mechanical properties and also biocompatibility. However, homogeneous dispersion of GNP into HA is very difficult since graphene atoms tend to stick together and agglomerate. To overcome this issue, ultrasonication has been used. This is due to the fact that not only can ultrasonication break up the agglomerates and reduce the particle size, but it can also improve the dispersion of the nanoparticles (Cengiz et al., 2008).

In this research, the synthesised HA powder was dispersed into GNP with the help of ultrasonication. The influence of different solvents and sonication on the dispersion of GNP into HA was investigated. The solvents used to disperse the GNP into HA were water, ethanol and acetone. Then the HA/GNP blend was then characterized using thermogravimetric analysis (TGA), x-ray diffraction (XRD), field emission scanning electron microscopy (FESEM), zeta-sizer, Brunauer-Emmett-Teller (BET) and Fourier transform infrared spectroscopy (FTIR).

2. Materials and methodology

2.1. Materials

The chemical used for synthesis of nanohydroxyapatite such as di-ammonium hydrogen phosphate (A.P.), calcium nitrate tetrahydrate (C.P.), ammonium solution (30%) (A.P.), and absolute alcohol 99.7% (Denatured) (A.P.) were purchased from LGC scientific, Malaysia. All chemicals were analytical grade and were used without further modification.

2.2. Sample preparation

A solution of 50mL of 1M calcium nitrate tetrahydrate and 35mL of 0.6M diammonium hydrogen phosphate was mixed with GNP dispersed in a solvent (water, ethanol, and acetone) using ultrasonication- Cole Palmer ultrasonic processor as illustrated in **Figure 1.** The pH of the solution was adjusted with ammonium solution. The different sets of HA/GNP blends prepared are shown in **Table 1.** Once the reactions were completed, the solutions were vacuum filtered and washed with water and ethanol. The washed precipitate (HA/GNP) was collected and kept in the oven to dry at 70°C for overnight. Later, the characterization of the HA/GNP blends were carried out.

Table 1: Sets of GNP/HA blends prepared

Sample	GNP Particle Size (nm)	GNP wt ratio (wt%)	Solvent
Sample 1	8	0.01	Water
Sample 2	8	0.01	Ethanol
Sample 3	8	0.01	Acetone

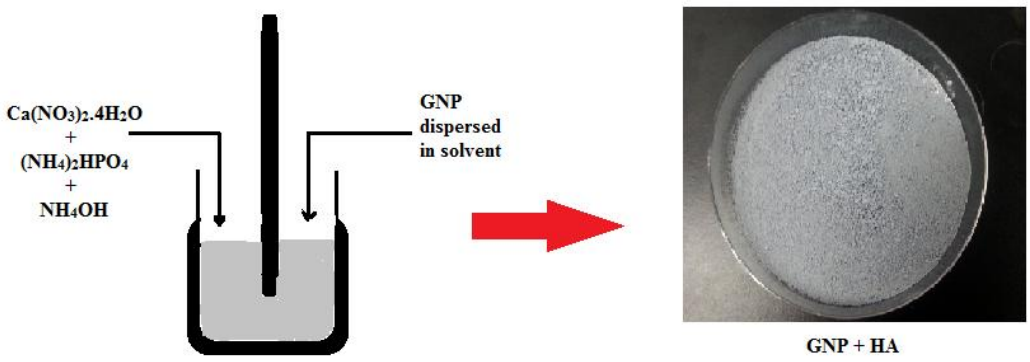

Figure 1: Synthesis and dispersion of HA into GNP

2.3. Characterization Tests

The particle size and surface morphology of the powder were examined with the help of field emission scanning electron microscope (FESEM, FEI Quanta 400) whereas the particle size distribution was measured using Zeta-sizer (Zetasizer nano ZS). The specific surface area of the powder was determined by Brunauer-Emmett-Teller (BET, micromeritics ASAP 2020 surface area and porosity analyser). Furthermore, using a computerized thermogravimetric analyzer (TGA, Mettler Toledo TGA/DSC 1 equipped with STAR^e System), the thermal stability of the HA/GNP blend was studied. The chemical functional group of the HA/GNP

blend was tested using Fourier transform infrared spectroscopy (FTIR, Perkin Elmer Spectrum 2000) by KBr pellets technique and the XRD patterns using X-ray diffraction analyser (XRD, Panalytical X'Pert Pro equipped with X'pert HighScore Plus system) using Cu-K_α radiation (λ = 0.15418nm).

3. Results and Discussion

Figure 2 depicts the FTIR spectrum of the GNP/HA blends where all three samples prepared resemble one another. From the figure, two peaks of phosphate functional groups (PO_4^{3-}) were observed at wavelength ~1030cm^{-1} and ~603cm^{-1}. These peaks are known as the stretching and bending modes of PO_4^{3-} group present in HA (Scalera et al., 2013, Gopi et al., 2008). However, at wavelength of ~825cm^{-1} presence of acidic phosphate group (HPO_4^{2-}) were detected (Hongquan et al., 2003). Other peaks shown at ~3446cm^{-1} with high intensity and at ~1636cm^{-1} with low intensity corresponds to the stretching and bending modes of the hydroxyl group (OH^-) in the HA (Singh, 2012). The OH^- group is as a result of the physically absorbed and lattice water present in HA (Granados-Correa et al., 2010). Furthermore, presence of nitrate group (NH_4^+) at wavelength of ~1384cm^{-1} is detected due to ammonium solution added during the synthesis process (Singh, 2012).

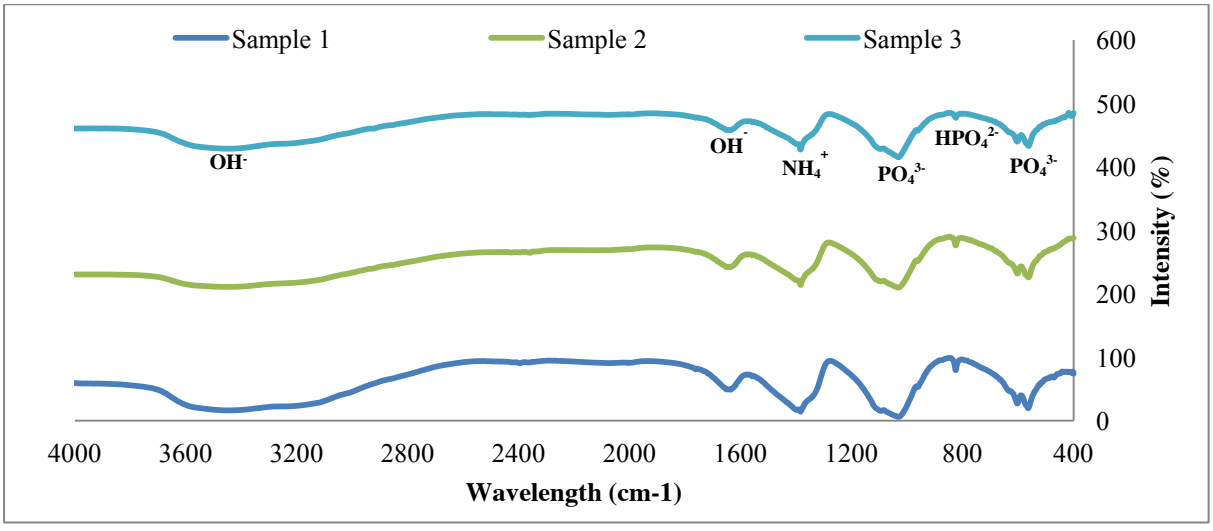

Figure 2: FTIR spectrum for GNP/HA blend

Figure 3 depicts the XRD pattern of the GNP/HA blend prepared by dispersing in different solvents. From the figure, it can be observed that the most intense and sharp lines are found between the 2θ angle of 20-60^o (Granados-Correa et al., 2010). The peaks found at 2θ angle

of 27°, 32-35°, 40-42°, 47-48°, 50°, and 54° respectively indicate presence of HA (Hui et al., 2010). However, the intensity of these peaks is low, indicating the synthesised blend is indeed amorphous phase.

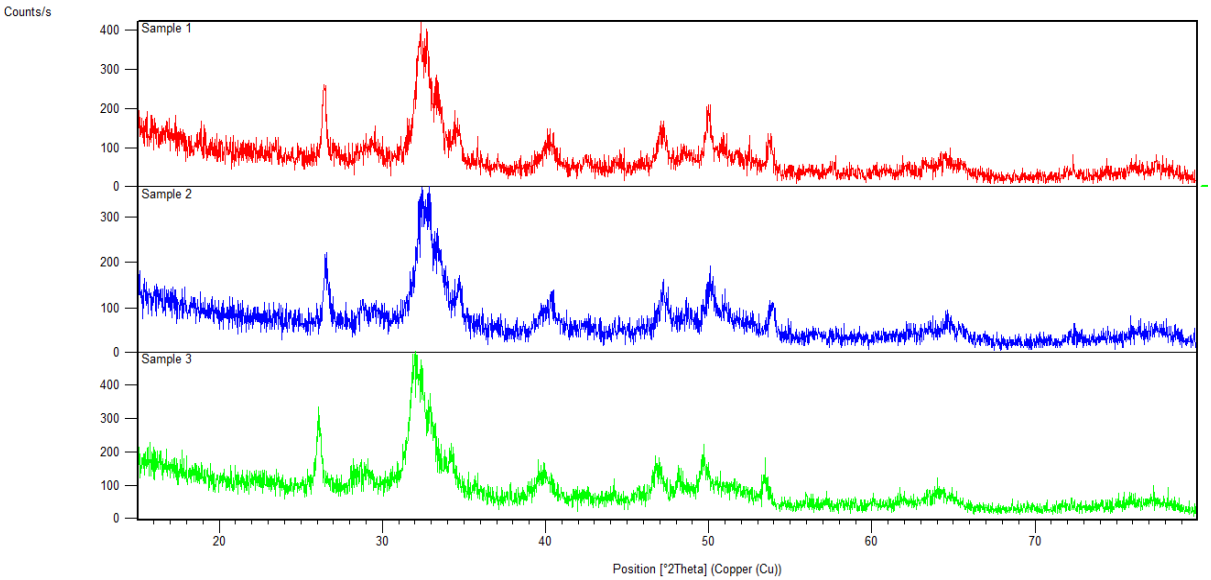

Figure 3: XRD pattern for GNP/HA blend

Figure 4 depicts the thermal stability of GNP and HA blends dispersed in different solvents, water, ethanol and acetone. From the figure, three stages of degradation can be observed. This could be caused by the removal of two water contents (absorbed and lattice) found in HA (peak 1 and 2, respectively) and the deformation of hydroxyapatite (peak 3) which takes place beyond 500°C. It was observed from the three solvents used to disperse GNP into HA, acetone (sample 3) has produced a more thermally stable GNP/HA blend compared to ethanol (sample 2) and water (sample 1) with remaining weight percentage of 72.14wt%, 69.55wt% and 66.74wt%, respectively. Furthermore, the dispersion of the GNP into HA was seen to vary with different solvents used as shown in **Figure 5**. The FESEM images of GNP/HA dispersed in acetone depicted in **Figure 5 (e,f)** showed the finest and homogenously dispersed blend compared to GNP dispersed in water and acetone. This was complemented with the particle size distribution obtained from the zeta-sizer shown in **Figure 6**, as well as the surface area of the GNP/HA blends measured by BET where GNP/HA dispersed in acetone (94.185m^2/g) was higher compared to the ones dispersed in ethanol (90.2839m^2/g) and water (87.6968m^2/g).

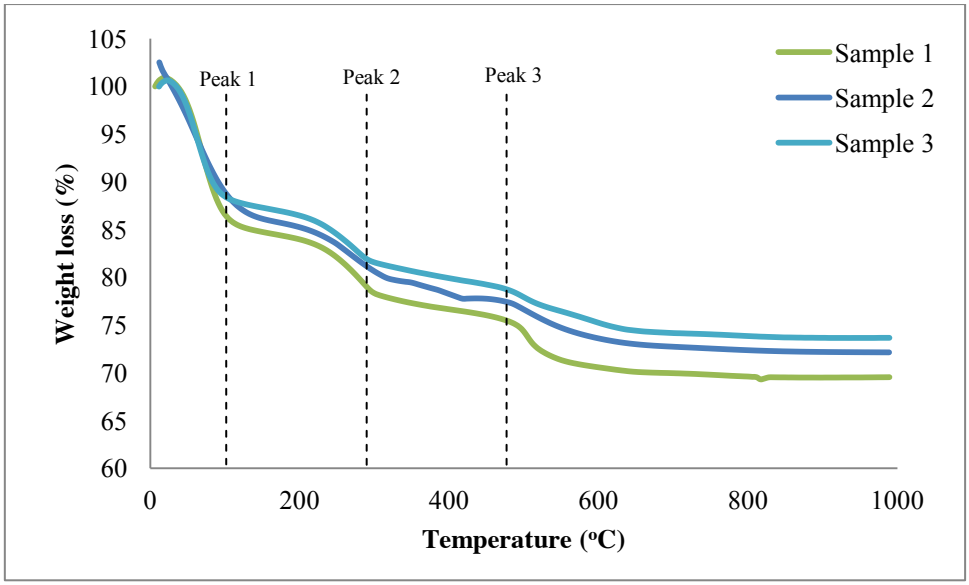

Figure 4: TGA results for GNP/HA blend dispersed in different solvents

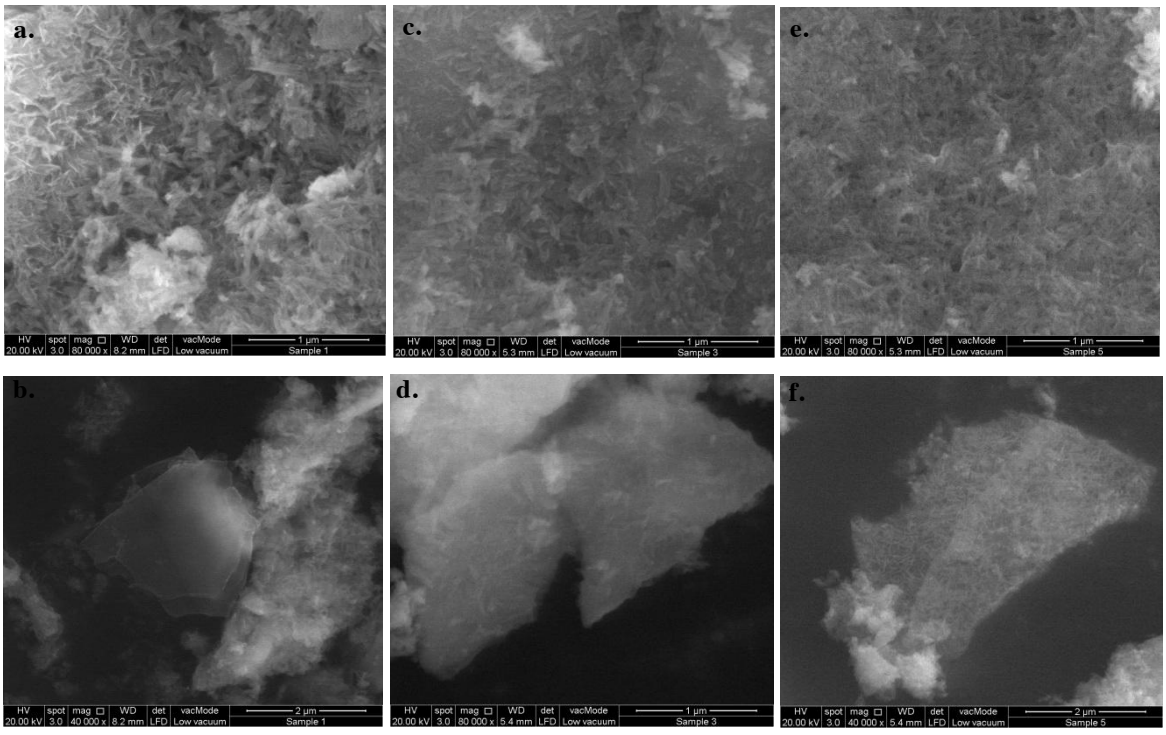

Figure 5: FESEM image for GNP/HA blend (a,b) sample 1, (c,d) sample 2 and (e,f) sample 3

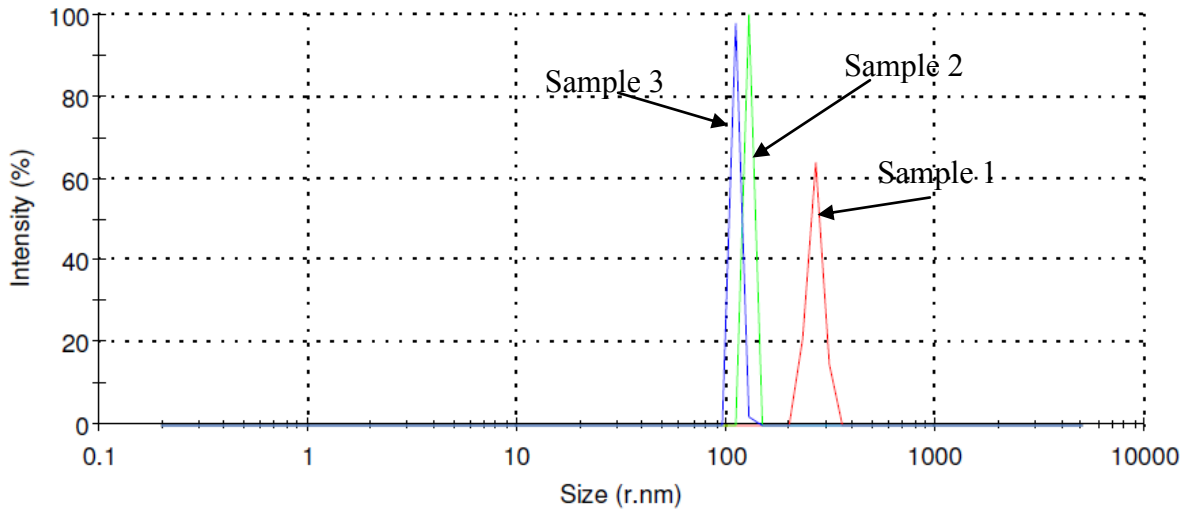

Figure 6: Particle size distribution using zeta-sizer for GNP/HA blend

4. Conclusion

In this study, homogenously dispersed GNP/HA blend was successfully prepared using precipitation method assisted with ultrasonication. The dispersion of the GNP in HA was greatly influenced by the solvents used such as water, ethanol and acetone. The FESEM results show that GNP was homogeneously dispersed into the HA when acetone was used as a dispersant solvent. This was further complemented by the zeta-sizer and BET results, revealing particle size of the synthesised HA/GNP blend has the characteristics of HA with smallest nanoparticle obtained in order of acetone < ethanol < water. Furthermore, the thermal stability of the GNP/HA blend was maximum when for acetone solvent compared to ethanol and water used.

Acknowledgement

The authors would like to acknowledge the financial support provided by the University of Nottingham, Malaysia campus research grant (UNR30005) for this research.

Reference

CENGIZ, B., GOKCE, Y., YILDIZ, N., AKTAS, Z. & CALIMLI, A. 2008. Synthesis and characterization of hydroxyapatite nanoparticles. *Colloids and Surfaces A: Physicochemical and Engineering Aspects,* 322**,** 29-33.

FAN, Z., WANG, J., WANG, Z., RAN, H., LI, Y., NIU, L., GONG, P., LIU, B. & YANG, S. 2014. One-pot synthesis of graphene/hydroxyapatite nanorod composite for tissue engineering. *Carbon,* 66**,** 407-416.

GOPI, D., GOVINDARAJU, K., VICTOR, C. A. P., KAVITHA, L. & RAJENDIRAN, N. 2008. Spectroscopic investigations of nanohydroxyapatite powders synthesized by conventional and ultrasonic coupled sol–gel routes. *Spectrochimica Acta Part A: Molecular and Biomolecular Spectroscopy,* 70**,** 1243-1245.

GRANADOS-CORREA, F., BONIFACIO-MARTINEZ, J. & SERRANO-GOMEZ, J. 2010. Synthesis and characterization of calcium phosphate and its relation to Cr (VI) adsorption properties. *Revista Internacional de Contaminacion Ambiental,* 26**,** 129-134.

HONGQUAN, Z., YUHUA, Y., YOUFA, W. & SHIPU, L. 2003. Morphology and formation mechanism of hydroxyapatite whiskers from moderately acid solution. *Materials Research,* 6**,** 111-115.

HUI, P., MEENA, S., SINGH, G., AGARAWAL, R. & PRAKASH, S. 2010. Synthesis of hydroxyapatite bio-ceramic powder by hydrothermal method. *Journal of Minerals and Materials Characterization and Engineering,* 9**,** 683.

LIEBSCHNER, M., WETTERGREEN, M., ASHAMMAKHI, N. & FERRETTI, P. 2003. Optimization of bone scaffold engineering for load bearing applications. *Topics in tissue engineering***,** 1-39.

SCALERA, F., GERVASO, F., SANOSH, K., SANNINO, A. & LICCIULLI, A. 2013. Influence of the calcination temperature on morphological and mechanical properties of highly porous hydroxyapatite scaffolds. *Ceramics International,* 39**,** 4839-4846.

SINGH, A. 2012. Hydroxyapatite, a biomaterial: Its chemical synthesis, characterization and study of biocompatibility prepared from shell of garden snail, Helix aspersa. *Bulletin of Materials Science,* 35**,** 1031-1038.

TUZLAKOGLU, K., BOLGEN, N., SALGADO, A. J., GOMES, M. E., PISKIN, E. & REIS, R. L. 2005. Nano- and micro-fiber combined scaffolds: A new architecture for bone tissue engineering. *Journal of Materials Science: Materials in Medicine,* 16**,** 1099-1104.

Mesoporous Materials Ga doped SBA-15 for Use as Support in Friedel Crafts Acylation: Activity and Stability

Fatima Zohra EL Berrichi[1], Leila Cherif [2], Cuong Pham-Huu [3]

1. Laboratoire de Chimie Physique, Université 08 Mai 45 Guelma BP401, Algeria .
2. Laboratoire de Catalyse et Synthèse Organique, Faculté des Sciences, Université de Tlemcen BP119, Algeria
3 Institut nstitut de Chimie et Procédés pour l'Energie, l'Environnement et la Santé (ICPEES) - UMR 7515
ECPM - Campus de Cronenbourg 25 rue Becquerel 67087 Strasbourg

Abstract

Gallium containing SBA-15 mesoporous materials with Si/Ga =10 and 60 were synthesized using a post and direct treatment procedure with an aqueous solution of $Ga(NO_3)_3$. The materials were characterized by means of BET, XRD and TEM. It appears that stable Ga-species were anchored to the siliceous matrix of SBA-15 or introduced in the framework via isomorphous substitution, thus generating acid properties in their host material. The catalytic activity of Ga doped SBA-15 materials has been evaluated in the Friedel-Crafts acylation of anisole with benzoyl chloride. In contrast to Ga-samples prepared by post-treatment, in situ GaSBA-15 present a lower stability in the acylation reaction. However, the catalytic results indicate that Ga containing SBA-15 mesoporous materials can be used as versatile and stable acid catalysts for Friedel–Crafts reaction with appropriate behavior depending on their preparation mode.

Keywords SBA-15, gallium, supported SBA-15, Acid catalyst, Friedel–Crafts

1. Introduction

Throughout the last decades, environmental and economic considerations have raised the interest to modify industrial important processes so that the use of harmful and toxic waste could be avoided. In this respect, heterogeneous catalysis plays a key role to replace liquid acids or superacids **[1, 2]** by solid acids like microporous zeolites or mesoporous materials of the M41S family **[3–5].** However MCM-41, which shows a highly ordered hexagonal array of narrow 1D pores, possess only a wall thickness less than 1 nm, thus reducing its thermal stability **[6]**. Recently a new type of ordered mesoporous material achieved by using a triblock copolymer as structure-directing agent under strongly acidic conditions, so called Santa-Barbara (SBA) has attracted great attention in the field of catalysis **[7–10]**. SBA-15 material possess a high surface area (600–1000 $m^2 g^{-1}$) and is formed by a hexagonal array of uniform tubular channels with tunable pore diameters in the range of 5–30 nm which are significantly larger than those of MCM-41**[5]**. The pore size can be varied on a relatively large range between 5 and 20 nm depending on the synthesis conditions. The SBA-15 material also exhibits a higher stability due to the greater wall thickness compared to the MCM-41 material **[7]** which render it more suitable for use as catalyst support in catalytic processes where thermal treatments and repeated regeneration were frequently encountered. Several studies dealing with the incorporation of transition metals like Al, V, Ti, Fe,. . .into the SBA-15 host via direct synthesis or post-synthetic grafting method to create active sites in these materials have already been published **[11–13]**. However, it is noteworthy that only few reports are available on the catalytic properties of mesoporous gallosilicates **[14–16].** Gallium is known to exhibit Lewis acid properties useful for Friedel–Crafts reactions **[1]** and its incorporation induces the creation of Bronsted acidity **[17]**. Therefore, in this investigation, an attempt has been made to evaluate and compare of high quality GaSBA-15 prepared by direct synthesis and post treatment in Friedel Crafts reaction. Before, the materials were analysis by powder X-ray diffraction (XRD), N_2 adsorption–desorption, H/D isotope exchange, and transmission electron microscopy (TEM).

2. Experimental

2.1. Sol–gel Preparation and Post Synthesis of Gallium Containing SBA-15

The GaSBA-15 direct synthesis was carried out as follows: 4 g of triblock copolymer poly (ethylene oxide) poly(propyleneoxide)poly(ethyleneoxide) EO20PO70EO20, Pluronic 123M) was dispersed in 120 g of distilled water (6.67 mol) and 8.64 g of HCl (0.24 mol) under stirring. 8.54 g (0.041 mol) of tetraethyl orthosilicate (TEOS) was added to the solution at 40°C under stirring and an appropriate amount of gallium nitrate were added in order to obtain samples having Si/Ga ratio of 10 and 60.. Gelation and ageing were carried out at 40°C for 24 h, followed by heating at 100°C for 48 h in a sealed Teflon flask. The solid formed was filtered, washed several times with distilled water and dried at room temperature. The tri-block copolymer template was removed by submitting the sample to calcination in air at 500°C (heating rate of 2 °C min^{-1}) during 6 h. However, the Ga/SBA-15 material was post- treated with an adequate quantity of nitrate solution $Ga(NO_3)_3$ at room temperature for 12h. The solid was filtered and washed with distillate water and dried at 100°C in an oven before characterisation.

To simplify, the samples synthesised in situ were named as follows: GaSBA-15(10), GaSBA-15(60) and their synthesised by

post treatment were named: Ga/SBA-15(10), Ga/SBA-15(60), respectively, corresponding to Si/Ga ratios of 10 and 60.

2.2. Catalytic Test

The benzoylation test was carried out in a liquid-phase continuously stirred batch reactor at 140° C. The reactants mixture, anisole (0.069 mol) and benzoyle chloride (0.025 mol), was introduced in the reactor at the reaction temperature. The catalyst load was 200 mg. After each test the catalyst was filtered and washed several times with dichloromethane and dried at 100 8C in an oven before reuse.

The conversion was monitored by withdrawing small amounts of the reaction mixture at different time intervals and analysing using a gas chromatography (Varian GC-3400) equipped with a capillary PONA column (50 m length and 0.1 mm film thickness).

2.3. Characterization Techniques

Low-angle powder X-ray diffraction was carried out on a Siemens D500 diffractometer (Cu Kα radiation) working in a mode with a step of 0.01° from 0.5° to 2° in a two-theta angle.
The nitrogen adsorption–desorption isotherm was carried out on a Micromeritics ASAP using nitrogen as adsorbant at liquid nitrogen temperature. Before measurement, the sample was outgassed at 300 8C for overnight in order to desorb moisture from the surface. Transmission electron microscopy (TEM) observation was conducted on a Topcon UHR 002B microscope working with an accelerated voltage of 200 kV with a point-to-point resolution of 0.17 nm.

3. Results and discussion

3.1. Characterization

Figure 1 shows the XRD powder patterns of the gallium containing SBA-15samples synthesized by post and direct treatment and with 10 and 60 Si/Ga ratio. The parent SBA-15 and the Ga-modified samples all show three well resolved peaks, which can be indexed to the (100), (110) and (200) reflexions of an ordered hexagonal P6mm space group. The (100) intensity remained almost unchanged for the materials prepared via two treatments –gel route with the gallium source, suggesting that the formation of gallium species has no influence on the ordered SBA-15 structure. The observed results were in good agreement with those already reported in the literature concerning the relatively high stability of the SBA-15 structure as compared to that of the MCM-41 material due to the presence of thicker walls in the SBA-15 material compared to that of the mesoporous silicas **[7, 16]**. The XRD patterns of the Ga containing SBA-15 reveal that the introduction of Ga , up to Si/Ga ratio of 60, did not modify the ordered structure of the mesoporous material. At high Ga loading (Si/Ga = 10) some structural modification was observed for Ga/SBA-15(10) and GaSBA-15(10). However, no diffraction lines corresponding to the Ga_2O_3 species were observed, which indicates that such species, if present, were in a very small size or as an amorphous phase.

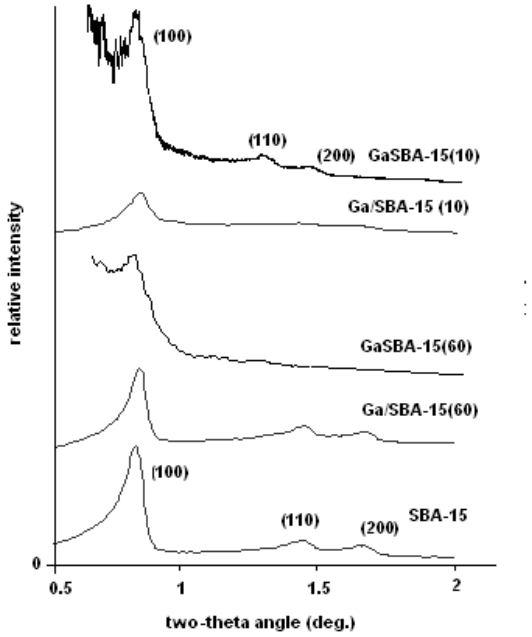

Figure 1. Low -angle XRD Powder Patterns of Parent SBA-15 and Ga Doped SBA-15 Materials with Different Si/Ga Ratios.

The unit cell parameter as increasing the gallium content for Ga doped SBA-15 by post treatment (Table 1) could be attributed to a partial collapse of hexagonal porosity caused by the modification induced by the gallium introduction in the mesoporous silica structure and indicates that the support structure was modified by the Ga species and partly confirms that this later was not simply deposited on the SBA-15 surface as Ga_2O_3 species. However, for samples prepared in situ, the unit cell parameter increases significantly with the increase of gallium content in the synthesis gel (Table 1), which could be accounted for the isomorphous substitution of tetravalent silicon by trivalent gallium owing to the larger crystal radius of Ga^{3+} (0.62A°) than Si^{4+}(0.40 A°) **[16, 18]**.

Table 1. Physical Characteristics of the SBA-15 and SBA-15 Doped with Various Amount of Gallium

Sample	Si/Ga (gel)	$d_{(100)}$ (nm)	a_o (nm)[a]	Porous volume ($cm^3 g^{-1}$)	Specific Surface Area ($m^2 g^{-1}$)
SBA-15	-	10,52	1214	1,22	1011
Ga/SBA-15(60)	60	10,49	1210	0,98	774
GaSBA-15(60)	60	11,18	1290	1,50	885
Ga/SBA-15(10)	10	10,32	1192	0,76	686
GaSBA-15(10)	10	11,24	1298	1,54	708

a: Unit cell parameter a = $2d100/\sqrt{3}$

Nitrogen adsorption-desorption isotherms of the SBA-15 and Ga containing SBA-15 (Si/Ga = 10 and 60) samples are displayed in Figure 2. The isotherms of samples exhibit a type IV isotherm with H1-type hysteresis, which is typical of mesoporous materials with one-dimensional cylindrical channels. The sharp inflection between the relative pressures $p/p_0 = 0.6$ and 0.9 observed in the isotherm corresponds to capillary condensation within uniform mesopores. The capillary condensation was shifted to higher relative pressures while increasing the gallium content of the sample. This can be attributed to an increase of the pore diameter when rising the Ga content of the sample (Table 1). However, the hysteresis inflection at high gallium loading (Si/Ga= 10) for

samples prepared by post treatment was less sharp indicating that the pore size of the material was less ordered and uniform compared to that of the samples prepared by direct synthesis. At low gallium loading (Si/Ga= 60) the hysteresis inflection was more sharp indicating that the pore size of the material was more ordered and uniform.

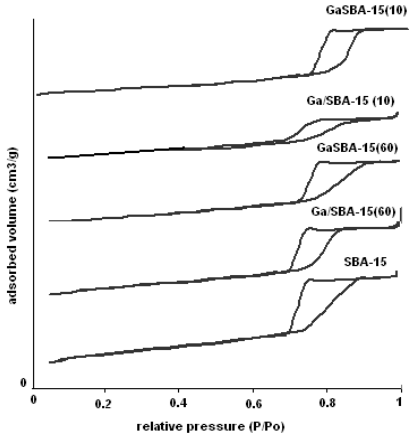

Figure 2. Nitrogen Adsorption–Desorption Isotherms of the SBA-15 Pure and Doped with Various Concentrations of Gallium.

These porosity measurements together with XRD results (Table 1) tend to confirm the partial insertion of Ga^{3+} in the siliceous framework (higher pore volume) while post-treated SBA-15 with a Ga-source led only to the bonding of Ga_2O_3 species to external silanol groups **[15]**.

The specific surface area was 1011 m^2/g for the pristine SBA-15 and deceased as increasing the gallium concentrations (Table 1). The decrease in the specific surface area of the SBA-15 when gallium was introduced could be partly related to the presence of gallium species with lower specific surface area and thus lowering the overall surface of the material. The anchoring of gallium on the SBA-15 surface also induced a decrease in the pore volume of the material (from 1,22 to 0,76) indicating a partial blocking of the mesochannels during gallium introduction for samples prepared by post treatment. On the other hand, The anchoring of gallium on the SBA-15 surface only induced a slight increase in the pore volume of the material (from 1,22 to 1,54) indicating that the during the gallium introduction by direct synthesis some pore blocking has occurred. Similar results have been reported on the Al-SBA-15 and Ga-SBA-15 **[16, 19].**

The arrangement of the SBA-15 mesopores after the addition of gallium source in the gel can be observed on TEM images (Figure 3). All SBA-15 samples including those with different Ga loading and treated by two proceeding show well-ordered hexagonal arrays of mesopores and unambiguously confirm that the hexagonal pore structure of the SBA-15 was retained. Even the sample having the highest Ga content (Si/Ga = 10) presents well-ordered 1D arrays of mesochannels (Figure 3 C and D).

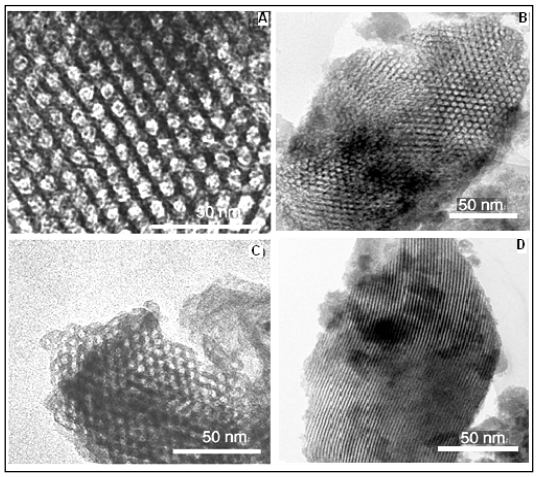

Figure 3. TEM Images of the SBA-15 Doped with Various Amounts of Gallium: (A and B) Ga/SBA-15: Si/Ga = 60, (C and D) GaSBA-15: Si/Ga = 10. The Slight Structure Disordered was Observed on the Sample with High Gallium Loading as Shown in (D) where Some Hexagonal Structure was Destroyed (arrow).

3.2. Catalytic Activity and Stability

3.2.1. Acylation of Benzoyl Chloride

Table 2 presents the conversion of benzoyle chloride over Ga doped SBA-15 with different Si/Ga ratios. The mole ratio anisole/benzoyle chloride was set to 2.8. The acylation activity was relatively high during the first cycling test with a complete conversion reached after 24 h on stream (Table 2). The catalysts exhibited almost no activity change during the successive catalytic cycles indicating that the deactivation process is relatively slow within the mesopores.

The selectivities toward the para- and ortho-methoxybenzophenone (para- and ortho ketone) isomers were about 93% and 5% respectively for Ga/SBA-15 (10) and GaSBA-15 (10). By comparison, the benzoyl chloride conversion was only about 80% over GaSBA-15 catalysts containing a lower Ga amount; i.e., Si/Ga = 60. . Since the activity of the latters is similar, it indicates that the sample which contains the highest Ga amount (Si/Ga = 10) exhibits a peculiar behaviour possibly due to a different location of Ga-atoms in the SBA-15 matrix. In addition, Ga/SBA-15(60) prepared by post-treatment exhibited a higher benzoyl chloride conversion than prepared via the sol–gel procedure at the same selectivity toward ortho and para isomers **[15].**

However, GaSBA-15 (10) exhibits a faster transformation of benzoyl chloride than its post-treated analog having the same Si/Ga ratio. This further support the presence of a different kind of acid sites in GaSBA-15 (10) catalyst. Furthermore, a comparison between Ga/SBA-15 (60) post-treated sample, with comparable Ga content and similar acidic properties, showed a different catalytic performance. In this sense, it is therefore possible that the sol–gel procedure allows the formation of different kinds of acid Ga-species, and depending the loading inside the mesopores, both their nature and location could be different. Bonardet et al. have studied the synthesis of Ga-SBA-15 materials via different procedures (sol–gel, post-treatment, change in the Ga-source) and have observed a drastic influence both on the physical properties and catalytic activity **[18]**.

3.2.2. Stability of the catalysts

While recycling the catalysts, after washing with dichloromethane, a drastic decrease in the benzoyl chloride or the BC (for the alkylation process) conversion was noticed (Table 2). Moreover, the activity loss was enhanced while increasing the Ga-content in the SBA-15 matrix. Choudary et al. have noticed the same trend for the aromatisation of propane over Ga-modified MFI catalysts **[20]**. The deactivation appears to be higher for these samples compared to post-treated Ga-SBA-15, where the stability was quite high during successive runs. The deactivation seems to be essentially due to irreversible adsorption of higher aromatics, leading to coke formation, which poisons the active sites. The higher amount of carbon deposited also supports the presence of strong acid sites on these ''in situ'' prepared Ga-SBA-15 materials, and the higher the Ga-loading, the higher the carbon deposition.

Table 2. SBA-15 Doped Gallim with Si/Ga = 10 and 60 Stability in the Benzoylation of Anisole Reaction

Catalyst	Number of catalytic run	Conversion (%)*	Selectivity (%)		
			para-ketone	*ortho*-ketone	Ester [a]
Ga/SBA-15 (60)	**1**	97	92	6	2
	2	92	100	0	0
	3	70	100	0	0
GaSBA-15 (60)	**1**	80	95	4,9	0,1
	2	74	31	66	3
	3	61	6	89	3
Ga/SBA-15 (10)	**1**	100	94	6	0,2
	2	99	93	7	0
	3	98	100	0	0
GaSBA-15 (10)	**1**	96	93	5	2
	2	90	55	44,8	0,2
	3	62	62	37	1

* : conversion after 24h of the reaction a: phenylbenzoate

5. Conclusion

High-quality mesoporous SBA-15 doped gallium materials with different Si-to-Ga ratios were successfully synthesized using a post-treatment and direct sol–gel procedure of the mesoporous material by an aqueous solution of gallium nitrate. The high stability of the SBA-15 material allows to maintain the mesoporous structure and pore size distribution after introduction of gallium. The characterization of the catalysts confirm that at high Ga loadings, a novel mesoporous Brönsted solid acid catalyst was prepared via Ga^{3+} introduction in the framework for catalysts obtained by direct sol–gel procedure and the anchoring of dispersed Ga-species (monomeric or polymeric) on the SBA-15 surface even at high Ga loading for catalysts prepared by post-treatment.Ga doped SBA-15 mesoporous silica materials appear to be suitable for an use as catalyst in liquid-phase acylation reaction. These catalysts exhibit a complete conversion of benzoyl chloride at a 90% selectivity toward para-methoxybenzophenone. A conversion above 90% of the acylating agent was reached for the solid acid at high Ga loading (Si/Ga =10). in combination with the post-treatment method and the sol–gel procedure allows to prepare mesoporous SBA-15 doped gallim catalysts and also to tailor their acidity via the introduction of Ga^{3+} ions in the framework or by grafting highly dispersed Ga-species on the outer surface. These catalysts exhibit a relatively an extremely high stability as a function of the reuse due to the presence of mesoporous network which favours the diffusion of reactants and products.

REFERENCES

[1] G.A. Olah, "Friedel Crafts and Related Reactions", Interscience Publishers, New York, 1964

[2] G.A. Olah, G.K.S. Prakash, J. Sommer, "Superacids", Wiley & Sons, New York, 1985.

[3] C.T. Kresge, M.E. Leonowicz, W.J. Roth, J.C. Vartuli, J.C. Beck, "Ordered Mesoporous Molecular Sieves Synthesized by a Liquid-Crystal Template Mechanism", Letters to Nature, Nature, Vol.359, pp.710- 712, 1992.

[4] A. Corma, "Preparation and Catalytic Properties of New Mesoporous Materials", Springer, Topics in Catalysis, Vol.4, pp.249-260, 1997.

[5] J.C. Beck, J.C. Vartuli, W.J. Roth, M.E. Leonowicz, C.T. Kresge, K.D.Schmitt, C.T.W. Chu, D.H. Olson, E.W. Sheppard, S.B. McCullen, J.B. Huggins, J.L. Schlenker, "A New Family of Mesoporous Molecular Sieves Prepared with Liquid Cristal Template", A.C.S. Publication, Journal of American Chemical Society, Vol. 114, no.27, pp. 10834- 10843, 1992.

[6] A. Taguchi, F. Schüth, "Ordered Mesoporous Materials in Catalysis", Elsevier, Microporous. Mesoporous. Materials, Vol.77, pp. 1-45, 2005.

[7] D.Y. Zhao, J.L. Feng, Q.S. Huo, N. Melosh, G.H. Fredrickson, B.F. Chmelka, G.D. Stucky, "Triblock Copolymer Synthesis of Mesoporous Silica with Periodic 50 to 300 Angstrom Pores", Science AAAS, Science, Vol. 279, no. 5350, pp.548-552, 1998.

[8] V. Dufaud, M.E. Davis, "Design of Heterogeneous Catalysts in Multiple Active Site Positoning in Organic-Inorganic hybrid Materials", ACS Publication, Journal American Chemical Society, Vol.125, pp.9403-9413, 2003.

[9] B.M. Lin, X.X. Wang, Q. Guo, W. Yang, Q.H. Zhang, Y. Wang, "Excellent Catalytic Performances of SBA-15 Supported Vanadium Oxide per Partial Oxidation of Methane to Formaldehyde", Publisher..J.Stage, Chemical Letters, Vol.32, no.9, pp.860-861, 2003.

[10] Y. Cao, J.C. Hu, P. Yang,W.L. Dai, K.N. Fan, "CuCl Catalyst Heterogenized on Diamide Immobilized SBA-15 for Efficient Oxidation Carbonylation of Methanol to

Dimethylcarbonate", Royal Society of Chemistry Publishing, Chemical Communications, no.7, pp. 908-909, 2003.

[11] A. Gedeon, A. Lassoued, J.L. Bonardet, J. Fraissard, "Surface Acidity Diagnostic and Catalytic Activity of AlSBA Materials Obtained by Direct Synthesis, Elsevier, Microporous Mesoporous Materials, Vol.44-45, pp. 801-806, 2001.

[12] W.H. Zhang, J. Lu, B. Han, M. Li, J. Xiu, P. Ying, Li, "Direct Synthesis and Characterization of Titanium-Substituted Mesoporous Molecular Sieve SBA-15", American Chemical Society Publications, Chemistry of Materials, Vol.14, pp. 3413-3421, 2002.

[13] Y.Y. Sun, S.Walspurger, J.P. Tessonnier, B. Louis, J. Sommer, "Highly Dispersed Iron Oxide Nanoclusters Supported on Ordered Mesoporous SBA-15: A Very Active Catalyst for Friedel–Crafts Alkylation", Elsevier, Applied Catalysis .A, Vol.300, pp. 1-7, 2006.

[14] K. Okumura, K. Nishigaki, M. Niwa," Prominent Catalytic Activity of Ga-Containing MCM-41 in the Friedel-Crafts Acylation", Elsevier, Microporous Mesoporous Materials, Vol.44, pp.509-516, 2001 .

[15] Z. El Berrichi, L. Cherif, O. Orsen, J. Fraissard, J.P. Tessonnier,E. Vanhaecke, B. Louis, M.J. Ledoux, C. Pham-Huu, "Ga doped SBA-15 as an Active and Stable Catalyst for Friedel–Crafts Liquid-Phase Acylation", Elsevier, Applied Catalysis. A General, Vol.298, pp.194-202, 2006.

[16] P. Selvam, S.E. Dapurkar, "Tertiary Butylation of Phenol over Mesporous MeMCM-48 and MeMCM-41 (Me= Ga, Fe, Al or B) Solid Acid", Elsevier, Catalysis Today, Vol. 96, pp. 135-141, 2004.

[17] M. Hafele, A. Reitzmann, D. Roppelt, G. Emig,"Hydroxylation of Benzene with Nitrous Oxide on H-Ga-ZSM5" Applied Catalysis A.General, Vol.150, pp. 153-164, 1997.

[18] B. Jarry, F. Launay, J.P. Nogier, V. Montouillout, L. Gengembre, J.L.Bonardet, "Characterisation, Acidity and Catalytic Activity of Ga–SBA-15 Materials Prepared Following Different Synthesis Procedures", Elsevier, Applied Catalysis A.General, Vol. 309,pp. 177-186, 2006.

[19] F.Launay, B.Jarry, J.L.Bonardet, "Catalytic Activity of Mesoporous Ga-SBA15 Materials in α-Pinene Isomerisation Similarities and Differences with Al-SBA15 Analogues", Elsevier, Applied Catalysis.A. General, Vol.368, pp.132-138, 2009.

[20] K. Mantri, A.K. Klginage, C. Sivadinarayana, Choudary.F V.R., in:V. Murugesan, B. Arabindoo, M. Palanichamy (Eds.)," Recent Trends in Catalysis", Narosa Publishing House, New Delhi, 1999, p. 389.

Dy Doped Nanocrystalline $SrAl_2O_4$: Eu Phosphor: Synthesis, Characterization and Calculation of Kinetic Parameters

D. S. Kshatri[1] and A. Khare[2*]
[1]Department of Physics, Shri Shankaracharya Institute of Professional Management and Technology, Raipur - 492 015 India
[2]Department of Physics, National Institute of Technology, G E Road, Raipur – 492 010 India
E-mail: akhare.phy@nitrr.ac.in

Abstract

Nanosized Dy doped $SrAl_2O_4$: Eu samples are prepared by combustion synthesis technique (CST). The $SrAl_2O_4$ co-doped with Eu^{2+} and Dy^{3+} ions and recrystallized with B_2O_3 flux is regarded as a useful green-emitting long persistence phosphor. The $SrAl_2O_4$ can be used safely as phosphorescent pigment for luminous watches, clocks and cold-lighting that emits no infrared radiation. We report the results of the characterization and optical studies made on $SrAl_2O_4$. The XRD, SEM and HRTEM have been employed to characterize the as prepared samples while optical properties are analyzed through thermolumineacence (TL) and afterglow decay curves. The kinetic parameters, which play vital role in characterizing a particular phosphor material, have been calculated and presented for reported samples.

1. Introduction

On the basis of microscopic point of view, thermoluminescence (TL) consists of a perturbation of the electronic system of insulating or semiconducting materials, from a state of thermodynamic equilibrium, via the absorption of external energy, i.e. produced by an ionizing radiation into a metastable state. This is then accompanied by the thermally stimulated relaxation of the system back to its equilibrium condition. Macroscopically, TL is a temperature-stimulated light emission from a crystal, after removal of excitation (i.e. ionizing radiation); thermoluminescence is a case of phosphorescence observed under condition of steadily increasing temperature. A plot of the light intensity as a function of temperature is called glow-curve. A glow-curve may have one or more maxima, called glow-peaks, each corresponding to an energy level trap (Mckeever and Chen 1997; Furetta and Weng 1998).

Noteworthy advancements have been made in TL based experiments during last couple of decades. However, the most important application of TL lies in radiation dosimetry (Marwaha *et al.* 1980; 1997) which spans areas of health physics and other biological sciences, radiation protection and personnel monitoring. TL experiments are equally helpful in defects and impurities related studies in solids. In these experiments, a phosphor is excited with some radiations for a desired period of time after which the exciting light is removed. Then material is heated at a constant rate and the light output is measured as a function of temperature of the phosphor and a TL glow curve is plotted. The position of the peaks on the temperature scale is a measure of the energy depth of the trapped electrons in the solid, while area under the peak specifies the number of electrons transferred into these traps by exciting radiations (Chandrashekhar 2012). The exciting source may be gamma rays, UV rays, alpha particles, electrons, ion beams, neutrons etc. The information of traps with their distribution in the band gap of solids is indispensable to understand the luminescence process which can be obtained by TL studies. Further, the dosimetric characteristics of TL materials chiefly depend on the kinetic parameters quantitatively describing the trapping–emitting centers responsible for the TL emission (Jiang 2009). The host-dopant combination plays a significant role in controlling PL and TL properties of the luminescent materials (Sharma *et al.* 2009; Yavetskiy *et al.* 2007). The determination of the kinetic parameters is, therefore a vigorous area of research and various techniques have been developed over the time to derive the kinetic parameters from the TL glow curve. There are plentiful methods given in the literature to analyze the TL glow curve and to find out the kinetic parameters namely activation energy (E), order of kinetics (b) and frequency factor (s). Some of them are the initial rise methods, peak shape methods, methods of various heating rates, curve fitting methods, etc. (Chen and Mckeever 1997) with their own advantages and disadvantages. With the advent of nanotechnology, there is still an extensive amount of research for new nanocrystalline phosphor materials with better TL and dosimetric properties. The importance of nanocrystalline materials has increased tremendously because of the enhanced optical, electronic and structural properties than their bulk counterparts due to quantum size effect and an increased surface to volume ratio.

The Strontium aluminate ($SrAl_2O_4$) belongs to the tridymite-like structure. The distinctive structure is formed with a three-dimensional frame-work of corner sharing AlO_4 tetrahedral. Each oxygen ion is shared by two aluminum ions so that each tetrahedron has one net negative charge. The charge balance

is achieved by the large divalent Sr^{2+} cation, which occupies interstitial site within the tetrahedral framework. The $SrAl_2O_4$ co-doped with Eu^{2+} and Dy^{3+} ions and recrystallized with B_2O_3 flux is regarded as a useful green-emitting long persistence phosphor (Nag and Kutty 2004; Ryu et *al.* 2008). $SrAl_2O_4$ can be used safely as phosphorescent pigment for luminous watches, clocks and cold-lighting that emits no infrared radiation. Recent papers on Dy co-doped $SrAl_2O_4$: Eu^{2+} show the effect of sensitizer ion on enhancement in luminescence intensity (Kamiyanagi *et al.* 2007; Clabau et al. 2007; Lu *et al.* 2007). However, with increasing concentration of the rare-earth Dy^{3+} ions as sensitizer have been of interest to study the effect on luminescence of this phosphor host. In the present work we have prepared and investigated $SrAl_2O_4$ nanocrystalline (NC) phosphor materials co-doped with Eu^{2+} and increasing concentration of Dy^{3+} ions as activator and sensitizer, respectively. The Dy^{3+} co-doping concentration is optimized and its effect on structure and TL characteristics is investigated. Crystalline phase and defect structure are investigated by powder XRD, SEM, HRTEM and TL characteristics are described by measuring TL emission intensity with temperature. We have presented here the detailed TL studies of UV (λ=365 nm) irradiated nanocrystalline $SrAl_2O_4$: Eu^{2+} phosphor with increasing concentration of Dy^{3+} ions. Further, we have used Chen's peak shape method to analyze the TL glow curves and hence calculated the trapping parameters for NC structures of this phosphor at a heating rate of $3^oC/s$.

2. Experimental

For preparing nanocrystalline $SrAl_2O_4$: Eu, Dy powder samples, stoichiometric amounts of strontium nitrate [$Sr(NO_3)_2$; Merck, 99.9 + %], aluminum nitrate [$Al(NO_3)_3.9H_2O$; Merck, 99.9 + %] and urea [$CO(NH_2)_2$; AR] are used as unprocessed materials. In addition to it, europium oxide [Eu_2O_3; Merck, 99.9 + %] and dysprosium oxide [Dy_2O_3; Merck, 99.9 + %] taken as co-activators are dissolved in concentrated nitric acid [HNO_3; AR] before transferring them to crucible. The appropriate amount of boric acid [H_3BO_3; AR] is used as the flux while the urea is used as fuel. Phosphor samples are prepared according to the mole ratio Eu^{2+}:Dy^{3+}:Sr^{2+}:Al^{3+} = 0.01:0.00:0.99:1, 0.01:0.01:0.98:1, 0.01:0.02:0.97:1, 0.01:0.03:0.96:1, 0.01:0.04:0.95:1, 0.01:0.05:0.94:1.

An alumina crucible with comparatively larger volume is used as a container within which chemical reaction takes place. After the solution is transferred into the crucible, it is placed into a furnace already maintained a temperature of 600 ± 5^oC. The reaction blend undergoes thermal dehydration and ignites at one stage with liberation of gaseous products such as oxides of nitrogen and carbon. The combustion propagates throughout the reaction mixture. Within 5 min., the furnace reaches the desired temperature and reaction starts giving yellowish flame. The mixture froths and bloats forming foam, which ruptures with a flame and glows to incandescence. This continues for next few seconds and as it is over, crucible is taken out of the furnace and kept in open to allow cooling. Upon cooling, we get fluffy form of material (combustion ash), which is then crushed for 1 h using agate pestle mortar (diameter-5") to get material in the powder form. The final pigments synthesis by heating the precursor combustion ash at 1200^oC in a weak reductive atmosphere (95% Ar + 5%H_2) for 3h to reduce the Eu^{3+} ions to Eu^{2+} (Chen *et al.* 2008; Shafia *et al.* 2010).

3. Results and discussion

3.1 XRD analysis

The typical XRD patterns of different Srx-Al_2O_4: $Eu^{2+}_{0.01}$, Dy^{3+}_y (x = 0.99, y = 0; x = 0.98, y = 0.01; x = 0.97, y = 0.02; x = 0.96, y = 0.03; x = 0.95, y = 0.04 and x = 0.94, y = 0.05) phosphor samples are presented in fig. 1 (a-f). When compared with international system for diffraction data-2014 (00-009-0039) and lattice parameters (a = 8.44, b = 8.82, c = 5.16, β = 93.41), the results show that the XRD peaks in the diffractogram are mainly due to $SrAl_2O_4$ phase and dopant ions Eu^{2+} and Dy^{3+} have no influence on the crystal structure of the tested samples (Nag and Kutty 2003). The peaks corresponding to 2θ values of 23^o, 33^o, 34^o, 35^o and 41^o resemble (020), (-211), (220), (211) and (031) planes and belong to low temperature $SrAl_2O_4$ monoclinic α-phase (Xiao *et al.* 2010). However, there are also a few other peaks, which may be ascribed to unreacted precursor powders (Park *et al.* 2003).

The following equation provides the relationship between the interplanar spacing 'd' of different planes (hkl) and corresponding lattice constant for monoclinic structure (Brandon and Kaplan 2008):

$$\frac{1}{d^2} = \frac{1}{\sin^2\beta}\left(\frac{h^2}{a^2} + \frac{k^2\sin^2\beta}{b^2} + \frac{l^2}{c^2} - \frac{2hl\cos\beta}{ac}\right) \quad (1)$$

where 'h', 'k' and 'l' are the Miller Indices and 'a', 'b', and 'c' represent the lattice constants. 'β' is one of the angles between axes ($\beta > 90^o$).

The particle size 'D' is determined using well known Scherrer's formula (Song and Zhang 2011):

$$D = \frac{K\lambda}{\beta\cos\theta} \quad (2)$$

where 'K' is shape factor with a value close to unity, 'λ'- the wavelength of X-rays employed, 'β' – the broadening of the diffraction line measured at half of its maximum intensity (radians), it is also known as the full width at half maxima (FWHM) and 'θ' is the Bragg's angle.

The average particle sizes calculated for $Sr_xAl_2O_4$: $Eu^{2+}_{0.01}$, Dy^{3+}_y (x = 0.99, y = 0; x = 0.98, y = 0.01; x = 0.97, y = 0.02; x = 0.96, y = 0.03; x = 0.95, y = 0.04 and x = 0.94, y = 0.05) phosphor samples are presented in table 1, which are in good agreement with nanocrystalline nature of prepared phosphors. Assessment of XRD data, as noticed from full width at half maxima (FWHM) values, the widths of XRD peaks are sufficiently large, which signify the samples belonging to nanophase (Lin *et al*. 2006).

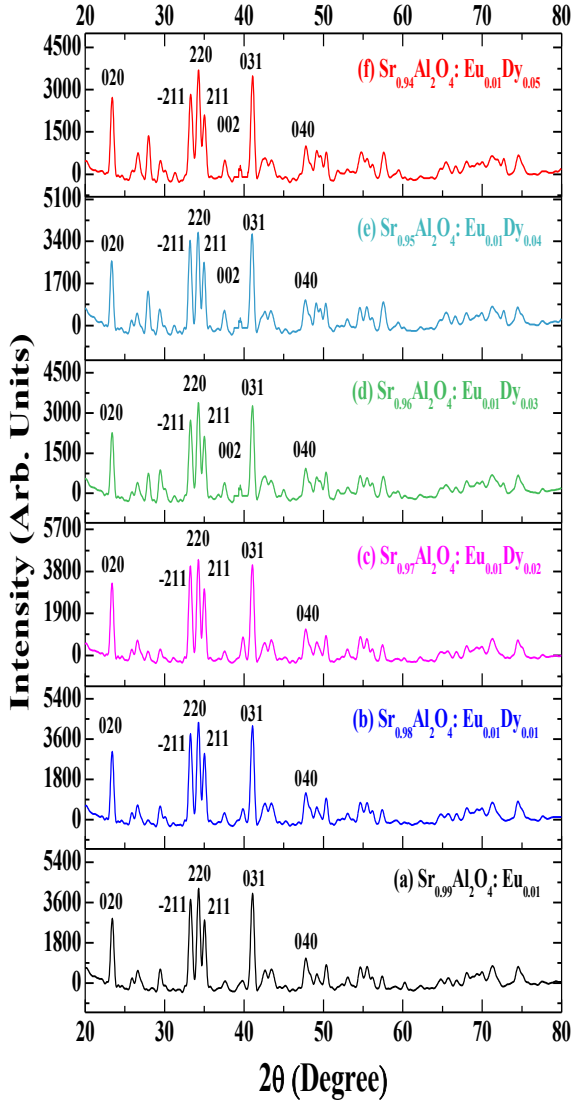

Fig. 1 (a-f) XRD patterns of nanocrystalline $SrAl_2O_4$: Eu^{2+}, Dy^{3+} phosphor samples

Table 1 The average crystallite size of different $SrAl_2O_4$: Eu^{2+}, Dy^{3+} phosphors

Samples	Average Crystallite Size (nm)
$Sr_{0.99}Al_2O_4$: $Eu_{0.01}$	86.0328
$Sr_{0.98}Al_2O_4$: $Eu_{0.01}$, $Dy_{0.01}$	100.6871
$Sr_{0.97}Al_2O_4$: $Eu_{0.01}$, $Dy_{0.02}$	95.2057
$Sr_{0.96}Al_2O_4$: $Eu_{0.01}$, $Dy_{0.03}$	95.7787
$Sr_{0.95}Al_2O_4$: $Eu_{0.01}$, $Dy_{0.04}$	97.5996
$Sr_{0.94}Al_2O_4$: $Eu_{0.01}$, $Dy_{0.05}$	71.0787

3.2 SEM analysis

SEM studies were carried out to investigate the surface morphology and the particle size of the synthesized phosphors. Fig. 2 presents the SEM images of NC $Sr_{0.97}Al_2O_4$: $Eu^{2+}_{0.01}$, $Dy^{3+}_{0.02}$ phosphor samples, which exhibits highest intensity with respect to samples prepared in other compositions. This observation is further discussed in terms of TL analysis. The SEM micrograph shows the irregular morphology with angularity and corners with varying grain sizes. As is well documented (Ayvacıkli *et al.* 2011), the phosphor powders are irregular particles with different shapes and sizes. In the present case also, the surfaces of the foams show a lot of cracks, voids and pores formed by the gases escaping during combustion reaction. In fact, the large amount of escaping gases dissipates heat and thereby averts the material from sintering and thus provides conditions for formation of nanocrystalline phase.

3.3 EDX analysis

The EDX study was further carried out to verify the elemental composition of the as-prepared final products. An EDX spectrum displays peak corresponding to the energy levels for which the largest part of X-rays were received. Each of these peaks is distinctive to an atom, and therefore corresponds to a single element. The taller a peak in a spectrum, the more concentrated the element is in the spectrum. Fig. 3 shows the EDX spectrum of most intense NC $Sr_{0.97}Al_2O_4$: $Eu^{2+}_{0.01}$; $Dy^{3+}_{0.02}$ phosphor sample. The results of EDX studies confirm that the products contain strontium (Sr), aluminium (Al), oxygen (O), europium (Eu) and dysprosium (Dy). It is observed that for each of the respective phosphor concentration, the distribution of the elements is fairly uniform. On the basis of calculations made for NC $Sr_{0.97}Al_2O_4$: $Eu^{2+}_{0.01}$, $Dy^{3+}_{0.02}$ phosphor sample, the ratios of atomic percent are shown in table 2, indicating that Eu^{2+} with Dy^{3+} ions are completely doped into $SrAl_2O_4$ host matrix (Xu *et al.* 2010).

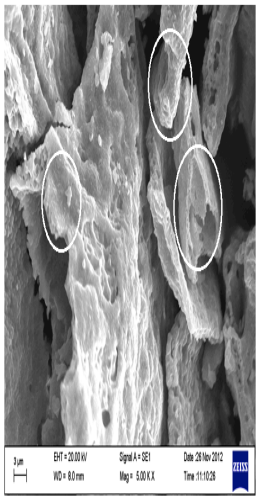

Fig. 2 SEM micrograph of $Sr_{0.97}Al_2O_4$: $Eu^{2+}_{0.01}$, $Dy^{3+}_{0.02}$

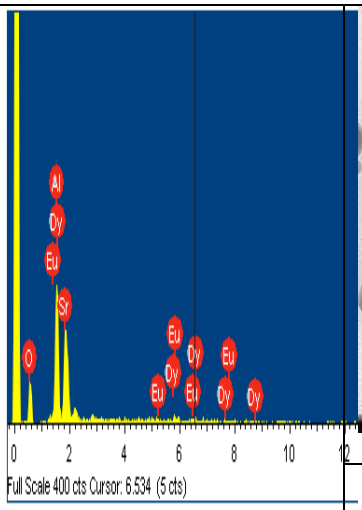

Fig. 3 EDX pattern of $Sr_{0.97}Al_2O_4$: $Eu^{2+}_{0.01}$, $Dy^{3+}_{0.02}$

Table 2 Atomic percents of elements in $Sr_{0.97}Al_2O_4$: $Eu^{2+}_{0.01}$, $Dy^{3+}_{0.02}$ phosphors

Elements	Atomic Percentage
Sr	12.12
Al	23.92
O	61.30
Eu	0.67
Dy	2.01

3.4 HRTEM Results

The HRTEM micrographs of nanocrystalline $SrxAl_2O_4$: $Eu^{2+}_{0.01}$, Dy^{3+}_{y} (x = 0.99, y = 0; x = 0.98, y = 0.01; x = 0.97, y = 0.02; x = 0.96, y = 0.03; x = 0.95, y = 0.04 and x = 0.94, y = 0.05) phosphor samples are presented in fig. 4 (a-f). The selected area electron diffraction (SAED) pattern corresponding to most intense sample is shown in inset. The crystallites are distributed randomly where size of smallest particle is found to be around 5.18 nm. Since, during the combustion reaction large amount of escaping gases dissipates heat and prevents the material from sintering, hence this facilitates the formation of nanocrystalline phase as observed in fig. 4. These results are quite encouraging, which support results of XRD studies and confirm the formation of nano-sized crystallites prepared by CST.

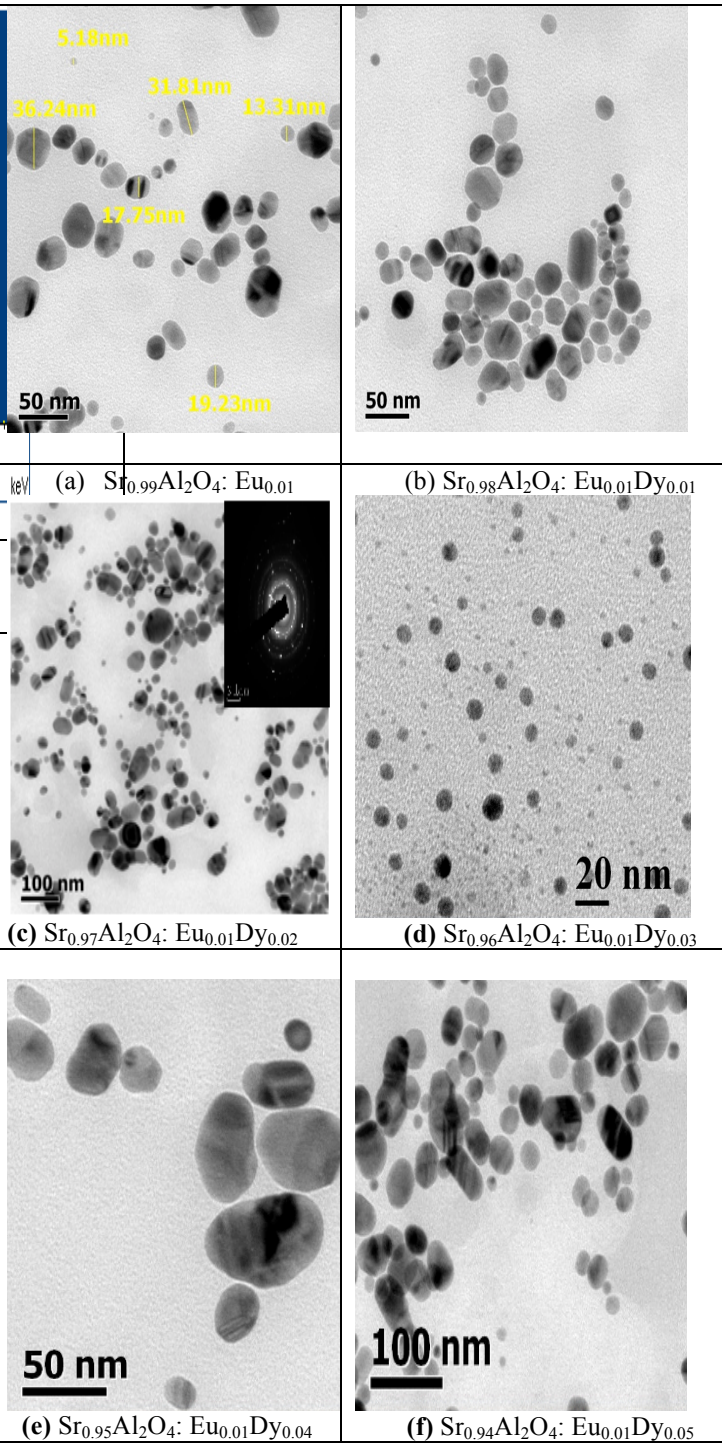

(a) $Sr_{0.99}Al_2O_4$: $Eu_{0.01}$ (b) $Sr_{0.98}Al_2O_4$: $Eu_{0.01}Dy_{0.01}$

(c) $Sr_{0.97}Al_2O_4$: $Eu_{0.01}Dy_{0.02}$ (d) $Sr_{0.96}Al_2O_4$: $Eu_{0.01}Dy_{0.03}$

(e) $Sr_{0.95}Al_2O_4$: $Eu_{0.01}Dy_{0.04}$ (f) $Sr_{0.94}Al_2O_4$: $Eu_{0.01}Dy_{0.05}$

Fig. 4 The HRTEM images of NC $SrAl_2O_4$: Eu, Dy phosphor samples

4. Analysis of TL glow curves and calculation of kinetic parameters

TL is the thermally stimulated emission of light following the absorption of energy from radiations. The radiations cause displacement of electrons within the crystal lattice of the substance. Upon heating, the trapped electrons return to their normal lower-energy states, releasing energy in the process. TL is an effective tool for diverse applications such as dosimetry, age determination, geology or solid state

defect structure analysis, etc. (Kshatri and Khare 2014).

Fig. 5 (a-f) shows TL glow curves for different nanocrystalline $Sr_xAl_2O_4$: $Eu^{2+}_{0.01}$, Dy^{3+}_y (x = 0.99, y = 0; x = 0.98, y = 0.01; x = 0.97, y = 0.02; x = 0.96, y = 0.03; x = 0.95, y = 0.04 and x = 0.94, y = 0.05) phosphor samples. The general nature of TL curves is observed to be similar in different cases except for $Sr_{0.97}Al_2O_4$: $Eu^{2+}_{0.01,}$ $Dy^{3+}_{0.02}$ phosphor. Each curve peaks in a temperature range 94-97°C and phosphor $Sr_{0.97}Al_2O_4$: $Eu^{2+}_{0.01,}$ $Dy^{3+}_{0.02}$ shows maximum TL intensity at 112°C indicating the trap-depth value to be maximum for this composition. It is also observed that varying concentration of Dy^{3+} does not affect the peak position much.

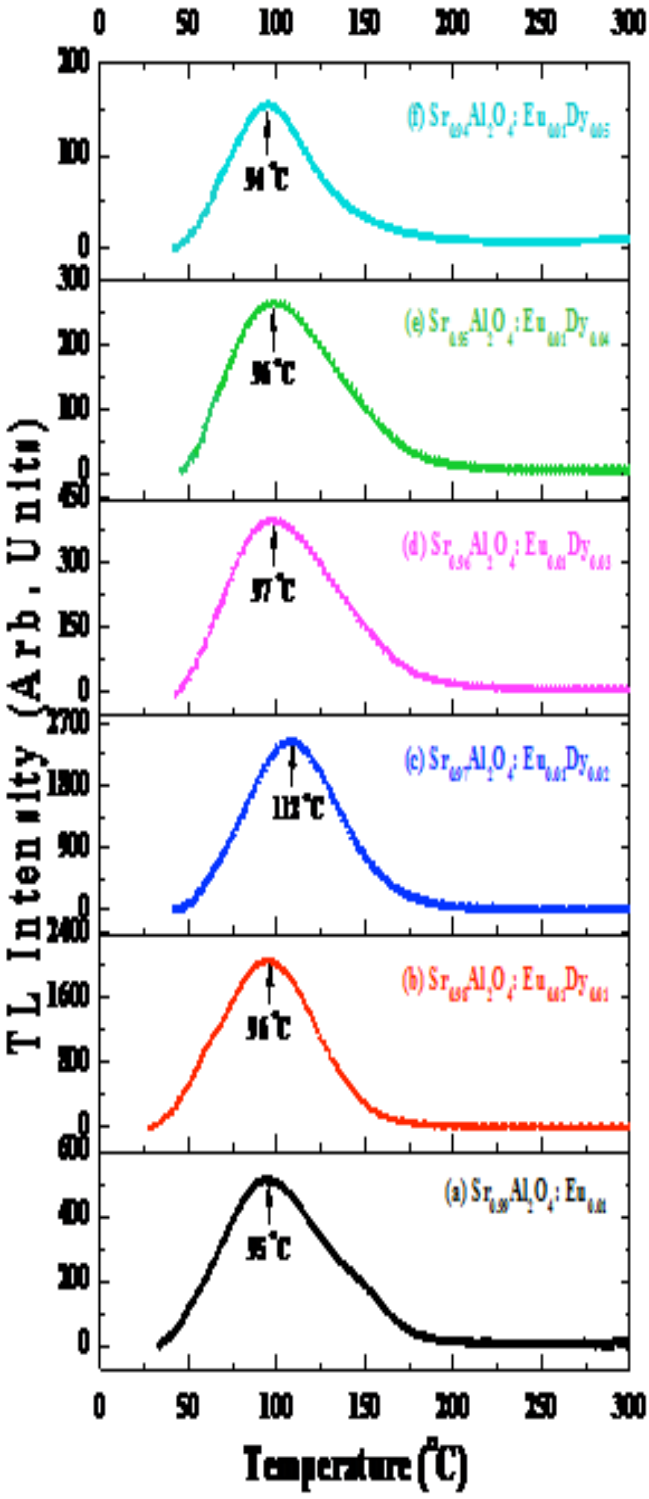

Figure 5 TL glow curves of different nanocrystalline $SrAl_2O_4$: Eu^{2+}, Dy^{3+} phosphor samples

However, the emission intensity is found to increase with increasing Dy concentration and for a particular molar concentration (y = 0.02), the intensity gets quenched (Mishra *et al.* 2012) and decreases for further concentrations (y = 0.03, 0.04 and 0.05). The probable reason for such quenching may be the increase in probability of non-radiative transitions of the luminescent molecules from the excited state to the ground state in comparison to the probability of radiative transitions. Fig. 6 shows the relative TL intensity with increasing Dy^{3+} concentrations for different $SrAl_2O_4$: Eu^{2+}, Dy^{3+} phosphor samples which depict the concentration quenching phenomenon of thermoluninescence.

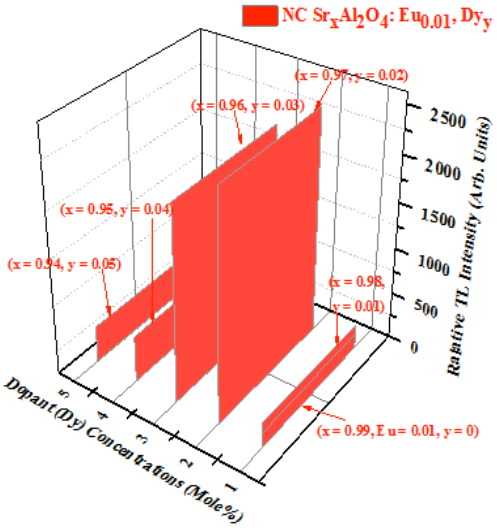

Fig. 6 Variation of integrated TL intensity with dopant concentrations

The determination of kinetic parameters has a vigorous area of research and various techniques have been developed to derive these parameters from the glow curves. In the present investigation, kinetic parameters of nanocrystalline $Sr_xAl_2O_4$: $Eu^{2+}{}_{0.01}$, $Dy^{3+}{}_y$ (x = 0.99, y = 0; x = 0.98, y = 0.01; x = 0.97, y = 0.02; x = 0.96, y = 0.03; x = 0.95, y = 0.04 and x = 0.94, y = 0.05) phosphor samples are calculated using Chen's peak shape method [29] also known as half width method. Fig. 7 (a-f) depicts the graph for calculation of kinetic parameters for different $SrAl_2O_4$: Eu^{2+}, Dy^{3+} phosphor samples. We, however, we apply peak shape method to the whole experimental glow curves and evaluate the kinetic parameters i.e. 'ω' (full width at half maxima of glow curve), 'δ' (the high temperature half width), 'τ' (the low temperature half width) and 'μ' (shape factor) which are related as (Chen and Kirish 1981):

$$\left.\begin{aligned} \omega &= T_2 - T_1 \\ \delta &= T_2 - T_m \\ \tau &= T_m - T_1 \\ \mu &= \frac{\delta}{\omega} \end{aligned}\right\} \qquad (3)$$

where 'T_m' is the peak temperature corresponding to the maximum TL intensity and 'T_1' and 'T_2' are temperatures corresponding to half of the TL intensity of the glow curves at the ascending and descending sides of the peaks respectively. The order of kinetics (b) is based on the value of shape factor (μ), that ranges between 0.42 and 0.52, the value close to 0.42 is for the first order and close to 0.52 is for the second order kinetics (Chen and Kirish 1981).

After determining the kinetic parameters, the activation energy (E) that resembles trap-depth value for different NC phosphors is calculated by Chen's method (Chen and Kirish 1981) using following equation,

$$E_\eta = C_\eta \frac{kT_m^2}{\eta} - b_\eta (2kT_m) \qquad (4)$$

where 'η' stands for 'τ', 'ω', 'δ' and the values of 'C_η' and 'b_η' are determined for the three methods are,

$$\left.\begin{aligned} C_\tau &= 1.51 + 3(\mu_g - 0.42) \\ C_\delta &= 0.976 + 7.3(\mu_g - 0.42) \\ C_\omega &= 2.52 + 10.2(\mu_g - 0.42) \\ b_\tau &= 1.58 + 4.2(\mu_g - 0.42) \\ b_\delta &= 0 \\ b_\omega &= 0 \end{aligned}\right\}$$

and the frequency factor (s) (Furetta 2003) is calculated using following equation,

$$\frac{\beta E}{kT_m^2} = s \exp\left(-\frac{E}{kT_m}\right)\left[1 + (b-1)\Delta_m\right] \qquad (5)$$

where 'β' is the linear heating rate (β = 3°C/s in the present investigation), 'b' is order of kinetics and 'k' is Boltzmann's constant (8.6×10^{-5} eVK^{-1}).

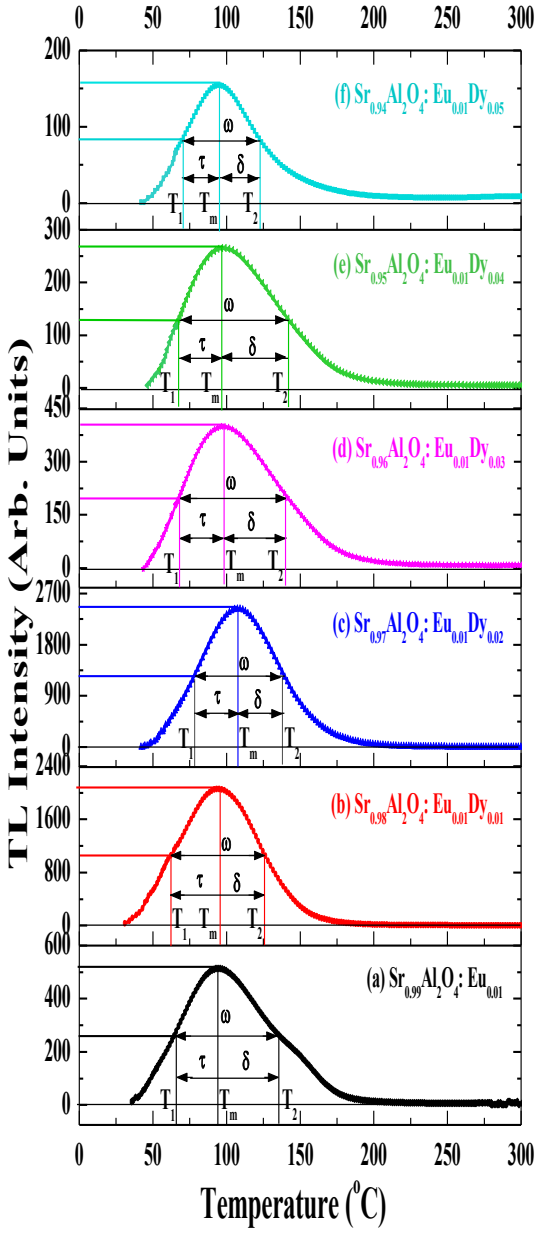

Fig. 7 The graph for calculation of kinetic parameters of nanocrystalline $SrAl_2O_4$: Eu^{2+}, Dy^{3+} phosphor samples

The values of kinetic parameters ('T_m', 'μ', 'b', 'E' and 's') calculated from TL glow curves for different $SrAl_2O_4$: Eu^{2+}, Dy^{3+} phosphor samples are shown in table 3. The values of shape factor (μ) indicate the second order of kinetics (Furetta 2003) for all the TL glow curves of different NC phosphor samples. The corresponding values of activation energy range between 0.48 and 0.71 eV for NC phosphors (Tanori *et al.* 2008). The maximum value Lu X., Shu W., Yu Q., Fang Q., Xiong X., Roles of doping ions in persistent luminescence of $SrAl_2O_4$: Eu^{2+},RE^{3+}phosphors, Glass Phys. Chem. 2007, 33: 62.

of activation energy (0.71 eV) for most intense NC $Sr_{0.97}Al_2O_4$: $Eu^{2+}{}_{0.01,}$ $Dy^{3+}{}_{0.02}$ phosphor sample supports the requirement of more thermal energy to de-trap the electrons from the trap-depth resulting in higher TL emission intensity.

The values of the frequency factor are smaller than the expected magnitudes of the lattice vibration frequency (10^{12}–10^{14} s^{-1}) (Tanori *et al.* 2008). It is noticed that unusually low-frequency factors are characteristics of localized transitions in which radiative recombination can take place without a transition of the holes (or electrons) into the valence (or conduction) bands (McKeever *et al.* 1995). In the present case the charge carrier is thermally stimulated into a Eu^{2+} excited state from which a transition into the recombination center is permitted. Low-frequency factors are already being reported by many authors in a diversity of phosphors materials (McKeever 1985). Unswerving and complete information on the kinetic parameters of these phosphors is still lacking and more investigation is imperative.

Conclusions

Combustion synthesis technique proves to be a viable method to prepare nanocrystaiiline $SrAl_2O_4$: Eu^{2+}, Dy^{3+} powder samples. The results of XRD studies confirm the α-phase monoclinic structure of $SrAl_2O_4$ and help in assigning (020), (-211), (220), (211) and (031) planes to different peaks. Comparison of FWHM values support the formation of nanocrystallites. The SEM results reveal that particles are distributed smoothly, covered large surface area. The EDX results confirm the doping of Eu^{2+} and Dy^{3+} in the $SrAl_2O_4$ host matrix. The TL emission intensity increases with greater concentration of Dy resulting in quenching at still higher concentrations. Different TL peaks fall in the temperature range 94-112°C indicating existence of only one trap center. The TL glow curves exhibit the second order of kinetics for different NC phosphor samples. The activation energy calculated for different NC samples ranges between 0.48 and 0.71 eV. The activation energy is found to be maximum (0.71 eV) for most intense $Sr_{0.97}Al_2O_4$: $Eu^{2+}{}_{0.01,}$ $Dy^{3+}{}_{0.02}$ phosphor sample showing the existence of deeper traps.

References

Ayvacıkli M., Ege A., Yerci S., Can N., Synthesis and optical properties of Er^{3+} and Eu^{3+} doped $SrAl_2O_4$ phosphor ceramic, J. Lumin. 2011, 131: 2432.

Brandon D., Kaplan W. D., Microstructural Characterization of Materials-2nd Edition, John Wiley and Sons Ltd. England, 2008.

Chandrashekhar M., Sunitha D. V., Dhananjaya N., Nagabhushana H., Sharma S. C., Nagabhushana

B. M., Shivakumara C., Chakradhar R. P. S., Thermoluminescence response in gamma and UV irradiated Dy_2O_3 nanophosphor, J. Lumin. 2012, 132 (7): 1798.

Chen L., Zhang Y., Liu F., Luo A., Chen Z., Jiang Y., Chen S., Liu R. S., A new green phosphor of $SrAl_2O_4:Eu^{2+},Ce^{3+},Li^+$ for alternating current driven light-emitting diodes, Materials Research Bulletin, 2012, 47: 4071.

Chen R., Mckeever S.W.S., Theory of Thermoluminescence and Related Phenomenon, World Scientific Press, Singapore, 1997.

Clabau F., Rocquefelte X., Jobic S., Deniard P., Whangbo M.H., Garcia A., Mercier T. L., On the phosphorescence mechanism in $SrAl_2O_4:Eu^{2+}$ and its codoped derivatives, Solid State Sci. 2007, 9: 608.

Furetta C., Weng P.S. Operational Thermoluminescence Dosimetry, World Scientific, 1998.

Furetta C., Handbook of Thermoluminescence, World Scientific, 2003.

Jiang L. H., Zhang Y. L., Li C. Y., Hao J.Q., Su Q., Synthesis, photoluminescence, thermoluminescence and dosimetry properties of novel phosphor $KSr_4(BO_3)_3$: Ce, J. Alloys Compd. 2009, 482: 313.

Kamiyanagi Y., Kitaura M., Kaneyoshi M., Temperature dependence of long-lasting afterglow in $SrAl_2O_4$:Eu,Dy phosphor, J. Lumin. 2007, 122–123: 509.

Kim T. K., Woo J. J., Choe H. S., Kang H. S., Jang H. K., Whang C. N., Thermoluminescence from Ultraviolet Exposed $MgAl_2O_4$, Radiat. Prot. Dosim. 1999, 84: 297.

Kshatri D. S., Khare A., Characterization and optical properties of Dy^{3+} doped nanocrystalline $SrAl_2O_4$: Eu^{2+} phosphor, J. Alloys Comp. 2014, 588: 488.

Lin Z., Gilbert B., Liu Q., Ren G., Huang F., A thermodynamically stable nanophase materials, J. Am. Chem. Soc. 2006, 128: 6126.

McKeever S.W.S., Thermoluminescence of Solid, London: Cambridge University Press, 1985.

Mckeever S.W.S., Chen R., Luminescence Models, Rad. Measur. 1997, 27 (5-6): 625.

Marwaha G.L., Singh N., Vij D.R., Mathur V.K., UV dosimetry by thermoluminescence of bismuth doped CaS, Radiat. Eff. 1980, 53: 25.

Marwaha G.L., Singh N., D.R. Vij, V.K. Mathur, CaS: Bi as U.V. dosimeter Mater. Res. Bull. 1979, 14: 1489.

Mishra G. C., Upadhyay A. K., Dwiwedi S. K., Dhoble S. J., Kher R. S., Correlation between thermoluminescence and mechanoluminescence of γ-ray-irradiated Dy-doped BaB_4O_7 phosphors, J. Mat. Sc. 2012, 47: 2752.

Nag, A., Kutty T.R.N., Role of B_2O_3 on the phase stability and long phosphorescence of $SrAl_2O_4$:Eu, Dy, J. Alloy. Compd. 2003, 354: 221.

Nag A., Kutty T.R.N., The mechanism of long phosphorescence of $SrAl_{2-x}BxO_4(0<x<0.2)$ and $Sr_4Al_{14-x}BxO_{25}$ $(0.1<x<0.4)$ co-doped with Eu^{2+} and Dy^{3+} , Mater. Res. Bull. 2004, 39: 331.

Park, J. K., Lim M. A., Kim C. H., Park H. D., White light-emitting diodes of GaN-based Sr2SiO4:Eu and the luminescent properties, Appl. Phys. Lett. 2003, 82: 683.

R. Chen, Y. Kirish, Analysis of Thermally Stimulated Processes, Pergamon Press, New York, 1981.

Ryu H., Singh B.K., Bartwal K.S., Effect of Sr substitution on photoluminescent properties of $BaAl_2O_4:Eu^{2+}$, Dy^{3+}, Physica B, 2008, 403: 126.

Shafia E., Bodaghi M., Tahriri M., The influence of some processing conditions on host crystal structure and phosphorescence properties of $SrAl_2O_4:Eu^{2+}$, Dy^{3+} nanoparticle pigments synthesized by combustion technique, Curr. Appl. Phys. 2010, 10: 596.

Sharma S.K., Pitale S.S., Malik M.M., Qureshi M.S., Dubey R.N., Spectral and kinetic characterization of orange-red emitting $Sr_3Al_2O_6:Eu^{3+}/Sm^{3+}$phosphor, J. Alloys Compd. 2009, 482: 468.

Song L., Zhang S., Hydrothermal synthesis and highly visible light-induced photocatalytic activity of zinc-doped cadmium selenide photocatalysts, Chem. Eng. J. 2011, 166: 779.

S.W.S. McKeever, M. Moscovitch, P.D. Townsend, Thermoluminescence Dosimetry Materials: Properties and Uses, Nuclear Technology Publishing, Kent, 1995.

Tanori O. A., Melendrez R., Montero M. P., Castaneda B., Chernov V., Yen W. M., Flores M. B., Persistent luminescence dosimetric properties of UV-irradiated $SrAl_2O_4$: Eu^{2+}, Dy^{3+} phosphor, J. Lumin. 2008, 128: 173.

Xiao L., Meng S., Junying Z., Tianmin W., Effect of mixing process on the luminescent properties of $SrAl_2O_4:Eu^{2+}$, Dy^{3+} long afterglow phosphors, J. Rare Earths, 2010, 28 (1): 150.

Xu Y. F., Ma D. K., Guan M. L., Chen X. A., Pan Q. Q., Huang S. M., Controlled synthesis of single-crystal $SrAl_2O_4$: Eu^{2+}, Dy^{3+} nanosheets with long-lasting phosphorescence, J. Alloys Comp. 2010, 502: 38.

Yavetskiy R.P., Dolzhenkova E.F., Tolmachev A.V., Parkhomenko S.V., Baumer V.N., Prosvirnin A.L., Radiation defects in $SrB_4O_7:Eu^{2+}$ crystals, J. Alloys Compd. 2007, 441: 202.

Oxide Ion Conduction in La^{2+} and Sr^{2+} Co-Doped Ceria/(Li-Na)$_2CO_3$ Multifunctional Nanocomposite electrolyte

Nandini Jaiswal[a], Shail Upadhyay[b], Devendra Kumar[c] and Om Parkash[d*]
[a,c,d] Department of Ceramic Engineering, Indian Institute of Technology
(Banaras Hindu University), Varanasi- 221005, (India).
[b]Department of Physics, Indian Institute of Technology
(Banaras Hindu University), Varanasi- 221005, (India).

ABSTRACT

Nanocomposite electrolyte in the system $Ce_{0.85}La_{0.125}Sr_{0.025}O_{1.9125}$/(Li-Na)$_2CO_3$ has been synthesized by mixing nanosized co-doped ceria powder prepared by citrate-nitrate gel auto-combustion method with eutectic mixture of carbonates. Synthesized powder has been characterized via DTA, XRD, SEM, thermal expansion and impedance spectroscopy. Complex plane impedance spectra show a complex nature. The main feature of impedance spectra is the absence of distinct grain boundary arc in contrast to doped ceria where distinct grain and grain boundary arcs have been observed. Conductivity increases very rapidly around the melting temperature of carbonate due to superionic transition at the interfaces formed between the ceria and carbonate phases. At the interfaces a space charge layer is formed consists of large number of mobile defects than that of the bulk. Conductivity of 0.12 S/cm has been observed at 500 °C with an activation energy 0.2 eV of conduction.

Keywords: Co-doped ceria; Nanocomposite; Electrical conductivity; LT-SOFC.

1. INTRODUCTION

For the last few years research on solid oxide fuel cells (SOFCs) has been focused to decrease the operating temperature of SOFCs by developing the new electrolyte material of high ionic conductivity. Many researches have been made on single phase doped and co-doped ceria based solid electrolytes. But these are still far from the commercial utilization. Recently ceria/salt based composite electrolytes are alternative solution for these problems because of its high ionic conductivity at low temperatures (300-600 °C) [1]. Among various ceria composites, the $Ce_{0.80}Sm_{0.20}O_{1.90}$ (SDC) or $Ce_{0.80}Gd_{0.20}O_{1.90}$ (GDC)-carbonate composites are most commonly used materials, which have been demonstrated to have the best performance in many LTSOFC applications. The two-phase ceria composite electrolytes, specifically the ceria-carbonate (Li_2CO_3-Na_2CO_3) (LNCO) containing one molten phase realized the superionic conductivity of 0.1 S-cm^{-1}at 600 °C [2, 3]. Interfacial superionic conduction is the characteristic of the composite electrolytes [4]. These composites have multi-ion conduction above the melting temperature of the carbonate. Due to this, these composites can be used for advanced applications such as electrolytic cells, ammonia synthesis, CO_2 separation etc [1].

In our previous work La^{3+} and Sr^{2+} co-doped ceria nano powders were prepared by citrate-nitrate auto-combustion method [5]. It was observed that the composition $Ce_{0.85}La_{0.125}Sr_{0.025}O_{1.9125}$ shows the highest ionic conductivity of all the compositions (1.50×10^{-2} S-cm^{-1} at 600 °C). In the present work nanocomposite based on $Ce_{0.85}La_{0.125}Sr_{0.025}O_{1.9125}$/LNCO (COLS/LNCO) has been synthesized and characterized by means of DTA, XRD, SEM, and thermal expansion. Electrical conductivity has been investigated by employing impedance spectroscopy technique. The objective is to reduce the cost of solid electrolyte by replacing La^{3+} ion by Sr^{2+} ion.

2. EXPERIMENTAL

2.1 Synthesis

a. Nanocrystalline co-doped ceria $Ce_{0.85}La_{0.125}Sr_{0.025}O_{1.9125}$ powder was synthesized using citrate-nitrate auto-combustion method as discussed in detail in our previously reported work [5]. This powder was mixed with binary mixture of carbonates (molar ratio of Li_2CO_3 and Na_2CO_3 is 52:48) in the weight ratio 70:30. Mixed powder was milled using Fritsch Pulverisette Ball Mill in acetone medium for 5 hrs. Milled powder was dried at 60 °C for 24 hrs in an electrical oven. Dried powder was calcined at 600 °C for 2 hrs. The calcined powder was pressed uniaxially into cylindrical pellets (diameter~15 mm, thickness~2 mm) under a load of 5 tons using a hydraulic press. Pellet was sintered at 700 °C for $1\frac{1}{2}$ hr.

b. 2.2 Characterization

Thermal behavior of the composite was studied using a SETARAM TGA/DTA in the temperature range 100-800 °C in Ar atmosphere. Powder X-ray diffraction technique was used to determine the phases and crystal structure using Rigaku X-ray diffractometer employing CuKα radiation with a Ni filter. Average crystallite size, D was determined using Scherrer's formula:

$$D = 0.9\lambda/\beta\cos\theta \quad (1)$$

where, $\beta = \sqrt{\beta_m^2 - \beta_s^2}$, is the full width at half maxima (FWHM) excluding instrumental broadening, λ is the wave length of X-rays and θ is Bragg angle. β is taken for the strongest Bragg's peak corresponding to (111) reflection for all the samples. Micrograph

*Corresponding Author: Tel:+91-542-6701791; Fax:+91-542-2368428
Email address: oprakash.cer@itbhu.ac.in

of chemically etched sample was recorded with scanning electron microscope of INSPECT 50 FEI. Bar of dimensions 50 mm ×10 mm ×4 mm were prepared for measurement of thermal expansion. The bar was sintered at 700 ^{o}C for $1\frac{1}{2}$ **hr.** Thermal expansion was measured using dilatometer in the temperature range 30-650 ^{o}C employing a heating rate of 10 ^{o}C/min in air.

Ag-paste was brushed on both the surfaces of a polished pellet followed by annealing at 700 ^{o}C (for 15 min) to make the electrical contacts. Impedance measurements were made using Novocontrol Alpha-A High Performance Frequency Analyzer in air in the temperature range 200-650 ^{o}C and frequency range 1Hz - 1MHz. Impedance data were collected using Windata program and were fitted using Zview software.

3. RESULTS AND DISCUSSION

3.1 Differential Thermal Analysis

DTA curve of the composite is shown in Fig.1. Two endothermic peaks have been observed in the DTA curve. One in the range 70-110 °C corresponds to evaporation of moisture absorbed in the sample. Other peak observed at 486 °C is ascribed to melting of the carbonate binary mixture. No chemical changes occur beyond 500 °C. Based on DTA results composite powder was calcined at 600 °C for 2 hrs.

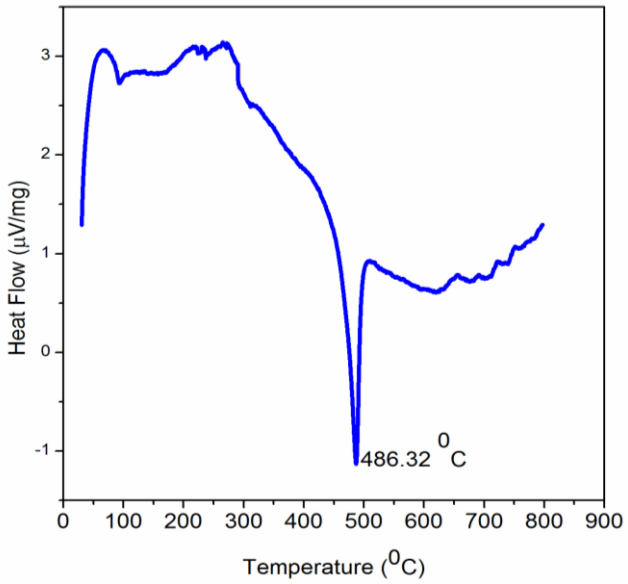

Fig. 1 DTA plot of COLS/LNCO composite

3.2 X-Ray Diffration

Figure.2 shows the powder X-ray diffraction pattern of the sintered COLS/LNCO powder. Diffraction peaks are well matching with the JCPDS file no. 43-1002 of cubic fluorite structure of ceria with space group Fm3m. Therefore, it can be concluded that there is no reaction between the ceria phase and carbonates. In the composite, carbonates exist as an amorphous phase. Density of the sintered sample has been found to be 85% of theoretical value. Average crystallite size determined from Scherrer's formula is 23 nm.

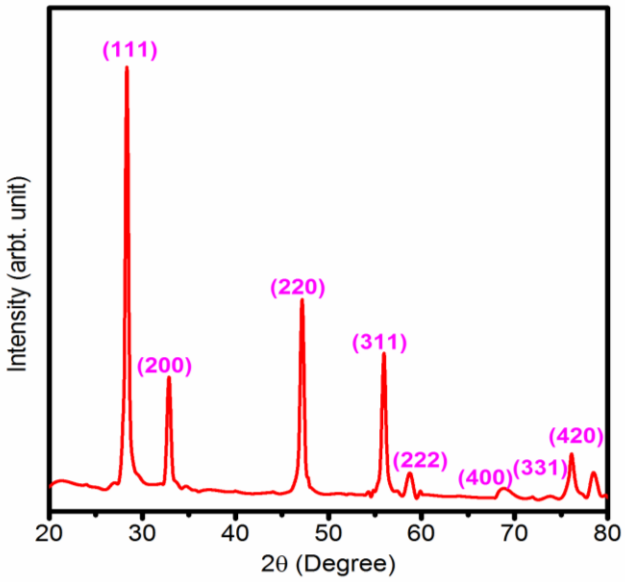

Fig. 2 XRD pattern of COLS/LNCO composite

3.3 Microstructure

Figure.3 shows SEM micrograph of the composite pellet. It can be seen from micrograph that the COLS particles are covered with molten carbonates. Therefore, morphology of the composite became amorphous.

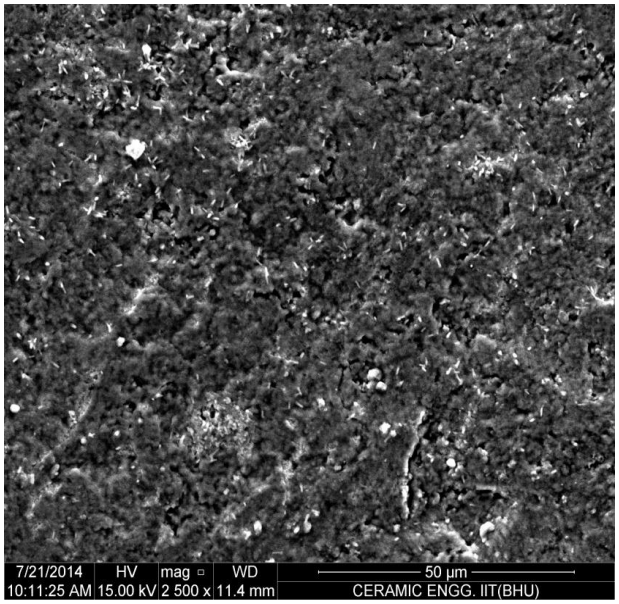

Fig. 3 SEM micrograph of COLS/LNCO composite

Due to low sintering temperature, microstructure is very loose but when temperature reaches melting temperature of carbonate molten carbonate fills in the interspaces and forms a dense structure.

3.4 Thermal Expansion

Thermal expansion curve of composition COLS/LNCO is shown in Fig. 4. It can be noted that the curve is linear throughout. Coefficient of thermal expansion is determined using following relation:

$$\alpha_{T_2-T_1} = \frac{dL}{L_0\,(T_2 - T_1)} \qquad (2)$$

Coefficient of thermal expansion (CTE) has been found to be 14.2×10^{-6}/K.

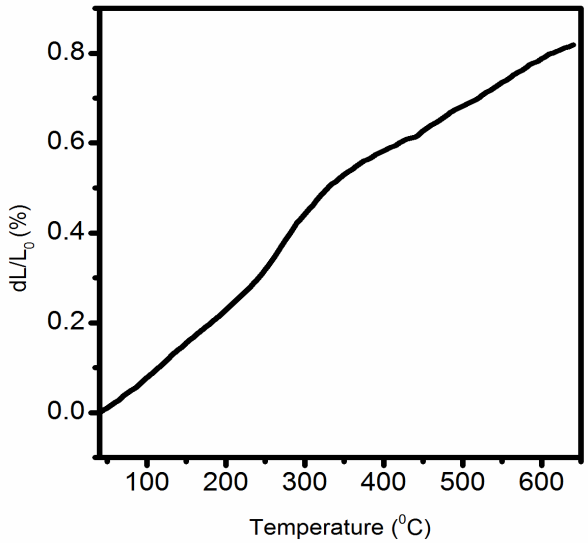

Fig. 4 Thermal expansion curve of COLS/LNCO composite

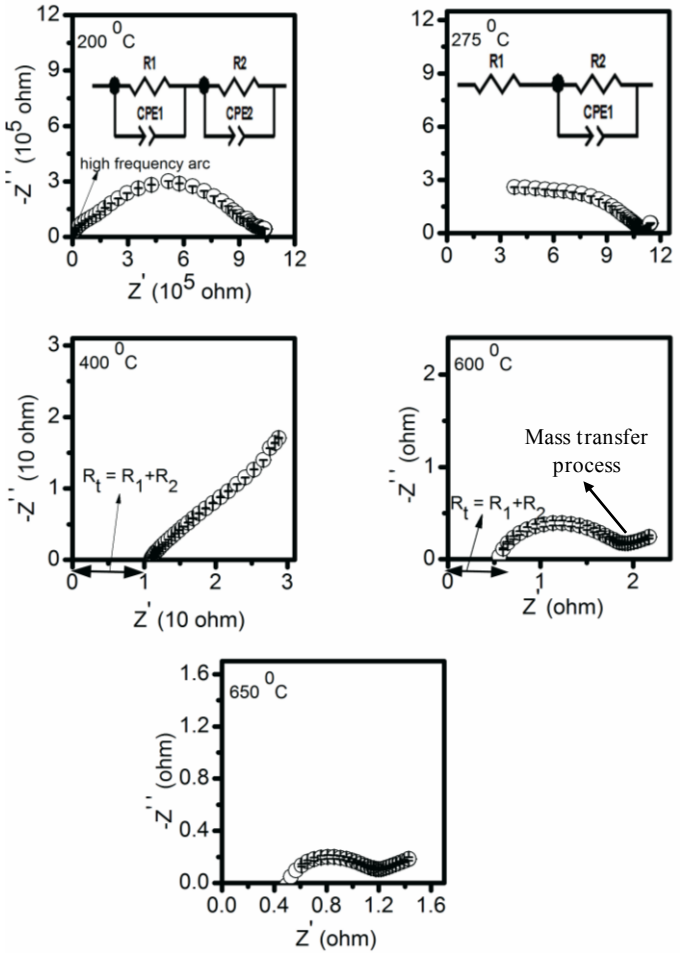

Fig. 5 Complex plane impedance plots of composition COLS/LNCO at different temperatures

3.4 Electrical Conductivity

Complex plane impedance spectra of the composite are shown in Fig. 5. At 200 ℃, two depressed arcs have been observed along with a spike at low temperature. High frequency arc corresponds to contribution of the grains and intermediate frequency arc ascribed to the grain boundaries contribution to the total resistance. A spike in the low frequency region corresponds to the electrode process. As temperature increases, relaxation frequency of various polarization processes increases leading to shifting of the arcs toward higher frequency.

The grains and grain boundaries arcs disappear above 350 ℃. At higher temperature only arc due to electrode polarization is observed. The arc due to electrode response is large because of the barrier between the ionic conduction in the electrolyte and electronic conduction in the electrode [2]. At 600 ℃, electrode arc is associated with a tail which is ascribed to the mass transfer process [2]. It has been clear from this distinct phenomenon that the conduction mechanism in the composite electrolytes is different from the ceria based singly phase electrolyte. Below 250 ℃, the equivalent circuit consisting of $(R_1\text{-CPE1})_{Grains}$ and $(R_2\text{-CPE2})_{Grain\ boundaries}$ connected in series is used to fit the impedance data. Above 250 ℃ equivalent circuit consists of $(R_1)_G$ and $(R_2\text{-CPE2})_{Grain\ boundary}$ connected in series. At a temperature above 350 ℃, the total resistance is determined from the intercept on the real axis (Z') on the high frequency side of electrode arc. Conductivity, σ, is calculated using the following formula:

$$\sigma = \frac{L}{S \times R} \qquad (3)$$

where L, S and R are the thickness, surface area and total resistance of the electrolyte.

Arrhenius plot for total ionic conductivity is shown in Fig. 6. It can be observed that a sharp increase in the conductivity has been observed at 325 ℃ in the Arrhenius plot of LSCO/LNCO. Conductivity of composite electrolyte is higher than that of LSCO in the higher temperature range > 325 ℃ while lower at temperature < 325 ℃. This transition temperature is related to softening of carbonates. But this temperature is lower than that of

melting temperature due to interaction between LSCO particles and LNCO. This results in threshold percolation to form a highly conducting continuous path at the interfaces [6]. Due to this non frozen liquid on the surface of ceria particles is formed which contributes to the conduction below the melting temperature. Conductivity of LSCO/LNCO composite reaches to 0.12 S-cm^{-1} at 500 ℃ while LSCO and LNCO have conductivity 3.9 ×10^{-3} S-cm^{-1} [5] and 4.73×10^{-2} S-cm^{-1}. Therefore, it implies that there is a new conduction mechanism in the composite rather the bulk conduction observed in LSCO. This leads to higher conductivity in the composite.

Conduction mechanism in the composite can be understood by solid state chemistry.

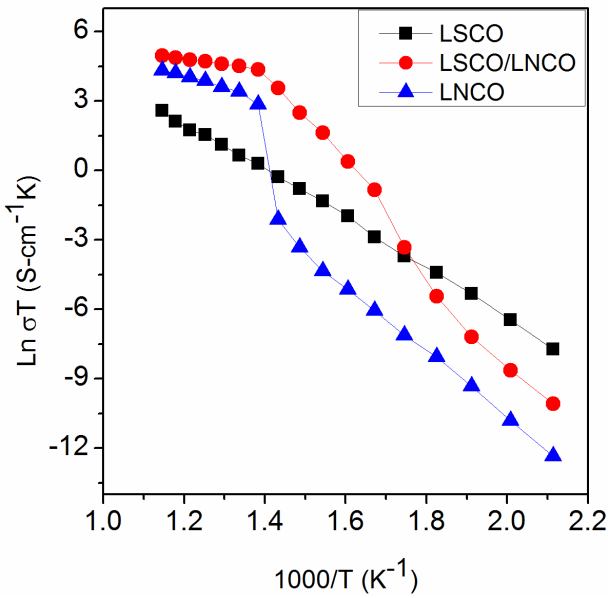

Fig. 6 Arrhenius plots for total ionic conductivity of all the compositions

Composite has large interface region between two constituent phases than that of single phase ceria electrolyte. At higher temperature, concentration of ionic defects at the interfaces and constituent phases increases due to melting from sublattice to the bulk [6]. After melting of carbonates M^+ (Li^+, Na^+) and CO_3^{2-} ions in the carbonates are highly mobile together with O^{2-} ions, resulting in higher conductivity than the co-doped ceria. After melting, carbonates fill in the interspaces. This generates more interfaces for ion transport. Amorphous layer on the LSCO particles increased disorder on the LSCO surface at rising temperature. This may make LSCO surface active to cause Li^+-O^{2-}/Na^+-O^{2-} interactions which facilitate O^{2-} ions conduction through the interfaces [7]. Activation energy of conduction is determined by fitting the conductivity data to Arrhenius equation as given below:

$$\sigma = \sigma_0 \, exp\left(\frac{-E_a}{kT}\right) \qquad (4)$$

where σ_0 is the pre exponential factor, k is the Boltzmann constant and T is the absolute temperature. Activation energy of conduction for composite is found to be 0.2 eV. This low value of activation energy indicates the interfacial conduction of O^{2-}. This shows that LSCO/LNCO composite is a potential electrolyte for LT-SOFCs which will be cheaper than LSCO. Compatibility with other cell component needs to be checked.

3. Conclusion

Nanocomposite LSCO/LNCO has been prepared by mixing $Ce_{0.85}La_{0.125}Sr_{0.025}O_{1.9125}$ nanosized powder prepared by citrate nitrate auto-combustion method with $(Li\text{-}Na)_2CO_3$ and sintered at 700 ℃ for $1\frac{1}{2}$ hr. Single phase formation has been observed in the composite. Micrograph show continuous distribution of both the phases with LSCO grains surrounded by amorphous carbonate phase. A sharp increase in the conductivity occurs at 325 ℃. This is attributed to superionic conduction at the interfaces. Composite, LSCO/LNCO shows the maximum conductivity of 0.12 S/cm at 500 ℃. Activation energy of conduction in LSCO/LNCO composite is found to be 0.20 eV. This may make this composite useful for application in LT-SOFCs (500 ℃).

4. Acknowledgement

We are thankful to Department of Science and Technology, New Delhi and MHRD for financial support.

5. References

[1] Liangdong, F., Chengyang W., Mingming, C., and Bin, Z. 2013. Recent development of ceria-based (nano) composite materials for low temperature ceramic fuel cells and electrolyte-free fuel cells. *J. of Power Sources*. 234 (Feb. 2013), 154-174.

[2] Xiaodi, W., Ying, M., Rizwan, R., Mamoun, M., and Bin, Z. 2008. Novel core shell SDC/amorphous Na_2CO_3 nanocomposite electrolyte for low temperature SOFCs. *Electrochem. Commn.* 10 (Oct. 2008), 1617-1620.

[3] Rizwan, R., Xiaodi, W., Ying, Ma., Xiangrong, L., and Bin, Z. 2010. Improved ceria-carbonate composite electrolyte. *Int. J. of Hydrogen Energy*. 35 (April 2010), 2684-2688.

[4] Bin, Z., Lic, S., and Mellander, B. E., 2008. Theoretical approach on ceria based two phase electrolytes for low temperature (300-600 °C) solid oxide fuel cells. *Electrochem. Commn.* 10 (Feb. 2008) 302-305.

[5] Nandini, J., Devendra, K., Shail, U., and Om, P. 2015. Preparation and characterization of $Ce_{0.85}La_{0.15-x}Sr_xO_{\{2-(0.075+x/2)\}}$ solid electrolytes for intermediate temperature solid oxide fuel cells. *Ionics*, DOI= *http*:// 10.1007/s11581-014-1190-4.

[6] Jianbing, H., Zongqiang, M., Zhixiang, Liu., and Cheng, W. 2007. Development of novel low temperature SOFCs with co-ionic conducting SDC-carbonate composite electrolytes. *Electrochem. Commn.* 9 (Oct. 2007), 2601-2605.

[7] Bin, Z., Xiangrong, L., and Schober, T. 2004. Novel hybrid conductors based on doped ceria and BCY20 for IT-SOFC applications. *Electrochem. Commn.* 6 (April 2004), 378-383.

Structural parameters of nanocrystalline calcium phosphate using CTAB as a cationic template

M. M. Méndez-González[1*], M. A. Valdés[2], M. García [2], G. Méndez G.[3]
[1]National Polytechnic Institute, ESFM-IPN, Laboratory of Biomaterialscs, Mexico City, Mexico
[2]Nanociencias y Nanotecnología, CINVESTAV, Apdo. Postal 14-740, 07000, México D. F.
[3]Technological University of San Juan del Río, Queretaro, México
*Email: mmendezg07@yahoo.com.mx

Abstract: The results of the effect of physicochemical variables such as pH, temperature, stirring time, dwell time and heat treatment on the synthesis and crystallinity of calcium phosphate using Cetyl Trimethyl Ammonium Bromide (CTAB) as a cationic template is presented with the in order to regulate the nucleation and growth of crystals. The results of the structural study performed calcium phosphate are also shown by X-ray diffraction (XRD), energy dispersive spectroscopy (EDS), infrared spectroscopy and scanning.

Keywords: nanocrystalline calcium phosphate ,physicochemical parameters, synthetic nanostructured ceramics, infrared spectroscopy, x-ray diffraction, biomedical applications.

INTRODUCTION

Thanks to nanotechnology new materials are being fabricated with special properties used in a variety of applications, such as the materials used as implants or bone substitute in the human body, these must be adapted to the changes that occur in the bone as it reconstructs constantly [1,2]. The main bone component is the calcium phosphate denominated as hydroxyapatite.

EXPERIMENTAL METODOLOGY

Calcium phosphate has been successfully synthesized using Cetyl Trimethyl Ammonium Bromide (CTAB) as a cationic template to obtain solution A. It is presented to regulate the nucleation and growth of crystals. Equal parts of $CaCl_2$, NH_4NO_3 and Na_3PO_4 were mixed and polymer polyethylene glycol 400 (PEG 400) were added to incorporate all reagents into one [3,4]. Solution B was obtained by continuously stirring deionized water and the CTAB for 30 minutes until everything was dissolved. Then, ammonium hydroxide NH_3OH was added and it was again stirred for 30 minutes. Finally, solution A was added by slow dripping to solution B while stirring constantly. NH_3OH was added to the mixture of solution A and B until a pH of 4.5, 9.0 and 9.5 was obtained. After this, the solution was heated to temperature of 80 ° C for one hour.

RESULTS

Experimental parameters are shown in Table 1. Structural behavior was determined by X-ray diffraction. In Figure 1, the diffraction patterns of calcium phosphate are shown, where the width and height of the peaks reveal that the calcium phosphate prepared has a small size and a good quality crystal. Infrared spectra is shown in Figure 2, where bands of groups OH^{1-}, $PO43^{-}$, P-O, and weak C-H are identified. The addition of CTAB, PEG 400, NH_3OH and ethanoic acid are crucial for the formation of the Nano rods[5,6]. EDS patterns shown Ca/P ratio of about 1.657, which is within the generally accepted range between 1.5-1.69 [7]. Morphology of the samples A, B and C is shown in Figure 3, 4 and 5 respectively.

CONCLUSION

Calcium phosphate was obtained with a Ca/P ratio of 1.657, Using CTAB as a cationic template to control the crystal size and PEG as a non-ionic surfactant.

Table 1. Experimental parameters

Sample	Drying Temperature (°C)	pH	Wash Time (Hr)
A	350	4.5	25
B	350	9.0	25
C	80	9.5	12

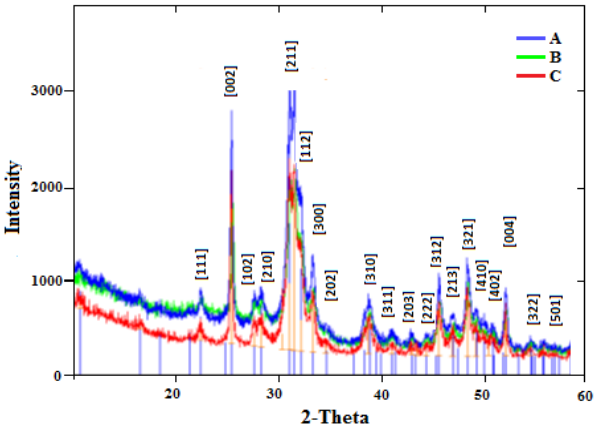

Fig.1 XRD diffraction patterns of samples A, B and C.

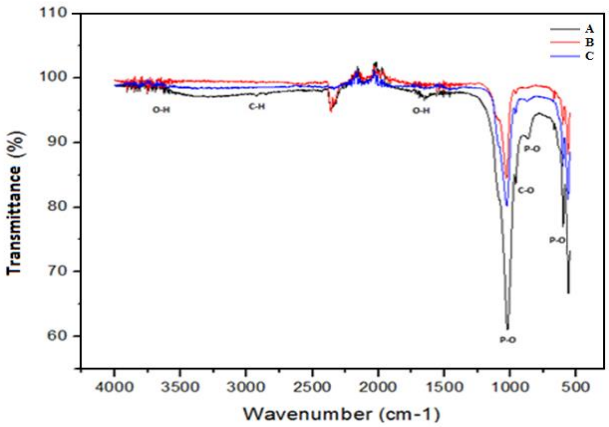

Fig . 2. FT- IR spectrum of samples A, B and C.

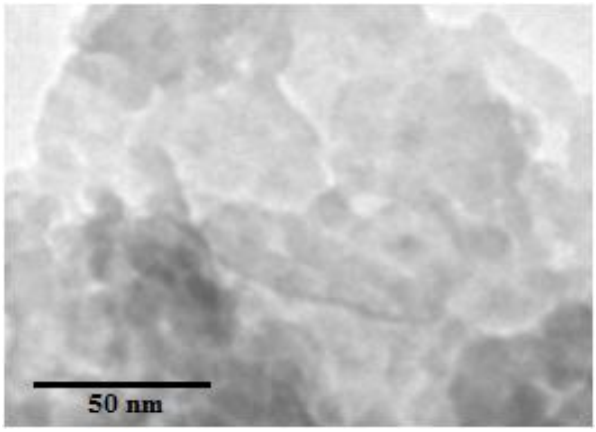

Fig. 3. Morphology of sample A.

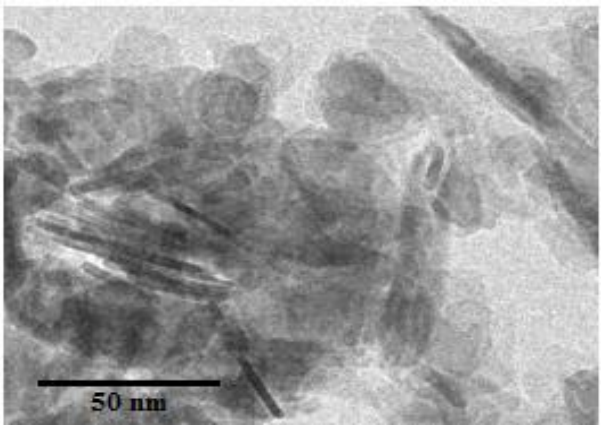

Fig. 4. Morphology of sample B.

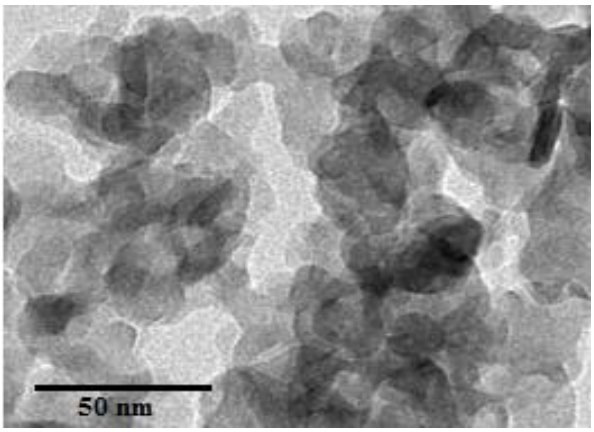

Fig. 5. Morphology of sample C.

References

1. Strampelli, B. (1999) Annal Ottal Clin Ocul , *Parma*, 89, 1039-1044.
2. Yingkai, L., Dedong, H. (2004) Materials Chemistry and Physics, 86, 69-73.
3. Temprano, J. (1993) Keratoprosthesis with tibial autograft. *Refract Corneal Surg*, 9, 192-193.
4. Dohlman, C. H., Nouri, M. , Barnes, S., (2003) Investigative Ophthalmology & Visual Science, 44, 1407-1411.
5. Sun, J. H., Gong, Y. J., Fan, W. H., Wu, D. (1999) Acta Phys. Chim. Sin. 15, 517.
6. Kim, B. S., Hrkach, J. S., Langer, R. (2000) Biomaterials, 21, 259. 8. P.J. Soltys, M.R. Etzel, Biomaterials Vol. 21 (2000) 37.
7. Wang, P., Tan, K. L., Kang, E. T. (2000) Biomater. Sci. Polym. Ed. 11, 169.

Correlation between Nanostructure and Mechanical Properties of Metals subjected to Severe Plastic Deformation

W.Bochniak, A.Korbel, P.Ostachowski
AGH University of Science and Technology, Mickiewicza Av. 30, 30-059 Krakow, Poland

Abstract: In this paper the nanostructural aspects of plastic deformation of metals, in particular the conditions leading to the replacement of homogeneous multi-system slip with a stratified rigid (dislocation less) shear strain in trans-granular shear bands, are analyzed. The main focus concerns the description of mechanical properties of the zones supersaturated with point defects which are generated as a result of the change of the deformation path and which determine the superplastic flow of metals. The paper gives scientific foundations for the development of new, unconventional plastic deformation technologies for metals, particularly in the area of severe plastic deformation processes - SPD (Estrin *et al*., 2013).

Keywords: severe plastic deformation, cyclic change of deformation path, point defects generation, plastic flow viscosity, superplasticity, KOBO method.

Nanostructural phenomena

Low temperature plastic deformation of metallic materials is a result of dislocation slip. For small plastic strain, the deformation process has been well described by the Orowan relation in which plastic strain ε - through the orientation factor M - depends on the length of the Burger's vector b, the density of slip dislocations ς_m and their mean free path x, in accordance with the following formula: $\varepsilon = M \cdot b \cdot \varsigma_m \cdot x$. However, in case of advanced deformation (SPD), the dislocation slip, although indispensable, is merely one of many elements of a complex deformation mechanism leading to localized plastic flow in shear bands.

As is commonly known, shear bands are a result of the change in the deformation path, either self-induced, or forced by external change in the loading scheme, occurring when secondary slip system (or systems), operating in the conditions of "alien" dislocation distribution (initially formed dislocation forest) is activated (Basinski *et al*., 1965). The crossing of slip dislocations and the forest dislocations resulting in local anchoring of the slip dislocations (the creation of jogs) and simultaneous folding of the free segments, leads to the formation of dipoles. Dipoles, which in fact are rows of point defects, are immediately disintegrated due to their low migration energy. In case of interstitial (own) atoms it is particularly low and equals only 0.06 – 0.15 eV (Damsk *et al*., 1963, Terentyev *et al*., 2004, Sato *et al*., 2007). This leads to the formation of zones supersaturated with point defects that have weak bonds with the surrounding areas (Korbel *et al*., 2015).

As suggested in paper(Korbel *et al*., 2011), metal undergoing a deformation process with a particular about loading scheme can lower its viscosity coefficient η even by 13 orders of magnitude to the value of 10^6 [Pa·s]. In this cause, the viscosity of plastic flow is determined by the presence of generated point defect exceeding the equilibrium level with an estimated concentration of 10^{-8}. Therefore, the strain bore by the shear bands can be treated as localized rigid shear of metal, which remains a solid but behaves like a Newtonian fluid (superplasticity). On the other hand, terminal stability of point defects exceeding the equilibrium level is limited by their annihilation or the formation of so called: „clusters"– lower energy configurations. Hence, in order to maintain a low value of the viscosity coefficient η, the change in deformation path should be cyclically recurred during the whole plastic deformation process. The KOBO method of metal forming (Korbel *et al*., 2013), in which the main deformation scheme is complimented by cyclic deformation, meets the aforementioned criterion.

It is worth to point out, that nanometric (~ 2 nm) point defects clusters of high density, typical for irradiation processes, have been observed in many deformed metals (e.g. Matsukawa *et al*., 2003), and a phenomenon of the dislocation-free plastic deformation is linked to the presence of „vacancy-type point defect clusters".

Experimental

Schemes of two KOBO deformation methods, as well as the obtained products, are presented below (figs 1 -3).

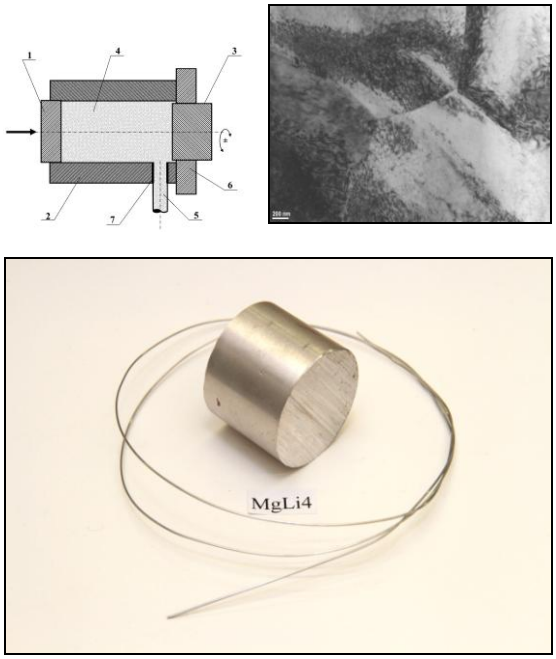

Fig.1. Scheme of the KOBO extrusion process (Korbel et al., 2011) and wire (structure and view) produced from magnesium alloy MgLi4 at room temperature and with extrusion rate λ = 10 000, designed to be used as surgical threads.

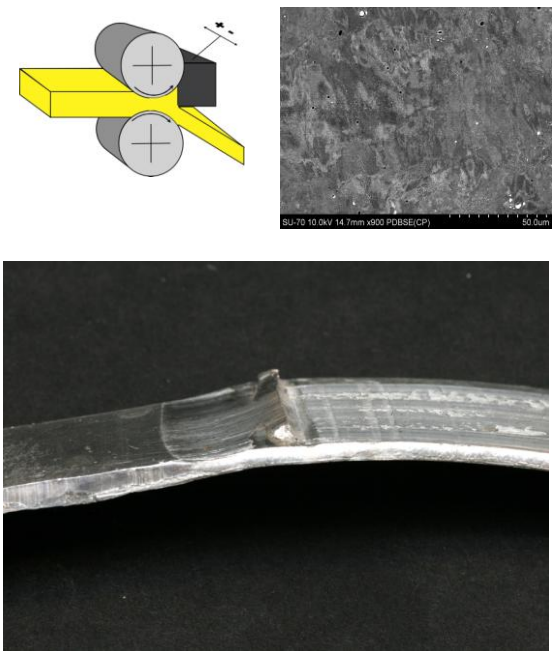

Fig.2. Scheme of a complex rolling by the KOBO method (Bochniak *et al*., 2015) and strip of aluminum alloy 7075 (structure and view), obtained as the result of this process.

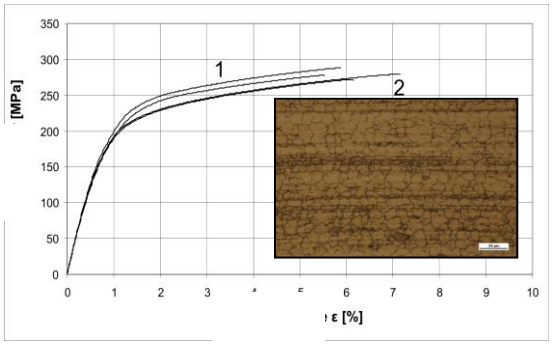

Fig.3. Mechanical properties and structure of wire produced from machining chips of magnesium alloy AZ91, by KOBO extrusion (as in Fig. 1) at room temperature.

To sum up, knowledge on the phenomena accompanying plastic deformation of metals allows for better exploitation of their potential mechanical properties.

Acknowledgments

This work was supported by the Polish Ministry of Science and Higher Education under Project No POIG.0103.01–0015/08.

References:

Basinski Z.S., Jackson P.J. (1965) *Phys. Stat. Sol*., 10, 45.

Bochniak W., Łagoda M., Brzostowicz A, Prokopowicz M. (2015) *Adv. Mater. Res*., 1079-1080, 50.

Damsk A.C., Dienes G.J. (1963) Point Defects in Metals, *Gordon and Breach Science Publishers, New York-London*.

Estrin Y., Vinogradov A. (2013) *Acta Mater*., 61, 782.

Korbel A., Bochniak W., Ostachowski P., Blaz L. (2011) *Metall. Mater. Trans*., 42A, 2881.

Korbel A., Bochniak W. (2013) *Philos. Mag*., 93, 1883.

Korbel A., Bochniak W.(2015) Stratified plastic flow in metals, *Adv. Mater. Res*., – in Preparation.

Matsukawa Y., Yasunaga K., Komatsu M., Kiritani M. (2003) *Mater. Sci. Eng*., A 350, 17.

Sato K., Yoshiie T., Xu Q. (2007) *Journ. Nuclear Mater*., 367-370, 382.

Terentyev D., Malerba L. (2004) *Journ. Nuclear Mater*., 329-333, 1161.

MWI Synthesis and Characterization of Highly Conductive R-(GO-(PS-PMMA))/AgNPs Nano composites and its Antibacterial Activity against *E.Coli*

Edreese H. Alsharaeh
Department of Chemistry, Alfaisal University
Riyadh, KSA, 11533

Abstract: This work presents study on the facile method for preparation of copolymer of styrene and methyl-methacrylate containing reduced graphene oxide/silver nanoparticles (PS-PMMA/RGO/AgNPs) nanocomposites using two different preparation techniques (i) a microwave irradiation (MWI) to obtain R-(GO-(PS-PMMA))/AgNPs nanocomposites and (ii) in situ bulk polymerization method to obtain RGO/AgNPs-(PS-PMMA) nanocomposites. The nanocomposites were characterized by FTIR, XPS, and Raman spectroscopy and XRD, SEM, HRTEM, DSC and TGA analysis techniques. These results showed that the MWI produced nanocomposites with enhanced morphological, structural and thermal properties as compared with nanocomposites by insitu method. The antibacterial activity of RGO/AgNPs-(PS-PMMA) and R-(GO-(PS-PMMA))/AgNPs nanocomposites against *E.coli HB 101 K-12,* shows an inhibition zone of 3 mm and 27 mm respectively. This result indicates that the nanocomposites prepared by MWI shows strong activity. Also the conductivity results shows that the nanocomposites prepared using MWI shows better conductivity than the insitu prepared nanocomposites

Keywords: Graphene; Graphene oxide; Silver nanoparticles; MWI; PS-PMMA.

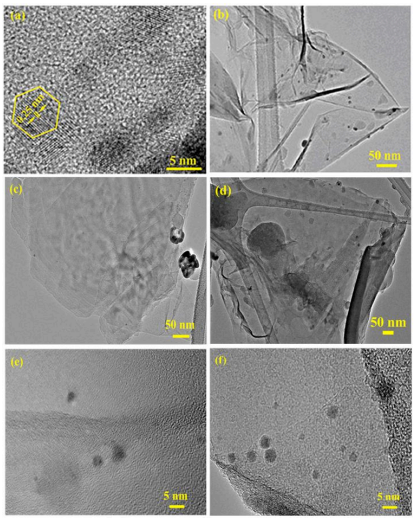

Figure 1: The HRTEM images of (a) AgNPs, (b) RGO/AgNPs, (c, e) GO/AgNPs-(PS-PMMA), and (d, f) R-(GO-(PS-PMMA))/AgNPs nanocomposites

References:

[1] Kampf, G., Dietze, B, Große-Siestrup, C., Wendt, C., Martiny, H. Microbicidal Activity of a New Silver- Containing Polymer, SPI-ARGENT II *Antimicrobial Agents And Chemotherapy* 1998, 42, 2440 – 2442.

[2] Fang, N., Lee, H., Sun, C., Zhang, X. Sub-Diffractionlimited Optical Imaging with Silver Superlens*Science* 308 2005: pp. 534 – 537.

[3] Sun, Y., Gates, B., Mayers, B., Xia, Y. Crystalline Silver Nanowires by Soft Solution Processing *Nano Letters* 2 2002: pp. 165 – 168.

[4] Nicewarner-Pena, S. R., Griffith Freemean, R., Reiss, B. D., He, L., Pena, D. J., Walton, I. D., Cromer, R.,Keating, C. D., Natan, M. J. Submicrometer Metallic Barcode *Science* 294 2001: pp. 137 – 141.

[5] Mock, J. J., Oldenburg, S. J., Smith, D. R., Schultz, D. A., Schultz, S. Composite Plasmon Resonant Nanowires *Nano Letters* 5 2002: pp. 465 – 469.

The investigation of different particle size Magnesium-doped zinc oxide ($Zn_{0.92}Mg_{0.08}O$) nanoparticles on the lubrication behavior of paraffin oil

R. B. Rastogi[1]*, Kalyani[1], V. Jaiswal[1], D. Kumar[2]
[1]Department of Chemistry, Indian Institute of Technology (BHU), Varanasi-221005, India
[2]Department of Ceramic Engineering, Indian Institute of Technology (BHU), Varanasi-221005, India

Abstract:

Magnesium-doped zinc oxide ($Zn_{0.92}Mg_{0.08}O$) ZMO nanoparticles of 23 nm particle size have been synthesized by auto-combustion method. The variation in particle size of these nanoparticles has been performed by their further calcination at 800 and 1000 ^{o}C for 2h and the corresponding calcined particles are designated as ZMO-1 and ZMO-2, respectively. The nanoparticles have been characterized by Powder-XRD, SEM, EDX and TEM. The effect of particle size on the antiwear lubrication behavior of paraffin base oil has been investigated on Four-ball lubricant tester. The tribological tests of these nanoparticles as antiwear additives have been studied at an optimized concentration (0.5%w/v) by varying load for 30 min test duration and by varying the test durations at 392N load. Various tribological parameters such as mean wear scar diameter (MWD), friction coefficient (μ), mean wear volume (MWV), running-in and steady-state wear rates show that these nanoparticles act as efficient antiwear additives and possess high load carrying ability. From these tribological tests it has been observed that the lubrication behavior of studied nanoparticles is strongly size-dependent. The best tribological behavior is shown by nanoparticles of the smallest size, ZMO. Being sulfur, halogen and phosphorous free, ZMOs nanoparticles have potential to be used as low SAPS lubricant additives. The SEM and AFM analysis of the worn surfaces lubricated with ZMO nanoparticles at 392N applied load for 60 min test duration show drastic decrease in surface roughness. The values of surface roughness of different additives is in good agreement with their observed tribological behavior.

Keywords: Four-ball tester, Antiwear lubricant additives, $Zn_{0.92}Mg_{0.08}O$ nanoparticles, Material characterization, Surface analysis: AFM, SEM.

1. Introduction

Lubricants play an important role to reduce friction and wear and increasing the life of contact interfaces. According to literature survey, a lot of organic compounds have been used as antiwear and extreme pressure lubrication additives. These additives molecule basically contain active elements such as phosphorous, sulfur, halogens, nitrogen and oxygen as well as polar groups for strong adsorption.[1] Additives with these active elements get adsorbed on the contacting metal surface and form a tribochemical film under lubricating conditions. This enhances machine efficiency by reducing wear and friction. Besides this, tribological performance of zinc, molybdenum and lanthanum complexes of dithiohydrazodicarbonamides, dialkyldithiophosphates, dithiocarbamates, tricresylphosphates, etc. have also been investigated.[2] Modern engine oils contain a large number of additives but the most influential compounds on the tribological performance of the lubricants are antiwear zinc dialkyldithiophosphates (ZDDPs). ZDDPs have been used in engine oils as multifunctional additives for more than 70 years and are probably the most successful antiwear additives ever discovered. However, the excessive use of ZDDPs has been limited due to their adverse impact on environment caused by poisoning of the catalytic converters since these contain high amount of Sulfated Ash, Sulfur and Phosphorous (SAPS).[3] Besides this, ZDDPs are also health hazardous and responsible for eye irritation, allergic contact dermatitis and mutagenicity.[4] Several norms are available which strictly limit the SAPS (Sulfated Ash, Phosphorous and Sulfur) contents of additives. According to ILSAC GF-5 the acceptable limits of phosphorous and sulfur is 0.08% and 0.5% respectively.[5] Therefore, a lot of efforts have been made to develop new antiwear additives which have low SAPS content.

In order to meet the aforesaid objectives, several substituted Schiff bases and thiosemicarbazones as antiwear additives were explored by *Rastogi et al*. Their synergistic action with organoborate show better tribological properties as compared to ZDDP. Besides this, *ß*-lactum antibiotics and stearic acid-modified zinc doped calcium copper titanate nanoparticles have been recently reported as efficient low/zero SAPS antiwear additives in paraffin base oil.[6,7] With continuous efforts in the field of development of nanoscience and nanotechnology, nanoparticles have attracted much attention due to their unique properties and applications in electronics, photonics, magnetism and tribology.[8] In tribology, several types of inorganic nanoparticles such as fullerene-like (IF) supramolecules of metal dichalcogenides MX_2 (M = Mo, W, etc.; X = S, Se) CaO, CuO, ZnO, TiO_2, CeO_2, lanthanum borate, etc.[9,10] The blends of these particles with lubricating oils improve the extreme pressure, antiwear and friction reducing properties of the lubricating base oil. A literature survey shows that various metallic nanoparticles have been used as lubricant additives for different purposes but very few reports are available on the mechanism of their action.

The objective of the current study is, therefore, to synthesize Magnesium doped zinc oxide nanoparticles ($Zn_{0.92}Mg_{0.08}O$; ZMO) of different size and explore the effect of particle size on the tribological behavior of paraffin base oil under boundary conditions. To accomplish this objective, various techniques have been employed to study the particle size, shape (morphology), chemical composition, tribological properties (friction and wear) and surface morphology of worn track (SEM and AFM) during present investigation.

2. Experimental section

2.1. Synthesis and characterization

Aqueous solutions of metal nitrates were mixed with an aqueous solution of citric acid maintaining at constant citrate to nitrate ratio of 0.3. The mixed solution was evaporated with continuous stirring at 200±5 °C until it gelled and finally burnt. Within a few seconds,

the combustion reaction completed giving blackish porous ash filling the container. The ash was calcined at 600 °C in air for 4 h. Thus prepared magnesium doped zinc oxide nanoparticles ($Zn_{0.92}Mg_{0.08}O$) named as ZMO, were further calcined at 800°C and 1000°C and designated as ZMO-1 and ZMO-2 respectively. The phase, composition and morphology of synthesized ZMOs nanoparticles have been characterized by Powder-XRD, SEM, EDX and TEM.

X-Ray diffraction data were indexed on the basis of a cubic unit cell similar to undoped ZnO (JCPDS 36-1451), Fig.1, which confirms the formation of single phase. The average crystallite size of the ZMOs nanoparticles was estimated as 23, 34 and 39 nm prepared at 600, 800 and 1000 °C, respectively using the Debye Scherrer formula:

$$D = k \lambda / \beta \cos\theta$$

Where, λ is the wavelength of the X-ray, k is a constant taken as 0.89, θ is the diffraction angle and β is the full width at half maxima (FWHM). The crystallite size derived from the XRD data. It is clearly observed from the XRD data that the average crystalline size increased with increasing temperature. The increased crystallite size with increasing temperature is mainly due to over grown grains resulting from the destruction of the grain boundaries at higher temperature.

A Transmission Electron Microscope (TEM) was used to investigate the size of ZMO nanoparticles. The TEM observation reveals that the ZMO nanoparticles possess almost a spherical shape (Fig.2). Further, it can be seen from TEM-images that the average particle sizes of ZMO nanoparticles are 22 nm which supports the XRD-data.

The EDX (energy dispersive X-ray) spectrum of the Mg-doped-ZnO nanoparticles (ZMO), Fig.3, comprises of Zn, O and Mg. Elemental analysis reveals the atomic percentages of Zn, O and Mg as 52.4%, 46.2% and 1.5% respectively.

2.2. Tribological Characterization

All the tribological testing was performed according to ASTM D4172 standard using neutral paraffin oil on four ball lubricant testing machine. Paraffin oil blends of ZMOs nanoparticles having concentration 0.00, 0.25, 0.5 and 1.0 % (w/v) were made by stirring for two hours on magnetic stirrer. The blends were further sonicated for one hour. The entire tests were carried out at an optimized concentration i.e., 0.5% w/v.

3. Results and Discussion

The lubrication properties of these different size ZMOs nanoparticles in paraffin oil have been evaluated on four ball tester machine. Figure 4 demonstrates the optimization result for the ZMO nanoparticles with different additive concentrations at 392N load; 1200rpm and for 60 min test duration. In absence of additive in the base oil, the mean wear scar diameter was found to be very large but in presence of ZMO nanoparticles it was fairly reduced at each concentration. As the concentration of ZMO nanoparticles in the base oil increases the reduction in the value of MWD also increases and it was found to be lowest at 1.0 % w/v. However, there is marginal increase in reduction of MWD at 1.0 % than that of 0.5% w/v. Therefore, 0.5% w/v was taken as optimized concentration and all the tribological tests were performed at 0.5% w/v concentration of ZMOs nanoparticles.

Figure 5 shows the changes in mean wear scar diameter (MWD) and average coefficient of friction in presence and absence of ZMOs nanoparticles in paraffin oil. The value of mean wear diameter (MWD) is much large in case of paraffin oil alone but in presence of different ZMOs nanoparticles it fairly reduces. In general, on addition of ZMOs nanoparticles to the paraffin oil both the friction coefficient and the MWD were significantly reduced. From the Fig.5, it can be clearly seen that the value of MWD and coefficient of friction significantly decreases for, ZMO(23nm), ZMO-1(34nm) and ZMO-2(39nm) but in case of ZMO-2a small increase in coefficient of friction (COF) is observed. The ZMO-2 having 39nm particle size, shows the increasing behavior in coefficient of friction values with

time (Fig.6). The smallest MWD and lowest coefficient of friction were found in case of surface lubricated with blend of ZMO nanoparticles (23nm) in base oil. This reveals that ZMO nanoparticles, used as additives, played a positive role in remarkably improving the tribological properties of paraffin oil.

Figure 6 shows the variation of coefficient of friction with sliding time at 392N applied load. The blends of ZMOs nanoparticles in paraffin oil show lower coefficient of friction values than the paraffin oil except ZMO-2. In general, coefficient of friction initially increases with time in all cases. After some time duration, the value of coefficient of friction reduces and it remains stabilized in case of ZMO and ZMO-1. However, the unusual trend of ZMO-2 may be due to its larger particles size and/or agglomeration. It was noted that ZMO-2 dispersed in paraffin oil tends to settle down after couple of hours, which reveals its poor dispersion stability. Under tribological conditions, the high pressure and temperature probably facilitate the agglomeration of ZMO-2 nanoparticles, resulting in high coefficient of friction values. This phenomenon is found to increase with the contact time.

The antiwear mechanism of the investigated additives may follow three different processes[8]: (i) the nanoparticles may melt, get welded on the shearing surfaces and react with sliding surfaces to form a tribofilm, (ii) or these may act as a third body on shearing surfaces i.e. like nano-bearings and (iii) or these may get tribosintered on the surfaces. From all the three possible mechanisms, these ZMOs nanoparticles may follow either nanobearings and/or tribosinterization mechanism at the steel-steel interface under operating conditions, minimizing metal-metal contact and thus friction and wear are reduced. Therefore, observed tribological behavior of ZMOs nanoparticles seems to be strongly size dependent, as given below.

ZMO > ZMO-1 > ZMO-2 > Paraffin oil

For determining wear rate, mean wear volume was calculated using Archard's equation based on elastic recovery.[11] The value of running-in and steady-state wear rate has been determined using linear regression model and their values are mentioned in Table 1. The lowest running-in and steady-state wear rate has been found in case of ZMO followed by ZMO-1 and ZMO-2.

3.1. Surface Characterization

The topography of the wear track has been studied by scanning electron microscopy (SEM) and Atomic Force Microscopy (AFM). Here for comparison of SEM images, ZMO nanoparticles is chosen which is better from all nanoparticles and paraffin oil. Figure 7 shows the SEM images of worn surface of steel balls under the lubrication of paraffin oil alone and ZMO nanoparticles at a load of 392 N for 60 min time duration. The MWD of steel ball lubricated with ZMO nanoparticles is notably smaller than the steel ball lubricated with base oil alone. The worn area lubricated with paraffin oil shows very deep scratches and groves illustrating metal-to-metal contact because of poor lubrication. The presence of ZMO in paraffin oil, improved the anti-wear property by reducing MWD compared to the surface lubricated with paraffin. The presence of shallow scratches and grooves on worn area indicates the role of ZMO nanoparticles as antiwear additives. The extent of surface smoothening in case of surface lubricated with ZMO nanoparticles is found to be much increased which filled the surface irregularities. Therefore, the new additives possess significant antiwear properties.

On comparing the plots in Fig.8, it has been found that the area as well as line roughness are extremely large in case of paraffin oil whereas these have magnificently reduced in presence ZMOs additives. A large differences in the average peak-valley height (2.63μm) is observed for the surface lubricated with paraffin oil alone whereas very small surface undulations are found in case of ZMOs (300-680 nm), Fig.8. Beside this, the value of

area roughness as well as line roughness has been found to be maximum for the base oil, however, these values are much lower in presence of ZMOs nanoparticles. Thus, the AFM-images also support the observed results of tribological tests.

4. Conclusion

Magnesium doped zinc oxide ($Zn_{0.92}Mg_{0.08}O$; ZMO) nanoparticles was synthesized by auto-combustion method and variation in particle size were made by increasing temperature. Formation of single phase was confirmed from the powder-XRD data of the different sized ZMOs nanoparticles. The average crystalline size of these nanoparticles was found to be 23, 35 and 39 nm for ZMO, ZMO-1 and ZMO-2, respectively. These blends effectively enhance the antiwear properties in base oil in order of decreasing particles size. ZMO nanoparticles as additives in paraffin oil exhibited excellent friction-reduction and anti-wear behavior. The running-in and steady-state wear rates of ZMOs nanoparticles have been found to be much lower than paraffin base oil. On the basis of observed tribological parameters, SEM and AFM results, it was inferred that addition of ZMOs nanoparticles significantly improved tribological characteristics of the paraffin oil by acting as nanobearing and/or tribosintering. Surface analysis by SEM and AFM also supports the observed tribological behavior of ZMOs nanoparticles.

Acknowledgement

One of the authors, Ms. Kalyani is thankful to CSIR-New Delhi, India for financial assistance as Senior Research Fellowship. The authors are thankful to the Head, Department of Metallurgical Engineering, Indian Institute of Technology (Banaras Hindu University) Varanasi, India for providing TEM with EDX and SEM facilities.

References

1. He, Z., Rao, W., Ren, T., Liu, W., Xue, Q. (2002), *Tribol. Lett*., 13, 87-93.
2. Spikes, H. *Tribol. Lett*., (2004), 17, 469-489.

3. Isaksson, M., Frick, M., Gruvberger, B., Ponten A., Bruze, M. (2002), *Contact Dermatitis*, 46, 248-249.
4. McFall, D. (2004**)**, Automakers Push 'Start' Button on GF-5 Oils. *Lube Report*, 4.
5. Kalyani, Jaiswal, V., Rastogi, R.B., Kumar, D. (2014), *RSC Adv.*, 4, 30500-30510.
6. Jaiswal, V., Rastogi, R.B., Kumar, R., Singh L. and Mandal, K.D. (2014), *J. Mater. Chem. A.*, 2, 375-386.
7. Astruc, D., Boisselier, E., Ornelas, C. (2010), *Chem. Rev*., 110, 1857-1959.
8. Battez, A.H., Gonzalez, R., Viesca, J.L., Fernandez, J.E., Fernandez, J.M.D., Machado, A., Chou, R., Riba, J. (2008), *Wear,* 265, 422-428.
9. Rapoport, L., Leshchinsky, V., Lapsker, I., Volovik, Yu., Nepomnyashchy, O., Lvovsky, M., Popovitz-Biro, R., Feldman, Y., Tenne, R.(2003), *Wear,* 255, 785-793.
10. Jaiswal, V., Kalyani, Rastogi, R.B. and Kumar, R. (2014), *J. Mater. Chem. A.*, 2, 10424-10434.
11. Sethuramiah, A. (2003), Lubricated wear science and technology, Tribology Series, Vol.42, Elsevier.

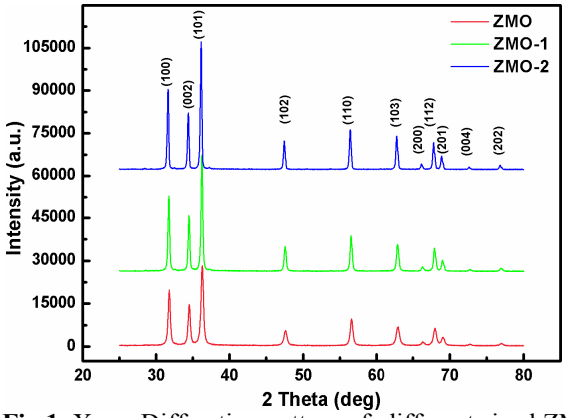

Fig.1. X-ray Diffraction pattern of different sized ZMOs nanoparticles

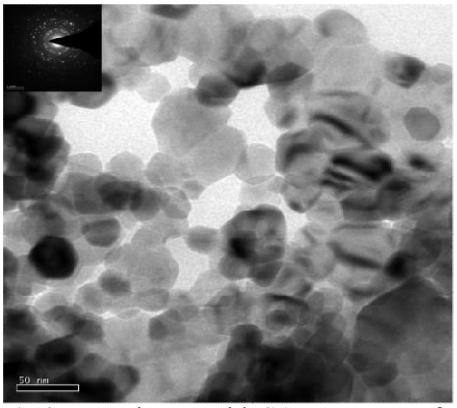

Fig.2. TEM-image with SAED pattern of ZMO nanoparticles

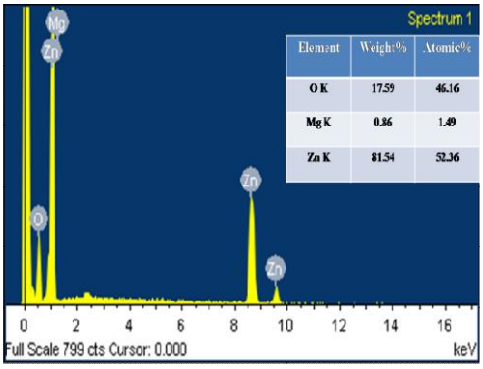

Fig.3. Energy dispersive X-ray spectrum showing constituents and chemical composition of ZMO nanoparticles

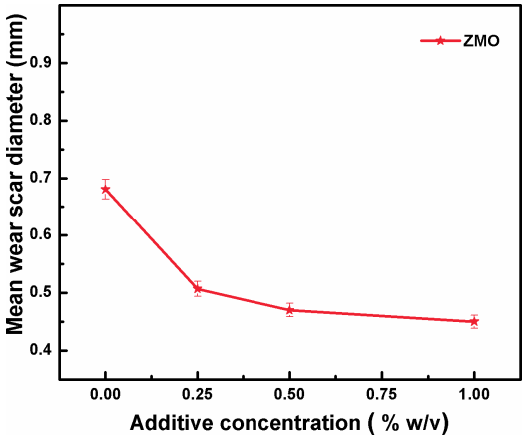

Fig.4. Variation of MWD for the paraffin oil as a function of increasing ZMO concentrations at 392N applied load for 60 min duration

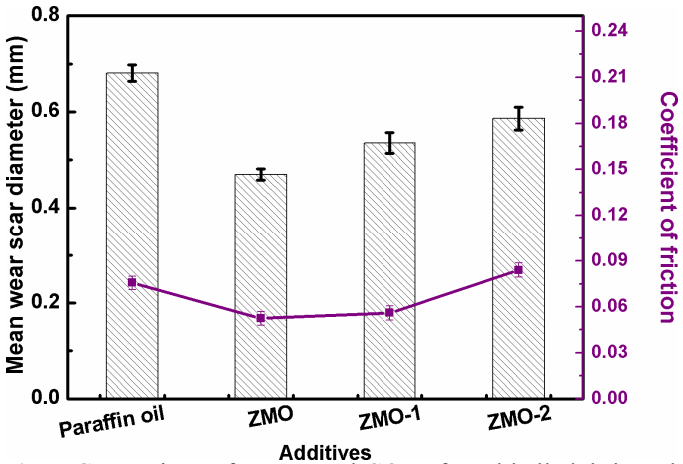

Fig.5. Comparison of MWD and COF of steel balls lubricated with 0.5 w/v % of ZMOs in paraffin oil at 392 N; rotating speed, 1200rpm; temperature, 75°C; test duration, 1 h

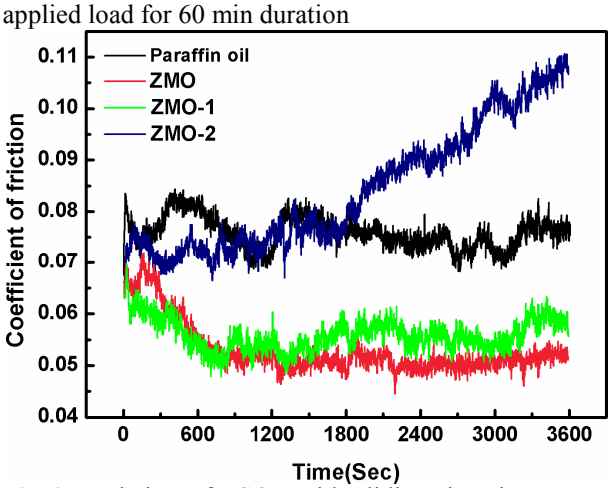

Fig.6. Variation of COF with sliding time in presence and absence of ZMOs additives (0.5 w/v %) in paraffin oil at 392N; rotating speed, 1200rpm; temperature, 75 °C; test duration, 1 h

Fig.7a

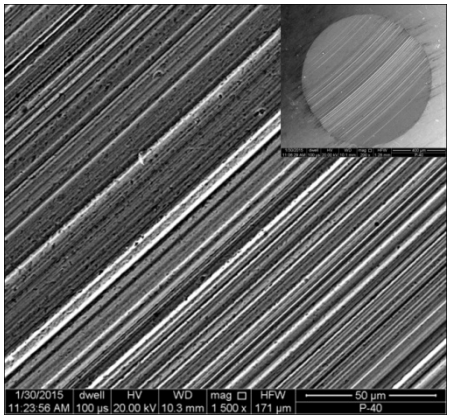

Fig.7b

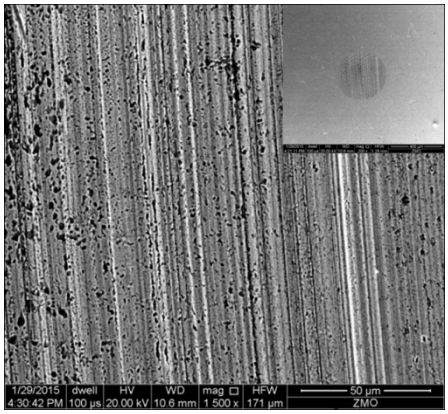

Fig.7. SEM micrographs of the worn steel surface lubricated with (a) Paraffin oil and (b) ZMO nanoparticles (0.5% w/v) in paraffin oil for 60 min test duration at 392N applied load

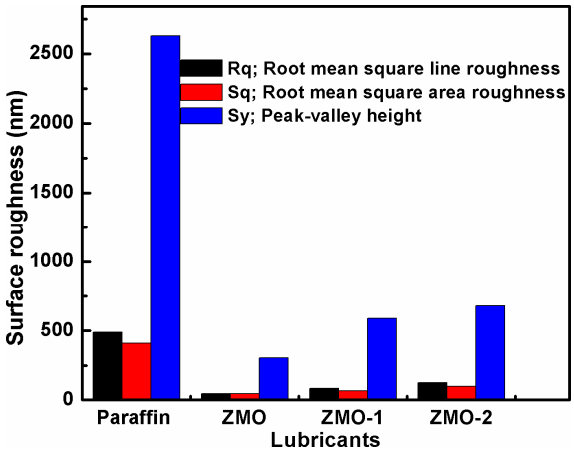

Fig.8. Surface Roughness parameters obtained from digital processing software of Nanosurf basic Scan 2 for different additives at 392N load for 60 min test duration

Table 1. Wear rates of paraffin oil in absence and presence of ZMOs nanoparticles as antiwear additives at 392N applied load for 90 min test duration

S.N.	Additives	Wear Rate (10^{-4}x mm^3/h)	
		Running-in	Steady-state
1.	ZMO	39.6	06.88
2.	ZMO-1	40.8	15.56
3.	ZMO-2	54.58	21.16
4.	Paraffin oil	69.99	38.88

Synthesis and characterization of bioactive glass-kalsilite composite for dental veneering

Author Name: Pattem Hemanth Kumar [a] and Vinay Kumar Singh [a]* Pradeep Kumar [b]

Affiliation: [a] Department of Ceramic Engineering, Indian Institute of Technology (BHU), Varanasi, India.

[b] Department of Chemical Engineering, Indian Institute of Technology (BHU), Varanasi, India.

Corresponding Author: Dr. Vinay Kumar Singh

E mail: vinaycer@gmail.com

ABSTRACT

A kalsilite glass-ceramic composites have been prepared by mechanochemical synthesis process for dental veneering application. The aim of the present study is to prepare bioactive kalsilite composite material for application in tissue attachment and sealing of the marginal gap between fixed prosthesis and tooth. Mechanochemical synthesis is used for the preparation of microfine kalsilite glass ceramic. Low temperature frit (LTF) and bioglass have been prepared using traditional quench method. The kalsilite composites aims to form a bioactive surface with the periodontal tissue attachment. Thermal, microstructural and bioactive properties of the composite material have been examined. The feasibility of the kalsilite to be coating on the base commercial opaque as well as the bioactive behavior of the coated specimen have been confirmed.

Keywords

Mechanochemical synthesis; Composite; Glass ceramics; Coating; Simulated body fluid; Dental ceramic

1. INTRODUCTION

Ceramic-metal restorations is a beauty of porcelain and strength of a metal substructure. Metal/ceramic alloys are being challenged by manufacturers of frequent low cast alloys which exhibit superior physical properties for their products [1-3]. However, during the past few years, the technologic parameters of dental ceramic alloys have been changed. Bioactive dental materials has been developed over the last decades [4]. They have abilities to develop an efficient attachment between the fixed soft periodontal tissue and prosthetic restorations [5]. Ceramic materials are regularly used in dental restoration which have specific properties such as similarity with natural tooth structure, wear resistance, high mechanical strength and durability in the oral environment. The main problem that occur with the patient's that the secondary caries and cement dissolution, resulting in the marginal gap between the existing tooth and restoration [6-7]. This causes a bacterial attack leading to pulp irritation or necrosis and finally remove the prostheses [8]. Alteration in this marginal gap leads to increase in the cell attachment and proliferation without affecting the physico-chemical and mechanical properties [9]. It can decrease or eliminate cement dissolution and prevent the bacterial adhesion on the cement surface [10].

The present work has been carried out to introduce a successful process for the fabrication of bioactive kalsilite glass ceramic composite materials with required characteristics for dental applications. Especially for porcelain fused to metal system (PFM) used for crown, bridges etc. In this work, bioactive glass and kalsilite based porcelain were prepared using a traditional melt-quenching method and mechanochemical route respectively [2]. This new composite material expected to has good thermal, bioactive and mechanical properties.

2. EXPERIMENTAL PROCEDURE

2.1 Preparation of kalsilite, bioglass and low temperature frit (LTF)

K_2CO_3, Al_2O_3, and SiO_2 were weighed in a stoichiometric ratio of kalsilite (1:1:1). The mixture was pulverized for 6 h in a high-energy planetary ball mill and fired at 1000 °C as reported in our previous work. The composition of bioglass were taken in a proportion of 45 wt. % SiO_2, 24.5 wt. % CaO, 24.5 wt. % Na_2O and 6 wt. % P_2O_5. These materials were mixed in an agate mortar for homogeneous mixing. Mixture was melt in a platinum crucible at 1400 °C for 1 h. The molten glass was quenched in water and dried at 110 °C for 2 hours in an electric oven. Dried powder was then pulverized to pass a 350 BSS mesh [3]. LTF was also prepared in the same manner.

2.2 Preparation of kalsilite composites

Composites were prepared by mixing 40 wt. % kalsilite, 45 wt. % bioglass and 15 wt. % LTF. Composition of COP-1 and COP-2 (as given in Table.1) were choose on the basis of different optimizations, which include glossiness of the surface, thermal expansion and translucency. Batch was ground in a planetary ball mill for 5 minutes to get a homogenous mixture. This ground material was further pelletized using a uniaxial hydraulic press by applying a load of 200 MPa. These pellets were heat treated at 960 °C with a heating rate of 80 °C/min using a VITA VACUMAT 40T according to a standard dental veneering firing cycle pre-programmed by VITA under vacuum. Vacuum was introduced at 500 °C and released at 960 °C.

The bonding of CMP-1 and CMP-2 coating materials was analysed on a substrate made of opaque, (from VITA VMK 95 1M2 opaque Product no. B330212, VITA Zahnfabrik, Bad sackingen, Germany). The substrate powder was pelletized in a

similar manner by heating at 960 °C. Veneer material were prepared by mixing of both composites (CMP-1 and CMP-2) in a modeling liquid with powder to liquid ratio of 0.3 to make a thick slurry. It was then spread manually using a spatula on the substrates. These specimens were fired up to 960 °C using VITA VACUMAT 40T.

2.3 Characterizations

2.3.1 Phase identification and microstructural analysis

X-ray diffraction of the composite (before and after heat treatment) was carried out using a portable XRD (Rigaku, Japan) employing Cu Kα radiation with Ni filter operating at 30 mA and 40 kV. Diffraction peaks were analyzed using standard JCPDS file (PDF-2 database 2003). Micrographs of the fractured sample were recorded using scanning electron microscope (SEM) (INSPECT 50 FEI).

2.3.2 Coefficient of thermal expansion (CTE)

CTE and the glass transition temperature (Tg) of the composite material were examined using a dilatometer (supplied by VB Ceramic Consultants, India). For CTE measurements, material was compacted into a rectangular bar (50×10×10 mm) using a uniaxial hydraulic press by applying a load of 200 MPa followed by heat treated up to 950 °C with heating rate 80 °C/min (according to manufacturer's instructions).

2.3.4 Preparation of SBF

SBF solution was prepared by dissolving analytical reagent grade NaCl, KCl, NaHCO3, MgCl2.6H2O, CaCl2 and KH2PO4 in double distilled water and buffered at pH 7.25 with trishydroxylmethyl aminomethane (TRIS) and 1N HCl at 35-37 °C. Its composition is given in Table 1 and it compared with the ionic concentration of human blood plasma [11].

2.3.5 Bioactivity test

The formulated composites has been veneered on the surface of the substrate to study its bioactivity and surface morphology. Furthermore the hydroxyapatite forming ability and adherence to the interface were also studied. The hydroxy apatite forming ability of the coated specimens ware observed through immersion in simulated body fluid (SBF). For these testing, three specimens of dimensions 10 mm diameter and 2 mm thickness were prepared and immersed in SBF (40 ml) for 7 and 21 days. At the end of all selected time period, samples were separate from the SBF solution, rinsed with distilled water and dried for further analysis. SBF treated samples were examined by SEM and FTIR to evaluate the possible formation of a hydroxyapatite (HAp) layer on the material surface, as a marker of bioactive behavior.

3.0 RESULTS AND DISCUSSION

3.1 Phase analysis

Figs. 1 and 2 shows the XRD pattern of both kalsilite composites before and after firing. Before firing kalsilite was detected to be only a crystalline phase along with the some amorphous phase. Furthermore Na_2O. SiO_2 phase has been found as a crystalline phase in both CMP-1 and CMP-2 after firing along with kalsilite as a major phase. This may form due to presence of some free Na_2O and SiO_2 components in the matrix.

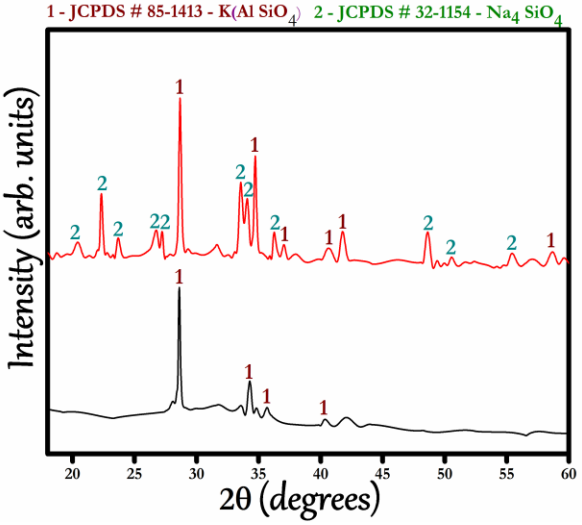

Fig. 1. XRD patterns of kalsilite composite before and after heat treatment

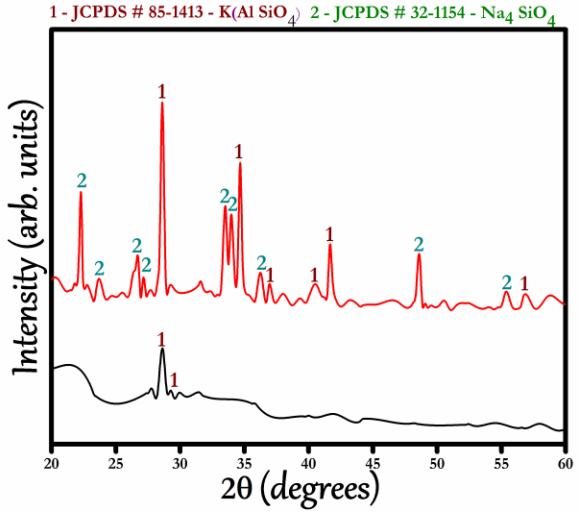

Fig. 2. XRD patterns of kalsilite MgF_2 composite before and after heat treatment

3.2 Coefficient of Thermal Expansion (CTE)

Thermal expansion is the furthermost important essentials for veneering glass-ceramic fused to metal restorations. When a dental ceramic is used on a substrate, then CTE must be exact to confirm good attachment of the dental prosthesis. There is a possibility of formation of the cracks if a mismatch among the CTE of the ceramic coating and the substrate exist. Fig. 3 shows the result of CTE curves of kalsilite composites. Values of CTE and glass transition (Tg) of the composites have been found to be 15.9×10−6 /°C and 535 °C for CMP-1, 15.6×10−6 /°C and 545 °C for CMP-2.

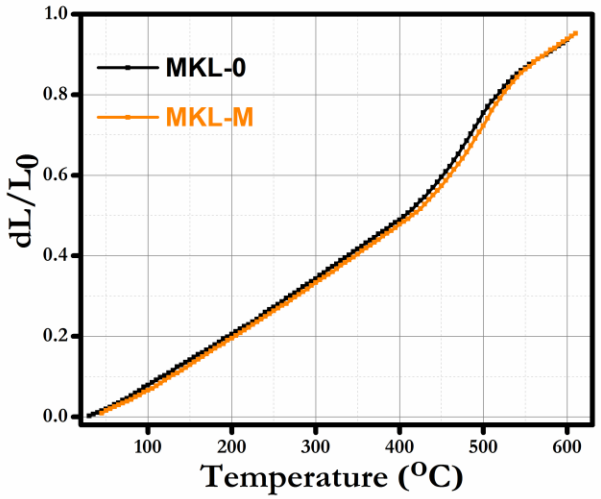

Fig. 3. CTE curves of kalsilite composites MCL-1

A high CTE of ceramic is required to assure a good bonding with the substrates. The existence of kalsilite phase in composite material causes an increase in the CTE value. Kalsilite has a high CTE value which improve the whole CTE of the dental ceramic and consequently thermally compatible with the substrates.

3.3 Interface layer

Fig. 4 and 5 shows the surface morphology of interface layer between the composite and the substrate (composite coated on commercial vita opaque substrate). This morphology is a confirmation of qualitatively good bonding between the composite and substrate. There are no cracks or peeling off or gap present in the interface region. This confirms that the CTE of composite and substrate are well coordinated.

3.4 Bioactivity in SBF

Kalsilite composite samples immersed in SBF solution has been analyzed with SEM and FTIR. Immersed in SBF led to formation of a HAp layer on the surface of the samples. Fig. 6 and 7 shows the development of HAp layer on the surface of the samples after immersing in SBF solution for 7 days. In FTIR (Figs. 8 & 9), strong peaks corresponding to stretching vibrations of PO_4^{-3} bond have been appeared in the range of 1150–900 and 650–500 cm^{-1}. This is the indication of the formation of hap layer on the surface of the sample after immersion in SBF for 7 days at 37 °C. The low intense peaks have been observed in the range 1500–1400 cm^{-1} which indicates the presence of CO_3^{-2} molecules in the sample. There is also a peak at 450 cm^{-1} allocated to the bending vibration mode of Si-O bond. The results of SEM is also in conformity with the results of FTIR. The thickness of hydroxyapatite layer increases with increasing the immersion time.

Composites	Kalsilite	Kalsilite MgF_2	Bioglass	LTF
CMP-1	40	-	45	15
CMP-2	-	40	45	15

Table-1 Batch composition of composites

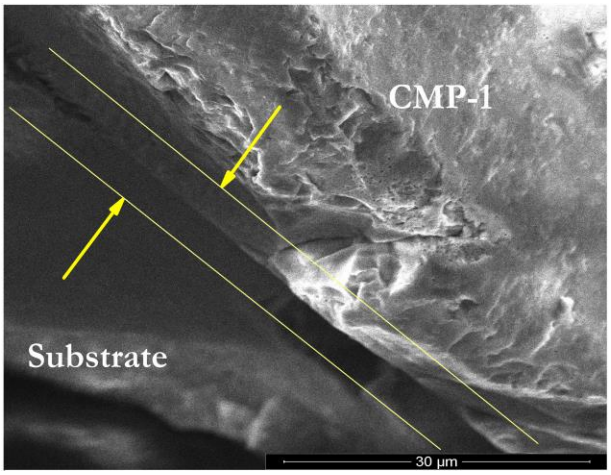

Fig. 4. SEM image of the fracture surface of CMP-1 interface of coated on subtract.

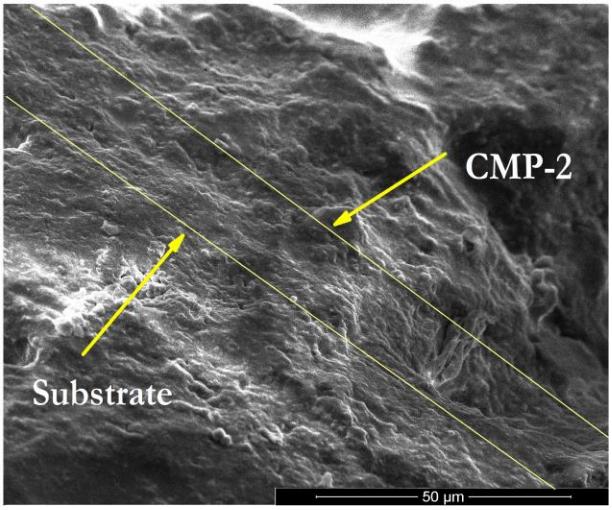

Fig. 5. SEM image of the fracture surface of CMP-2 interface of coated on subtract.

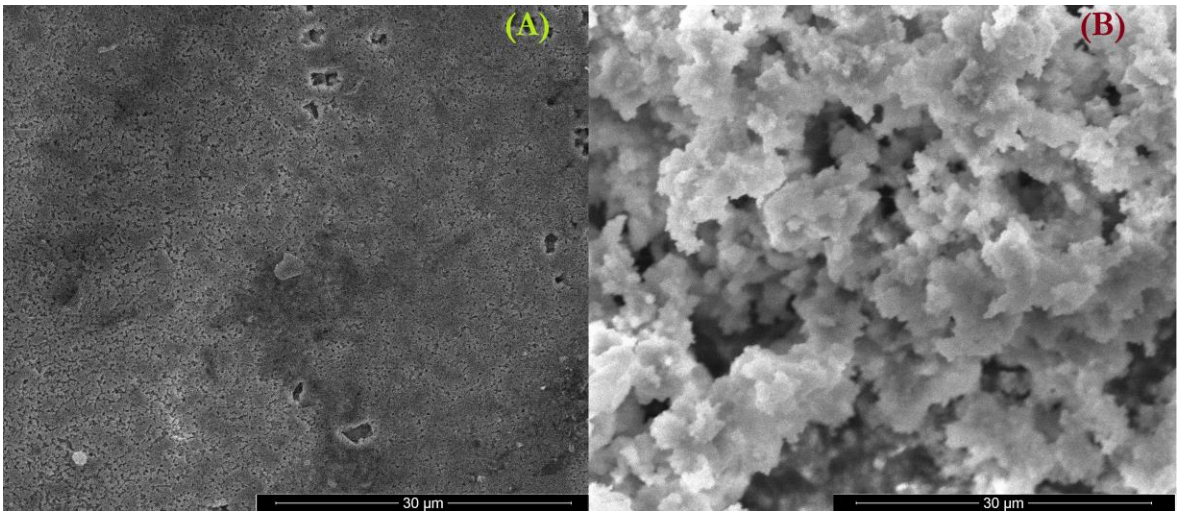

Fig. 6. SEM pictures of the CMP-1 (A) before and (B) after immersion for 7 days in SBF solution, presenting hydroxy apatite formation.

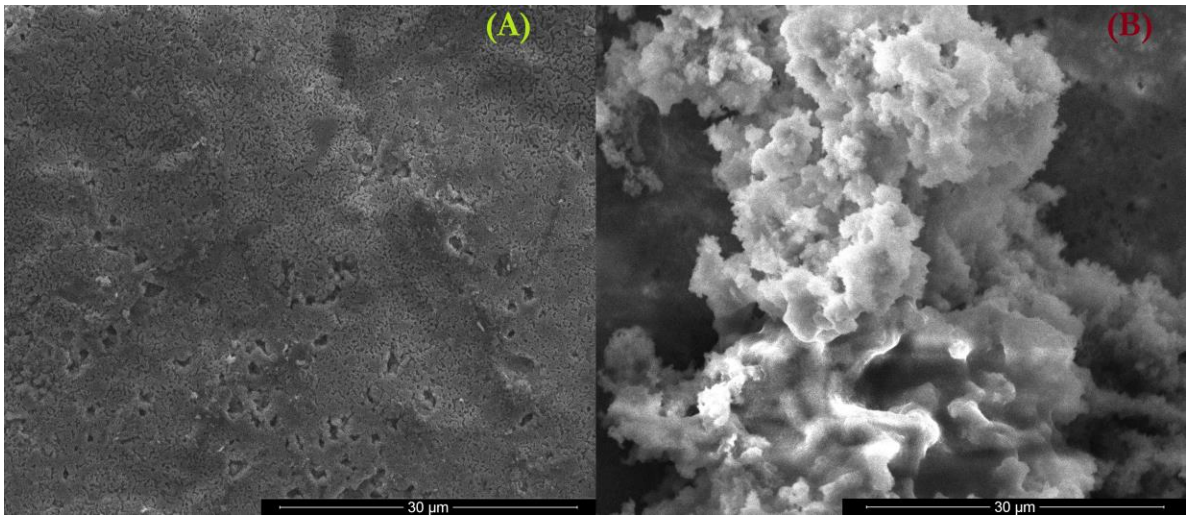

Fig. 7. SEM pictures of the CMP-2 (A) before and (B) after immersion for 7 days in SBF solution, presenting hydroxy apatite formation.

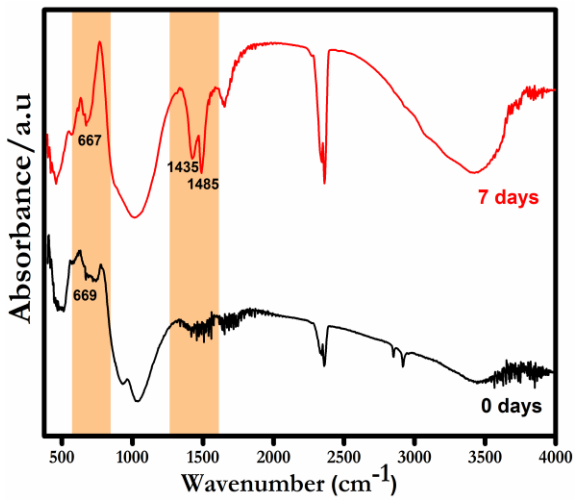

Fig. 8. FTIR Absorbance bands of the CMP-1 before and after immersion in SBF solution for 0 and 7 days.

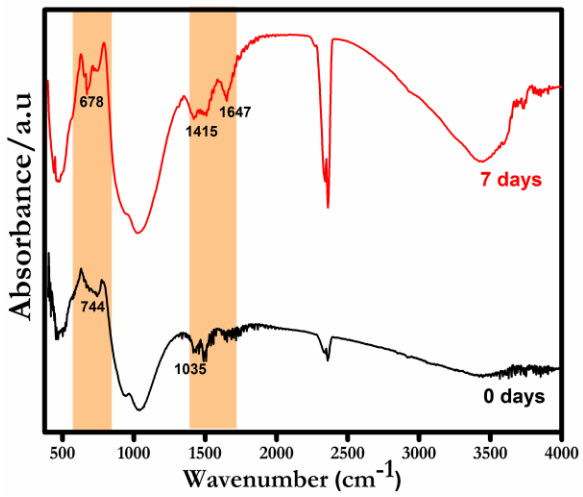

Fig. 9. FTIR Absorbance bands of the CMP-2 before and after immersion in SBF solution for 0 and 7 days.

4. Acknowledgement

The authors gratefully acknowledge the financial support of DST [(TDT Division), Reference No. DST/SSTP/UP/197(G) 2012], Ministry of Science & Technology, New Delhi, India.

5. REFERENCES

[1]. Mclean JW and Sced IR, 1973. The gold alloy/porcelain bond. *Trans Br. Ceramic Soc*. 5 (1973), 229-238.

[2]. Kumar PH, Srivastava A, Kumar V, Jaiswal N, Kumar P and Singh VK, 2014, Role of MgF_2 addition on high energy ball milled kalsilite: implementation as dental porcelain with low temperature frit. *Journal Advanced ceramics* 3 (August. 2014), 332-338.

[3]. Kumar PH, Srivastava A, Kumar V, Sharma S, Singh H, Kumar P, and Singh VK, 2014, Role of CaF_2 on mechanochemically synthesized leucite as dental veneering glass ceramics. *Advances in Applied Ceramics*. 114 (September. 2015) 107-113.

[4]. Chatzistavrou X, Esteve D, Hatzistavrou E, Kontonasaki E, Paraskevopoulos K and Boccaccini AR, 2010, Sol– gel based fabrication of novel glass-ceramics and composites for dental applications. *Mater. Sci. Eng., C*. 30 (March. 2010) 730-739.

[5]. Chatzistavrou X, Tsigkou O, Amin HD, Paraskevopoulos K, Salih V and Boccaccini AR, 2012, Sol–gel based fabrication and characterization of new bioactive glass–ceramic composites for dental applications. *J. Eur. Ceram. Soc*. 32 (May. 2012), 3051-3061.

[6]. Ahmed Al-Noaman, Simon C.F. Rawlinson and Robert G. Hill, 2013, Bioactive glass-stoichiometric wollastonite glass alloys to reduce TEC of bioactive glass coatings for dental implants. *Mater. Lett*. 94 (December. 2013), 69–71.

[7]. M. Kokoti, A. Sivropoulou, P. Koidis and P. Garefis, 2001, Comparison of cell proliferation on modified dental ceramics *J. Oral Rehabil*. 28 (September. 2001), 799-804.

[8]. E. Kontonasaki, A. Sivropoulou, L. Papadopoulou, P. Garefis, K. Paraskevopoulos, P. Koidis, 2007, Attachment and proliferation of human periodontal ligament fibroblasts on bioactive glass modified ceramics. *J. Oral Rehabil*. 34 (January. 2007), 57-67.

[9]. S. Pitaru, H. Tal, M. Soldinger, A. Grosskopf, M. Noff and J. Periodont, 1988, Partial regeneration of periodontal tissues using collagen barriers. Initial observations in the canine. 59 (June. 1988), 380-386.

[10]. Meijering AC, Creugers NH, Roeters FJ and Mulder J, 1998, Survival of three types of veneer restorations in a clinical trial a 2.5-year interim evaluation. *J Dent*. 26 (September. 1998), 563-568.

[11]. Kokubo T and Takadama H, 2006, How useful is SBF in predicting in vivo bone bioactivity. Biomaterials. 27 (May. 2006) 2907-2915.

Nanopore Formation by Controlled Electrical Breakdown: Efficient Molecular-Sensors

S. Abdalla, F. M. Al-Marzouki, and A.M. Abdel-Daiem
Department of Physics, Faculty of Science, King Abdulaziz University Jeddah, P.O. Box 80203, Jeddah 21589, Saudi Arabia

Abstract

Controlled electrical breakdown is used in order to produce efficient nanopore sensors. This phenomenon can be used to precisely fabricate these nanopore-sensors through membranes of polydimethylsiloxane micro-arrays. This can be carried out when localizing the electrical potential through a suitable microfluidic channel. Organic molecules such as DNA and different protein-molecules can be easily and precisely detected using this procedure: Controlled electrical breakdown technique.

Introduction

Detecting the presence of a single organic molecule has attracted the interest of researchers with recent techniques based on the production of nano-pores. It is widely used nowadays to get precise results [1, 2]. This is achieved when applying external electric field on an ultra-thin aperture (nano-scale) which lies on an insulating membrane. This membrane is submerged in an ionic electrolyte [3]. Organic molecules such as DNA and proteins can be electrophoretically forced to move towards certain nanopores (NPs) [4- 6]. The driven motion results in net variation in the electrical conduction which leads to exact data concerning the driven molecule; in particular charges deposited on it, its length, size, shape etc. In addition, some studies have shown that this technique is applicable to DNA-sequencing [7], protein unfolding [8] and detection [9]. Good mixing of protein aqueous pores in lipid bi-layer-membranes can form active nano-pores [10]. However, because lipid the bi-layer-membranes have very weak mechanical properties, the applied voltages to the pores are limited and thus the application of this method is limited. But solid state nano-pores are more robust within wider ranges of application conditions: Temperature, electric field, pH, etc [11, 12]. Solid state nano-pores have more tendencies to combine with molecular electronic devices inside a strong lab-on-ship device [13]. Zhao et al [13] have presented multiple scenarios to embedding nano pores through different microfluidic systems. In general, using high energy electron (or ion) beams through ultra-thin nano dielectric membrane gives good NPs [14]. In addition, focused ion beam or tunneling electron microscope leads to different integration-problems because a nanopore should be fabricated before integrated in micro channel (MC). This makes a real need to a strictly correct the line-of-sight aligned through the whole device. In general, the typical procedures for nano-devices techniques base on the creation of NPs through wet environment are difficult with high vacuum techniques. Different authors have recently shown another possible solution for this technique: controlled electrical breakdown [15, 16]. Sufficiently high electric field is applied to an insulating membrane through 1 M KCl leads to immediate fabrication of single nanopore with about one nanometer diameter [17, 18]. The presented technique is normal based on integration of nanopore sensors through complicated micro-devices and may be up to lab-on-chip devices. We propose, in this study, a nano-device containing five times one array of solid state NPs and when handling the electric breakdown in each polydimethylsiloxane MC independently, leading to certain localization of electric field on certain domains of a single SiNx- membrane. Along the extent of all MCs the whole membrane is extend in the presence of a solution, then another one which has only a tinny domain of the membrane is open. The noise features within the device is characterized to validate the incorporation of NPs to the micro-device in order to detect the translocation of the organic molecules.

Method and Experimental Procedure

On 3 mm-frame size commercial Si-wafer, 20 nm-thick thick SiNx-membrane has been installed between arrays of PDMS-MCs. The present devices have used geometries having at least 5-MCs installed on one side of the membrane; however, the proposed device gives the possibility to have another single-common MC access the other side as shown in figures 1: (a, b, c, d). Figures 1-a and 1-b show arrangement of 5- MCs having a broad two hundreds micrometers wide and fifty micro-meters height placed on the membrane to about fifteen micrometer width.

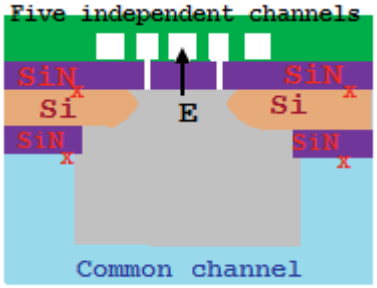

Fig. 1a

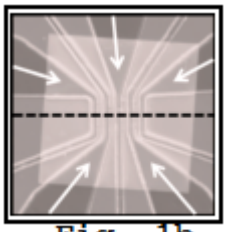
Fig. 1b

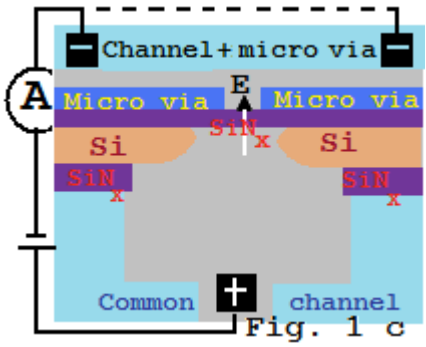

Fig. 1 c

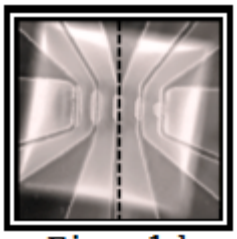
Fig. 1d

Fig. 1: (a) and (c) 5channels device Micro-via layer is added to the micro-channels which fix the electric field and charge in the solution to a well definite domains on the membrane (scale is not conserved). Symmetrical electric field can be produced in the micro channels when adding another similar electrode which is illustrated by dashed-line in fig 1-c. (b) and (d) 5 micro channels constructed on a SiNx membrane which is isolated by an insulator layer; the bleck dashed line represents the direction of the cross sectional views in (a) and (c).

The separation distance between channels is twenty fife micrometers. The other device shows has been designed in order to control nano pore creation by controlled electric breakdown through every microfluidic channel. By this configuration the area has been kept minimum in which allows more reduction of electrical noise through the ionic solution. In the other device, a 200µm-layer of PDMS, two hundred micro meter thick layer of PDMS is combined with an arrangement of apertures with length 40 µm < L < 120 µm has been utilized in order to create suitable microfluidic vias that connects the micro-channels to a fix and well known domain at middle of the membrane which is illustrated in figures 1-c and 1-d. The PDMS layer is, then, linked to the arrangement of 5-microchannels, in addition to the principal channel. About three mm-thick layers of PDMS with 250 micrometer x 100 micrometer high fluidic channel is oxygen-plasma bonded to a glass-wafer, in all devices. Also, 2 mm aperture has been punched within the principal bottom micro-channel to permit fluidic entrance. To smooth and to compensate for the Si-thickness, a 100 micro meter thick PDMS layer has been spin-coated near the chip. On a hot plate, the PDMS layer has been crud at eighty Centigrade foe about on half hour. Different holes have been punched to ensure silver/silver-chloride electrodes to permit electrical and fluidic rapid movements within the channels. The electrical conductance of the MC lies in the range 10-5 (ohms)-1 in M KCl solution when placing the electrodes about 5-mm from the center of the membrane. In order to reduce the MC hydrophobicity, the whole device has been faced to oxygen plasma at 70 watts for about 300 seconds [19]. Figures 1-a and 1-b illustrate a discipline of 5-MCs, two hundred micrometer wide times fifty micrometer height acuminate at the membrane till about fifteen micrometers. These MCs are completely independent and they are disconnected by about twenty five micrometer apart. In another device-configuration, the microfluidic channels have been planned in order to control the nanopore formation by the electrical breakdown in the middle of the membrane. By this configuration, the noise has been minimized by reducing the area of membrane exposed to the electrolyte. Here, a layer of polydimethylsiloxane has been used in order to produce to form micro fluidic vias which can connect the different MCs as it is illustrated in figure 1-c and 1-d. The configuration of 5-MCs has been then bonded to the polydimethylsiloxane layer.

Polyethylene has been used to link the MCs to sample; then pressure has been used to initiate the flow. Under a suitable applied voltage of about 0.2 volts < V < 1 volt, the validity of device has been tested and effective sealing between MCs is more than ten Giga ohms. This has been achieved when measuring ionic current between MCs with one mole potassium chloride solution.

Results and discussion

Applying controlled external electric field to each of the channels found on the membrane allows the formation of controlled breakdown that creates individual NPs. For example, 10 volts up to 14 have been applied to MCs creates NPs in some seconds or one minute. Leakage electrical current has been formed through the SiNx-membrane-membrane-membrane due to the application of that external potential and the creation of nanopore is found, during 0.1 second, when an abrupt increase of this leakage current occurs. To get the desired nanopore size, one can vary and control both the applied electric potential and the response time. Following the electric breakdown, the creation of nanopore is repeated several times on a single membrane but found at channels. To verify the validity of the device, sensitive experimental characterization data have been carried out compared with a suitable low

noise amplifier : Axopatch 200B (Molecular devices). In addition, to get more fine NPs, one has applied an ac-electric signal with amplitude 5 volts across the membrane which has minimized the electrical noise and re-install nanopore to be ready for another use. The electrical resistance of nanopore is so sensitive to the pore diameter which depends on the initial value of the breakdown. This resistance has been estimated in electrolyte by measuring the ionic current within the nanopore when sweeping the external voltage between negative 0.2 volts and positive 0.2 volts. Following the work of Kowalczyk et al [20], we consider the nanopore to be as a cylinder of effective diameter d which could be estimated from its conductance considering the following [20]

$$G = \sigma\left(\frac{4L}{\pi d^2} + \frac{1}{d}\right) \qquad (1)$$

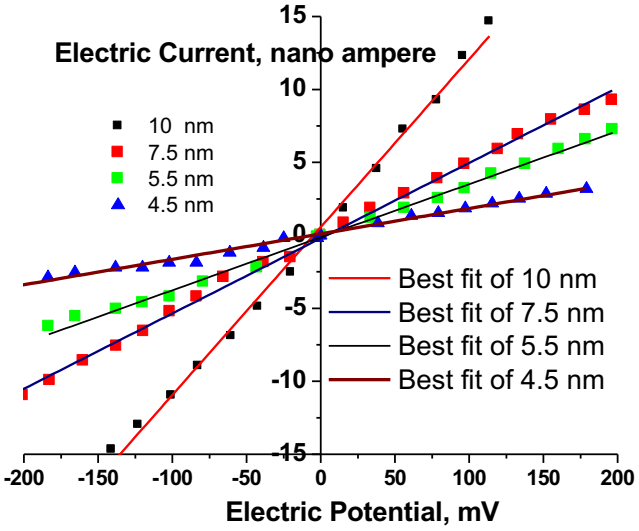

Fig (2) *I- V*: Current- voltage characteristics is illustrated which lead to estimation of nanopore radius when application a model of electrical conduction through a single device containing 5-micro channels. Symbols represent experimental data for different nanopore radius: 10nm, 7.5nm, 5.5nm, 4.5nm; while lines are for best fitting value after equations (2-a, -b, -c, -d).

Here, σ is the electrical conductivity of the solution (electrolyte) and L is the active-length of the nanopore-bulk which is considered to be equivalent to the thickness of the SiNx-membrane. Fig (2) shows the current – voltage characteristics in 1 M KCl solution which claims an ohmic behavior with pH value around 7.5. The corresponding electrical conductivity is ~ 10 Ω^{-1} cm^{-1} for the examined five NPs. The size of these NPs lies in the range between 3 nm and 10 nm (within the five examined channels). The experimental data shown in figure (2) lead to an empirical equation that gives the best fit to experimental results in Fig (1) as following:

For 10.0 nm nanopore: $I = 0.569 + 0.115V$ (2-a)
For 7.50 nm nanopore: $I = -0.19 + 0.0516V$ (2-b)
For 5.50 nm nanopore: $I = -0.12 + 0.0363V$ (2-c)
For 4.50 nm nanopore: $I = 0.10 + 0.01746V$ (2-d)

The strict linear behavior of I- V curves reflects the ohmic behavior of the electrical conduction within the nanopore. These four empirical relations give an electrical conductance G (Ω^{-1}) as a function of the nanopore diameter (d) as following:

G (Ω^{-1}) = 0.12 + 0.035 d (3)

Briggs et al [21] have shown that the estimated nanopore diameter has an accuracy error about 0.5 nm due to the surface charge which is ignored in equation (1); while the accuracy of both solution electrical conduction and membrane thickness is ~ 0.3 nm. It is worth mention that the high dielectric values of the device controls the electrical noise arising at higher frequencies while noises arising at lower frequencies are typically of the type-1/f [22, 23]. So, it is important to minimize the area disclosed to the electrolyte to reduce noise in high frequency range. This ameliorates, also, the ratio signal/noise ratio at high bandwidth [24, 25]. Figures 1a and 1b show a comparison between the five channel devices with and without micro paths. It is worth noting that when inserting nano-pores using the above mentioned technique, one should take into account the architecture of the microfluidic design as the electrical characteristics are very sensitive to the design. Also, protein samples have been detected and even captured by nano pores integrated in microfluidic channels which have no micro-via. The net efficiency of the process has been notably decrease when using micro channels with no output path. More than thousand bio molecular activities can be detected by the present device. Faradic effects play, also, some role in the electrical conduction through the membrane. This has been noticed when replacing the electrodes we did not have the same experimental data. This is due to asymmetry in the electric potential at the membrane which affects the field in the micro fluidic channel. One can, also think about some additional charges lies at the edge of the membrane; because an area which is stress in excess on bonding against layer of polydimethylsiloxane (not far from the silicon support region). The electric charges lay in this area prevent the translocation of polymers rich in electric charges and on the same time permits

the cross of polypeptides which are poorer in electric charges. Nanopore should be fabricated in such a way that it should be in the membrane-center in order to be far from edges. This increases the device efficiency and allows more symmetrical electric field at the center of device. By this technique, DNA molecule precisely can be detected in a pH 10-solution. Moreover, the asymmetry of the electric field can be highly decreased when using pairs of electrodes biased from the same external electric source, in the top independent channels which lay on either side of the membrane. By this scenario, five out of six devices tested in pH 8 can detect minimum one thousand activities of bio molecular translocation incidents.

Conclusions

Controlled electrical breakdown has been successfully used to fabricate solid-state NPs are using many-sided scenarios with different microfluidic mediums. The main feature of our work is the integration of NPs into lab-on-ship micro/nano-system which highly stretched the fabrication/assembly techniques. Different microfluidic paths with different microfluidic channels increases the sensibility and efficiency of device also, it decreases the electrical noise when using high-bandwidth. In addition, the diversity of uses increases when sharing a common micro channel with a system of discipline of NPs; in particular when a priceless protein is drove to the common channel with different NPs (with different size and / or different functions i.e. either in parallel or in series). This architecture allows detecting several samples on the sample time using the different micro channels

References

[1] del Rio Martinez JM1, Zaitseva E, Petersen S, Baaken G, Behrends JC., Automated formation of lipid membrane microarrays for ionic single-molecule sensing with protein NPs., Small. 2015 Jan 7;11(1):119-25. doi: 10.1002/smll.201402016. Epub 2014 Aug 13.

[2] Wenhong Li, Nicholas A. W. Bell, Silvia Hernández-Ainsa, Vivek V. Thacker, Alana M. Thackray, Raymond Bujdoso, and Ulrich F. Keyser, Single Protein Molecule Detection by Glass NPs, ACS Nano, 2013, 7 (5), pp 4129–413, DOI: 10.1021/nn4004567

[3] Silvia Hernández-Ainsa and Ulrich F. Keyser, DNA origami NPs: developments, challenges and perspectives, Nanoscale, 2014, 6, 1412, DOI: 10.1039/c4nr04094e

[4] M. D. Baaske, M. R. Foreman, F. Vollmer, Single-molecule nucleic acid interactions monitored on a label-free microcavity biosensing platform, Nat. Nanotechnol. 9, p. 933-939, 2014. doi:10.1038/nnano.2014.180]

[5] Y.-Q. Wu, D. Y. Zhang, P. Yin, F. Vollmer, Ultraspecific and highly sensitive nucleic acid detection by integrating a DNA catalytic network with a label-free microcavity, Small 10(10), p. 2067-2076, 2014. doi:10.1002/smll.201303558

[6] M. A. Santiago-Cordoba, S. V. Boriskina, F. Vollmer, M. C. Demirel, Nanoparticle-based protein detection by optical shift of a resonant microcavity, Appl. Phys. Lett. 99, p. 073701, 2011. doi:10.1063/1. 3599706

[7] Pulcu, G.S., Mikhailova, E., Choi, L.-S. and Bayley, H. Continuous observation of the stochastic motion of an individual small-molecule walker. Nature Nanotechnology 10, 76-83 (2015). DOI: 10.1038/NNANO.2014.264

[8] Rodriguez-Larrea, D. and Bayley, H. Multistep protein unfolding during nanopore translocation, Nature Nanotechnology 8,288–295(2013)doi:10.1038/nnano.2013.22

[9] Kevin J. Freedman, S. Raza Haq, Joshua B. Edel, Per Jemth, and Min Jun Kim, Single molecule unfolding and stretching of protein domains inside a solid-state nanopore by electric field, Sci Rep. 2013; 3: 1638. DOI: 10.1038/srep01

[10] Jiwook Shim, Younghoon Kim, Gwendolyn I. Humphreys, Ann M. Nardulli, Farhad Kosari, George Vasmatzis, William R. Taylor, David A. Ahlquist, Sua Myong, and Rashid Bashir, Nanopore-Based Assay for Detection of Methylation in Double-Stranded DNA Fragments, ACS Nano, 2015, 9 (1), pp 290–300, DOI: 10.1021/nn5045596

[11] Anderson BN, Muthukumar M, Meller A. (2013) pH Tuning of DNA Translocation Time through Organically Functionalized NPs. ACS Nano. 7 (2), 1408–1414.

[12] Anderson dela Torre R, Larkin J, Singer A, Meller A. (2012) Fabrication and characterization of solid-state nanopore arrays for high-throughput DNA sequencing. Nanotechnology. 23(38):385308. doi: 10.1088/0957-4484/23/38/385308

[13] Zhao Y, Chen D, Yue H, French JB, Rufo J, Benkovic SJ, Huang TJ., Lab-on-a-chip technologies for single-molecule studies, Lab Chip. 2013;13(12):2183-98. doi: 10.1039/c3lc90042h. Epub 2013

[14] Crick CR, Albella P, Ng B, Roschuk T, Ivanov AP, Cecchini MP, Bresme F, Maier SA, Edel JBet al., 2015, Precise Attolitre Temperature Control of

Nanopore Sensors using a Nanoplasmonic Bullseye, Nano Letters, Vol: 15, ISSN: 1530-6992
[15] Abdalla S (2012) Electric Breakdown Through Nano Dielectric Films. J Material Sci Eng 1:e102. doi: 10.4172/2169-0022.1000e102
[16] Stoloff DH, Wanunu M. Recent trends in NPs for biotechnology, Curr Opin Biotechnol. 2013 Aug; 24(4):699-704
[17] Branton D, DW Deamer, A Marziali, H Bayley, SA Benner, T Butler, The potential and challenges of nanopore sequencing, Nature biotechnology 26 (10), 2008, 1146-1153

[18] H Kwok, K Briggs, V Tabard-Cossa, Nanopore fabrication by controlled dielectric breakdown, 2014, PloS one 9 (3), e92880
[19] Makusu Tsutsui, Sakon Rahong, Yoko Iizumi, Toshiya Okazaki, Masateru Taniguchi and Tomoji Kawai, Single-molecule sensing electrode embedded in-plane nanopore, Scientific Reports 2011, number:46 doi:10. 1038/srep00046
[20] W. Kowalczyk, A. Y. Grosberg, Y. Rabin and C. Dekker, Nanotechnology, 2011, 22, 315101
[21] K. Briggs, H. Kwok and V. Tabard-Cossa, Small, 2014, 10, 2077–2086
[22] Min-Hyun Lee, Ashvani Kumar, Kyeong-Beom Park, Seong-Yong Cho, Hyun-Mi Kim, Min-Cheol Lim,Young-Rok Kim and Ki-Bum Kim, A Low-Noise Solid-State Nanopore Platform Based on a Highly Insulating Substrate, Scientific Reports 4, 7448, 2013, doi:10.1038/srep07448
[23] R M M Smeets, N H Dekker and C Dekker, Low-frequency noise in solid-state NPs, 2009 Nanotechnology 20 095501 doi:10.1088/0957-4484/20/9/095501
[24] Yue Wang, Qiuping Yang and Zhimin Wang, The evolution of nanopore sequencing, Frontiers in Genetics, 2015, 5, 1-20, doi: 10.3389/fgene.2014.00449
[25] Tal Gilboa and Amit Meller, Optical sensing and analyte manipulation in solid-state NPs, Analyst, 2015, DOI: 10.1039/C4AN02388A, http://pubs.rsc.org/en/content/articlehtml/2015/an/c4an02388a

Synthesis and characterization of length-controlled ZnO nanorods

I. Musa, N.Qamhieh, and S. T. Mahmoud
Department of physics, United Arab Emirates University, Al-Ain,P.O.Box 15551,
United Arab Emirates

Abstract: Well-crystallized ZnO nanorods of controlled lengths were synthesized by chemical route method without surface modification. The morphology and structure of the nanorods were characterized by transmission electron microscopy, and X-ray diffraction. It was observed that the ZnO nanorods are hexagonal-shaped with diameters in the range of 12-14 nm and length of 100-200 nm based on synthesis of nanorods and growth time. The UV-Vis spectroscopy have been performed at room temperature. The absorption spectrum reveald that the nanorods in different lengtht have a sharp absorption edge at about 365 nm.

Keywords: ZnO nanorods, XRD, UV-Vis spectroscopy.

1. Introduction

Zinc oxide (ZnO) is n-type semiconductor materials and has a direct wide band gap of 3.37 eV at room temperature with high exciton binding energy (60 meV)[1,2]. ZnO is a well-known luminescent material which can be applied in optoelectronic devices such as, light emitting diodes, lasers, sensors[3], and photovoltaic devices[4]. In addition, ZnO exhibits two emission bands in the UV and visible range at room temperature[5]. The relative intensity of these bands depends on the fabrication processe of ZnO which affects the size of nanoparticles[6] or nanorods.

In this work, high-quality ZnO nanorods were assembled from colloidal nanoparticles. Various lengths of ZnO nanorods were obtained based on growth time, which plays an important role in the formation process.

2. Experimental

ZnO nanorods at different growth time and with average lengths of 100-200 nm were synthesized in different steps. First, colloidal solution of ZnO was prepared to produce nanoparticles with an average diameter of 3 nm using Spanhel and Anderson method [7]. In the second step, Hoyer's method [8] was used with some modifications. The solution containing the 3 nm nanoparticles was heated to 60 ^{o}C and mixed with deionized water for different time periods of 2, 6,18, and 48 hours.

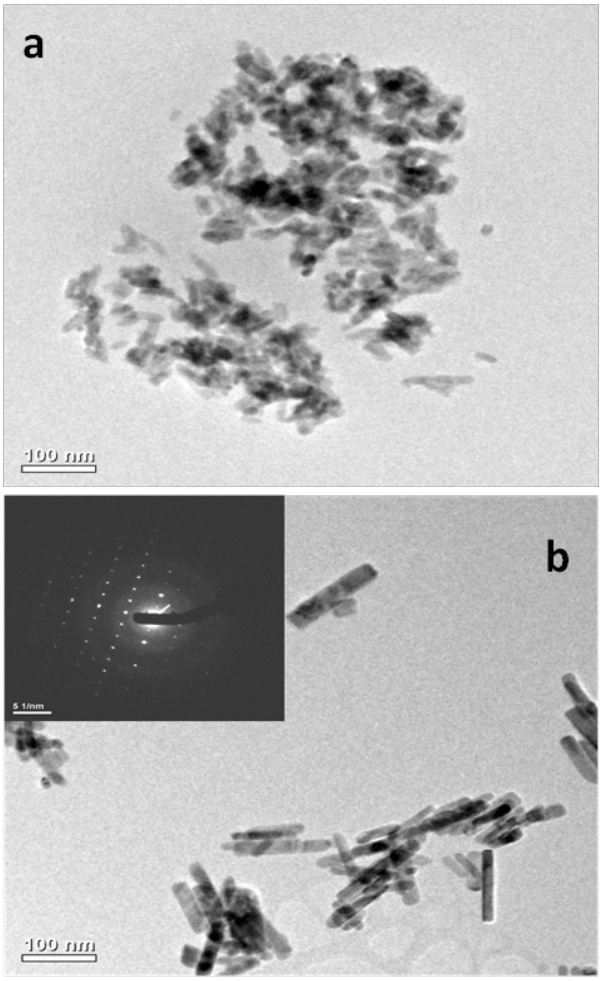

Figure 1: TEM images of ZnO nanorods in different lengths. (a) time growth for 2hr, (b) time growth for 48 hr and the inset shows electron diffraction pattern evidencing well crystallized nanorods.

During this procedure, a white powder was formed and precipitated, and then the solution was centrifuged and washed with an ethanol–water mixture (19:1) four times to remove physisorbed ionic compounds. The shape and length of ZnO nanorods were analyzed using transmission electron microscope (TEM). Powder X-ray diffraction (XRD) patterns were obtained at room temperature using Shimadzu 6100 XRD and CuKα radiation (λ= 0.15406nm). Absorption spectra of ZnO nanorods were obtained using Jasco UV–Visible spectrophotometer.

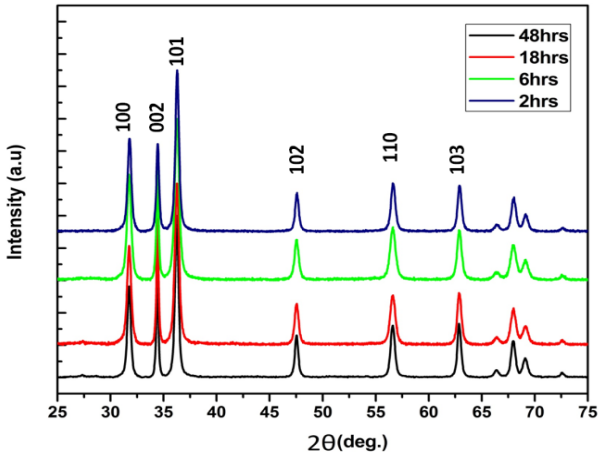

Figure 2: XRD pattern for ZnO nanorods.

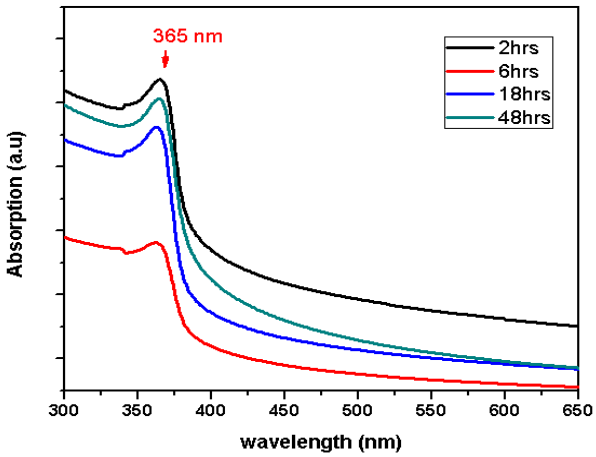

Figure 3: UV-Visible absorption spectra for different time-growth of nanorods.

3. Result and Discussion

A transmission electron microscopy (TEM) image for ZnO nanorods with growth time of 2 hours is displayed in Figure 1(a). In this image, the average diameter is about 12 nm and length around 50 nm.TEM images of ZnO nanorods with growth time of 48 hours shows Zno nanorodes of average diameters 12-to 14 nm and length 150 to 200 nm are presented in Figure 1(b). The inset of Figure 1(b) shows electron diffraction pattern evidencing well crystallized nanorods.

Figure 2 demonstrates the XRD pattern of the ZnO nanorods of various growth times (2, 6, 18 and 48 hours). The diffraction peaks and the observed pattern can be attributed to the presence of hexagonal wurtzite crystallites according to the standard JCPDS (No. 036-1451) with lattice constants of a = 3.251Å and c = 5.208 Å. No excess peaks observed, which indicates that no complex products were formed.

Figure 3 shows the room-temperature UV–Visible absorption spectra of ZnO nanorods of various average lengths 50 to 200 nm. The ZnO nanorods exhibits a sharp absorption edge spectrum peaked at about 365 nm.

4. Conclusion

The effect of synthesis parameters on the structure and morphology of ZnO nanorods growth at different periods of time were studied. Various lengths of ZnO nanorods have been obtained based on the growth time. This parameter plays an important role in the formation process.

Acknowledgment

This work was financially supported by UAEU Program for Advanced Research (UPAR) under grant number 31S112.

References

[1] Monge M, Kahn M L, Maisonnat A and Chaudret B 2003 Room-temperature organometallic synthesis of soluble and crystalline ZnO nanoparticles of controlled size and shape *Angew. Chem. Int. Ed Engl.* **42** 5321–4

[2] Prades J D, Cirera A, Ramon Morante J and Cornet A 2007 Ab initio insights into the visible luminescent properties of ZnO *Thin Solid Films* **515** 8670–3

[3] Meulenkamp E A 1998 Synthesis and Growth of ZnO Nanoparticles *J. Phys. Chem. B* **102** 5566–72

[4] Ravirajan P, Peiró A M, Nazeeruddin M K, Graetzel M, Bradley D D C, Durrant J R and Nelson J 2006 Hybrid Polymer/Zinc Oxide Photovoltaic Devices with Vertically Oriented ZnO Nanorods and an Amphiphilic Molecular Interface Layer *J. Phys. Chem. B* **110** 7635–9

[5] Debasis Bera L Q 2008 Photoluminescence of ZnO quantum dots produced by a sol–gel process *Opt. Mater.* **30** 1233–9

[6] Musa I, Massuyeau F, Cario L, Duvail J L, Jobic S, Deniard P and Faulques E 2011 Temperature and size dependence of time-resolved exciton recombination in ZnO quantum dots *Appl. Phys. Lett.* **99** 243107–243107 – 3

[7] Spanhel L and Anderson M A 1991 Semiconductor clusters in the sol-gel process: quantized aggregation, gelation, and crystal growth in concentrated zinc oxide colloids *J. Am. Chem. Soc.* **113** 2826–33

[8] P. Hoyer, R. Eichberger, H. Weller, Ber. Bunsen-Ges 1993 *Phys Chem* **97** 630

Optical characteristics of aluminum-doped ceria nanoparticles

Nader Shehata[1,2,3], Ishac Kandas[1,2], Kathleen Meehan[4]
[1]Department of Engineering Mathematics and Physics, Faculty of Engineering, Alexandria University, Egypt.
[2]Center of Smart Nanotechnology and Photonics (CSNP), Smart Critical Infrastructure (SmartCI) research center, Alexandria University, Egypt.
[3]Bradley Department of Electrical and Computer Engineering, Virginia Tech, United States.
[4]School of Engineering, University of Glasgow, Scotland, United Kingdom.

Abstract: In this paper, we are studying the impact of aluminum doping in the optical and structural characteristics of ceria nanoparticles. Aluminum-doped ceria nanoparticles, synthesized by chemical perciptation, show reduced optical direct bandgap up to 3.10 eV, larger fluorescence intensity, smaller grain size up to 5.25 nm, with increasing the doping concentration of aluminum. The shown results confirm that the aluminum dopant improves the conversion process from Ce^{+4} ionization states to Ce^{+3} states with more oxygen vacancies. This nanostructures show promising sensitivity to dissolved oxygen based on optical fluorescence quenching technique.

Keywords: ceria nanoparticles, fluorescence quenching, oxygen vacancies, aluminum dopant, oxygen sensing.

Introduction:
In last few years, cerium oxide (ceria) nanoparticles have been extensively studied because of its high oxygen storage capabilities and the large diffusivity of oxygen vacancies. That makes ceria nanoparticles helpful for gas sensors and oxygen pumps [1, 2]. Doping ceria nanoparticles with some tri-valent elements is a promising technique to improve the ionic conductivity of ceria [3]. Aluminum dopant has been shown its promising potential to improve the catalytic activity of ceria [4]. This work represents optical study of ceria nanoparticles doped with aluminum. The study includes the study of optical absorbance dispersion, corresponding direct bandgap, and visible fluorescence intensity under near UV excitation. Then, the synthesized aluminum-doped ceria nanoparticles have been used to detect the dissolved oxygen (DO) based on fluorescence intensity quenching with increasing the DO concentration. That could be helpful in applying the synthesized nanoparticles in DO sensor for environmental monitoring.

Experimental work:
Aluminum-doped ceria nanoparticles are prepared using a chemical precipitation technique [5]. Initially, (0.475g, 0.45g, and 0.425g) of cerium (III) chloride (heptahydrate, 99.9%, Aldrich chemicals) have been mixed with (0.025g, 0.05g, and 0.075g) of aluminum (III) chloride (heptahydrate, 99%, Aldrich chemicals), respectively. The mentioned concentrations present the doping percentages of aluminum in the host ceria with 5, 10, and 15 wt.% respectively. Then, the precursors are stirred in 40 mL de-ionized water. The solution is stirred at rate of 500 rpm for 24 hours through two stages. In the first step, the solution heated to 50^{o}C in normal atmosphere while stirring; 1.6 mL of ammonia is then added after one minute to ensure that the solution becomes homogenous. The synthesized nanoparticles are imaged using TEM, Phillips EM420.
Regarding the optical characterization, the solution of the synthesized nanoparticles has been analyzed in UV-Vis Shimadzu spectroscopy to measure the absorbance spectrum and then the direct bandgap is calculated. The fluorescence intensity of the synthesized nanoparticles solution is analyzed using the same fluorescence setup designed by the authors in ref [6]. The excitation wavelength would be 430 nm and the fluorescent emission is detected over the visible range. Then, the same setup is used to detect optically the dissolved oxygen, which is added to the solution of the synthesized nanoparticles. The quenching of fluorescence intensity peak is detected with variation of DO concentration

Results & Discussion:
The optical absorbance spectrum of the synthesized nanoparticles is shown in figure 1a. The corresponding direct bandgap (E_g) is calculated using equation (1), as shown in Fig. 1b.

$$\alpha E = A^{*}(E - E_g)^{1/2} \quad (1)$$

where A* is a material-dependednt constant based on effective masses of carriers and refractive index. The direct bangap has been reduced with increasing the doping concentration as shown in Fig. 1b, and it reaches to 3.10 eV at doping concentration of aluminum up to 15 wt.%. Compared to undoped ceria nanoparticles with bandgap of 3.27 eV "dotted line on E-axis", the shown results give an evidence that the aluminum dopant improves the conversion process from Ce^{+4} ionization states to Ce^{+3} states with shifting the direct bandgap close to 3 eV [5, 7].
Fig. 2 shows the increase of visible fluorescent emission peak with increasing the doping concentrations "dotted line referes to the visible fluorescence intensity peak of undoped ceria nanoparticles". That is another evidence that the doping could improve the formation of the tri states of cerium ionization states which could be responsible for the fluorescence

emission [7,8]. Fig. 3 shows TEM image of the synthesized nanoparticles with mean grain size up to 5.25 nm.

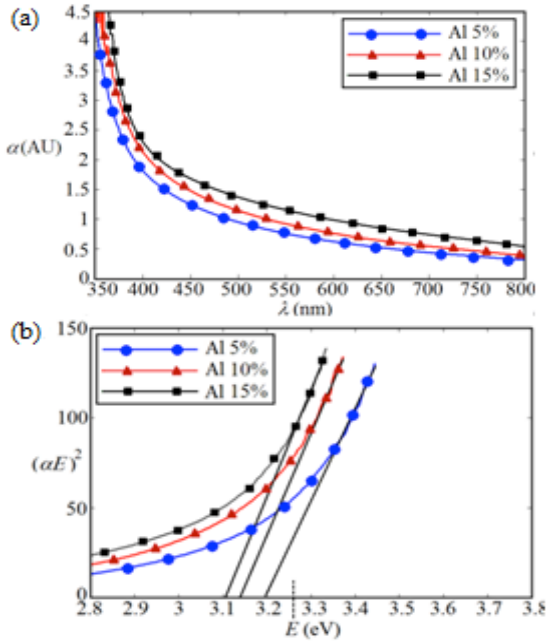

Fig.1: a) Absoebance dispesion and, b) direct bandgap calculations of the aluminum doped ceria nanoparticles

Regarding oxygen sensing application, Fig. 4 shows the quenching of visible fluoresce intensity peak with increasing the concentration of dissolved oxygen. This graph could be helpful in sensing the DO concentration depending on the variation of fluorescence intensity peak.

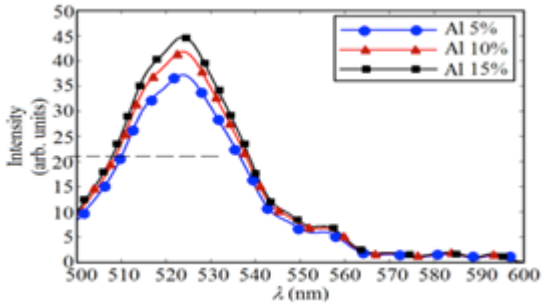

Fig.2: Visible fluorescence emission of the aluminum doped ceria nanoparticles under excitation of 430 nm.

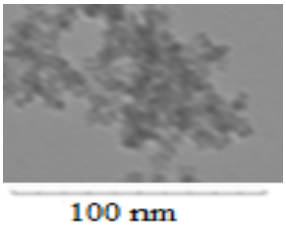

Fig.3: TEM image of aluminum doped ceria nanoparticles (with Al 15 wt.%)

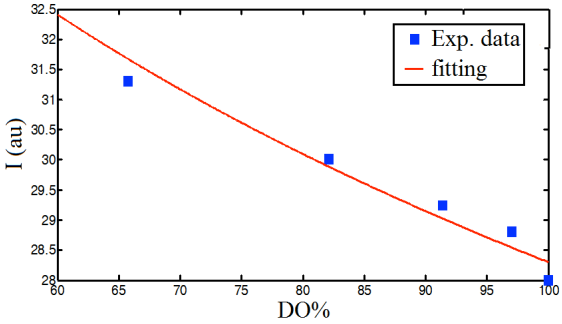

Fig.4: Quenching of intensity with variation of DO concentration (Al 5%)

Conclusion:

Aluminum-doped ceria nanoparticles, synthesized by chemical perciptation, show reduced optical direct bandgap, larger fluorescence intensity, smaller grain size, with increasing the doping concentration of aluminum. The shown results confirm that the aluminum dopant improves the increase of Ce^{3+} states with more oxygen vacancies. These nanoparticles show fluorescence intensity change according to variable dissolved oxygen concentration based on optical fluorescence quenching technique.

References:

[1] E. J. Park, J. Choi, Y. K. Park and K. Park, "Oxidative stress induced by cerium oxide nanoparticles in cultured BEAS-2B cells," *Toxicology*, vol. 245, no. 1-2, pp. 90–100, 2007.

[2] J. L. Lu, H. J. Gao, S. Shaikhutdinov and H. J. Freund, "Morphology and defect structure of the CeO_2(111) films grown on Ru(001) as studied by scanning tunneling microscopy," *Surf. Sci.*, vol. 600, pp. 5004–5010, 2006.

[3] V. V. Kharton, F. M. Figueiredo, L. Navarro, E. N. Naumovich, A. V. Kovalevsky, A. A. Yaremchenko, A. P. Viskup, A. Carneiro, F. Marques and J. R. Frade, "Ceria-based materials for solid oxide fuel cells," *J. Mater. Sci.*, vol. 36, pp. 1105–1117, 2001.

[4] T. Dhannia, S. Jayalekshmi, M. C. S. Kumar, T. P. Rao and A. C. Bose, "Effect of aluminum doping and annealing on structural and optical properties of cerium oxide nanocrystals," *J. Phys. Chem. Solids*, vol. 70, pp. 1443–1447, 2009.

[5] N. Shehata, K. Meehan, M. Hudait, N. Jain, "Control of oxygen vacancies and Ce^{+3} concentrations in doped ceria nanoparticles via the selection of lanthanide," *J. Nanopart. Res.*, vol. 14, pp. 1173-1183, 2012.

[6] N. Shehata, K. Meehan, I. Hassounah, M. Hudait, N. Jain, M. Clavel, S. Elhelw, and N. Madi, "Reduced erbium-doped ceria nanoparticles: one nano-host applicable for simultaneous optical down- and up-conversions," *Nanoscale Res Lett.* 2014; 9(1): 231.

[7] N. Shehata, K. Meehan, D. Leber, "Fluorescence quenching in ceria nanoparticles: A dissolved oxygen molecular probe with a relatively temperature insensitive Stern-Volmer constant up to 50°C," *J. Nanophotonics*, vol. 6, pp. 063529/1-11

[8] P. Patsalas, S. Logothetidis, L. Sygellou and S. Kennou, "Structure-dependent electronic properties of nanocrystalline cerium oxide films," *Phys. Rev. B*, vol. 68, pp. 035104, 2003.

Investigating of the flammability, Impact strength, and physical properties of wood flour/polypropylene composite

Afshin Tavasoli (Corresponding author)

Department of Agriculture, Faculty of Landscape Design, Mashhad Branch, Islamic Azad University, Mashhad, Iran, Tel: 09112732203 E-mail: tavasoliaf@gmail.com

Ahmad Samariha

Young Researchers and Elites Club, Science and Research Branch, Islamic Azad University, Tehran, Iran, E-mail: a_samariha@yahoo.com

Abstract

This study aims to investigate the effect of the content of wood flour on flammability, Impact strength, and physical properties of wood flour/polypropylene composite. For this purpose, the content of wood flour was considered taken at 40, 50, and 60%, with the size of the remaining flour on sieves being of mesh 60, and the MAPP content being 2 wt %, respectively. Properties of flammability, impact strength, and water absorption and thickness swelling were measured according to relevant ASTM standards. The obtained results showed that increasing the wood flour content to 60 wt.%, the impact strength decreased. The water absorption and thickness swelling of composites was lowered with the decrease in wood flour content. With increasing the wood flour content to 60 wt.%, the limiting oxygen index increased.

Keywords: flammability, Impact strength, water absoption, and thickness swelling

1. Introduction

Many research organizations and institutes have or are currently conducting research on wood-plastic composites that will provide more durable and cost-competitive products by using waste materials. The reutilization of waste materials in the production of wood-plastic composites (WPCs) can have advantages to the economy, environment, and technology. Polypropylene (C3H6) (PP) is a thermoplastic with a semi-crystalline polymer structure, and it is used in a wide assortment of applications. PP has an excellent resistance to stress and a low specific gravity. PP is readily able to be mechanically recycled several times using conventional equipment. Attempts have been made to reuse these waste plastics in order to reduce the environmental impact and consumption of the virgin plastics (Hannequart 2004). Past studies have demonstrated that the recycled plastics possess similar mechanical properties but are much cheaper than their virgin counterparts (Panthapulakkal et al. 1991). Water absorption and thickness swelling are the most important problems in the production wpcs and exposed to environmental conditions thus, determining their end use applications (Arbelaiz et al., 2005). Water absorption can deteriorate both mechanical properties and dimensional stability in such composites. Therefore, hygroscopic characteristics have to be taken into account as limiting parameters in the design of WPCs with

regard to their final applications (Adhikary et al., 2008).

Limited oxygen index (LOI), one of the most important ways to evaluate flammability of materials. This method applies to substances that are capable of burning in oxygen (Hindersinn 1990). Although the use of halogenated compounds as flame retardant agents are gradually diminishing due to environmental problems yet these are still in use owing to various advantages like low cost, miscibility and low reduction in physical/mechanical properties of the flame retardant system. The advantage of using reactive flame retardant monomer compared to other flame retardant additives is that they can be used at relatively lower concentration. Since they are incorporated in the polymer structure, they can improve the compatibility with the polymer as well as reduce the migration of flame retardant agent to the surface. The addition of a relatively low amount of silicon-based compounds (silicones, silicas, organosilanes, silsequioxanes and silicates) to polymers has been reported to substantially improve their flame retardancy (Hamdani et al., 2009). The purpose of this research was to studying the effect of wood flour content on Impact, Physical and flammability properties of wood flour/Polypropylene composite

2. MATERIALS AND METHOD

2.1. Wood Flour

Commercial wood flour of populous (60 mesh-sized, Aria cellulose Co.) was used as a filler.

2.2. Polymer matrix

Polypropylene, V30S (density=0.92g/cm3, MFI=18 g/10min) was supplied by Arak Petrochemical Co. (Iran).

2.3. Coupling Agent:

Maleic anhydride grafted polypropylene (PP-g-MA) provided by Solvay with trade name of Priex PGM3010 was used as coupling agent.

2.4. Sample Preparation

Before sample preparation, sawdust fir flour was dried at (70±5) ˚C for 24 h. Then PP, wood flour, and MAPP were weighed and bagged according to formulations given in Table 1 and then mixed in a co-rotating twin-screw extruder (Collin) at the Iran Polymer and Petrochemical Research Institute. Wood flour, granules of Polypropylene, were properly mixed with the coupling agent and then poured into the funnel of the extruder. The compounded materials were then ground using a pilot scale grinder (WIESER, WGLS 200/200 model). The resulting granules were dried at 105 °C for 24 h.

To make the final samples with the injection-molding machine, the produced ocomposite mixture must first be transformed into granules. This was done in a pilot crusher. The yielded granules were dried in a laboratory oven and prepared for the injection. Test samples were made in a

single-screw extruder equipped with a pressure molding system.

2.5. Measurements

After molding, samples of notched impact strength was tested according to ASTM 256 standards, respectively. Water absorption tests were carried out according to ASTM D-7031-04. Three specimens of each formulation were selected and dried in an oven for 24 h at 102±3ºC. The weight and thickness of dried specimens were measured to a precision of 0.001 g and 0.001 mm, respectively. The specimens were then placed in distilled water and kept at room temperature. For each measurement, specimens were removed from the water and the surface water was wiped off using blotting paper. Weight and thicknesses of the specimens were measured after 2 and 24 hours immersion. The values of the water absorption in percentage were calculated using the following equation 1.

$$WA\ (t)\ \frac{W(t)-W(o)}{W(o)} \times 100 \qquad (1)$$

Where WA (t) is the water absorption at time t, W_o is the oven dried weight, and W (t) is the weight of specimen at a given immersion time t.

The values of the thickness swelling in percentage were calculated using equation. 2.

$$TS\ (t)\ \frac{T(t)-T(o)}{T(o)} \times 100 \qquad (2)$$

Where TS (t) is the thickness swelling at time t, T_o is the initial thickness of specimens, and T (t) is the thickness at time t.

2.6. Limited Oxygen Index

The limiting oxygen index (LOI) was derived according to ASTM D-2863. The wood fiber reinforced composites were subjected to burning tests as standard size by preparing specimens of each composition with the dimensions of 15 mm long, 5 mm wide and 1.2 mm thick. ASTM D2863 is a method to determine the minimum concentration of oxygen in an oxygen / nitrogen mixture that will support a flaming burn in a testing specimen. During the test, a certain volumetric concentration of specimen in a tube is ignited with a hydrogen flame on top of the sample by gradually varying the oxygen and nitrogen gas concentration at fixed rates.

2.7. Statistical Analysis

The statistical analysis was conducted using SPSS programming (Version 11.5) method in conjunction with the analysis of variance (ANOVA) techniques. Duncan multiply range test (DMRT) was used to test the statistical significance at $\alpha = 0.05$ level.

3. Result and Discussion

3.1. Impact Strength.

The Duncan table divided the mean values obtained from measuring the notched impact strength of natural fiber-plastic composites at three different levels of the wood flour (40, 50, and 60 wt.%) into two distinct groups. The impact strength of the sample containing 60 wt.% wood flour was lower than those at other wood percentages (Figure. 1). The presence of lignocellulosic materials creates areas of stress concentration and crack initiation. The impact strength will decrease with further addition of filler materials. On the other hand, the presence of wood flour increases the energy absorbed by wood flour-PP composites. As a result, the addition of lignocellulosic filler leads to higher stress concentration areas and initiate the growth of cracks (Tajvidi, 2003). This is also in accordance with the findings in (Farsi, 2012).

3.2. Physical Properties

Figures 2 and 3 shows the short-term values of the water absorption and thickness swelling for the composites. Generally, the water absorption and thickness swelling increased with the wood flour content. The wood flour content induced significant water absorption and thickness swelling. These results are similar to those reported by (Pecina *et al*. 1998) for wood/plastic (polypropylene) composites as well as by (Carvajal *et al*. 1985), and (Talavera *et al*. 2007).

3.3. Limited Oxygen Index

The results showed that wood flour increases the limiting oxygen index of the sample increases. The sample, the more oxygen is needed for combustion and process the sample burns slower and more time with previous results correspond to (Denault, 2008; Stark et al., 2010).

Composites are usually pores and pores and volatiles, usually by combining or building are created during the process. The open pores are connected and form a barrel or have a cavity. Oxygen passes through these holes usually increases the combustion process. The cellulose fibers are further enhanced oxidation resistance is more porous structure and the decrease of oxygen and prevent oxidation decreases. Increased oxygen index means that more oxygen is needed to burn the sample and the conditions for its combustion is more difficult. Limited oxygen index (LOI), a widely used method as a simple and precise method for the determination of fire self-extinguishment, was adopted to evaluate the flame retardant properties of wood–fiber/PP/APP/silica composites.

4. Conclusion

The most important results obtained from this investigation can be summarized as follows.

1. On increasing the wood flour content to 60 wt.%, the impact strength decreased.

2. The water absorption and thickness swelling of composites was lowered with the decrease in wood flour content.

3. With increasing the wood flour content to 60 wt.%, the limiting oxygen index increased.

References

Adhikary, K. B., Pang, S., and Staiger, M. P. (2008). Long-term moisture absobption and thickness swelling behavior of recycled thermoplastics reinforced with pinus radiata sawdust, Chemi Engineer J. 142, 190-198.

Arbelaiz, A., Fernandez, B., Cantero, G., Llano-Ponte, R., Valea, A. and Mondragon, I. (2005). Mechanical Properties of Flax Fiber/Polypropylene Composites: Influence of Fiber/Matrix Modification and Glass Fiber Hybridization. J. Compos. Mater., 36: 1637-1644.

ASTM D 2863, Standard for Flammability of Plastic Materials for Parts in Devices and Appliances, Underwriters Laboratories INC. (UL), 1994.

Carvajal, O., J. Puig, J.A. Leal and M.E. Rodriguez, (1985). Influencia del contenido de meollo sobre la calidad los tableros de particulas Revista ICIDCA 29(3): 19-24.

Denault, (2008). Proceeding of international conference on flax and other bast plants, p .211, sasktoon, Canada.

Farsi, M. (2012). Some of the mechanical and thermal properties of wheat-straw-filled PP composites," Fibers and Polymers, 13, 515-521.

Hamdani S, Longuet C, Perrin D, Lopez-cuesta JM and Ganachaud F. Flame retardancy of silicone-based materials. Polymer Degradation and Stability. 2009; 77:465-495. http://dx.doi.org/10.1016/j.polymdegradstab.2008.11.019.

Hannequart, J.P. (2004). Good Practice Guide on Waste Plastics Recycling: A Guide by and for Local and Regional Authorities, Association of Cities and Regions for Recycling (ACRR), Belgium.

Hindersinn , R, (1990). Historical Aspect of polymer Fire Retardance, Fire and Polymer, 87-95.

Panthapulakkal, S., Law, S., and Sain, M. (1991). "Properties of recycled high-density polyethylene from milk bottles," Journal of Applied Polymer Science 43(11),2147-2150.

Pecina, H., G. Kuhne and J.P. Stephan, (1998). Holzspanplatten mit Sekundar-polypropylene Bindung. Holz als Roh Werkstoff, 56(2): 114.

Stark, N.M , White, R.H, Muller, S.A & Osawald (2010). polym. Degrad stabil , 95, 1903.

Tajvidi, M. (2003). Studying Engineering and Viscoelastic Properties of Composites Made from Thermoplastic Polymers and Natural Fibers Using Dynamic-Mechanic Analysis. Ph.D. Thesis, Faculty of Natural Resources, Tehran University, p.205.

Talavera, F., S. Silva Guzman, H.G. Richter, S. Duenas and R. Quirarte, (2007). Effect of production variables on bending properties, water absorption and thickness swelling of bagasse/plastic composite boards. Industrial Crops and Products, 25: 1-7.

Table 1. Composition of the studied formulations.

Sample Code	PP Content (wt%)	Wood flour Content (wt%)	PP-g-MA Content (wt%)
1	60	40	2
2	50	50	2
3	40	60	2

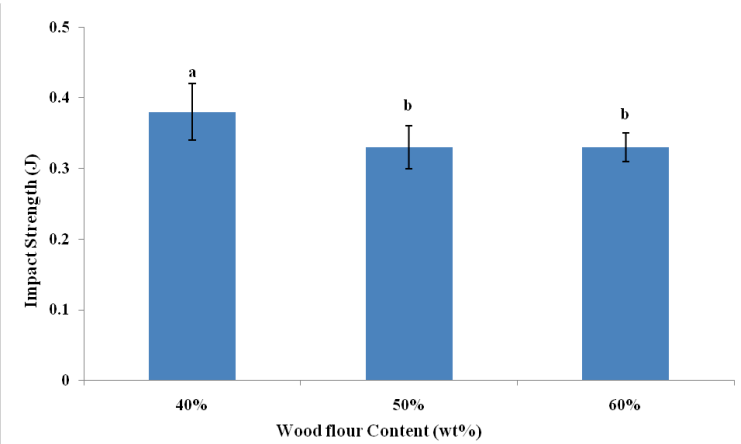

Figure. 1. Effect of the content of wood flour on the impact strength

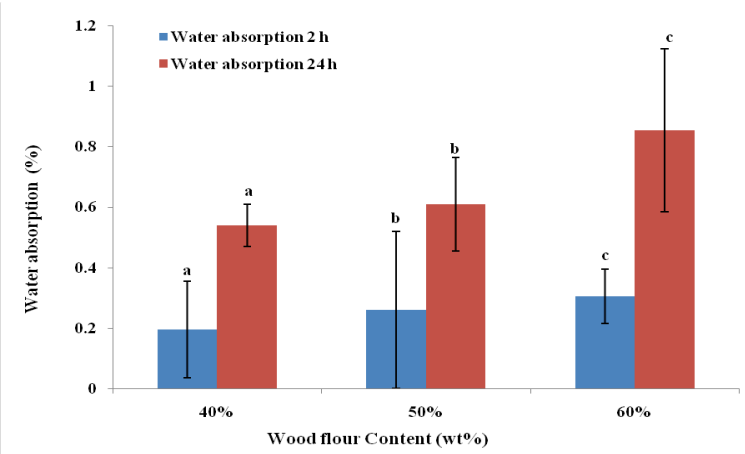

Figure. 2. Effect of the content of wood flour on the water absorption

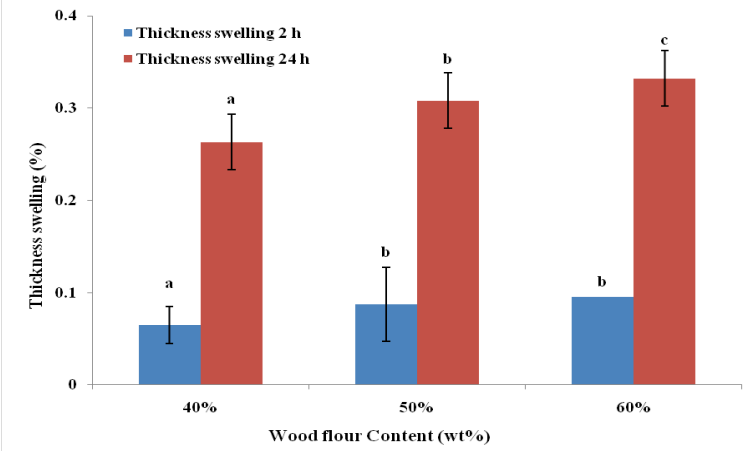

Figure. 3. Effect of the content of wood flour on the thickness swelling

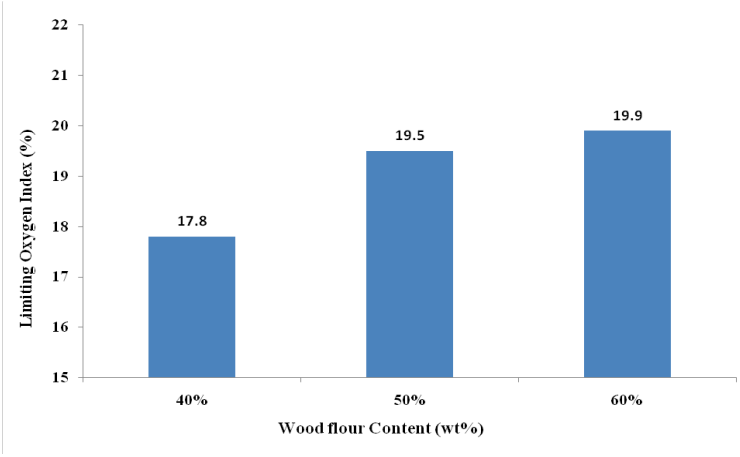

Figure. 4. Effect of the content of wood flour on the limiting oxygen index

Torsional Resonators under Mixed-frequency Excitation for Improved Bandwidth

Saad Ilyas[*], Abdallah Ramini[*], Arpys Arevalo[**], and Mohammad I. Younis[*]
[*]Physical Sciences and Engineering (PSE),
[**]Computer, Electrical and Mathematical Sciences and Engineering Division (CEMSE),
King Abdullah University of Science and Technology, 23955-6900 Thuwal, KSA
saad.ilyas@kaust.edu.sa, mohammad.younis@kaust.edu.sa

Abstract
We present an experimental and theoretical investigation of a micro machined mirror under a mixed frequency signal composed of two harmonic AC sources. The micro mirror is made of Polyimide as the main structural layer.

The experimental and theoretical dynamics are explored via frequency sweeps in the desired neighborhoods. One frequency is fixed while the other frequency is swept through a wide range to study the dynamic responses. To simulate the behavior of the micro mirror, it is modeled as a single degree of freedom system, where the parameters of the model are extracted experimentally. Good agreement is reported among the simulation results and the experimental data. These responses are studied under different frequencies and input voltages. The results show interesting dynamics, where the system exhibits primary resonance, and combination resonances of additive and subtractive type. The mixed excitation is demonstrated as a way to increase the bandwidth of the resonator near primary resonance, which can be promising for resonant sensing applications in the effort to increase the signal-noise ratio over extended frequency range.

Keywords
Micro Mirror, Mixed-frequency excitation, Multi-frequency excitation, Resonators, Electrostatic actuation, Polyimide, Bandwidth

1. INTRODUCTION

Exploring and exploiting the interesting dynamical behavior of MEMS is a widely studied area of research as most MEMS devices exhibit interesting dynamic behaviors introduced by either electrostatic actuation [1,2], stiffness [1] or damping [2]. It is necessary to understand these behaviors in order to either exploit them efficiently or avoid them, if needed. Considerable efforts have been directed recently to understand many of the complex dynamics phenomena at the micro scale including dynamics pull-in [1, 3] and parametric excitation [4-8]. These interesting phenomena also have been proposed for useful applications in mass sensing [9, 10], low activation voltage switches [11], and digital logic designs [12].

Recently the mixed frequency excitations of the micro and nano resonators have inspired great interest due to their exciting and motivating behaviors. These resonators have been proposed in applications in areas like spectroscopy [13, 14] because of their remarkable properties, where they have helped in calculating the refractive index of materials accurately and rapidly. Also, they were implemented in atomic force microscopy [15-21] to convey several levels of information about the sample under test, where every mode of vibration is responsible for a different kind of data (first mode for surface topology, second mode for charge distributions, etc). Another recent use of mixed-frequency excitation is in digital logic devices [12], where mixing of different frequencies result in distinct output frequencies, and hence enable logic operations. In addition, mixing of frequencies through quadratic electrostatic forces has been proposed in [22-27] to realize down converters, mixers, and filters. Mixed-frequency excitation has been used in NEMS resonators to avoid the feed through parasitic by generating a low frequency term [28]. In addition, it presents a way to detect a high frequency signal in NEMS by converting it into a low frequency signal using mixing without losing any information. Frequency modulation and digital demodulation of a carbon nanotube NEMS in transistor geometry is presented in [29]. A tunable carbon nanotube electromechanical oscillator using frequency mixing is presented in [30]. The identification and the

characterization of bending vibrations of suspended semiconducting Single Walled Carbon Nano Tube resonators at room temperature, by using them as frequency mixers, is presented in [31].

The micro mirror is an exciting MEMS structure that has been widely used in optics [32, 33]. Also, seesaw type motion of a micro mirror has enabled the design of complementary universal MEMS logic devices [34, 35]. The dynamics of micro mirrors under mixed-frequency excitation has not yet been explored. The full potential and use of mixed frequency excitation and its exploitation for practical MEMS applications has not yet been investigated in depth, especially for torsional actuators and micro mirrors. Due to the interesting dynamics and exciting behavior of systems under this excitation it is necessary to exploit these dynamics in micro mirrors for sensing and actuations applications in MEMS. In this work, we investigate the dynamic behaviors of a micro mirror under mixed frequency excitations.

The organization of the paper is as follows. In Section 2 we discuss the design and fabrication process of the polyimide micro mirror based on surface micromachining techniques. Next, the mathematical model using lumped parameter techniques is discussed in Section 3. Section 4 presents the experimental setup and procedures used in gathering all the experimental data. Section 5 presents different case studies performed in order to understand the behavior of the system under mixed-frequency excitation. Next, Section 6 presents a discussion on the possible application and areas to be explored further. Finally, Section 7 summarizes the results and presents the conclusions.

2. DESIGN AND FABRICATION

2.1 Design

A micro mirror is basically a plate clamped by two flexure beams on both sides, which undergo torsion as the mirror actuates. The proposed micro mirror is a similar device as shown in the schematics in figure.1.

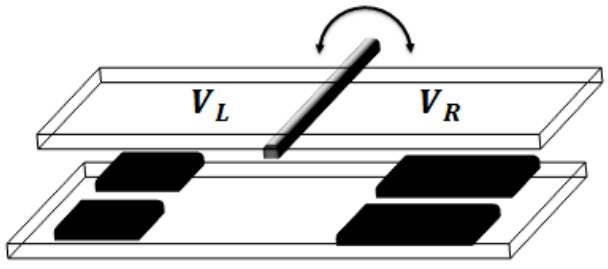

(a)

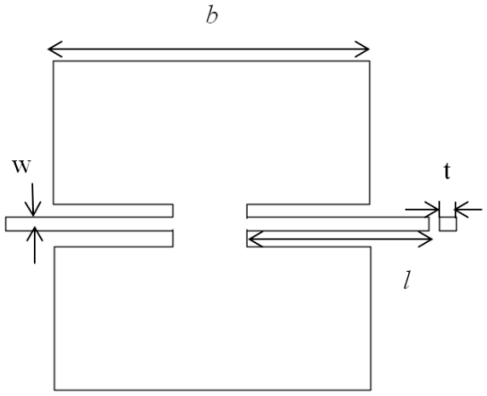

(b)

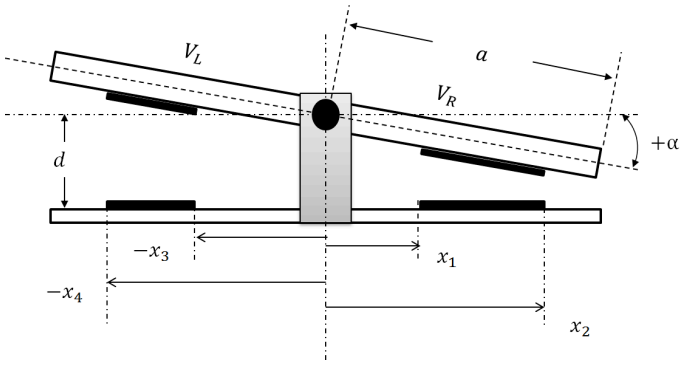

(c)

Figure. 1. Schematic views of the micro mirror (a) 3D view. (b) Top view. (c) 2D side view.

This mirror can be actuated in three different ways: The first way of actuation is through the right half of the mirror, which has larger fixed electrodes compared to the left side. The second way is through actuating the smaller electrodes on the left size. Finally, it can be actuated by one electrode of each side. Depending on the actuation type, various equilibrium positions of the mirror and its natural frequency can be set. Figure.2 shows a simulated plot of frequency against actuation voltage for the three methods of actuation. It can be noticed how at a single fixed voltage the device can be actuated at three different frequencies. Alternatively, a single fixed frequency of the device can be activated using three different voltages depending on how the device is excited. This method can prove useful in resonator applications as it provides three different control points. We can choose to operate around any one depending on the actuation method. This paper considers the case of electrostatic actuation through the right half of the mirror, which has the larger fixed electrodes.

Table 1 summarizes the measured dimensions and other important parameters of the system under consideration.

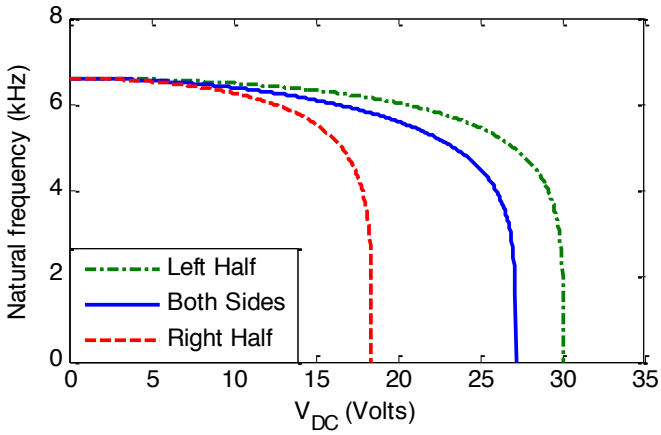

Figure. 2. Variation of the fundamental natural frequency against voltage under three methods of actuation (Left Half: smaller electrodes, Right half: larger electrodes, Both sides: one electrode on each side).

Table.1 Specifications of the micro mirror

Length of the device	**535 µm**
$2a$	**150 µm**
Width of the device	**97.5 µm**
b	**222.5 µm**
Electrode location	**-105 µm**
x_1	**-185 µm**
Electrode location	**30 µm**
x_2	**42.5 µm**
Electrode location	**100 µm**
x_3	**15 µm**
Electrode location	**5 µm**
x_4	**5 µm**
Smaller electrode thickness	**4.38 mrad**
b_l	**18.4 volts**
Larger electrodes thickness	
b_r	
Flexure beam length	
l	
Flexure beam width	
w	
Flexure beam thickness	
t_b	
Gap	
d	
Maximum tilt angle of mirror	
α_{max}	
Pull in voltage for right half	

2.2 Fabrication

The micro mirror is fabricated using a 6 layer fabrication process based on surface micromachining techniques. Figure.3 shows the fabrication cross section of the right half of the mirror. It is approximately 7 µm thick in total comprising of a polyimide structural layer with a nominal thickness of 6 µm. Also, it is separated by a 5µm gap from its bottom electrodes, which are patterned on the Si substrate. Metal_0 layer of 50nm/250nm of Cr/Au forms these fixed ground electrodes. A 50nm/250nm/50nm layer of Cr/Au/Cr forms the Metal_1 layer patterned onto the structural layer forming the movable gate electrodes. Anchors are used to hold the actuator to the ground as well as to provide electrical signal to the moveable gate electrodes whereas dimples are incorporated to avoid the electrical shorting of the electrodes upon pull in. Metal_2 layer, as shown in figure.3, comprises of 450nm of Ni patterned similar to Metal_1 layer to avoid the bimorph effect and to have a straight structure.

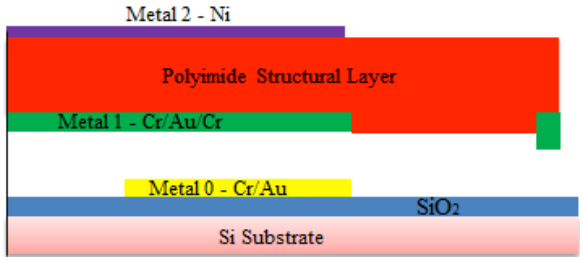

Figure. 3. Fabrication process cross-section of one side of the mirror.

Figure.4 shows the SEM image of the fabricated micro mirror. The image shows two anchors holding the mirror through flexure beams and allowing its torsional motion. The patterned metal visible on top of the polyimide structural layer is Ni used to counter for the bimorph effect.

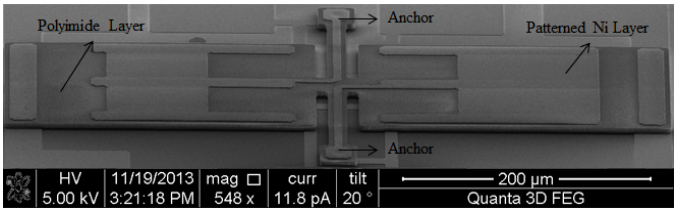

Figure. 4. A SEM image of the fabricated micro mirror.

3. MODELING

The mirror is modeled as a single degree of freedom system [36]. The equation of motion can be expressed as

$$I\alpha + c\alpha + K_t\alpha = M_R - M_L \tag{1}$$

Where, I is the mass moment of inertia, c is the damping constant, K_t is the torsional stiffness, M_L is moment on the left side of mirror, and M_R is the moment on the right side of the mirror, which can be expressed as

$$M_R = \frac{\varepsilon b_r V_R}{2\alpha^2}\left[\frac{d}{(d-x_2\alpha)} - \frac{d}{(d-x_1\alpha)} + \ln\left\{\frac{(d-x_2\alpha)}{(d-x_1\alpha)}\right\}\right] \tag{2}$$

Where, ε is the dielectric constant of gap medium, V_R is the potential difference on the right side of mirror and α is the tilt angle of the mirror. Similarly

$$M_L = \frac{\varepsilon b_l V_L}{2\alpha^2}\left[\frac{d}{(d-x_4\alpha)} - \frac{d}{(d-x_3\alpha)} + \ln\left\{\frac{(d-x_4\alpha)}{(d-x_3\alpha)}\right\}\right] \tag{3}$$

Where V_L is the potential difference on the left side of mirror, which can be expressed as

$$V_L = V_R = \left[V_{DC} + V_{AC1}\cos(\Omega_1 t) + V_{AC2}\cos(\Omega_2 t)\right]^2 \tag{4}$$

Where, V_{AC1} is the amplitude of the first AC source, V_{AC2} is the amplitude of the second AC source, V_{DC} is the polarization voltage and Ω_1, Ω_2 are the first and second excitation frequencies, respectively.

The torsional stiffness K_t of the flexures can be calculated as

$$K_t = \frac{2GJ_P}{l} \tag{5}$$

Where G is the shear modulus and J_P is the polar moment of inertia. The parameter J_P can be calculated as [37]

$$J_P = \frac{1}{3}wt_b^3\left(1 - \frac{192t_b}{\pi^5 w}\sum_0^\infty \frac{1}{[2n+1]^5}\tanh\left[\frac{(2n+1)\pi w}{2t_b}\right]\right) \tag{6}$$

Next we introduce the following normalized parameters:

$$\theta = \frac{\alpha}{\alpha_{\max}} \tag{7}$$

$$\alpha_{max} = \frac{d}{a} \tag{8}$$

$$\gamma_1 = \frac{x_1}{a}; \gamma_2 = \frac{x_3}{a} \tag{9}$$

$$\beta_1 = \frac{x_2}{a}; \beta_2 = \frac{x_4}{a} \tag{10}$$

$$\hat{t} = \frac{t}{T}; \quad \mu = \frac{cT}{I}; \quad T = \sqrt{\frac{I}{K_t}} \tag{11}$$

Using (7-11), the final normalized equation is written as

$$\theta + \mu\theta + \theta = \frac{\eta_1}{\theta^2}\left[\frac{1}{(1-\beta_1\theta)} - \frac{1}{(1-\gamma_1\theta)} + \ln\left(\frac{(1-\beta_1\theta)}{(1-\gamma_1\theta)}\right)\right] - \frac{\eta_2}{\theta^2}\left[\frac{1}{(1-\beta_2\theta)} - \frac{1}{(1-\gamma_2\theta)} + \ln\left(\frac{(1-\beta_2\theta)}{(1-\gamma_2\theta)}\right)\right] \tag{12}$$

Where θ is the normalized tilt angle and

$$\eta_1 = \frac{\varepsilon b_r V_R}{2\alpha_{max}^3 K_t} \quad ; \quad \eta_2 = \frac{\varepsilon b_l V_L}{2\alpha_{max}^3 K_t} \tag{13}$$

4. EXPERIMENTAL SETUP

Figure.5 (a) shows a schematic of the experimental setup. The micro mirror is placed inside the vacuum chamber with a laser coming from a Laser Doppler Vibrometer (LDV) pointing directly at it to take the measurements. The LDV generates all the experimental results as displacement, which is then converted into tilt angle by relating the vertical displacement of the mirror with length span of half of the mirror. A data acquisition card, (DAQ) NI 6251from National Instruments, is used to acquire the data from the LDV. A resistor is installed to limit the current passing through the circuit in the event of pull in. It is worth mentioning that when driving this mirror harmonically by capacitive forces, there might be very small current generated in the current-limiting resistor due to the time varying capacitor. However, this is negligible compared to the current that would pass in the case of a pull-in (short circuit), which is the intended purpose of the resistor (i.e., to protect the mirror when pulled-in and when passing a current across it.)

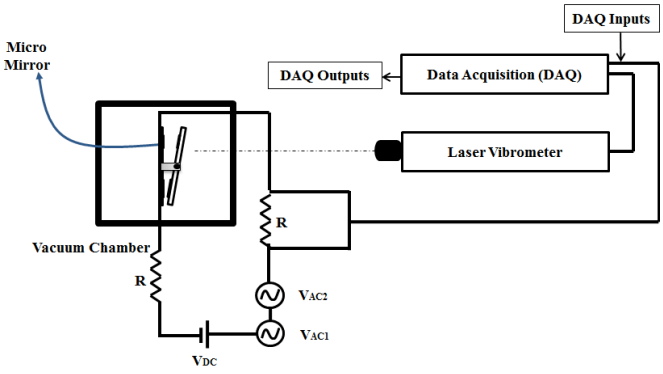

(a)

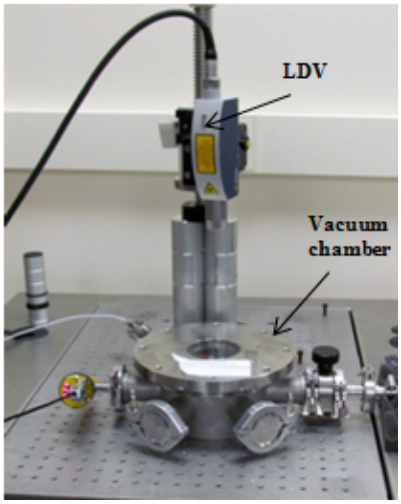

(b)

Figure. 5. (a) Schematic of the experimental setup. (b) LDV pointing at the micro mirror inside the vacuum chamber.

5. MIXED-FREQUENCY EXCITATION RESULTS

Next, we demonstrate and show results for the mirror under mixed-frequency excitation signals. The combination resonances look similar to what has been reported in [38, 39] due to the presence of quadratic nonlinearity. However, in the present case, these resonances are activated due to both effects of quadratic nonlinearities, due to the electrostatic force, and due to the quadratic form of the voltage in the numerator of the electrostatic force expression. To better understand this, one can expand the quadratic voltage term in (4), which yields

$$V_R = V_L = {V_{DC}}^2 + {V_{AC1}}^2.\cos^2(\Omega_1 t) + {V_{AC2}}^2.\cos^2(\Omega_2 t)$$
$$+2V_{DC}.V_{AC1}.\cos(\Omega_1 t) + 2V_{DC}.V_{AC2}.\cos(\Omega_2 t)$$
$$+V_{AC1}.V_{AC2}.[\cos\{(\Omega_1 - \Omega_2)t\} + \cos\{(\Omega_1 + \Omega_2)t\}] \quad (14)$$

It is clear from (14) that the last term is responsible for producing the apparent resonances of additive and subtractive type. An additive type resonance will appear when the sum of the fixed frequency (Ω_1) and variable frequency (Ω_2) equals the natural frequency (ω_n) of the system i.e. $\Omega_1+\Omega_2=\omega_n$, whereas a subtractive type resonance appears when the difference of the fixed frequency and variable frequency equals the natural frequency of the system i.e. $\Omega_1-\Omega_2=\omega_n$. Note that in this paper we assume Ω_1 to be the fixed frequency and Ω_2 to be the variable frequency for all of the experimental results.

5.1 Results and discussions

The primary natural frequency of the system is calculated using the finite element software ANSYS [40]. These results are obtained by basic modal analysis over the geometry of the micro mirror meshed using 3-D solid brick elements. The primary resonance frequency is calculated to be at 6.62 kHz. Figure.6 shows the experimentally measured and theoretically calculated primary natural frequency of the system, which is consistent with that of the finite element calculation. The *y* axis scale shows the displacement measurement obtained from the laser vibrometer as well as the tilt angle α calculated from relating the measured displacement to the length span of one side of the mirror. From now onwards all the plots will be shown against the tilt angle α as it relates more closely to the motion of the micro mirror.

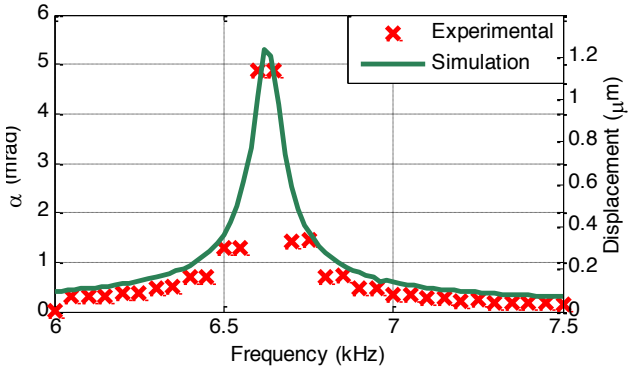

Figure. 6. Frequency response sweep at V_{DC}=3V, V_{ACI}=1V to estimate the natural frequency of the mirror (around 6.62 kHz).

The method of extracting the damping coefficient ξ, the gap d, and the stiffness K_t is explained in details in [41]. The effective mass moment of inertia I is then calculated by using the results of the experimentally calculated natural frequency value ω_n and torsional stiffness K_t in the below equation

$$I = \frac{K_t}{\omega_n^{\,2}} \qquad (15)$$

The extracted parameters of the device are given in Table 2.

Table. 2 Extracted Parameters of the Micro mirror

Torsional stiffness of the device K_t	**$3.2e^{-8}$ N/m**
Effective mass moment of inertia I	**1.8082e-17 kgm^2**
Damping ratio ξ	**0.02**

Next, we show the results for various loading cases, where we fix one of the AC frequencies and vary the other one in the neighborhood of primary resonance. The effects of varying the fixed frequency and the applied voltage on the combination resonances are studied in these cases. The simulation part of the results is obtained by numerically integrating (12) in time using Runge-Kutta method [40]. All the results are post-processed and presented in the form of frequency response plots.

5.1.1 Case 1: V_{DC}=2V, V_{AC1}=2V, V_{AC2}=1V, and Ω_1=500 Hz

Initially, we consider the case when Ω_1 is equal 500 Hz and Ω_2 is swept over 2 kHz frequency range around the primary resonance. One can note the resulting frequency response curve in figure.7. The Figure shows the resonances of subtractive type at 7.1 kHz, due to the Ω_1-Ω_2 term in (14), and the additive type at 6.1 kHz, due to the Ω_1+Ω_2 term in (14), as expected. It can also be observed that the model accurately predicts these combination resonances and the amplitude of the peaks are also in good agreement. The deviation between theory and experiment can be attributed to the fact that we use lumped-parameter model for the distributed-parameter system (beams and plate).

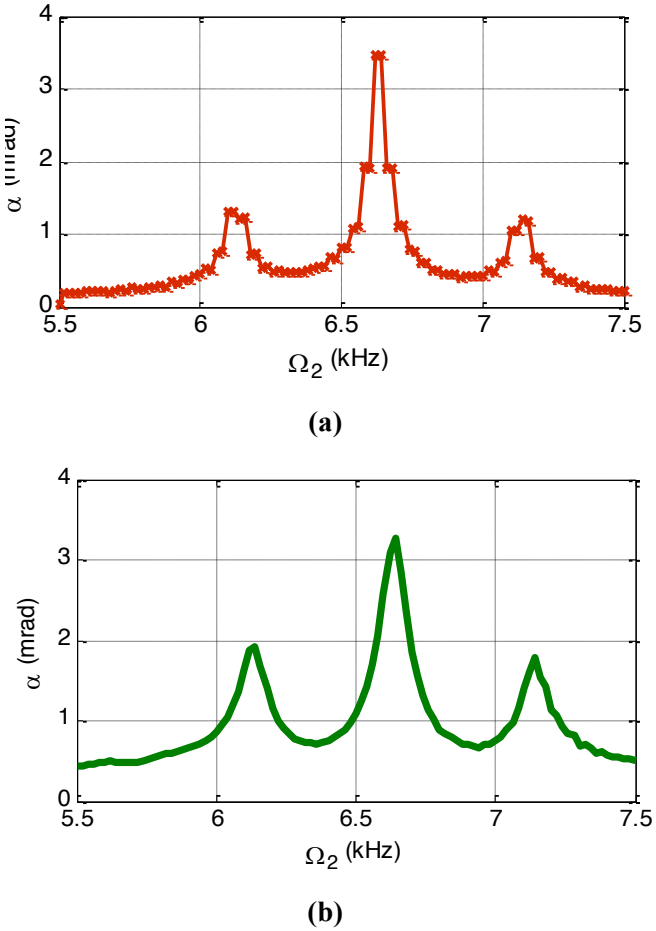

Figure. 7. (a) Measured frequency response sweep for V_{DC}=2V, V_{AC1}=2V, V_{AC2}=1V, Ω_1=500 Hz. (b) Simulated frequency response sweep for V_{DC}=2V, V_{AC1}=2V, V_{AC2}=1V, Ω_1=500 Hz.

5.1.2 Case 2: V_{DC}=2V, V_{AC1}=5V, V_{AC2}=1V and Ω_1=2 kHz

Next, we consider another case just to further demonstrate that the shifting of the additive and subtractive resonances at the desired frequencies is controlled by the fixed frequency through the mixing. Figure.8 demonstrates the experimental result for the additive type resonance, when Ω_1 is fixed at 2 kHz. The resonances here are expected at 4.6 kHz (additive type) and 8.6 kHz (subtractive type).

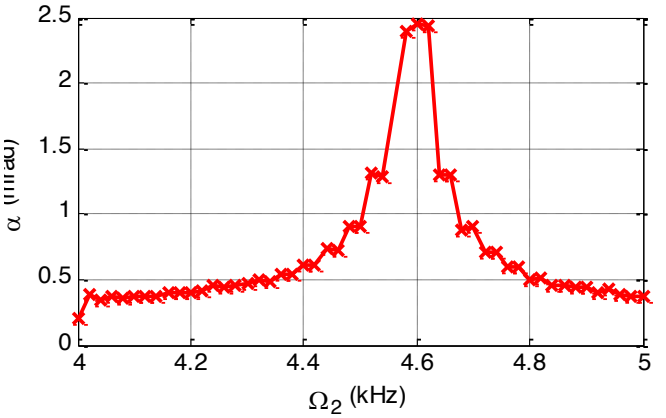

(a)

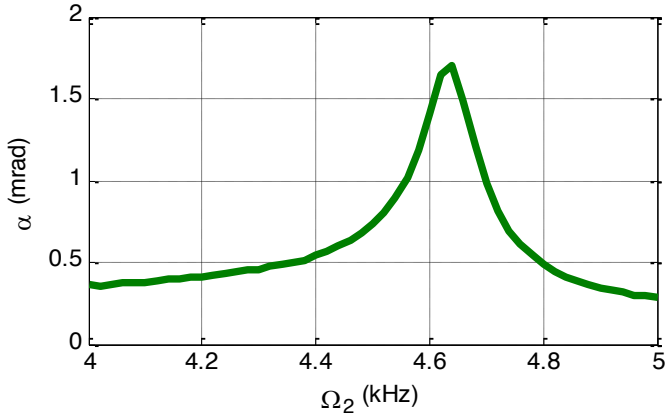

(b)

Figure. 8. (a) Measured frequency response sweep for V_{DC}=2V, V_{AC1}=5V, V_{AC2}=1V, Ω_1=2 kHz. (b) Simulated frequency response sweep for V_{DC}=2V, V_{AC1}=5V, V_{AC2}=1V, Ω_1=2 kHz.

5.1.3 Case 3: V_{DC}=2V, V_{AC1}=5V, V_{AC2}=1V, and Ω_1=100 kHz

In this case, we study the behavior of these resonances at a very high fixed frequency compared to the natural frequency of the mirror i.e. 100 kHz. Figure.9 compares the experimental data of this case with and without mixed-frequency excitation. Resonance is activated at 106.6 kHz due to the Ω_1-Ω_2 condition of the combination resonances in case of mixed frequency-excitation while no response from the system is observed in case of only single frequency excitation. Using this technique, we can shift any one of the additive or subtractive type resonances to any desired frequency. Also a huge difference in amplitude can be observed between the single source and mixed-frequency excitation, which shows the effectiveness of this method. A similar peak (not shown) is also activated at 94.4 kHz, again due to the Ω_1-Ω_2 term (100-94.4 = 6.6 kHz), which is essentially a subtractive type. Hence, resonance is observed at Ω_2 = 94.4 kHz.

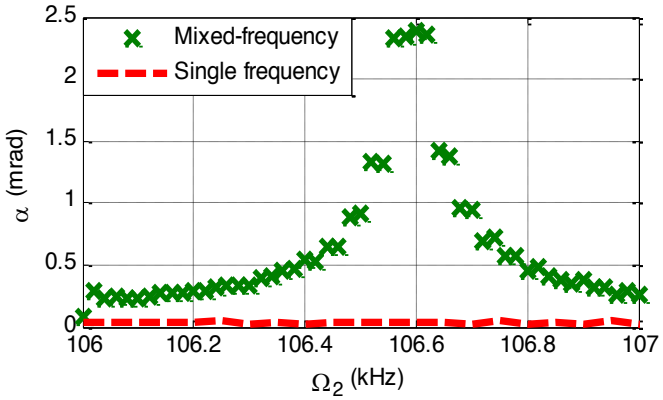

Figure. 9. Measured frequency response sweep for V_{DC}=2V, V_{AC1}=5V, V_{AC2}=1V, Ω_1=100 kHz.

5.1.4 Case 4: V_{DC}=2V, V_{AC1}=variable, V_{AC2}=1V, Ω_1=500 Hz

It is also clear from (14) that if the voltage (V_{AC1}) associated with the fixed frequency (Ω_1) is increased and the rest of the parameters are kept the same, it results in higher amplitude of the combination resonances. Figure.10 demonstrates this effect from the experimental data obtained for different values of V_{AC1}. It shows how the amplitude increases from 1.2 mrad to 3.2 mrad until it is almost equal to the amplitude at primary natural frequency. Also, an increase in the amplitude of regions between the resonances can also be observed. This can effectively increase the bandwidth of the resonator, using the mixed-frequency excitation. In another words, mixed-frequency excitation can be proposed as an effective way to excite resonance sensors to achieve large signal-noise ratio over extended range of frequency, and thus avoiding the problem of a narrow sharp response over a limited range of frequency, which negatively affects the performance of devices, such as MEMS gyroscopes.

The results of the above discussed cases show that resonances can be activated at any frequency with the desired amplitude as long as we properly choose the input voltages. The ability to generate multiple resonance peaks and the ability to control how close they can be activated to each other as well as their amplitude without changing the geometry of the device is very promising feature that can be widely used in many MEMS applications, such as resonant sensors and other applications.

6. Discussion

6.1 Resonators Applications

As indicated earlier, the mixed-frequency excitation can effectively increase the bandwidth of resonators. This occurs when the combination resonances (additive and subtractive) get closer to the primary natural frequency as the fixed excitation frequency gets small. This results in increasing the bandwidth around the primary resonance. Figure.11 shows the experimental results of reducing the fixed frequency to small values and its effect on the bandwidth of the micro mirror. In this Figure, we increase the bandwidth around the primary natural frequency. Also, very high amplitude of the combination resonances can be achieved by selecting the proper voltage input. This proves that using mixed-frequency excitation can increase the bandwidth in resonators without making any changes to the device design or sacrificing much of its maximum amplitude. This can be advantageous in applications, such as MEMS gyroscopes, where mismatch problems can result in a huge loss in the signals [43].

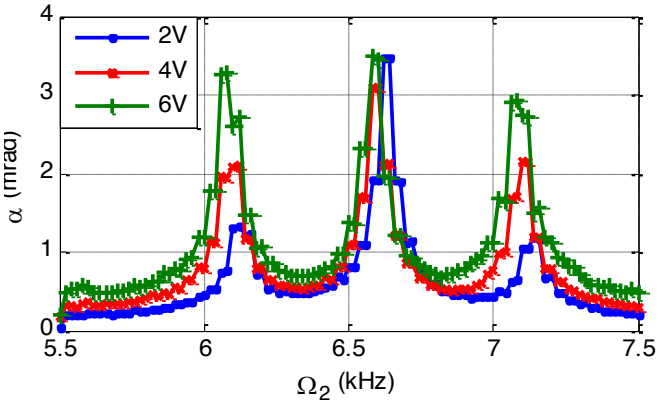

Figure. 10. Measured frequency response sweep for V_{DC}=2V, V_{AC1}= variable, V_{AC2}=1V, Ω_1=500 Hz.

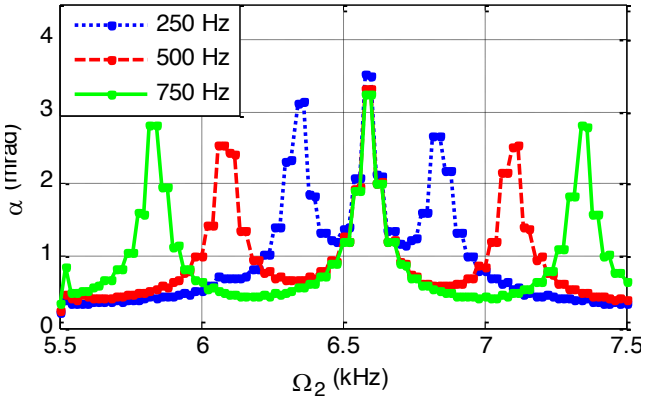

Figure. 11. Measured frequency response sweep for V_{DC}=2V, V_{AC1}=5V, V_{AC2}=1V, Ω_1= variable.

The bandwidth can be further increased if more than two sources of excitation are applied, since each new frequency gives rise to two new resonance peaks around the primary resonance. Figure.12 shows simulation results of a case where the mirror is excited with four AC frequency sources. It can be observed that there are six resonances surrounding the primary resonance; each associated with the respective fixed frequencies, which in this case are 100Hz, 200Hz and 350Hz. It can be observed that the bandwidth of resonators can be effectively increased without introducing any complexity in the design or fabrication.

6.2 Energy Harvester Applications

Contrary to the previous case, where the fixed frequency was given a value close to zero, if the magnitude of the fixed frequency is set very close to the primary natural frequency, the additive type resonance can be activated at a very small frequency range (close to 0 Hz). Figure.13 shows the effect of setting the fixed frequency very close to the primary natural frequency based on experimental data. It can be observed that very high amplitude peaks are activated between 100-300 Hz depending upon the fixed frequency value. However, we cannot observe anything in the case of a single source excitation (V_{AC1}=0). Also in this Figure, the amplitude of the sub resonance is very high and is spread across a wide range of frequencies when the fixed frequency is very close to the natural frequency i.e. 6.4 kHz. This can be promising for energy harvesting; since it provides the system with resonances of very high amplitudes at very low frequency ranges regardless of the natural frequency of the system. It also allows targeting any frequency range where these energy harvesters are

desired to operate, which otherwise is possible only by changing the design and refabricating a new device. Of course, the energy efficiency of adding an external source at a fixed frequency to activate the combination resonance needs to be investigated in details before judging on the suitability of this method and its feasibility.

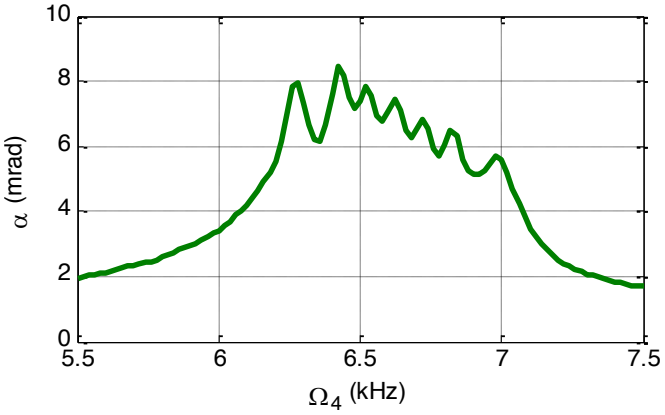

Figure. 12. Simulated frequency sweep for V_{DC}=1.5V, V_{AC1}=1.85V, V_{AC2}=1.85V V_{AC3}=2.5V, V_{AC4}=2.5V, Ω_1= 100 Hz, Ω_2= 200 Hz, and Ω_3= 350 Hz.

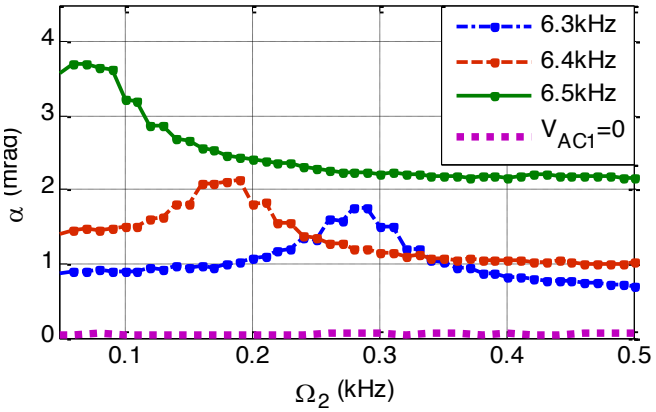

Figure. 13. Measured frequency sweep for V_{DC}=2V, V_{AC1}=5V, V_{AC2}=1V, Ω_1= variable.

7. Conclusions

Multi and mixed-frequency excitation has been studied both theoretically and experimentally based on a Polyimide micro-mirror. The mixed frequency excitation can be effectively used in resonators and resonant sensors to increase their bandwidths, by pushing the combination resonances close to their primary natural frequencies and by maintaining the overall amplitude in the vicinity of the primary natural frequency. Furthermore, it is possible to implement this method for energy harvesters to force the combination resonances to small range of few hundred Hertz and to maintain very high amplitude at that range. All of this is enabled due to the precise control over the amplitude and frequencies of these combination resonances, provided by the mixed-frequency excitation.

8. ACKNOWLEDGMENTS

This work has been supported through King Abdullah University of Science and Technology (KAUST) research funds.

9. REFERENCES

[1] Nayfeh A H, Younis M I and Abdel-Rahman E M. 2007. Dynamic pull-in phenomenon in MEMS resonators *Nonlinear Dynamics* **48** 153-63

[2] Li P, Hu R and Fang Y. 2007. A new model for squeeze-film damping of electrically actuated microbeams under the effect of a static deflection *Journal of Micromechanics and Microengineering* **17** 1242

[3] Krylov S and Maimon R. 2004. Pull-in dynamics of an elastic beam actuated by continuously distributed electrostatic force *Journal of vibration and acoustics* **126** 332-42

[4] Yamaguchi H, Okamoto H and Mahboob I. 2012. Coherent control of micro/nanomechanical oscillation using parametric mode mixing *Applied Physics Express* **5** 014001

[5] Mahboob I, Nier V, Nishiguchi K, Fujiwara A and Yamaguchi H. 2013 Multi-mode parametric coupling in an electromechanical resonator *Applied Physics Letters* **103** 153105

[6] Yamaguchi H and Mahboob I. 2013. Parametric mode mixing in asymmetric doubly clamped beam resonators *New Journal of Physics* **15** 015023

[7] Mahboob I and Yamaguchi H. 2008. Piezoelectrically pumped parametric amplification and Q enhancement in an electromechanical oscillator *Applied Physics Letters* **92** 173109

[8] Mahboob I, Mounaix M, Nishiguchi K, Fujiwara A and Yamaguchi H. 2014. A multimode electromechanical parametric resonator array *Scientific reports* **4**

[9] Younis M I and Alsaleem F. 2009. Exploration of new concepts for mass detection in electrostatically-actuated structures based on

nonlinear phenomena *Journal of Computational and Nonlinear Dynamics* **4** 021010

[10] Zhang W and Turner K L. 2004. A mass sensor based on parametric resonance. In: *Proceedings of the Solid State Sensor, Actuator and Microsystem Workshop, Hilton Head Island, SC,* pp 49-52

[11] Fargas-Marques A, Casals-Terré J and Shkel A M. 2007. Resonant pull-in condition in parallel-plate electrostatic actuators *Microelectromechanical Systems, Journal of* **16** 1044-53

[12] Mahboob I, Flurin E, Nishiguchi K, Fujiwara A and Yamaguchi H. 2011. Interconnect-free parallel logic circuits in a single mechanical resonator *Nature communications* **2** 198

[13] Adair R, Chase L and Payne S A. 1987. Nonlinear refractive-index measurements of glasses using three-wave frequency mixing *JOSA B* **4** 875-81

[14] Levenson M. 1974. Feasibility of measuring the nonlinear index of refraction by third-order frequency mixing *Quantum Electronics*

[15] Garcia R and Herruzo E T. 2012. The emergence of multifrequency force microscopy *Nature nanotechnology* **7** 217-26

[16] Forchheimer D, Platz D, Tholén E A and Haviland D B. 2012. Model-based extraction of material properties in multifrequency atomic force microscopy *Physical Review B* **85** 195449

[17] Hornstein S and Gottlieb O. 2012. Nonlinear multimode dynamics and internal resonances of the scan process in noncontacting atomic force microscopy *Journal of Applied Physics* **112** -

[18] Westra H, van der Zant H and Venstra W. 2012. Modal interactions of flexural and torsional vibrations in a microcantilever *Ultramicroscopy* **120** 41-7

[19] Ruppert M G, Fairbairn M W and Moheimani S. 2013. Multi-mode resonant control of a microcantilever for Atomic Force Microscopy. In: *Advanced Intelligent Mechatronics (AIM), 2013 IEEE/ASME International Conference on*: IEEE) pp 77-82

[20] Karvinen K and Moheimani S. 2014. Control of the higher eigenmodes of a microcantilever: Applications in atomic force microscopy *Ultramicroscopy* **137** 66-71

[21] Sebastian A, Shamsudhin N, Rothuizen H, Drechsler U, Koelmans W W, Bhaskaran H, Quenzer H J, Wagner B and Despont M. 2012. Note: Micro-cantilevers with AlN actuators and PtSi tips for multi-frequency atomic force microscopy *Review of Scientific Instruments* **83** 096107

[22] Erbe A and Blick R H. 2002. Silicon-on-insulator based nanoresonators for mechanical mixing at radio frequencies *Ultrasonics, Ferroelectrics and Frequency Control, IEEE Transactions on* **49** 1114-7

[23] Pourkamali S, Abdolvand R, Ho G K and Ayazi F. 2004. Electrostatically coupled micromechanical beam filters. In: *Micro Electro Mechanical Systems, 2004. 17th IEEE International Conference on.(MEMS)*: IEEE) pp 584-7

[24] Wong A-C and Nguyen C-C. 2004. Micromechanical mixer-filters (" mixlers") *Microelectromechanical Systems, Journal of* **13** 100-12

[25] Fedder G K. 2005. CMOS-MEMS resonant mixer-filters. In: *Electron Devices Meeting, 2005. IEDM Technical Digest. IEEE International: IEEE) pp 274-7*

[26] Chen F, Brotz J, Arslan U, Lo C-C, Mukherjee T and Fedder G K. 2005. CMOS-MEMS resonant RF mixer-filters. *In: Micro Electro Mechanical Systems, 2005. MEMS 2005. 18th IEEE International Conference on: IEEE) pp 24-7*

[27] Koskenvuori, M., and I. Tittonen.. 2008. GHz-range FSK-reception with microelectromechanical resonators. *Sensors and Actuators A: Physical 142.1: 346-351.*

[28] Lin, A. H., Lee, J. Y., Yan, J., & Seshia, A. A. 2010. Methods for enhanced electrical transduction and characterization of micromechanical resonators. *Sensors and Actuators A: Physical, 158(2), 263-272.*

[29] Gouttenoire, V., Barois, T., Perisanu, S., Leclercq, J. L., Purcell, S. T., Vincent, P., & Ayari, A. 2010. Digital and FM Demodulation of a Doubly Clamped Single-Walled Carbon-Nanotube Oscillator: Towards a Nanotube Cell Phone. *Small, 6(9), 1060-1065.*

[30] Sazonova, V., Yaish, Y., Üstünel, H., Roundy, D., Arias, T. A., & McEuen, P. L. 2004. A tunable carbon nanotube electromechanical oscillator. *Nature, 431(7006), 284-287.*

[31] Witkamp, B., Poot, M., & van der Zant, H. S. 2006. Bending-mode vibration of a suspended nanotube resonator. Nano letters, 6(12), 2904-2908.

[32] Hornbeck, L. J. 1993. Current status of the digital micromirror device (DMD) for projection television applications. In Electron Devices Meeting, 1993. IEDM'93. Technical Digest., International (pp. 381-384). IEEE.

[33] Dudley, D., Duncan, W. M., & Slaughter, J. 2003. Emerging digital micromirror device (DMD) applications. In Micromachining and Microfabrication (pp. 14-25). International Society for Optics and Photonics

[34] Tsai, C. Y., & Chen, T. L. 2010. Design, fabrication and calibration of a novel MEMS logic gate. Journal of Micromechanics and Microengineering, 20(9), 095021.

[35] Tsai, C. Y., Kuo, W. T., Lin, C. B., & Chen, T. L. 2008. Design and fabrication of MEMS logic gates. Journal of Micromechanics and Microengineering, 18(4), 045001.

[36] Younis M I. 2011. MEMS Linear and Nonlinear Statics and Dynamics: Mems Linear and Nonlinear Statics and Dynamics vol 20: Springer).

[37] Timoshenko S P and Goodier J N. 1970. Theory of Elasticity. McGraw-Hill, NewYork.

[38] A. H. Nayfeh, Introduction to perturbation techniques: John Wiley & Sons, 2011.

[39] Elnagar A and El-Bassiouny A. 1992. Response of self-excited three-degree-of-freedom systems to multifrequency excitations *International journal of theoretical physics* **31** 1531-48

[40] ANSYS® Academic Research, Release 15.0, Help system, Structural analysis guide, ANSYS, Inc.

[41] Ramini A, Younis M I and Su Q T. 2013. A low-g electrostatically actuated resonant switch Smart Materials and Structures 22 025006

[42] Butcher J. C. 1987, The numerical analysis of ordinary differential equations: Runge-Kutta and general linear methods: Wiley-Interscience.

[43] Acar. C, Shkel. A. 2008. MEMS vibratory gyroscopes.Springer.

Preparing transperence condictive glass by using APCVD system

Nagam T. Ali[1], Baha T. Chiad [2] Nathera A. Ali[2]
Talib Zeedan Taban Al-mosawi [3]
[1]Minstry of science and technology, Baghdad (Iraq)
[2]Phsices Department, College of Science, University of Baghdad,
[3]Phsices Department, College of Science, University of Al-Mustansiriya
Nagam2105@gmail.com, Tel. 07903182831[2]

Abstract

In this research tin oxide doped with Indium (SnO_2: In) was prepare by using a chemical vapor deposition method under normal atmospheric pressure APCVD. Several films were prepared by using different ratios of indium (Sn: In = 1: 0.1,1: 0.3,1: 0.6,1: 0.8) at glass substrate temperature (450^0 C) and the flow of gas (1.5 L / M) and a time of 10 minutes and using tin chloride (SnCl2: 5H2O) purity of 99.98% as starting material. The survey was conducted using an X-ray diffraction (XRD) were, also the surface morphology by using atomic force microscope (AFM). Optical properties have been studied by using UV-Vis spectroscopy. Electric properties studied by (Van Der Pauw) principle. through spectroscopic study of these films was found to have a high transmittance in the visible region from the spectrum and high reflectivity to the infrared region, which qualifies it for use as Anti-reflection coating in same time very low resistivity(2.07*10-7 Ω.cm)..

Keywords: SnO_2, thin films, APCVD, conductive glass.

Introduction

Tin Oxide (SnO_2) is a wide band gap n- type semiconductor, which can be efficiently used as transparent conducting oxide. Because of its unique electrical and optical properties, SnO_2 thin films have been widely used in photocell devices, and opt-electrical displays. The films are chemically inert, mechanically hard and can resist high temperature. Indium tin oxide (ITO) thin film is a highly degenerate n-type semiconductor which has a low electrical resistivity of 2 – 4.3 x 10-24 Ω-cm. The low resistivity value of ITO films is due to a high carrier concentration because the Fermi level (EF) is located above the conduction level (EC).The degeneracy is caused by both oxygen vacancies and substitutional tin dopants create d during film deposition. The carrier concentration of high conductivity ITO films is in the range of 1020-1021 cm^{-3}.

Doped or undoped SnO_2 films can be prepared by many methods such as spray Pyrolysis, electron beams evaporation, chemical vapor deposition, sputtering. APCVD is the most widely used technique to deposits materials quickly. High quality films are produced by APCVD. In the present study, pure and Indium doped SnO2 thin films were prepared by thermal evaporation technique with different growth parameters.

Material and method

Doped and undoped Tin oxide thin film prepared by homemade cold wall reactor APCVD with glass substrate, figure (1) . $SnCl_2.5H_2O$ was used as start material with O_2 gas. The glass slides substrate were cleaned ultrasonically by Trichloroethylene (TCE), acetone, ethanol followed by distilled water and dry with N_2.the deposition temperature was 450 ^{0}C and gas flow rate was(1.5 L/min) and deposition time is about 10 min. X-Ray diffraction (CuKα) radiation with a wavelength λ =1.5418 Å at 2θ values between 20° and 60 was used to study the crystal structure. (SEM) and (AFM) were used for investigate the morphology and roughness of surface. The optical properties were studied by UV-Visible spectroscopy. Thickness and reflectivity was measured by (TEProbe 2.4), the electric measurement had made by Hall measurements.

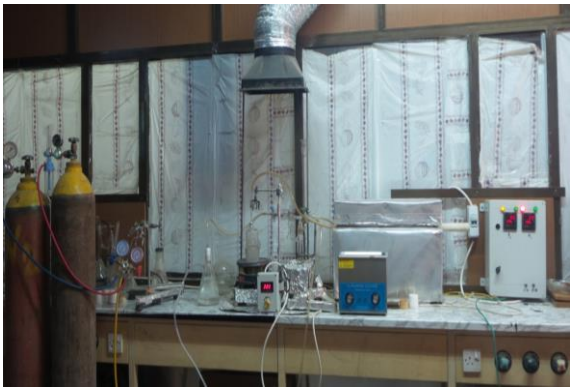

Figure (1) atmospheric pressure chemical vapor deposition system (APCVD)

Results and discussion

In this study doped and undoped SnO_2 have been prepare by using (APCVD) system. The initial results show for undoped tin oxide films a high transparency for UV-Vis region about (80-89)% with a polycrystalline and uniformity in grain distribution depending on XRD, atomic force microscopy and scanning electron microscope, grain size was (16.75) nm and roughness was (1.82) nm, electric measurement show a low conductivity ($2.95x10^{-5}$)1/Ω.cm and high resistivity ($3.38x10^{+4}$) Ω.cm. As show in figures (2, 3, 4, 5, 6) Sequentially.

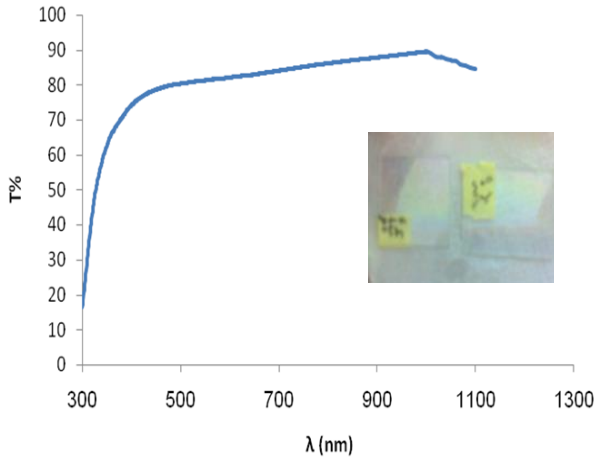

Figure (2) illustrating the transmittance of SnO_2 thin fim at glass substrat temperature (450^0 C)

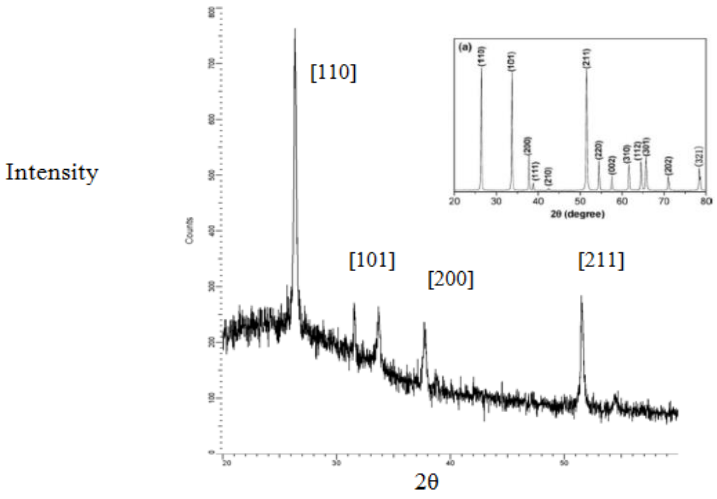

Figure (3) XRD spectra for undoped tin oxide film

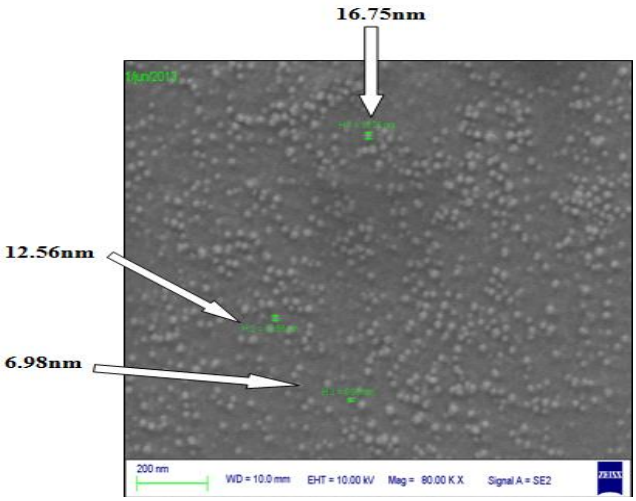

Figure (4) SEM image for undoped tin oxide film

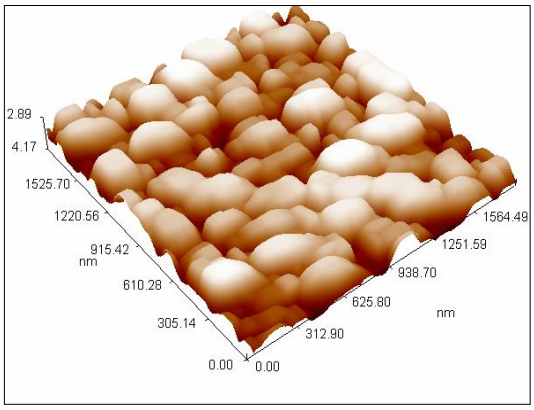

Figure (5) surface morphology by AFM image in 3-D for undoped tin oxide film

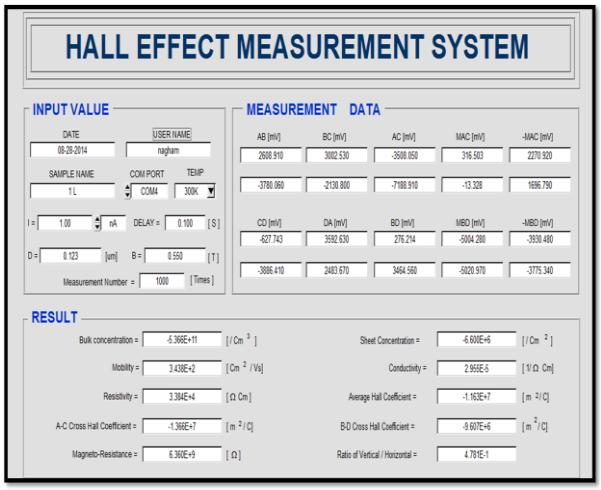

Figure (6) Hall Effect measurement for undoped tin oxide film

For doped SnO_2 with indium , many ratio would take (Sn: In= 1:0.1,1:0.3,1:0.6,1:0.8) trying to get a less value for resistivity where ,it had studied its optical and surface morphology properties as it seen in figures(7),(8) maximum transmittance was about (80)% for (1:0.8), surface roughness increase with doping ratio where the grain size became larger and more uniform distribution.

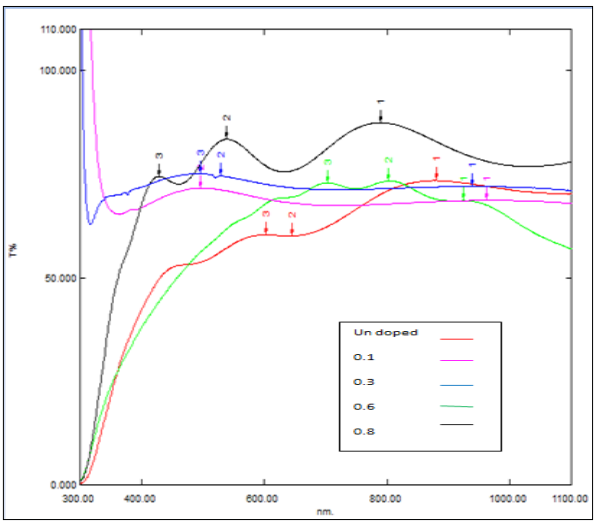

Figure (7) transmittance curve of undoped and doped tin oxide with indium with different ratios

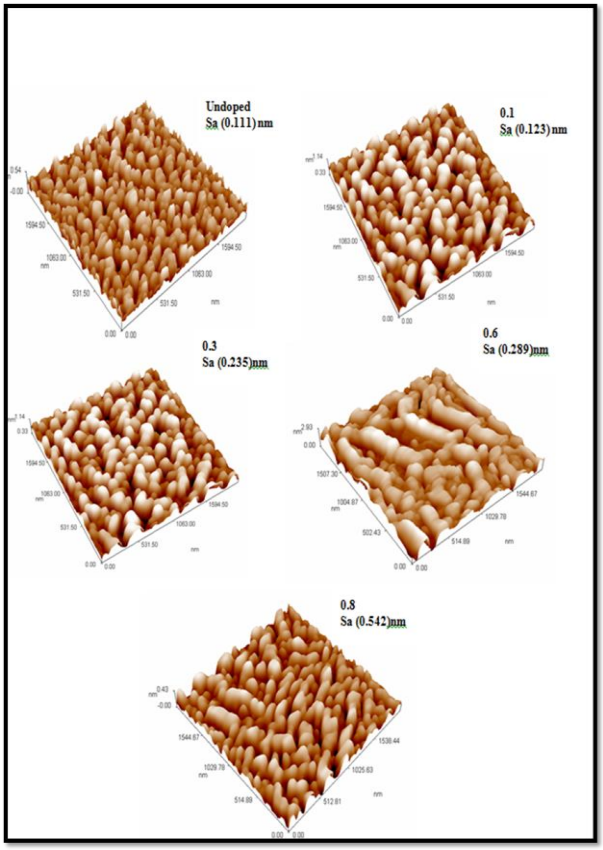

Figure (8) 3-D AFM image for un doped and doped tin oxide with indium with different ratios

Through thickness and resistivity measurement it's seen that maximum reflection was for doped tin oxide (1:0.6) with max conductivity ($1.06*10^{+6}$)1/Ω.cm this because the conductivity and reflectivity for IR depend on the same intrinsic properties like mobility and carrier concentration. As it shown in figure (9) and table (1).

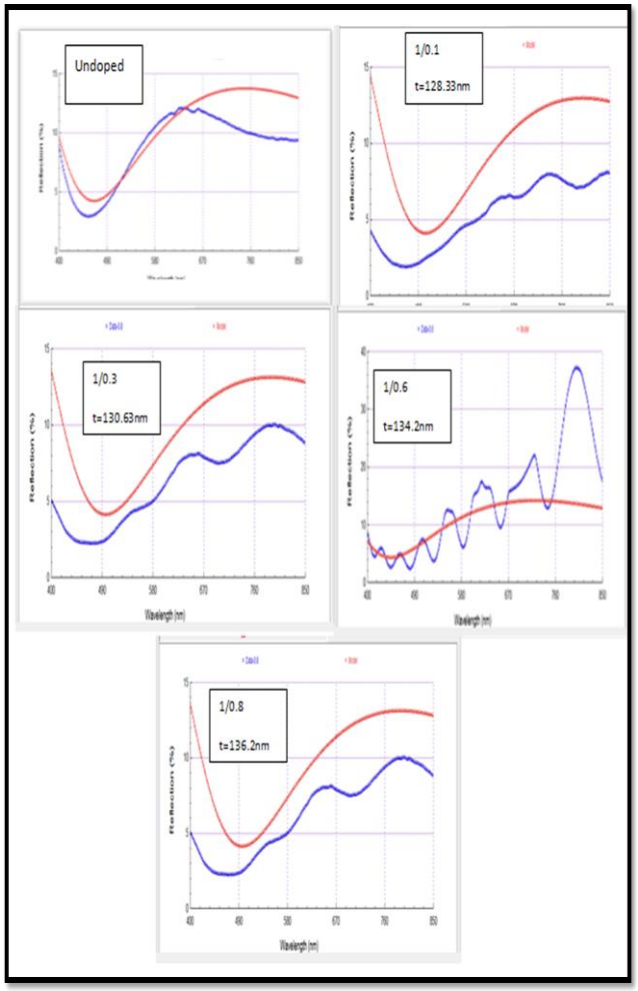

Figure (9) thickness and reflectivity measurement for undoped and doped tin oxide doped with indium with different ratios

Table (1) Hall measurements for undoped and doped tin oxide with indium with different ratios

Sample	R_H(m2/c)	Carrier type	N_{sheet} (cm^{-1})	σ (1/Ω.cm)	μ_H(cm2/V.c)	Resistivity (Ω.cm)
Undoped (SnO_2) IL	$-1.163*10^{+7}$	n	$1.75*10^{+6}$	$1.715*10^{-5}$	$6.11*10^{+2}$	$5.83*10^{+4}$
(SnO_2-In) (1-0.1)	$-2.09*10^{+6}$	n	$3.88*10^{+7}$	$3.92*10^{-4}$	$8.20*10^{+1}$	$2.54*10^{+4}$
(SnO_2-In) (1-0.5)	$-3.65*10^{+7}$	n	$2.18*10^{+6}$	$8.77*10^{-6}$	$8.20*10^{+1}$	$1.13*10^{+5}$
(SnO_2-In) (1-0.6)	$-7.55*10^{-7}$	n	$1.85*10^{+19}$	**$1.06*10^{+6}$**	$8.01*10^{+0}$	**$2.07*10^{-7}$**
(SnO_2-In) (1-0.8)	$-4.30*10^{-6}$	n	$9.42*10^{+16}$	$4.83*10^{+4}$	$2.08*10^{+1}$	$9.4*10^{-5}$

Conclusions

1- Tin oxide (SnO_2) films were prepared successfully using chemical vapor deposition system under normal atmospheric pressure reactor with cold wall reactor locally manufactured.
2- We obtained thin film with good visual quality and transparent to visible light.
3- We obtained reflective coating for IR region of the spectrum.
4 -we obtained thin films with high conductivity and resistivity than we can use it as transparent electrodes**.**

References:

Afify, H.H., F. S. Terra and R. S. Momtaz. (1996). Substrate temperature effects on the tin oxide.

Alam, M. J. and D.C. Cameroon. (2000). Optical and electrical properties of transparent conductive ITO thin films deposited by sol-gel process. Thin Solid Films 377-378: 455-459.

Debajyoti, Das and R. Banerjee (1987) Properties of Electron Beam Evaporated Tin oxide Films.Thin Solid Films.147: 321.

Davolos, C.A. Achete, and M. Cremona(2007) Indium tin oxide films prepared via wet chemical route. Thin Solid Films 516(2-4): 193-197.

Manoj, P.K., Benny Joseph, V.K. Vaidyan and D. Sumangala Devi Amma(2007)Preparation and characterization of indium-doped tin oxide thin films. Ceramics International.33(2), 273.

Mika Yamaguchi, A. Ide-Ektessabi, H.Nomura and N. Yasui. (2004) Characteristics of indium tin oxide thin films prepared using electron beam evaporation. Thin solid films 447-448: 115.

POLLUTION IN THE CHANNEL OF OUED RIGH AND DIEBACK PALM

BENGUERGOURA LARADJ Samia* and REMINI Boualem**

*Department of Industrial Chemistry, Blida University, Blida 9000, Algeria, samialaradj@yahoo.fr,
**Department of Water Science, Blida University, Blida 9000, Algeria, reminib@yahoo.fr

Abstract

For the 150 km long, the ancestral canal of Oued Righ evacuates water leachates into the Chott Melghir that includes 50 oases. The excess water caused by discharges of urban sewage and drainage water, caused a huge problem, which is the upwelling of groundwater, which led to an imbalance in the valley. water table near the soil surface, is one of main cause of soil sterilization of several agricultural areas in the Valley. The physico-chemical and water pollution of the canal, and the water table have shown that the quality of these waters present very high salinity (class C5), with electrical conductivity up to 26.30 ms/cm, an SAR> 28 (S4 class), the water hardness and The values of organic matter (OM), and dry residue are very important, Thus canal water is mostly of very poor quality, charged with mineral salts, it is a brackish water of the sodium chloride facies.

Keywords: Canal – Degradation – Water – Palm – Sol – Oued Righ

1. Introduction

The Oued Righ valley, located east of the septentrional Sahara, is a broad asymmetrical syncline pit characterized by the existence of a sandy soil, mainly siliceous and formed pure quartz therefore insoluble [1]. The system of agricultural production in this region is essentially the phoéniculture that constitutes its main frame. If the valley of Oued Righ escaped the phenomenon of recovered water before the eighties, thanks to one big channel said (Oued Righ) which extends over a length of 136 km and acts role of main collector of excess water. The canal transits a rate of approximately 5 m^3/s, or about 120 to 160 million m^3/year [2. However over the years, the entire oasis shows a progressive fall in quantity and quality. This phenomenon has resulted in increased rates of discharge of sewerage and drainage water (Figure 1). A portion of the wastewater is no pre-treatment, joined the main collecting duct. The absence of natural outlets for receipt of waste, adequacy and effectiveness have caused of imbalances. We then observe flooding caused by the back water in the oasis, and the depletion of groundwater resulting in the wound thereof and salinization. The oases of the valley of Oued Righ could be rightly called oasis sick of too much water [3. Many palms are flooded in winter (Palm Tinedla, Djemaa, Ferdjaouenne and El Goug). Secondary salinization after irrigation with highly mineralized water, permanent hardness resulted suffocation palms of Oued Righ [4] (Figure 2). In this perspective we sum fixed as objective analysis of water discharges at different points in the collecting duct which communicates with the water table, and the impact of these waters and the relationship between the channel and the water on the degradation of palm cultivation.

Fig.1. Discharge point of wastewater

Fig.2. Degradation of palm

2. Presentation of the study area

Region of Oued Righ is located in the south eastern Algeria (Figure.3), it spreads over 150 km long . It is located in two wilaya: Ouargla and El Oued. It is bordered to the north by the plateau Still, to the east by the Great Erg Oriental in the South by the extension of the Grand Erg Oriental and west by the sandstone plateau. This region is characterized by an elongated depression from south to north. Highest coast is 100 meters in El Goug upstream and -30 meters in Chott Merouane downstream [5]. The slope is generally very low (1 ‰). This slope allows excess water to flow to the north. Region of Oued Righ has nearly 50 oases and covers around 25,000 ha of palm . These oases are aligned on a north-south axis.

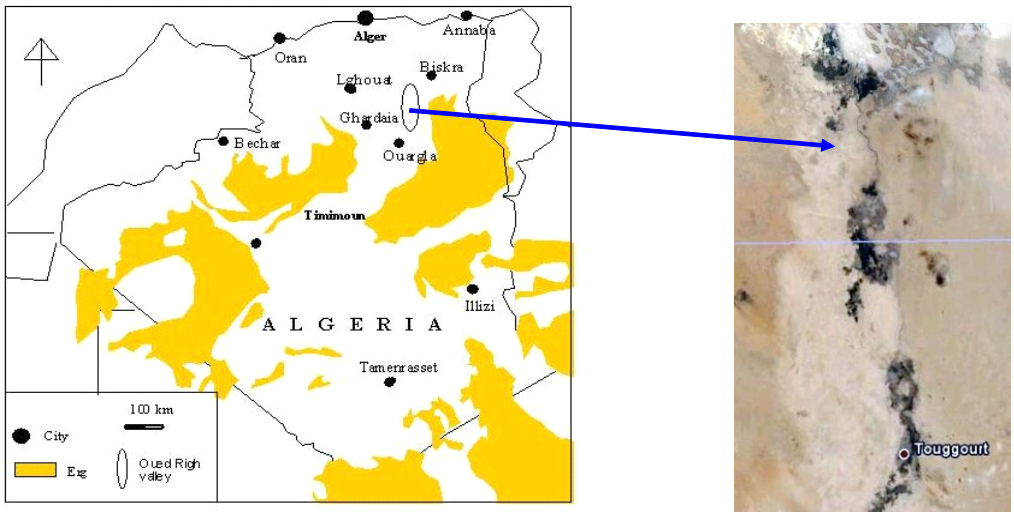

Fig.3. Location of the valley Oued Righ

3. Materials and methods

Nine water samples were collected during the period of February 2009, May 2010 and October 2010 on a 30 km stretch of the canal. On groundwater, five samples were collected starting from the station Kerdeche to Sidi Slimane (46 km). The samples were collected manually in plastic bottles on the identification of each point. The assay procedures are

derived from standard methods of analysis. Different analytical methods have been used as metric methods, electrochemical or spectroscopic.

4. Results and Discussion

4.1. Study of physico-chemical parameters and pollution in the canal

Temperature affects the degree of evapotranspiration and therefore it acts on the salinity of the water. In this study, the temperature is generally variable with an average of 22.5 °C. The results obtained for the canal waters and the waters of the groundwater table during the period (2009-2010) are shown in (Tables 1 and 2).

The pH and electrical conductivity (EC) is very high in the canal (fig. 4). However, these values have a maximum at the station 12 of the water table. The canal water is very hard water. The waters of station 12 at the tablecloth have a maximum hardness[6].

Table 1. Parameters of water quality of Oued Righ channel

pH	7.3 at 8.3
E.C (ms/cm)	1500 at 26300
T.H (°f)	73 at 582
Dry residue (mg/l)	2249 at 16528
O.M (mg/l)	44.5 at 111

Table 2. Parameters of water quality groundwater

pH	7 at 7.71
E.C (ms/cm)	6.04 at 17.90
T.H (°f)	219 at 408
Dry residue (mg/l)	5141 at 14920
O.M (mg/l)	7.93 at 52.86

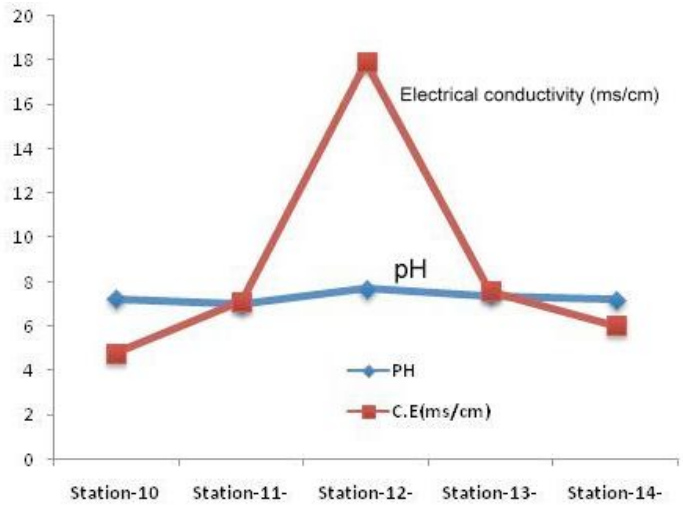

Fig.4. Evolution of pH and EC of water of groundwater

The results obtained for the dry residue are very important for the majority of canal water (May 2010 and October 2010) due to the evaporation of water (Figure 5). Indeed content of

salts can exceed 12 g/l of dry residue in most solutions discharges into the canal. It should be noted that the upper limit allowed is 10 g/l for sustainable agriculture[7. One can notice that the values of the dry residue arrive until 14920 mg/l at station 12 or the water becomes unpleasant (figure 6).

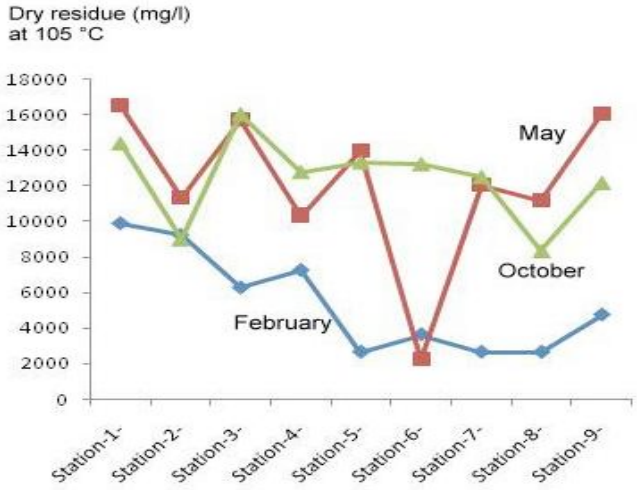

Fig.5. Spatio-temporal evolution of the dry Residue of water channel

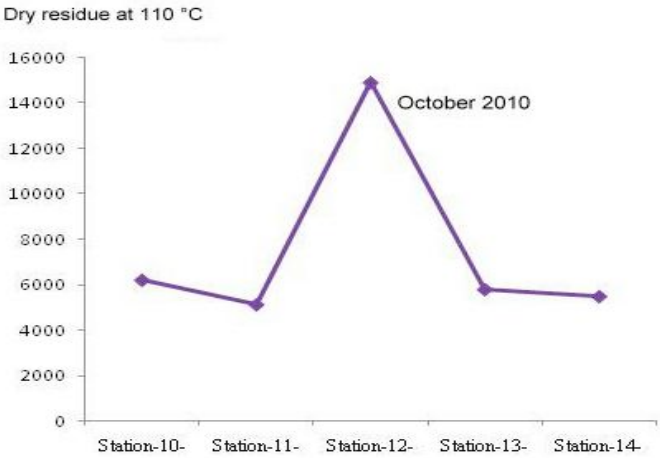

Fig.6. Evolution of dry residue in water groundwater

According to the classification of sewage water with a level of organic materials OM> 15 mg/l is classified as highly polluted water. We see in (Figure 7) that the canal this rate of organic materials OM> 50 mg/l. Next spatiotemporal evolution, the rate of organic matter ranges from 46 mg/l (station 2) to 111 mg/l (station 9) during the month of October 2010. However, this wastewater contaminates the groundwater, which was confirmed at the station 12 (figure.8). In this case, all the benefits of organic matter to the soil, such as: better porosity, good permeability, good ventilation, better soil warming [8]and good water retention [9] will be absent. Organic matter releases minerals that are essential to the nutrition and development of cultures[10]. However salinity exists in the canal waters and groundwater is the main cause of decline palms[11]. The increase in soil salinity inhibits its activity and therefore the microbiological decomposition of organic matter. This leads to a decrease in crop yields.

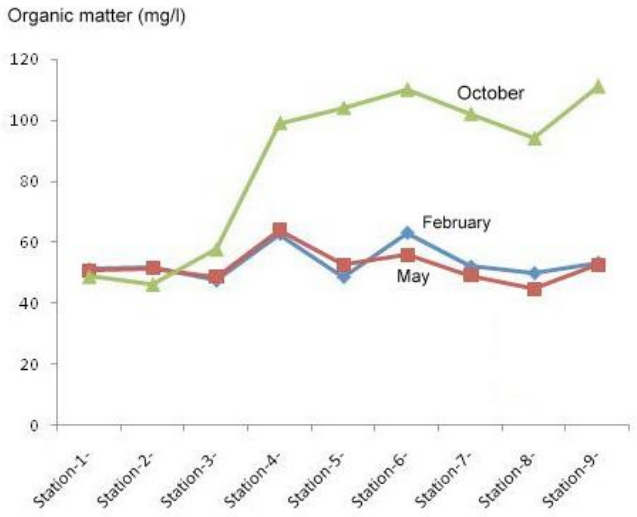

Fig.7. Spatio-temporal evolution of Organic Matter of water channel

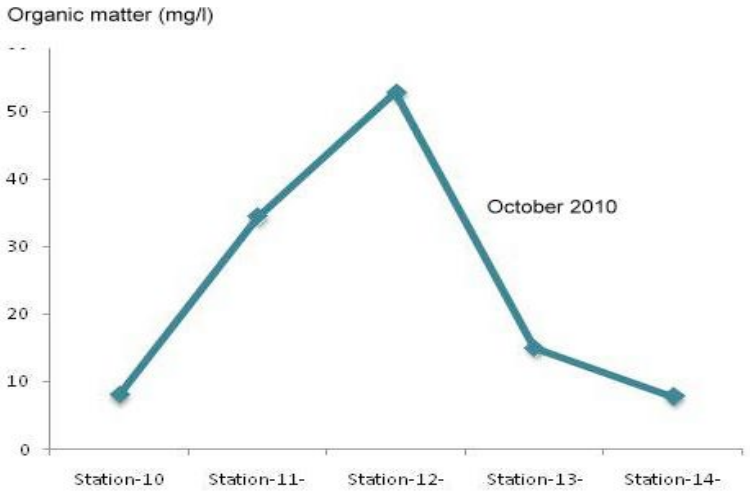

Fig.8. Evolution of organic matter in water groundwater

4.2. Hydrochemistry of canal water and groundwater

Agricultural practices, including the establishment of irrigation systems have an effect on water quality. The mineral salts in irrigation water have an impact on the soil and plants. They can cause changes in soil structure and disrupt the development of vegetation[12]. The distribution of palm and associated crops in the ground root system gives an overview on the degradation of phoeinicicole heritage due to the contamination of groundwater by salinity and wastewater channel. To assess the water quality of the Oued Righ channel and water of groundwater, we used Schoeller Berkaloff diagram to represent the chemical facies of several water samples. Each sample is represented by a broken line. The concentration of each chemical element is represented by a vertical line on a logarithmic scale. When the lines are growing, a chemical change of facies is demonstrated [13]. We notice that the mineralization Cl- and Na + is dominant almost at 9 stations along the Canal, followed by mineralization ions SO_4^{2-} and Ca^{2+}, or even a high concentration of Mg^{2+} ions. We point out on the Sodium Chloride Facies majority (figure 9 (a and b)), with absence of bicarbonate facies. However there is a clear dominance of sodium ion, followed chloride and sulfate ions, at the station 12 groundwater which is grown all around the canal area.This confirms that the dominant

hydrochemical facies is a chloride-sodium. So mineralization waters of the web is linked to Cl^- and Na +. The line of station 10 which has a higher concentration of Sodium ions that Sulfate ions give the type of facies Sulfated - Sodium. The facies type bicarbonate waters groundwater is absent.

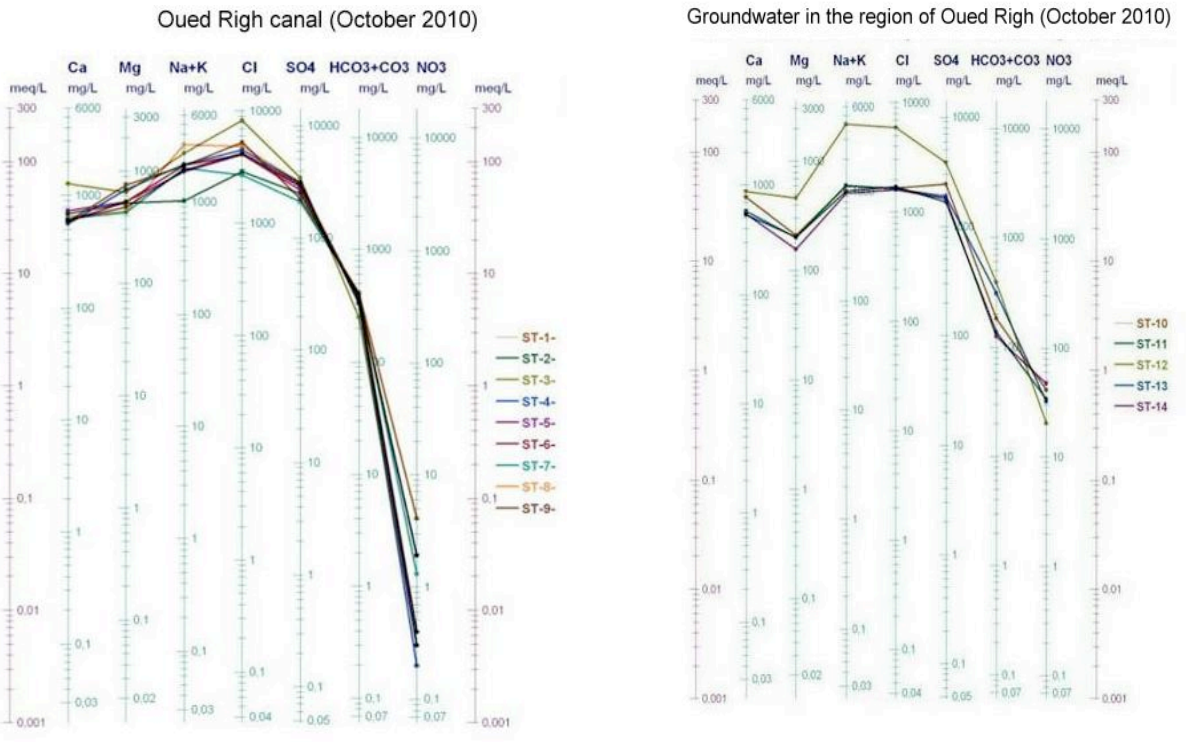

a) Canal **b) Ground water**

Fig.9. Schoeller diagram Berkaloff to the canal and water groundwater (October 2010)

4.3. Water-soil relationship and its impact on the culture of the date palm

The Region to Oued Righ is characterized by low rainfall and high evaporation. Its underground water is too loaded with chlorides and sulfates or the existence of the risk of soil salinization. A study requires a good estimate of some parameters of salinity in relation to agricultural use in the canal waters and the waters of the aquifer. This risk is determined using the value of Sodium absorbent SAR (Sodium Absorption Ratio). For the same conductivity, the risk is even greater than the coefficient is higher. Proposed by Richards classification is very useful to characterize and reliable irrigation water.

The results obtained by the Richards diagram of the different stations water channel (Figure 10 (a and b)) show that they are class C5S3. In this case, the water is high mineralization. They are used only in exceptional circumstances. The C5S4 class affects virtually the majority of canal water. The waters are strongly mineralizes. There is not recommended for irrigation. For water the water table, we note the C4S3 and C5S3 classes for stations 10, 11 and 14 used only in exceptional circumstances. The C5S4 class appears at stations 12 and 13 advised not for irrigation. Water quality and water channel of the web are of very poor quality. So, there is a possible contamination between the two.

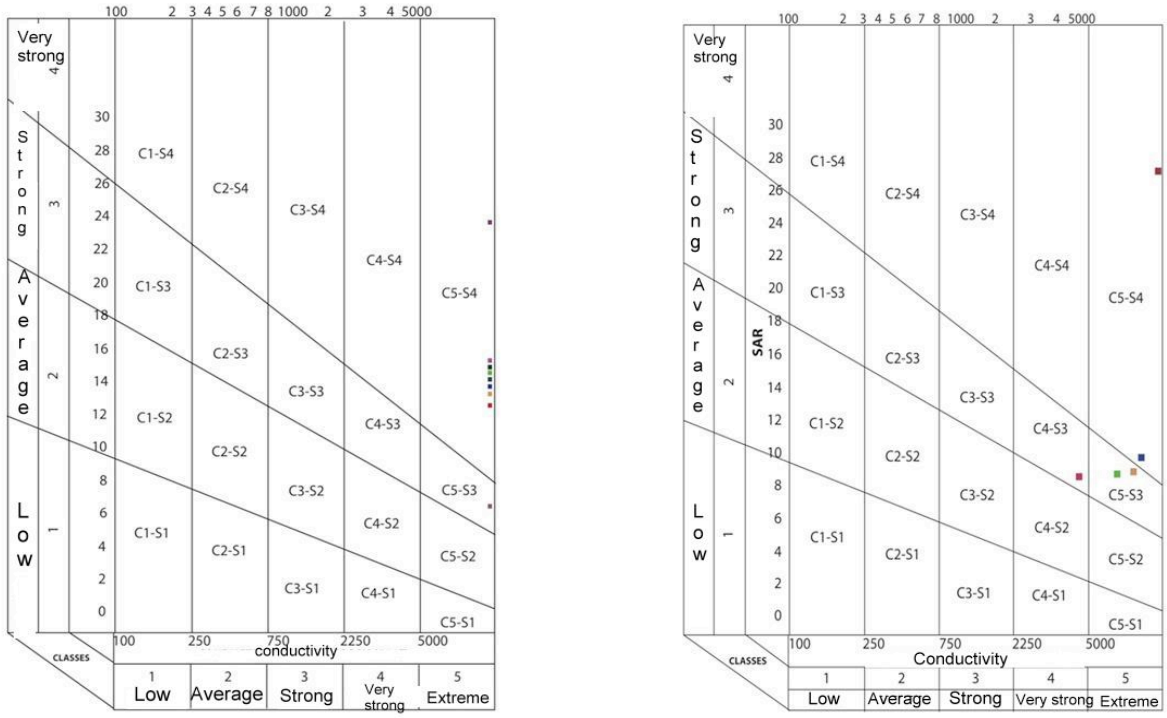

a) Canal *b) Ground water*

Fig.10. RICHARDS diagram of canal water and groundwater

Conclusion

The region of Oued Righ is characterized by the presence of sandy soil mainly siliceous and trained so insoluble pure quartz. The water table is contained in the clay-evaporite sandy quaternary levels. The piezometric surface thereof has a regular fluctuation in this region relatively flat where the waters are struggling to evacuate the static level of the shallow aquifer fed by the drainage and urban waste Touggourt increased steadily thus approaching the soil surface. The comparison of concentrations of the chemical elements of the water channel has highlighted the dominance of saliferous Gypsiferous ions and ions versus acquisition carbonate in salinity. The canal is excessively salty, very hard, slightly basic, and hyper-chlorinated global chemical facies sodium. Irrigation water is of very poor quality and mostly belongs to C5S4 class. As for the environmental aspect of the sources of pollution of the channel, values in Sec residue and organic matter are higher than the national and international standard.

The pollution is felt at the station Kardéche upstream channel where the flow velocity is low. It may be noted that pollution also increases the station Zaouia El Abidia or the width and depth of the channel decreases. So the speed of the flow of water also decreases.

The monitoring of the evolution of the water quality of the water table surrounding the channel shown that the contamination of the water is very pronounced at station 12 (station Sidi Slimane). Degraded water channel are routed in areas that favored the percolation of groundwater contamination. The combined action of a climate characterized by intense evapotranspiration and the presence of a shallow water table that most soils undergo secondary salinization. We even noticed undesirable phenomena such as degradation of palm trees surrounding the canal.

References

[1] Benhaddya M. 2007. Contribution to the inventory of trace elements in soils and groundwater in the region of the Oued Righ. Memory of magister. University of Oum El Bouaghi, 131p.

[2] Khadraoui A., 2005. Soil and agricultural water in oases of Algeria, characterization, constraints and development proposals. EMPAC Editions, Algeria, 324p.

[3] Cote M, 1998. Patients' oasis of too much water. Journal drought, No. 9, pp. 123-30.

[4] SOGREAH 1970. Participation in the development of the Oued Righ. Agropedological study. Manuscript, 201p.

[5] Dubost D., 1991. Ecology, Land and Agricultural Development Algerian oasis. PhD in geography and planning in the Arab world. Université François Rabellais Tours (France), Volume 2.

[6] Benguergoura Laradj,S and Remini,B, 2013.The releases of wastewater in the Oued Righ valley: the palm groves in decline, publisher, Taylor& Francis, London.V.52 –issue-10-12pp 2187-2192 .

[7] Djennane A., 1990. Finding status of areas south of Algerian oasis. National Board of dates, Algeria, Mediterranean option, Serie A, No. 11, the oasis agricultural systems.

[8] Mustin M., 1987. The management of compost organic matter. The agricultural use of composts and more generally organic materials. Dulux French Editions. Paris, 954p.

[9] Jones C. and Jacobsen J., 2001. Plant nutrition and soil fertility . Montana university, www.colostate.edu/depts/coopExt/TRA/plants/nutrient/PDF.

[10] Bollag et al, 1998. Interaction between soil minerals, organic compounds and microorganisms. Scientific Edition, Regist 404, Symposium No. 41.

[11] Rietz, D.N and Haynes,R.J, 2003. Effects of irrigation-induced salinity and sodicity on soil microbial activity. Soil biology & biochemistry 35, pp 845-854.

[12] Person, J, 1978. Irrigation and drainage in Tunisia problem of soil salinity and water. Bulletin of BRGM, 2nd series, section III, No. 2, pp. 143-151.

[13] Roland S, 2012. Diagrammes version ,5-9, graphTxt ,1-6 : http://www.Iha.Uvin-avignon.fr/LHA-Logitiels-htm